Novel Zinc Containing Phosphate Glasses for Glass–Ionomer Cements for Bone Cement Applications

by

Nasima Kanwal

Thesis submitted in partial fulfillment of the requirements of the Degree of Doctor of Philosophy
2014

School of Biological and Chemical Sciences
Queen Mary University of London, UK

Declaration

I, Nasima Kanwal, confirm that the research included within this thesis is my own work or that where it has been carried out in collaboration with, or supported by others, that this is duly acknowledged.

I attest that I have exercised reasonable care to ensure that the work is original, and does not, to the best of my knowledge break any UK law, infringe any third party's copyright or other Intellectual Property Right, or contain any confidential material.

I accept that the College has the right to use plagiarism detection software to check the electronic version of the thesis.

I confirm that this thesis has not been previously submitted for the award of a degree by this or any other university.

The copyright of this thesis rests with the author and no quotation from it or information derived from it may be published without the prior written consent of the author.

Signature: Nasima Kanwal

Date: 08/01/2014

Abstract

Glass-ionomer cements (GICs) are acid base reaction cements used in dentistry for restorative applications. In conventional GICs aluminosilicate glass is used to react with a polyalkenoic acid such as poly acrylic acid. Glass–ionomer cements have the potential to be used for bone cement applications, however there is a concern over the neurotoxicity of aluminium in the glass component of these cements. In this work zinc containing phosphate glass based glass–ionomer cement has been developed for the bone cement application. In this relation structure of zinc containing phosphate glasses in the system Na_2O:CaO:ZnO:P_2O_5 ranging from metaphosphate compositions to invert phosphate compositions has been examined. Various advanced techniques in solid state nuclear magnetic resonance (NMR) such as dipolar recoupling and solid state NMR of low γ quadrupolar nuclei (^{67}Zn and ^{43}Ca) and neutron diffraction have been employed. Special emphasis has been focused on structural role of zinc in glasses of different composition and the effect of different cations on coordination of zinc along with the effect on phosphate tetrahedra. ^{67}Zn and ^{43}Ca solid state NMR spectra of selected glass samples have been successfully acquired at ultrahigh field 900 MHz using Solid Echo pulse sequence. In addition solid state NMR spectra of two polymorphs of crystalline $Zn(PO_3)_2$ have also been acquired at 850 MHz using DFS–WURST–QCPMG pulse sequence in order to distinguish between the magnitude and orientation of electric field gradient (EFG) of zinc in octahedral and tetrahedral coordination.

Structure determined through various techniques has been related to the dissolution behaviour of glass compositions from metaphosphate to invert phosphate. A decrease in pH of surrounding medium has been observed due to the presence of zinc. Insertion of ZnO_4 tetrahedra between PO_4 tetrahedra has been observed in invert phosphate glasses with high zinc oxide content which renders them suitable for glass–ionomer cements. Glass–ionomer cement from glass composition $10Na_2O$:50ZnO:10CaO:$30P_2O_5$ and hydroxyapatite and, acrylic acid and vinyl phosphonic acid co-polymer has been produced successfully.

Acknowledgement

First of all I would like to thank my supervisors Dr Isaac Abrahams and Dr Natalia Karpukhina for their day to day help, support and guidance. I could not have imagined having better supervisors than them. I consider myself very fortunate to have supervisors with different expertise and being part of two different departments which expanded my knowledge of the structural chemistry of materials for practicing dentistry. I am especially very thankful to Dr Isaac Abrahams for spending so much time with me on neutron diffraction data analysis.and RMC calculations I am particularly grateful to Dr Natalia Karpukhina for being my inspiration to become a solid state NMR expert, transferring her solid state NMR knowledge, funding my attendance to all the conferences and so many other things.

I am also very grateful to, Dr Harold Toms, NMR facility manager at Queen Mary University of London for his help to set up all kinds of NMR experiments, his quick and prompt assistance with complicated NMR software and hardware and irretrievable willingness to share his knowledge and expertise of NMR. I am also very thankful to Dr Alex Hannon for his collaboration and training about neutron diffraction experiments and sparing his time during ICG (International Congress on Glass) in Italy to explain to me neutron diffraction data analysis and simulation procedures. My special thanks are to Prof Robert Hill for sharing his knowledge of biomaterials and glass–ionomer cements. I am very thankful to both Prof Robert Hill and Dr Natalia karpukhina for providing me an opportunity to work for GSK (GlaxoSmithKline) on their Sensodyne Repair and Protect toothpaste.

I am very thankful to Dr Rory Wilson for collecting all X–ray diffraction data and being always very kind to me.

Queen Mary, University is thanked for awarding me a Queen Mary Post Graduate Research Fund (PGRF) to travel to Canada and Prof David Bryce, University of Ottawa, Canada, is thanked for providing me an opportunity to access an ultrahigh field solid state NMR spectrometer and collect all my ^{67}Zn and ^{43}Ca solid NMR spectra of glass compositions presented in this thesis. Fred Perras, Prof David Bryce' PhD student, and Victor Terkish, the 900 MHz NMR facility manager at the National

Research Council of Canada, Ottawa are also thanked for their help in setting up experiments.

Dr John Hanna and Dinu Luga are thanked for their help to acquire ^{67}Zn NMR spectra on the 850 MHz NMR spectrometer at the University of Warwick.

Last but certainly not least, I express my gratitude and thanks to my husband, Ansar Iqbal for his love, affection and all kinds of support. I cannot find words to express my gratefulness for him. I could have never done my PhD without him by my side. My very special thanks are due to my cute and brilliant son, Ali for giving meaning to our hard life.

I would like to thank all my friends and all those people who helped me during my PhD.

Table of contents

List of Figures

Chapter 1 Introduction

Chapter 2 General Experimental Methods and Characterisation Techniques

Chapter 6 Glass–ionomer Cements

Appendices

List of Tables

Chapter 1 Introduction

Chapter2 General Experimental Methods and Characterisation Techniques

Chapter 3 Zinc Containing Metaphosphate Glasses

Summary

In this work zinc containing phosphate glasses have been developed for their potential applications for glass–ionomer cement. Different techniques such as solid state NMR and neutron diffraction have been used to determine the local environment of constituent cations in a range of phosphate glasses from metaphosphate to invert phosphate. Determined structures have been related to the dissolution behavior of glasses. Advanced solid state NMR techniques such as dipolar recoupling have been used to determine the structure, along with NMR spectroscopy of low gamma quadrupolar nuclei such as ^{67}Zn and ^{43}Ca. Studies involving these nuclei are rare due to their unfavorable nuclear magnetic properties, low natural abundance and small spectral frequency.

Neutron diffraction data has been used to reveal detail of the short range order in a selection of glasses. Conventional fitting of total radial distribution functions $T(r)$ has allowed for details of P–O, Zn–O to be established. In addition, an attempt has been made to Reverse Monte Carlo modelling to model the intermediate range structure using neutron diffraction data in the $Zn(PO_3)_2$, $NaZn(PO_3)_3$ and $NaZn_{0.5}Ca_{0.5}(PO_3)_3$ glass systems. Structure of sodium, calcium and zinc containing glasses in the range from metaphosphate to invert phosphate has been investigated with techniques described above and related to their dissolution behaviour in different solutions. Effect of presence of zinc oxide on dissolution and pH has been related to its structural role as well as results are compared with dissolution studies of similar zinc free compositions from literature. Structural changes with increasing amount of zinc oxide and fixed phosphate content in invert phosphates has also been investigated. Attempts have been made to prepare glass–ionomer cements from all prepared glass compositions. Finally glass–ionomer cement (GIC) has been successfully prepared from zinc containing invert phosphate glass composition and acrylic acid and vinyl phosphonic acid co-polymer. Properties of GIC have been optimised by varying the invert phosphate glass composition, and adding tartaric acid, silicate based glasses and hydroxyapatite.

Chapter 1 Introduction

1.0 Aims of Work

The main objective of this work was to develop novel zinc containing phosphate glass based glass-ionomer cement for bone cement application and to investigate the short and intermediate range structures of zinc containing phosphate based glasses, especially in terms of the structural role of zinc and its effect on the properties of glass and resultant cement.

1.1 Introduction to Biomaterials and Biomedical Glasses

The use of metals or other materials to replace damaged or diseased parts of the body dates back several millennia. The ancient Chinese and Aztec peoples used gold in dentistry, glues, waxes and tissues in reconstructing missing parts of the body[1]. However infection after implant restricted their success until Lister's aseptic surgical technique was developed in the 1860s[2]. Today biomaterials are used to improve human health by restoring the function of almost every natural living tissue and organ except the brain and spine. Biomaterials are used in[3]

1) Orthopaedics (joint replacement, bone cement, bone plates)
2) Artificial ligaments and tendons
3) Cardiovascular applications (blood vessels, heart valves)
4) Ophthalmic applications (intra–ocular lens, contact lens)
5) Dental applications (segment or entire teeth)
6) Drug–Delivery systems (drug reservoirs in implantable devices)

One of the most prominent application areas of biomaterials is orthopaedics. Arthritis and osteoporosis affect the movable joints such as knee, hip, shoulder and ankle. Arthritis is the biggest cause of disability in the UK. Every year about one million patients worldwide undergo total hip arthoplasty (THA) surgery[4]. A variety of metals, polymers and ceramic materials are used for orthopaedic surgery (Fig. 1.1). Fig. 1.2 shows some other examples of applications of biomaterials.

(a)

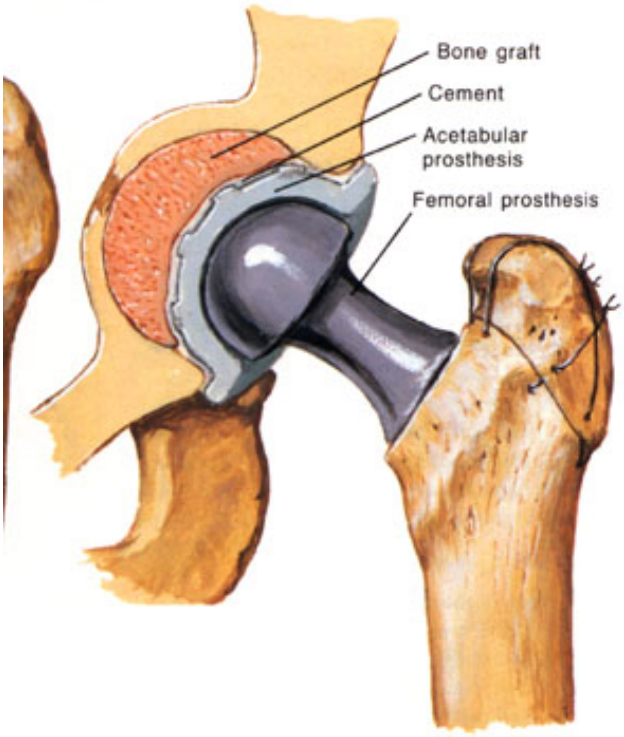

(b)

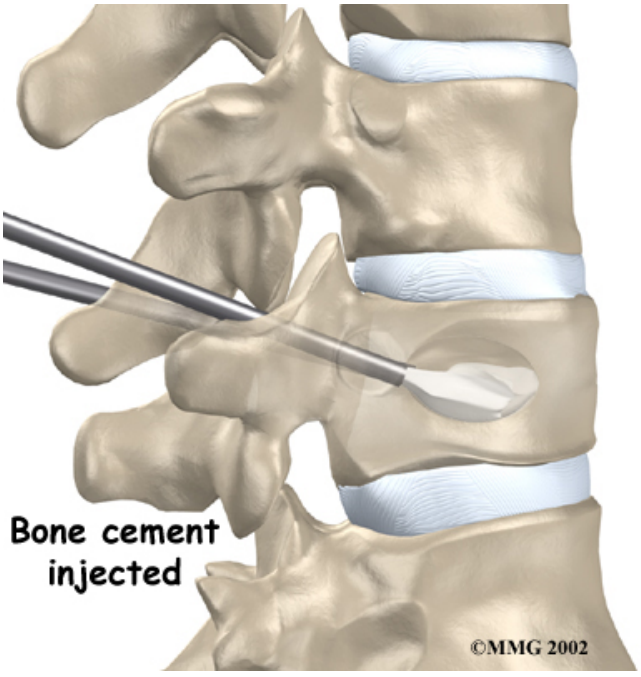

Fig.1. 1. (a) Joint arthroplasty (b) Verteboplasty.

(a)

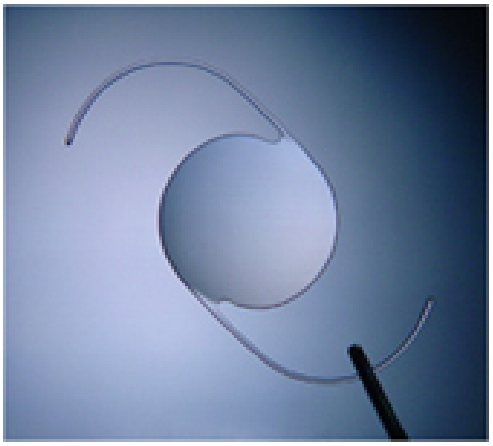

(b)

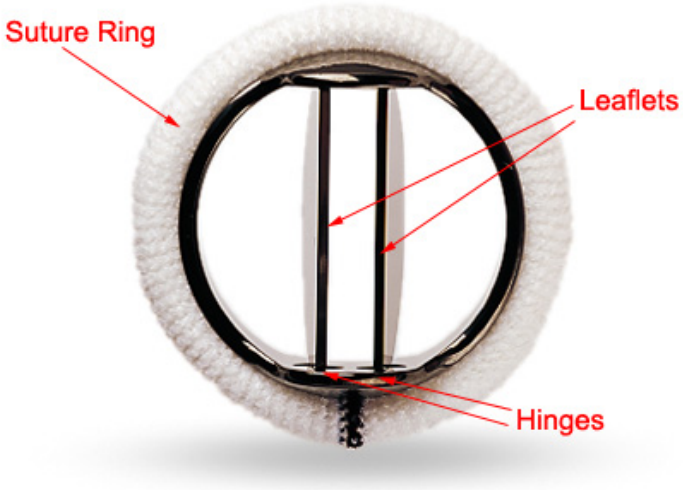

(c)

Fig.1.2. (a) Intra–ocular lens (b) Substitute heart valve. (St. Jude Medical® Mechanical Heart Valve) (c) Polyurethane, Teflon and Dacron vascular grafts[5].

A biomaterial is defined as "a substance (excluding drugs) or a combination of substances (either synthetic or natural) employed for the treatment, improvement or substitution of organism tissues, organs or function"[6]. Hench *et al*[7] has categorised biomaterials into four classes (1) nearly inert, (2) nearly inert microporous, (3) resorbable and (4) surface active (bioactive). Each of these classes is briefly described below.

1.1.1 Bio–inert Materials

Up to the 1970s, biomedical materials were used that had physical properties to suite the function of the replaced tissue with minimal toxicity[8]. These were typically based on metals or alloys (titanium, stainless steel, and cobalt–chrome) and dense or porous ceramics (Al_2O_3 or ZrO_2). They are described as bio–inert because they show no or only weak interaction with tissue upon implantation, which was considered to be a favourable feature. These materials could be cast or machined and pressed into place during application to yield a suitably tight fit and thus the implant–tissue interaction is essentially mechanical in nature. A fibrous tissue capsule of variable thickness is formed upon contact with the biological fluid. Where the fit is tight, this fibrous layer is thin and reduces relative movement at the implant–tissue interface. Interfacial movement under external stress leads to loosening and deterioration of the mechanical fit.

1.1.2 Bio–inert Microporous Materials

Micro–porous inert materials are a special class of inert material and differ from the more traditional smooth surface inert materials in their surface porosity. The porous surface allows for tissue growth into the micropores in a way that mimics natural tissue intergrowth, allowing for better long–term stability of the interface. The complication with these materials is the absence of real chemical adhesion with the tissues and poor mechanical strength due to their porosity[7].

1.1.3 Resorbable Materials

The limitations of bio–inert materials resulted in research into biodegradable or resorbable materials, such as calcium phosphate. In these materials, the degradation

or resorption is accompanied by tissue growth, with the biomaterial gradually replaced throughout the lifetime of the implant. As the implant is replaced by new tissue, its strength progressively decreases, which can result in destabilisation of the implant/tissue interface. Thus the decrease in strength and stability of this interface limit applications. Polylactic–polyglycolic acid and porous calcium phosphate ceramics are successful examples of these materials[9].

1.1.4 Bioactive Materials

The limitations of resorbable materials were solved by the introduction of surface active or bioactive materials. A bioactive material is the one that elicits a specific biological response at the interface of the material, which results in the formation of bonds between the tissue and the material. This concept is now used in a large number of biomaterials, with a range of thicknesses of interfacial bonding layers[10].

1.1.4.1 Bioactive Glass

The first bioactive glass, Bioglass, was developed by Hench at the University of Florida[11]. Bioglass or 45S5 has a molar composition 46.1% SiO_2:24.4% Na_2O:26.9% CaO: 2.6% P_2O_5. Hench *et al*[9,12] investigated the mechanism of interaction of 45S5 and showed that it produced biologically reactive hydoxycarbonate apatite (CHA), which is closely related to the mineral component of natural bone. This provides an ideal environment for the cellular reaction, with proliferation and differentiation of osteoblasts to form new bone. This results in a mechanically strong bond to the implant surface and at the same time passivates the glass to further degradation, which would otherwise extend to the rest of the glass surface . They showed that these glasses can form a strong bond with hard (bone) and in some cases soft (muscle and tendon) connective tissue through a sequence of rapid chemical processes that follow their *in vivo* or *in vitro* contact with a physiological test solution

In vitro testing of bioactivity of bioactive glasses is typically performed in simulated body fluid (SBF) as proposed by Kokobu *et al*.[13, 14]. SBF is an aqueous acellular solution whose composition of inorganic ions is almost equal to blood plasma.

Tests in SBF are easy and quick ways to evaluate the surface reactivity of new biomaterials in aqueous solutions. In these tests, if a layer of carbonatehydroxy apatite (CHA) is formed on the material surface, then the material is considered bioactive because, materials able to form (CHA) *in vitro* presumably will bond with living tissue on implantation. The mechanism of bond formation between tissue or bone and implant material can also be revealed through *in vitro* tests.

Bioactive melt derived glasses are used as filling materials, for example 45S5 ($46.1SiO_2$: $26.1CaO$: $24.4Na_2O$: $2.6P_2O_5$) (originally marketed as PerioGlass and now sold as NovaBone) is used to repair jaw defects caused by periodontal disease, or as hard tissue replacement such as the small bones of the middle ear[15] (Fig. 1.3). Its success was supported by early *in vivo* studies[16-18]. NovaBone now owned by GSK as NovaMin is used in toothpaste for the treatment of hypersensitive teeth[19] (Fig. 1.4). Studies have shown that very fine particles of glass attach to the dentine and form an CHA layer that is similar to enamel[20, 21]. Nowadays, toothpaste containing NovaMin and a source of fluoride are sold by GlaxoSmithKline (GSK). In these systems, flouridated apatite is formed and is more resistant to acid attack than CHA. This is supported by studies on other fluoride containing bioactive glasses which readily form fluoridated apatite[22-25].

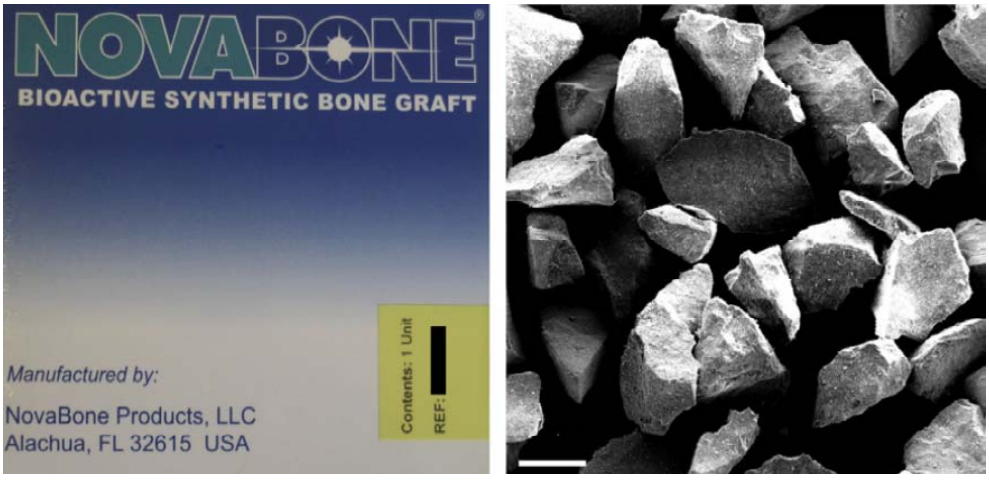

Fig.1. 3. NovaBone packaging, with an SEM image of the particles. Scale bar is 200 μm[20].

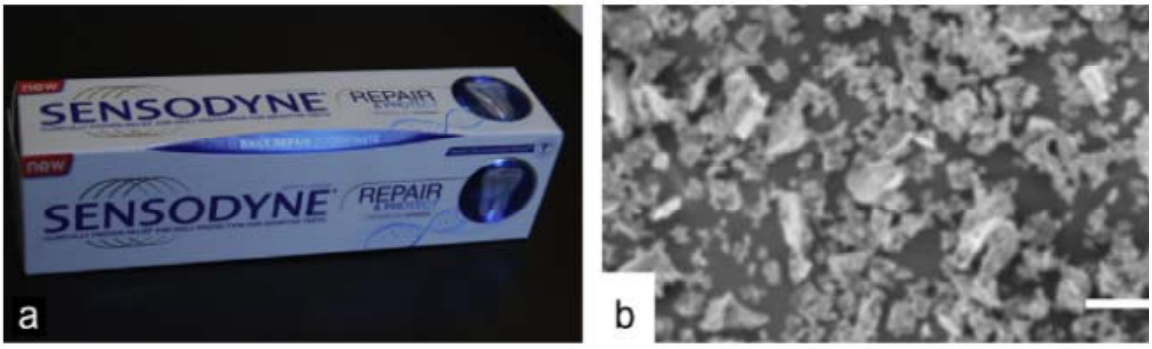

Fig.1. 4. (a) Photograph of Sensodyne Repair and Protect, which contains NovaMin. (b) SEM image of NovaMin particles (bar = 20 μm)[20].

The relatively poor mechanical properties of these glasses limit their application for load bearing devices. However when combined with metals, inert ceramics or polymers mechanical properties can be improved[26-29].

1.1.4.1 Bioactive Glass Composites

Biodegradable polymers such as poly lactic acid (PLA) and poly glycolic acid (PGA) have been used clinically for many years[30]. Bio-composites consisting of bioactive glass and a biodegradable polymer have been shown to have higher compressive strengths than polymers alone. Bioactive glass particles are added as a filler in a polymer matrix such as ploy lactic acid (PLA) poly glycolic acid (PGA) and their co–polymer[31], however bioactive glass composites produced by thermally induced phase separation are found more promising for bone regeneration. A thin pore wall of foam allows the bioactive glass to be exposed. The strength of the foam scaffold is controlled by controlling the porosity[32]. In addition, polymer coatings have been applied to highly porous bioactive glass ceramics, which could improve resistance to fracture. However, they do not improve mechanical strength. More recently bioactive glass composite nanofibres have been produced by electro–spinning[33].

1.1.5 Phosphate Based Biomaterials

Phosphate based biomaterials have been in use for many years. They are particularly interesting due to their close chemical relationship to the inorganic phase of natural bone. Materials such as zinc phosphate and calcium phosphate have been used as luting cements and bone cements, respectively for around 50 years.

The excellent biocompatibility and bone repair properties of calcium phosphate cements have made them ideal materials for dentistry and orthopaedics. Self–setting cements based on these materials can be easily handled by clinicians. This property has given them an advantage over conventional bioceramics. Cement formulation and the presence of additives determine the physico–chemical properties of the cements[34,35]. The final setting product of calcium phosphate cements is dependent on pH, with hydroxyapatite (HA, $Ca_{10}(PO_4)_6(OH)_2$) formed at pH values above 4.2, and below this pH calcium hydrogen phosphate ($CaHPO_4$, monetite) or calcium hydrogen phosphate dihydrate ($CaHPO_4.2H_2O$, brushite) are formed. HA forming cements have been successfully used for filling purposes, but they are non–resorbable. Brushite cements are more soluble at pH = 7.4, so they are more resorbable under physiological conditions.

While, most work has been done on apatite cements[36-39], recently brushite cements have also been introduced into the market due to their potential advantages. Brushite cements are prepared from β–tricalcium phosphate (β–TCP, $Ca_3(PO_4)_2$), monocalcium phosphate monohydrate ($Ca(H_2PO_4)_2.H_2O$, MCPM), β–TCP–phosphoric acid or β–TCP–polyphosphoric acid[40, 41]. Since brushite has such a fast setting reaction, retarders need to be added to the cement to keep the cement workable over an adequate time period[42].

Phosphate based glasses, have also gained attention as biomaterials and have found use as controlled release glasses (CRGs), due to their solubility. High solubility and the absence of polyphosphate pecipitates in fermentation media make them a

useful source of phosphate ions for growth of recombinant Escherichia Coli to a density 40% higher than that obtained with typical fermentation media[43].

Trace elements such as copper, cobalt and selenium are incorporated into soluble phosphate glasses for treatment of trace element deficiencies in ruminanat animals. These glasses are manufactured under the trade name Cosecure®[44, 45]. Copper containing CRG is used for non–toxic predetermined release of copper as molluscicides to control the snail hosts of schistosomiasis. Silver releasing CRGs are used clinically to treat long term infection in dwelling catheters. A ball of silver releasing CRG is inserted between urine collecting bag and catheter, which treats urine as it flows through it from bladder to urinary bag[46].

Gough[47] has observed early primary craniofacial osteoblast attachment and spreading on binary sodium phosphate glasses, although attachment was difficult due to the high solubility of such glasses. The biocompatibility of those glasses was related to their degradation and ion release. Sodium calcium phosphate glasses lend themselves to application as biodegradable scaffolds for hard tissue engineering. Knowles *et al*.[48-51] have studied glasses in this system with different substitutions and found them to be suitable materials for soft and hard tissue interfaces, with an enhancing effect on osteoblast and fibroblast differentiation. Uo *et al*.[52] studied the dental pulp cell cytocompatibility of sodium calcium phosphate glasses and found that cytotoxicity decreases with decrease in P_2O_5 and an increase in calcium oxide content and attributed it to change in pH and ionic concentration.

A number of phosphate glass systems have been developed by the incorporation of various metal oxides for hard tissue applications[53-56]. Release of ions from these oxides into biological medium stimulates cell response. For example, Sr^{2+} ions incorporated into phosphate glasses have been shown to promote osteoblast differentiation and inhibit osteoclast differentiation[57, 58]. Incorporation of ions known for their antibacterial action e.g. those of copper, silver, or gallium provides an alternative for treatment of infection[59-63]. Such materials could be placed at the site of infection. Similarly, phosphate glass based scaffolds with incorporation of antibiotic

drugs can be used to prevent implant related infection which is the main cause of revision surgery [64].

Phosphate glass fibres can be potentially used for soft tissue engineering. They can act as templates with muscle cells growing along their axis and forming myotubes. The scaffold permits the in growth of vascular tissue or muscle and not only provides a framework for cell orientation, proliferation and growth, but encourages these through ion release[65] [66]. Phosphate glass composites with different polymers have been investigated and rendered suitable to replace commonly used metal plates in orthopaedic surgery[67-70]

1.2 Introduction to Glasses

1.2.1 History

Glass is one of the oldest materials known to man still in use today, with decorative applications such as the first glass beads of early history to the fiber–optic technology of today's internet. Obsidian, formed naturally from cooled volcanic magma, was used as a cutting tool in the Stone Age. The exact time of the first glass synthesis is unknown, however glass beads made by Egyptians dating back to around 5000 BC have been recognised as the oldest man made glass. The Syrians invented the blowpipe technique for glass manufacture in around 200 BC, while metal coated mirror glass and window panes became common in 79 AD. Furnaces of that time could not reach temperatures above 1000°C.

Glass makers invented a two stage process for glass synthesis: a primary stage where raw materials were melted into ingots and a secondary stage where the ingots were remelted to make into different objects. In Europe, glass technology first arrived in Venice, Italy, through trade with Byzantines, where both processes, the melting of raw materials and final synthesis were combined together. In the seventeenth century

Louise Lucas invented the roll casting process for the production of plate glass at Saint Gobain (Paris, France).

Until the 13th century, glass was considered a precious material used for decorative purposes, stained glass windows of churches and other luxury goods. Technical applications of glass such as spectacles to correct vision and lenses for microscopes were introduced in mid 13th century. Zacharias and his son developed glass lenses for use in telescopes in 1608. Lead containing glass was introduced in the 18th century for better optical applications of glasses and to remove chromatic aberration. In the 19th century Otto Schott produced completely chromatic aberration free glass through the introduction of borate glasses. Glass light bulbs produced by Thomas Edison in the late 19th century were the first mass produced glass items in history. The chemical synthesis of soda ash by Ernest Solvay and development of tank furnaces led to the mechanisation of glass synthesis and the reduction of production costs in 20th century[71].

Modern research continues the tradition of Otto Schott in designing new compositions for different applications. In 1969 Wilson used aluminosilicate glass for glass–ionomer cements for dental applications[71]. In 1969 Hench introduced sodium calcium and phosphate containing silicate based glass called Bioglass for biomedical applications[11].

1.2.2 Glass Structure

Glasses are amorphous materials, with no long range crystallographic order, that exhibit a glass transition temperature. According to Tamman[72], the first investigator of glass constitution, a glass can be regarded as a "strongly under cooled liquid". However, this definition does not define sol–gel glasses. According to Zachariasen, glasses can be defined as three dimensional disordered infinite networks of building units of low coordination number, e.g. silicate and phosphate tetrahedra in SiO_2, P_2O_5, respectively. He defined the following rules for the formation of glasses in oxide systems.[73]

- An oxygen atom is not linked to more than two glass forming atoms.

- The coordination number of the glass forming atom is small.
- The oxygen polyhedra share corners with each other not edges or faces.
- The polyhedra are linked in a three dimensional network.

The coordination number of constituent atoms in a glass determines its role as network former, intermediate or modifier.[73]. According to Zachariasen, ions in oxide glasses can be classified as follows.

- Network formers, with a co–ordination number of 3 or 4. Examples include Si^{4+}, P^{5+}, B^{3+}, Ge^{4+}, As^{5+} etc.
- Network modifiers, with a coordination number ≥ 6 such as Na^{+}, K^{+}, Ca^{2+}, Ba^{2+} etc.
- Network intermediates, where ions can serve either as a network former in the presence of another network former and/or a network modifier. They have coordination numbers either 4 (network former) or 6 to 8 (network modifier). Examples include Al^{3+}, Zn^{2+}, Mg^{2+} etc.

Dietzel has attributed this coordination environment to the size and polarizibility of the constituent ions. He applied the fundamental physical relationship for the "attraction and repulsion" P between electrical charges Q_1 *and* Q_2 at a distance a

$$P = Z_1 e Z_2 e / a^2 \qquad 1.1$$

For anions and cations we obtain

$$K = Z_c Z_a e^2/(r_c + r_a)^2 = Z_c Z_a e^2/a^2 \qquad 1.2$$

where K is the interacting force, Z_c and Z_a are the valencies of the cation and anion, e is the electronic charge and r_c and r_a are the radii of cations and anions, respectively. Thus:

$$a = r_c + r_a \qquad 1.3$$

Dietzel introduced the term *F* (Field strength), where:

$$F = Zc/a^2 \qquad 1.4$$

During the process of glass formation a cation with lesser field strength must be satisfied with higher coordination. Dietzel related Zachariasen's classification of network former, modifier and intermediate to their field strength Table 1.1[72]

Table 1. 1 Relationship of field strength of cations to their role in glasses (after Dietzel[72])

Role in glass structure	$\approx Z/a^2$	Example
Network modifier	0.1 – 0.4	K^+, Na^+, Li^+, Ba^{2+}
Intermediate	0.5 – 1.0	Al^{3+}, Be^{2+}, Zr^{4+}, Zn^{2+}
Network former	1.5 – 2.0	Si^{4+}, P^{5+}, B^{3+}, Ge^{4+}

1.2.3 Kinetics of Glass Formation[72, 74]

Glass formation usually involves the rapid cooling of a liquid or vapour avoiding any detectable (10^{-6}) volume fraction of crystallisation. Crystallisation involves two processes, nucleation and crystal growth. Nucleation is the formation of small clusters of atoms or nuclei which, once they reach a critical size, can then grow to give the final crystalline product. Nuclei may be homogeneous or heterogeneous. Nucleation is a temperature dependent process and can be described by an Arrhenius type equation (Eqn 1.5)

$$I = A \exp[-(W + \Delta G_r) / kT] \qquad 1.5$$

where *I* is the homogeneous nucleation rate, *A* is the pre–exponential factor, *k* is the Boltzmann constant, *W* is the activation energy for ion migration and ΔG_r is the free energy associated with achieving a cluster of atoms of critical radius, *r*.

If the nucleation rate, *I,* (in s^{-1}) and growth rate *u* (in s^{-1}), are known as functions of temperature, the time required to attain a crystalline volume fraction of 10^{-6} can be plotted as a function of temperature as described by equation (Eqn.1.6)

$$10^{-6} = (\pi/3) I u^3 t^4 \qquad 1.6$$

The plot (Fig. 1.5) is called a TTT (time temperature transformation) curve or a nose curve after its shape, which is a result of competition between thermodynamic and kinetic factors for both nucleation and growth rates.

As the temperature approaches T_m (melting temperature) the time required to form the specified volume fraction of crystal approaches infinity since *I* and *u* approach zero. At very low temperature, the values of *I* and *u* also approach zero, due to the very high viscosity of the melt. T_n, the temperature corresponding to the "nose", represents the least favourable conditions for glass formation to occur.

From the TTT curve, it is possible to calculate the rate of cooling required to avoid crystallisation above the volume fraction and hence form a glass.

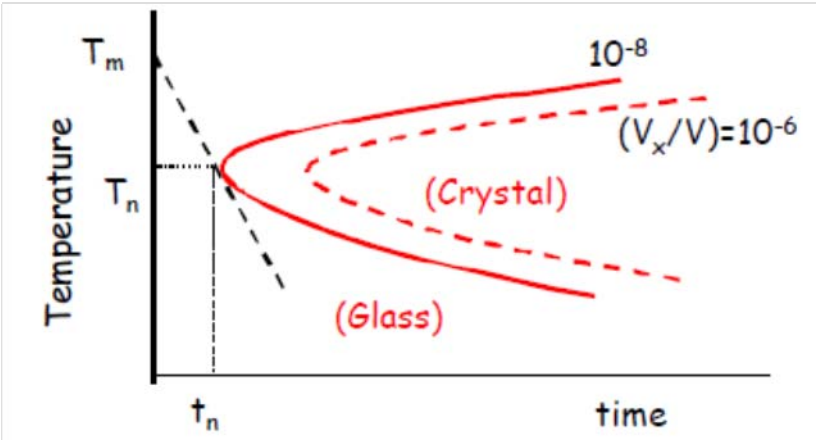

Fig.1. 5. Schematic representation of a TTT curve in a glass forming system.

1.2.4 Glass Transition Temperature (T_g)

A liquid can undergo two processes upon cooling. Crystallisation may occur or the liquid may become super cooled at a temperature below the melting temperature, T_m, and become more viscous. The viscosity increases with decreasing temperature, and may ultimately form a glass. The crystallisation is followed by an abrupt change in volume, whereas glass formation is characterised by gradual change in slope of volume change, as the liquid cools down as shown in Fig. 1.6. The temperature at which the super cooled liquid changes to a glass is called the glass transition temperature (T_g). The T_g of a material can be determined by differential scanning calorimetry (DSC) (as described in chapter 2), differential thermal analysis (DTA) or dilatometry. Glass transition is actually a continuous process and hence T_g is not well defined. The T_g of a particular material depends on the thermal history of the material, thus T_g determined by heating the same glass at different heating/cooling rates can differ by 10 to 20%[75].

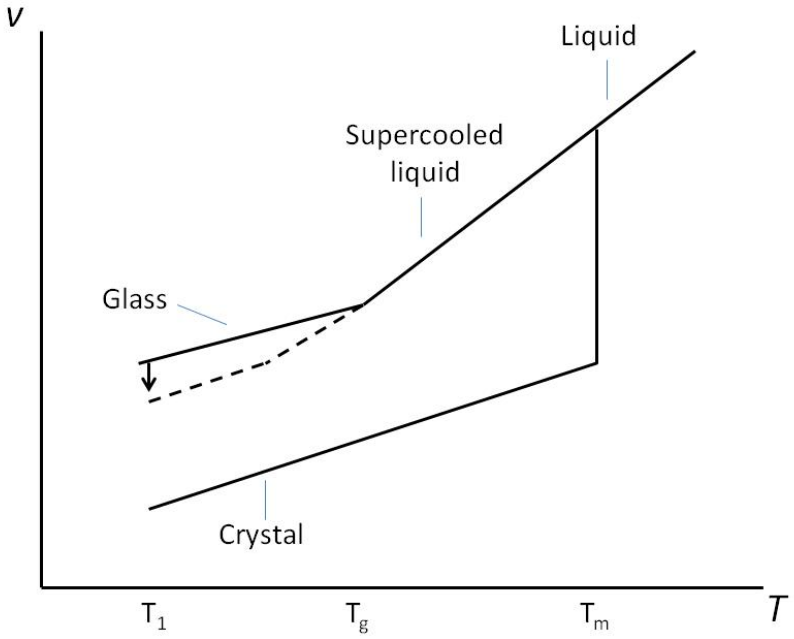

Fig.1. 6. Schematic illustration of volume change (*V*) with temperature (*T*) as a supercooled liquid is cooled through the glass transition temperature (T_g). Volume change with crystallisation is also shown. Vertical arrow shows the change in volume of glass due to relaxation processes if held at temperature T_1.

1.2.5 Eutectic Compositions

A eutectic composition is a composition between two chemical systems which are miscible in the liquid state but immiscible in the solid state. At this composition the melting temperature is depressed and the possibility of crystallisation is reduced as the liquid is less supercooled. The decrease in melting temperature at the eutectic composition is related to the large negative excess free energy of mixing[75].

1.3 Phosphate Glasses

The basic structural unit of phosphate glasses is the PO_4 tetrahedron. Phosphorus has an electronic configuration of [Ar] $3s^2$, $3p^3$ and therefore has five valence electrons. In oxide systems, the favoured coordination is tetrahedral, which can be considered as sp^3 hybridisation of the phosphorous valence shell atomic orbitals, with the third *p* electron promoted to an empty 3*d* orbital, where a strong π bonding molecular orbital is formed with the 2*p* orbitals on the oxygen atoms.

The parent network former in phosphate glasses is phosphorus pentoxide, P_2O_5, whose structure is made up of corner sharing PO_4 units. Each PO_4 unit shares three out of four oxygen atoms with other PO_4 units, whereas the fourth oxygen, called terminal oxygen (O_T). is doubly bonded. This gives an average formula per phosphorous atom of $[PO_{2.5}]^0$. Crystalline P_2O_5 exists as three crystalline polymorphs. H, O and O′. The H form is hexagonal with discrete P_4O_{10} molecules arranged in an adamantine like structure. O and O′ are orthorhombic polymeric forms. The crystal structure of the O′ polymorph is shown in Fig 1.7. O′ is a low density (2.72 g/cm^3) form with a three dimensional structure, whereas the O form is a high density (3.05 g/cm^3) polymorph which consists of interconnected P_6O_6 rings and adopts a layered structure. Vitreous phosphorus pentoxide is highly hygroscopic and volatile. Neutron diffraction[76, 77] studies have shown that $v-P_2O_5$ consists of PO_4 tetrahedra linked to three other tetrahedra forming a three dimensional random network.

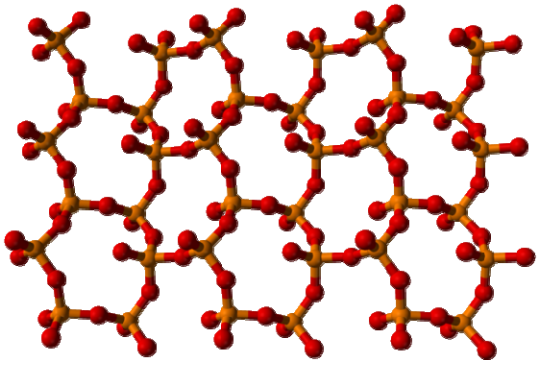

Fig.1. 7. Part of an o'–(P_2O_5) layer[78]

Addition of modifier oxides to v–P_2O_5 depolymerises the network and increases the number of non–bridging oxygen atoms (NBO) at the expense of (BO) bridging oxygen atoms, resulting in the formation of negatively charged non–bridging (NBO) oxygens, which are charge balanced with positively charged metal cations.

1.3.1 Classification of Phosphate Glasses

It is useful to classify phosphates according to level of condensation i.e. the number of bridging oxygen atoms (BOs). This is normally done using the Q^n notation commonly used in silicate systems. In this notation Q describes the coordination number (quaternary) and *n* the number of bridging oxygen atoms. Thus phosphate species in the fully condensed P_2O_5 system are denoted Q^3, whereas orthophosphates which contain the isolated PO_4^{3-} anion are denoted Q^0. The different speciation in phosphates is shown schematically in Fig. 1.8.

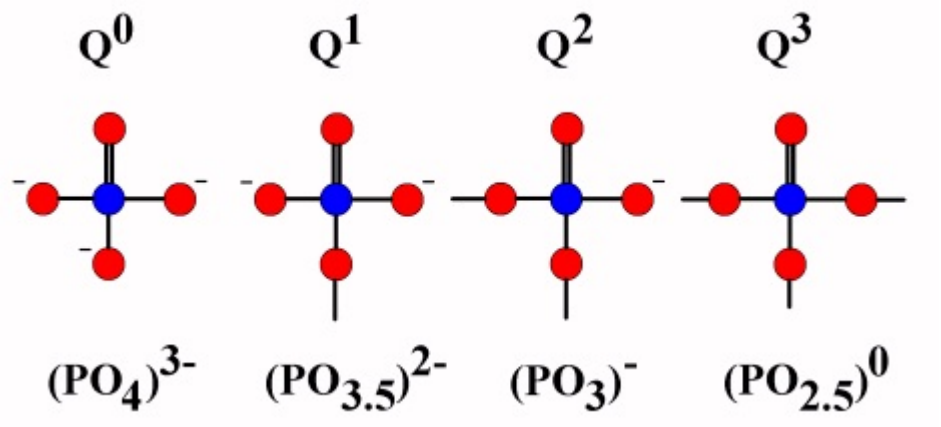

Fig.1. 8. Q^n notation in phosphate systems[79].

In simple binary systems the fraction of different phosphate species in glasses with compositions $xM_2O:(1-x)P_2O_5$ or $xMO: (1-x)P_2O_5$ can be predicted from van Wazer's equations[80].

1.3.1.1 Ultraphosphate Glasses

Ultraphosphate glasses contain a combination of Q^2 and Q^3 species. For simple binary systems based on group 1 or group 2 metals they can be generally represented by the formulae $xM_2O:(1-x)P_2O_5$ or $x(MO):(1-x)(P_2O_5)$, where $0 < x < 0.5$. The fraction (f) of different species in such glass compositions can be calculated from van Wazer's simple depolymerisation model[80].

$$f(Q^2) = x/(1-x) \qquad 1.7$$

$$f(Q^3) = (1-2x)/(1-x) \qquad 1.8$$

The structure of ultraphosphate glasses has been studied by a number of authors. Hoppe *et al*[77, 81, 82] have studied the structure of vitreous P_2O_5 and identified two peaks at distance of 14.32 nm and 15.81 nm corresponding to phosphorus oxygen double bond and single bond respectively. They found a peak area for the P–O single bond three times larger than that for the P–O double bond and concluded that vitreous P_2O_5 consists of corner sharing PO_4 tetrahedra. Suzuya et al[83] found a P_4O_{10} molecular packing model for vitreous P_2O_5 through their neutron diffraction studies

and identified the destruction of the three dimensional PO_4 network structure by the addition of alkali metal cations, which was also confirmed through ^{31}P MAS–NMR studies of sodium ultraphosphate glasses. Evolution of Q^2 species at the expense of Q^3 species is observed with the addition of sodium oxide content in agreement with Van Wazer's depolymerisation model[84-86]. The concurrent increase in non–bridging oxygen (NBO) with the increase in alkali metal oxide content studied through X–ray photoelectron spectroscopy and FTIR also follows this structural model quantitatively[87, 88].

The proportions of Q^2 and Q^3 species depend on composition, however they may be linked in a number of different ways to from the network[89]. Meyer[90] concluded that chemically ordered Q^3-Q^2 linkages exist in alkaline earth phosphate glasses from the similarities in the Raman spectra of crystalline and stoichiometric glass compositions. It has been shown that ultraphosphate glasses retain a quasi-layered v-P_2O_5 structure up to 20 - 25 mol% of modifier cations, after which the Q^3 layers are consumed to form Q^2 tetrahedra[83, 91]. The composition at which this transition from Q^3 three dimensional network to Q^2 occurs depends on the valence and coordination of modifying cations. The density and other physical properties such as glass transition temperature also depend on the type of modifier cation. Hoppe[92] has explained the packing densities in terms of coordination environment of modifier cations. He proposed that structure and properties of ultrphosphate glasses depend on the number of terminal oxygen available to coordinate modifier cation.

The highly hygroscopic nature of ultraphosphate glasses restricts their applications as biomaterials. However, Kasuga *et al.*[93] extracted high strength crystalline β–calcium metaphosphate from the crystallized product of calcium ultraphosphate glasses for biomedical applications. The extent of the hygroscopic nature depends on the type of cations. For example Meyer *et al.*[94] prepared ultraphosphate glasses with CaO and ZnO content up to 15 mol% and found that zinc containing glasses are less hygroscopic than the calcium ultraphosphate glasses. This is the opposite of the behaviour in metaphosphate glasses where calcium phosphate glasses are more stable than zinc metaphosphate glasses. He has attributed this

contrasting behaviour to the difference in structure of metaphosphate and ultraphosphate glasses.

1.3.1.2 Metaphosphate Glasses

Glass compositions with formulae $50M_2O{:}50P_2O_5$ or $50(MO){:}50(P_2O_5)$ are called metaphosphate glasses and consist of Q^2 species only. The glass network is made up of infinitely long chains or rings of Q^2 phosphate tetrahedra, which are linked together through non bridging oxygens (NBOs) and metal cations. Typically metaphosphate glasses can have an average chain length ranging between 40 – 100 phosphate tetrahedra when terminated by hydroxyl groups, however chain lengths of up to 1000 tetrahedra have been reported in anhydrous alkali metal metaphosphate glasses. Crystalline metaphosphates made from Kurroll's salt are reported to have a chain length of 10,000 phosphate tetrahedra[95]. The presence of infinitely long chains diminishes the possibility of the existence of cyclic anions, which would reduce the average chain length. In general, the fraction of cyclic anions is greatest in metaphosphate glass compositions. The properties and chain conformation of these glasses depend on the field strength of the modifier cations. This has been shown through ^{31}P MAS-NMR spectroscopy with an increase in NMR peak width observed with increase in field strength of modifier cations[86], [96]. Similar conclusions have been reached from total X- ray and neutron scattering studies of various metaphosphate glass compositions [97], [98]. The glass transition temperature and hence the rigidity of glass network also increases with increasing field strength of the modifier cations. This has been attributed to the increasing covalent character of the terminal M–O bond, with increasing field strength of modifier cation[89]

1.3.1.3 Polyphosphate Glasses

Polyphosphate glasses have composition $xM_2O{:}(1-x)P_2O_5$ or $x(MO){:}(1-x)(P_2O_5)$ where $x < 0.5$. These glass compositions are made up of Q^2 and Q^1 species. Q^1 species can be chain terminating units or exist as pyrophosphate dimer units depending on composition. At the pyrophosphate composition ($x = 0.67$) the structure is dominated by pyrophosphate units. Contrary to the stochiometric calculations, fractions of Q^2 and

Q^0 species can be observed at the pyrophosphate composition as seen in $67ZnO.33P_2O_5$ using ^{31}P MAS-NMR due to disproportionation of Q^1 species[99].

$$2Q^1 \longleftrightarrow Q^2 + Q^0 \qquad 1.9$$

The fraction of Q^1 and Q^2 species in polyphosphate glass compositions can be calculated as follows:

$$f(Q^1) = 2x - 1 / 1 - x \qquad 1.10$$

$$f(Q^2) = 2 - 3x / 1 - x \qquad 1.11$$

The average chain length of polyphosphate glasses can be calculated according Van Wazer's equation

$$n_{av} = 2(1-x)/(2x-1) \qquad 1.12$$

Where n_{av} is the average chain length and x is the mole fraction of metal oxide. It can be seen from this equation that average chain length decreases with the increase in value of x.

The average chain length in polyphosphates has been measured using various techniques such as ^{31}P multi dimensional MAS–NMR spectroscopy[100-101]. Q^n connectivity in phosphate glasses has been revealed through DQ (double quantum) and TQ (triple quantum) ^{31}P MAS-NMR experiments which probe through space dipolar recoupling[102, 103] or through bond J coupling[104] between Q^n species. Witter *et al.*.[100, 105] resolved the bonded units adjacent to Q^n species in binary calcium phosphate glasses through DQ ^{31}P MAS-NMR and determined the chain length distribution in this glass system. In addition, the chain length of polyphosphate glasses has been calculated through XPS[100, 106, 107]. As the cross bridging between terminal oxygens (O_T) and cations form the network, the properties of polyphosphate glasses depend more on the type of modifier cation and less on the phosphate content. Monovalent cations have only a small effect, whereas cations such Fe^{2+}, Al^{3+}, Mg^{2+}, Zn^{2+} strengthen the network by forming covalent type cross bridging [108-110]. The strength of this network formed due to cross bridging depends on the field strength of cation. The higher the field strength of cation the stronger network, hence the higher the glass transition

temperature. The effect of different cations on the P–O(T)–M linkage is manifested in ^{31}P MAS-NMR spectroscopy through change in the chemical shift[111].

1.4 Introduction to Glass-ionomer Cements

Glass-ionomer cements are restorative materials used in dentistry for filling teeth and as luting cements. These materials are based on reaction of a silicate glass powder and a polyalkenoic acid and are therefore acid base reaction cements. The base is a fluoride containing calcium aluminosilicate glass powder and an acid, typically polyacrylic acid. The resulting product is a salt hydrogel which acts as a binding matrix[112].

Wilson[113] first prepared dental cement by mixing silicate glass powder with polyacrylic acid, but this material was unworkable. Wilson and Kent[114] observed that the setting of cement was controlled by the Al_2O_3/SiO_2 ratio in the glass. This enabled them to prepare more reactive glasses with polyacrylic acid (ASPA1). This material still had the problem of minimal working time and a slow post hardening process. In addition the cement was sensitive to water. Wilson and Crisp[115] later discovered that inclusion of tartaric acid in the formulation enhances the working time and increases the setting rate. This was the first practical glass-ionomer cement and was termed ASPA11.

1.4.1 Classification of Glass-ionomer Cements

Glass-ionomer cements can be classified according to their composition or usage. Each of these classifications is described below.

1.4.1.1 Classification by Composition

1.4.1.1.1 Conventional Glass-ionomer Cements

Conventional glass-ionomer cements are those first described by Wilson and Kent. They are derived from a simple alkenoic acid, such as polyacrylic acid and the glass component is flouroalumino silicate. The three essential components of the glasses in these systems are silica, alumina and calcium fluoride. The ability to form cements is related to glass composition. The silica:alumina ratio is very important and needs to be 2:1 or more by mass to allow cement formation[113, 115, 116].

1.5.1.1.2 Hybrid-ionomer Cements or Resin Modified Glass-ionomers

Resin modified glass-ionomer cements were developed in 1990[117]. These are glass-ionomer cements that contain a small quantity of water soluble polymerizable resin. Resin modified glass-ionomers (RMGIs) were developed to improve the mechanical properties, decrease setting time and attenuate moisture sensitivity of glass-ionomer cements. RMGIs are a hybrid of glass-ionomers and composite resins and are usually formulated from flouroalumino silicate glasses, photo initiators, polyacrylic acid, water and a water soluble methacrylate monomer such as hydroxyethylmethacrylate (HEMA)[118, 119]. Setting in these glass-ionomers is described as a series of overlapping steps. Protons from polyacrylic acid liberate metal ions and fluoride ions resulting in a silica hydrogel. The rising aqueous phase pH causes precipitates of salt to form from migrating ions, which act to cross-link polyacrylic acid chains. This process takes several minutes. The resin reaction rate is very fast, although the complex, photo initiated polymerization results in diffusion controlled, polymer chain propagation[120].

1.5.1.1.3 Metal Reinforced Glass-Ionomer Cements

Metal reinforced glass-ionomer cements were first introduced in 1977. The addition of silver amalgam alloys to conventional materials increased the physical strength and provided radio opacity. However, these cements are poor in aesthetics and exhibit less abrasion resistance than regular glass-ionomer cements.

McLean and Gasser in 1985 developed the cerment-ionomer cement to improve the abrasion resistance and strength of glass-ionomer cements. These cermets, unlike simple mixtures of glass and metal powder, contain glass and metal powder sintered to high density that can be made to react with polyacids to form cement. Ion leachable calcium flouroalumino silicate glasses are used. The resulting cements can be polished to attain a metal finish. Any of the precious metals currently used in dentistry can be used, but silver and gold are the most suitable. The glass metal powders are compressed in a pelletizer at a pressure (300 MPa). The resulting glass metal pellets are fused at temperature of 800°C and the sintered glass-metal composite is finally ground to fine powder.

1.4.1.2 Classification of Glass-Ionomer Cements on the Basis of Usage[121]

1.4.1.2.1 Luting Agents (Type I)

Fine grained glass powders with a maximum grain size of 15 µm or less are used in these cements for the flow properties and minimal film thickness required. Radio opacity is obtained by replacing calcium with strontium or lanthanum.

1.4.1.2.2 Aesthetic Filling Material (Type II)

Translucency is required for anterior restoration. Glasses with high a silica/alumina ratio are clear and cements formed from them tend to harden slowly.

1.4.1.2.3 Bis Reinforced Filling Material (Type II)

These cements are not aesthetic, but are more abrasion resistant. These are cermet (glass metal) derivatives of type II cements.

1.4.2 Glass Component of Glass-ionomer Cements

The composition of glasses can be varied greatly. The glasses used in commercial glass-ionomer cements are all aluminosilicates, containing additionally phosphorus, sodium, calcium and fluoride. Glass is prepared by fusing the precursor oxides or carbonates at temperatures typically in the range 1200 to 1500°C [122]. The resulting melt is quenched either by pouring it onto a cool metal plate and then into water or by direct quenching in cold water. The product, which is a coarse frit, is then ground to a fine powder with particle size 45 μm for GICs for filling applications and 15 μm for luting purposes[123]. The glass composition is very important in determining the type of glass-ionomer cement. The main glass used by Wilson and co-workers was based on the systems SiO_2:Al_2O_3:CaO or SiO_2:Al_2O_3:CaF_2[124].

The properties of ionomer cements are different from those of normal silicate glasses, because they are decomposed by acids and this property is mainly due to the presence of aluminium. Aluminium can enter the silica network, replacing the silicon, resulting in a negative charge, which makes the glass susceptible to acid attack. The initial work in this field was carried out assuming that the basicity of the glass should be enough to compensate the reduced acidity of polyacrylic acid[125]. The setting rate can be modified with the addition of tartaric acid[126]. Basic glasses as described by Wilson *et al.*[116] are still used in most glass-ionomer cements.

In addition to aluminosilicates, two alternative series of glasses have been prepared for use in glass-ionomer cements. These are aluminoborate[127-129] and zinc silicate glasses[130]. The aluminoborate glasses showed higher compressive strength and sharper setting time, however they had poor hydrolytic stability. Two types, of zinc silicate glasses have been examined CaO:ZnO:SiO_2 and Al_2O_3:ZnO:SiO_2. Glass-ionomer cements with high compressive strengths and water stability have only been produced from alumina zinc silicate glasses. Unlike fluoroaluminosilicate glasses properties of these cements do not depend on aluminium/silicate ratio. The structural role of zinc in these glasses is described as a network intermediate, just like aluminium in fluoroalumino silicate glasses. However cements produced from these glasses were not strong enough for clinical use.

1.4.3 Polyelectrolyte Component of GICs

Polyelectrolytes, as their name indicates, are both polymers and electrolytes. The polyelelectrolytes used in glass–ionomer cements can be described as polyalkenoic acids. These acids are homopolymers or copolymers of unsaturated mono- di- and tri- carboxylic acids. The most commonly used polyalkenoicacid in glass–ionomers is polyacrylic acid. However, commercially successful glass-ionomers have also been prepared from acrylic/maleic copolymers. Their properties are not the same as those of cements prepared from acrylic acid homopolymer. In particular, they do not become stronger with time. They attain maximum compressive and flexural strength in the first few months of their life-time, which then starts decreasing with time.[131,132] The strength of set cements depends on the molecular weight of polyalkenoic acid.

1.4.4 Setting Process/ Chemistry of Glass-Ionomer Cements

Conventional glass-ionomer cements are prepared from a powder of ion leachable glass and polyacrylic acid, which is available either as liquid or dried powder, with water added at the time of preparation. When the glass powder and aqueous liquid are brought together, acid attacks the glass powder, causing the leaching of metal ions from the glass powder and forming a salt hydrogel matrix.

In the early stages of reaction, the acid attacks the surface of the glass powder. As cations are removed, the glass network breaks down into silicic acid, which polymerises at the surface into silica gel. Ions in the glass *i.e*. Ca^{2+}, Al^{3+} and F^{-} are released into the aqueous phase. As the concentration of these ions increases, the pH of the aqueous phase also increases. Increase in pH causes the conversion of polyacrylic acid into polyacrylates. At a critical pH and ion concentration, precipitation of polyacrylate takes place. When this process reaches a certain limit, the cement sets. The process continues in the post-hardening phase[121].

The detail of the setting chemistry of cements has been studied using a number

of techniques such as: Fourier transform infrared spectroscopy[133], multinuclear magnetic resonance spectroscopy[134-137] stray-field imaging[111], pH change[138] and electron probe micro analysis[139, 140]. When the components are mixed, acid protons rapidly attack the glass particles. This attack is not uniform, it takes place preferentially at calcium rich sites. Barry *et al.*[139] has explained this initial release of calcium with the assumption that calcium preferentially occupies those parts of the glass network where tetrahedral aluminium has replaced silicon. Aluminium will require additional cation to maintain electroneutrality, since aluminium is +3 compared to the +4 charge of silicon. Aluminium is also more basic than silicon hence these sites are not only calcium rich, but also they are also more basic. Infrared spectroscopic studies by Crisp *et al.*[133] also support that calcium polyacrylate is responsible for initial setting, at least in the absence of tartaric acid, and the hardening process occurs due to slower formation of aluminium polyacrylate. However Cook[141] reported a study in which he showed that aluminium was present in the setting matrix in the early cure process. Later Wasson and Nicholson[142] also supported the findings of Cook and showed clearly that aluminium was released in the early phase of setting by washing cement forming glasses with dilute acid and then analysing the solution with inductively coupled plasma optical spectroscopy. They postulated that aluminium was released in such a form that it was not readily available for reaction.

It had previously been thought that sodium and silicon do not take part in matrix formation. Hatton and Brook[140] studied thin film sections of set cements of glass G338 (24.9SiO_2: 14.2Al_2O_3: 12.8CaF_2: 19.2Na_2AlF_6: 4.6AlF_3: 24.3$AlPO_4$) using transmission electron microscopy and X-ray analysis and identified three regions, namely, remnant glass particles, silicon rich layer around the glass particles and the matrix. Phosphorus was also found in the matrix. Wasson and Nicholson carried out further studies to test the suggestion that silicon and phosphorus form inorganic networks within the matrix. They prepared cement from glass G338 and acetic acid[143]. They found that the cement was not water stable initially, but became so after 6 hours. IR studies showed that there was rapid formation of aluminium acetate and calcium acetate, but it did not result in water stability. The ageing of this cement over six months, like conventional

cement showed that it was the inorganic network that increased the compressive strength of the cement over time[144] The initial hardening is due to the formation of stiff, ionically cross linked polyacrylate and post hardening is due to the inorganic network of silicon and phosphorus oxides.

1.4.4.1 Role of Aluminium and Silicon in Cement Setting

According to Zachariasen's classification of ions, aluminium is considered to be a network intermediate *i.e* it does not form glass network on its own, however in the presence of sufficient amount of silica it adopts a tetrahedral geometry and becomes the part of glass network in association with SiO_4 tetrahedra. However, mutual sharing of oxygen between AlO_4 tetrahedra is unfavourable due to instability of AlO_4 species. This creates an overall negative charge on the glass network, which is charge balanced by additional positive charge from modifier cations (e.g. Na^+,Ca^{2+}) which makes the resulting glass basic and susceptible to acid attack. Aluminium is found in 4, 5 and 6 coordination in aluminium containing glasses[137]. Four-fold coordination arises when the aluminium is forced into the network, whereas the presence of 5 and 6 coordinate aluminium indicates aluminium in a network modifying role.

Various techniques have been used to investigate the role of aluminium in the setting chemistry of glass–ionomer cements. Recently MAS–NMR spectroscopy has been used to probe the environment of different species in precursor glass and set cements. Pires *et al.* [145] studied the role of aluminium and silicon in the cement setting process using ^{27}Al MAS–NMR and ^{29}Si MAS–NMR spectroscopy. Their results showed that three aluminium species are present in precursor glass particles, with four, five and six coordinate environments. Al^{3+} ions present in the surface layer leach into the cement matrix during acid attack. Al^{3+} cations cross-linking the polymer chain create a second six-coordinate species in the cement. Only a small proportion of the four-coordinate species is leached into the cement. A small amount of a second four-coordinate species is generated in the surface layer of the glass due to modification of that layer during acid attack. ^{29}Si NMR spectra revealed that leaching of Al^{3+} ions from the glass causes a recondensation of the silicate framework. Generally five-coordinate

species are preferentially located in the reactive surface layer of the glass rather than the inert core. Hill *et al.* [136] also performed long-term studies on the setting chemistry of glass-ionomer cements with various glass compositions using ^{27}Al and ^{29}Si MAS-NMR spectroscopy. They also found the evolution of six-coordinate aluminium with the setting of cements. In addition, they identified the role of glass composition in the setting of cements and attributed the existence of 5 coordinate aluminium in 1 year set cement to high phosphate content in the precursor glass, since the presence of Al–O–P linkages slows the glass dissolution.

For simple $CaO:Al_2O_3:SiO_2$ glasses, the glass reactivity and cement properties are connected with the alumina/silica ratio. However, many commercial glasses used for glass-ionomer cements contain significant amounts of other components. For example, the commonly used glass G338 contains significant amounts of phosphorus, fluorine and sodium as AlF_3, CaF_2, NaF and $AlPO_4$. These also affect the properties and setting process of the resulting cements. Hill *et al.*[146] examined the role of other glass components on the properties of cements. They found that the alumina/silica ratio has no influence on the properties of cements, formed from multi-component glasses. They suggested that the presence of phosphorus in the glass, which balances the aluminium charge, reduces the number of Al-O-Si bonds available for acid hydrolysis. They also suggested that P-O bond hydrolysis is a significant factor in glasses with high phosphate component.

1.4.4.2 Role of Fluoride in the Setting Process of Cements

Before the rate modifying effect of tartaric acid was known, Kent *et al.*[147] observed the role of fluoride in the working properties of glass-ionomers, while developing cements high in fluoride content. They observed that glasses without fluoride did not form workable cements. They assumed that fluoride changed the setting reaction in the cement. Crisp and Wilson[148] and Barry and coworkers[139] in 1979 proved that the working time of cements depends upon the amount of fluoride released from the glass. They suggested two reasons for the increased working time: (1) formation of metal complexes which reduce the binding of cations with anionic

sites on the polyelectrolyte chains; (2) formation of complexes increases hydrogen ion concentration, thus increasing the acidity of the paste and delaying pH dependent gelation. Details of the role of fluoride in the setting reaction of glass-ionomer cements are not clear. Fluoride also seems to enhance the compressive strength of the resulting cement. Fluoride containing cements have compressive strengths up to 200 MPa or more after 24 h, whereas fluoride free cements have rarely been made with compressive strength above 100 MPa. This has been attributed to the formation of metal complexes of the type AlF_2^+ and AlF^{2+}, that are well established in other chemical systems[149]. However, there is no direct evidence of the presence of such species. Furthermore there is another possibility that fluoride ions bond strongly to the carboxyl group of the polyalkenoic acid (e.g. poly acrylic acid) through hydrogen bonding. Emsley *et al.*[150] described the hydrogen bond between fluoride and carboxylic group as the strongest bond formed in a solution of potassium fluoride and formic acid.

1.4.5.3 Role of Tartaric Acid in the Setting of Cements

In the 1970s Wilson and Crisp[151], [152] discovered the effects of (+)-tartaric acid on the setting process. Addition of tartaric acid to a cement mixture, improves the manipulation of the cement and increases its working time[153]. The stereochemistry of tartaric acid influences its effect. It is the (+)-isomer of tartaric acid which alters the properties of cements. The mechanism how (+)-tartaric acid effects the setting process of cement is not very clear. However, based on NMR and Fourier transform infrared spectroscopies it has been suggested that tartaric acid reacts faster than polyacid because of its higher acidity and forms metal tartrate chelates. Nicholson[154] has demonstrated through Fourier transform infrared spectroscopy that, in the presence of tartaric acid, calcium polyacrylate forms slowly, whereas aluminium polyacrylate forms rapidly. The role of tartaric acid in slowing down the initial setting and increasing the strength of cement despite numerous studies still remains a mystery.

1.4.6 Zinc Containing Glass-ionomer Cements

Towler *et al.*[155] have studied glass-ionomer cements prepared from aluminium free zinc containing silicate based glass and polyacrylic acid. They found that cements can be prepared from zinc based glasses with mechanical strength slightly lower than commercial aluminium based GICs. The high concentration of zinc ions released was shown to be toxic by cell culture methods. In other work, they studied the zinc ion release from glass-ionomer cements prepared from calcium zinc silicate glass with polyacrylic acids of different concentration and molar mass. Their findings showed that the amount of zinc ions released decreases with increasing concentration of polyacrylic acid. They suggested that release of active ions can be controlled by increasing the P:L (powder: liquid) ratio and the concentration of PAA (poly acrylic acid)[156]. Towler *et al.*[157] further studied working and setting times, compressive and flexural strength as well biological activity of GICs prepared from zinc containing silicate glasses of two compositions, differing by proportion of calcium content with PAA of low and high molecular weight. Glass-ionomer cements could be prepared from both glasses, although the glass composition with low calcium content was more reactive than the other glass. They attributed this reactivity to lower calcium content. Their results also indicated that the setting time decreases with the increase of molecular weight or concentration of polyacrylic acid. Studying the mechanical properties of all types of cements, they concluded that they follow a similar trend to conventional aluminium based cements, *i.e.* compressive and flexural strength increases with both concentration and molecular weight of PAA (polyacrylic acid) and maturation time. However, these cements do not have compressive strengths comparable to aluminium based cements, with values approximately one quarter of the aluminium based cements after 30 days maturation. The results also showed that cements prepared from high molecular weight PAA and glass compositions with high calcium content are biologically active.

Eberhardt *et al.*[158] prepared aluminium free polyalkenoate bone cement with sintered zinc calcium silicate glass and a polyalkenoate with a pendant methacrylate group as well as acryloyl beta-alanine (non HEMA co-monomer). They used a two

component (liquid/powder) system for cement preparation. The liquid component was prepared by mixing the polymer (35%-55% of total liquid, by weight) with $K_2S_2O_8$ (0.25%) and distilled water (20%-30%). The powder was prepared by mixing the filler with encapsulated ascorbic acid (0.3% of filler, by weight). Redox initiation in water using ascorbic acid (activator) was used to allow extended working and curing times. They also used tartaric acid. The inclusion of a methacrylate group gave a reduction in solubility of the polymer, so a biocompatible amino acid derivative, acryloyl beta-alanin (ABA) served as a co-solvent for the polymer. They studied the effect of different factors, on compressive strength and curing time, such as sintering of the glass, polymer content, polymer to liquid ratio and different co-monomers. Their results showed that the best powder to liquid (P/L) ratio was 2.5. Their results also indicated that the more acidic the co-polymer the stronger the acid base reaction and thus the higher the compressive strength and curing time. Acryloyl beta-alanin (ABA) is the strongest acid, so gives cement with high compressive strength and curing time. The effects of P/L ratio and different co-polymers on shrinkage were also studied. Shrinkage is reduced with increasing P/L ratio. ABA exhibited minimum shrinkage. Thus, their studies showed that amino acid, modified cement has the lowest shrinkage, longest curing time and high compressive strength.

Hill *et al.*[159] suggested that glass–ionomer cements could be prepared from ZnO:CaO:SiO_2 on the basis of previous work that zinc can act as a network intermediate. They prepared calcium zinc silicate glasses of different compositions and studied their structure and reactivity using different techniques, *i.e.* MAS-NMR spectroscopy, DTA-TGA and X-ray diffraction. They prepared cements by thoroughly mixing the glass powder with PPA powder and distilled water on a glass plate with three P/L ratios 2:1, 1:0.9 and 1:1.36. They calculated the cross link density (CLD) of each glass composition. The glass transition temperatures (T_g) were recorded by thermal analysis. Lowering of T_g was described in terms of changes in the CLD values, indicative of network disruption. ^{29}Si NMR analysis showed the glasses with low ZnO and high CaO content contained Q^2/Q^3 species, while glasses with high ZnO and low CaO content contained Q^1 species. Glasses with Q^2/Q^3 species facilitate cement formation. Their results also correlate with the rheology of the cements.

Towler *et al.*[160] produced zinc based polyalkenoate cements with improved setting times and mechanical properties. They investigated methods of increasing working times and strength of zinc based glass poly alkenoate cements as well as their bioactivity. They used trisodium citrate (TSC), since it is present in bone and incorporation of it in calcium phosphate cements (CPCs) increases the working time and compressive strength. They also observed the effect of addition of strontium to the glass on the working and setting time of resultant cement. Their results showed that the working and setting time decreased with increased amount of SrO for the cements prepared from low concentrations of PPA, however the trend was not observed for higher concentrations of PPA. Biaxial flexural strength and compressive strength were not affected significantly by increasing the amount of strontium. Working and setting times of the resultant cements increased with increasing amount of TSC (trisodium citrate). After one day the compressive strength (CS) of GPCs (glass polyalkenoate cements) containing TSC was much greater than without TSC (control GPCs). After seven days, the CS values of control GPCs (glass polyalkenoate cements) and mGPCs (zinc modified glass polyalkenoate cements) with 5 wt% TSC were almost same, but after 30 days that for mGPCs with 10% TSC was much greater than that for the control GPCs. However, there was little difference in the biaxial flexural strength between mGPCs containing 5% and 10% TSC. Further to their findings above they investigated the anti bacterial effects of their cements and zinc ion uptake by the surrounding tissue. They attributed the antibacterial effect of their cements to the presence of Na^{+}, Zn^{2+} ions and TSC and also found the migration of Zn^{2+} to the surrounding tissue[161].

Towler and coworkers[162] prepared a series of SrO:CaO:ZnO:SiO_2 glasses, varying the amount of SrO in each composition, replacing CaO, and evaluated the structure and reactivity of these glasses when mixed with an aqueous solution of PAA. They measured the glass transition temperature with DTA-TGA (differential thermal analysis-thermal gravimetric analysis) and characterized the structure of the glasses using X-ray diffraction and MAS-NMR spectroscopic techniques. Using network connectivity calculations, they found that ZnO works as a network modifier, with all

glasses similar in structure. The T_g values for each glass deviated by only 2°C from the mean value. ^{29}Si NMR spectra were consistent with Q^2 speciation. They attributed the decreasing working and setting time, with increasing substitution of SrO to the greater electronegativity of Sr and hence increased basicity of the glass network.

1.6 References

1. C. M. Agrawal, *Jom-Journal of the Minerals Metals & Materials Society*, 1998, **50**, 31-35.
2. J. Park and R. S. Lake, *Biomaterials: An Introduction*, Springer, New york, USA, 2007.
3. N. R. Patel and P. P. Gohil, *International Journal of Emerging Technology and Advanced Engineering*, 2012, **2**, 91-101.
4. U. Holzwarth and G.Cotogno, *Total Hip Arthroplasty*, Luxembourg, 2012.
5. A. Tathe, M. Ghodke and A. P. Nikalje, *International Journal of Pharmacy and Pharmaceutical Sciences*, 2010, **2**, 19-24.
6. R. Barbuci, *Integrated Biomaterials Science*, Kulwer, 2002.
7. L. L. Hench and J. Wilson, *Material Research Society Symposium Proceedings*, 1986, **55**, 65-75.
8. L. L. Hench, *Science*, 1980, **208**, 826-831.
9. S. M. Barinov and V. S. Komlev, *Inorganic Materials*, 2011, **47**, 1470-1485.
10. L. L. Hench and J. Wilson, *Science*, 1984, **226**, 630-636.
11. L. L. Hench, *Journal of Materials Science-Materials in Medicine*, 2006, **17**, 967-978.
12. L. L. Hench, R. J. Splinter, W. C. Allen and T. K. Greenlee, *Journal of Biomedical Materials Research symposium*, 1972, **334**, 117-141.
13. A. Oyane, H. M. Kim, T. Furuya, T. Kokubo, T. Miyazaki and T. Nakamura, *Journal of Biomedical Materials Research Part A*, 2003, **65A**, 188-195.
14. T. Kokubo and H. Takadama, *Biomaterials*, 2006, **27**, 2907-2915.
15. K. R. Rust, G. T. Singleton, J. Wilson and P. J. Antonelli, *American Journal of Otology*, 1996, **17**, 371-374.
16. A. E. Fetner, M. S. Hartigan and S. B. Low, *Compendium (Newtown, Pa.)*, 1994, **15**, 935-939.
17. A. E. Fetner, S. B. Low, J. Wilson and L. L. Hench, *Journal of Dental Research*, 1987, **66**, 298-298.
18. E. J. G. Schepers and P. Ducheyne, *Journal of Oral Rehabilitation*, 1997, **24**, 171-181.
19. L. Gendreau, A. P. S. Barlow and S. C. Mason, *The Journal of clinical dentistry*, 2011, **22**, 90-95.
20. J. R. Jones, E. Gentleman and J. Polak, *Elements*, 2007, **3**, 393-399.

21. Z. Wang, T. Jiang, S. Sauro, D. H. Pashley, M. Toledano, R. Osorio, S. Liang, W. Xing, Y. Sa and Y. Wang, *Australian Dental Journal*, 2011, **56**, 372-381.
22. E. Lynch, D. S. Brauer, N. Karpukhina, D. G. Gillam and R. G. Hill, *Dental Materials*, 2012, **28**, 168-178.
23. M. Mneimne, R. G. Hill, A. J. Bushby and D. S. Brauer, *Acta Biomaterialia*, 2011, **7**, 1827-1834.
24. D. S. Brauer, M. Mneimne and R. G. Hill, *Journal of Non-Crystalline Solids*, 2011, **357**, 3328-3333.
25. D. S. Brauer, A. Al-Noaman, R. G. Hill and H. Doweidar, *Materials Chemistry and Physics*, 2011, **130**, 121-125.
26. C. Loty, J. M. Sautier, S. Loty, S. Hattar, A. Asselin, M. Oboeuf, T. Kokubo, H. M. Kim, H. Boulekbache and A. Berdal, *Connective Tissue Research*, 2002, **43**, 524-528.
27. J. A. Juhasz, S. M. Best, R. Brooks, M. Kawashita, N. Miyata, T. Kokubo, T. Nakamura and W. Bonfield, *Biomaterials*, 2004, **25**, 949-955.
28. J. M. Gomez-Vega, E. Saiz and A. P. Tomsia, *Journal of Biomedical Materials Research*, 1999, **46**, 549-559.
29. J. M. Gomez-Vega, A. Hozumi, E. Saiz, A. P. Tomsia, H. Sugimura and O. Takai, *Journal of Biomedical Materials Research*, 2001, **56**, 382-389.
30. K. Rezwan, Q. Z. Chen, J. J. Blaker and A. R. Boccaccini, *Biomaterials*, 2006, **27**, 3413-3431.
31. H. H. Lu, S. F. El-Amin, K. D. Scott and C. T. Laurencin, *Journal of Biomedical Materials Research Part A*, 2003, **64A**, 465-474.
32. A. R. Boccaccini and J. J. Blaker, *Expert Review of Medical Devices*, 2005, **2**, 303-317.
33. G. Poologasundarampillai, K. Fujikura, A. Obata and T. Kasuga, *Express Polymer Letters*, 2011, **5**, 873-881.
34. M. Otsuka, Y. Matsuda, Y. Suwa, J. L. Fox and W. I. Higuchi, *Journal of Biomedical Materials Research*, 1995, **29**, 25-32.
35. Y. Miyamoto, K. Ishikawa, M. Takechi, T. Toh, T. Yuasa, M. Nagayama and K. Suzuki, *Biomaterials*, 1998, **19**, 707-715.
36. L. Yu, Y. Li, K. Zhao, Y. Tang, Z. Cheng, J. Chen, Y. Zang, J. Wu, L. Kong, S. Liu, W. Lei and Z. Wu, *Plos One*, 2013, **8**, e62570.

37. S. X. Zhou, J. Z. Ma, Y. Shen, M. Haapasalo, N. D. Ruse, Q. Z. Yang and T. Troczynski, *Journal of Materials Science-Materials in Medicine*, 2013, **24**, 355-364.
38. A. Ito, M. Otsuka, H. Kawamura, M. Ikeuchi, H. Ohgushi, Y. Sogo and N. Ichinose, *Current Applied Physics*, 2005, **5**, 402-406.
39. U. Thormann, S. Ray, U. Sommer, T. Elkhassawna, T. Rehling, M. Hundgeburth, A. Hens, M. Rohnke, J. Janek, K. S. Lips, C. Heiss, G. Schlewitz, G. Szalay, M. Schumacher, M. Gelinsky, R. Schnettler and V. Alt, *Biomaterials*, 2013, **34**, 8589-8598.
40. E. Sahin and M. Ciftcioglu, *Journal of Materials Chemistry B*, 2013, **1**, 2943-2950.
41. F. Tamimi, Z. Sheikh and J. Barralet, *Acta Biomaterialia*, 2012, **8**, 474-487.
42. G. Cama, F. Barberis, M. Capurro, L. Di Silvio and S. Deb, *Materials Chemistry and Physics*, 2011, **130**, 1139-1145.
43. C. Curless, J. Baclaski and R. Sachdev, *Biotechnology Progress*, 1996, **12**, 728-728.
44. T. N. Osullivan, J. D. Smith, J. D. Thomas and C. Drake, *Environmental Science & Technology*, 1991, **25**, 1088-1091.
45. J. Burnie, T. Gilchrist, S. R. I. Duff, C. F. Drake, N. G. L. Harding and A. J. Malcolm, *Biomaterials*, 1981, **2**, 244-246.
46. T. Gilchrist, D. M. Healy and C. Drake, *Biomaterials*, 1991, **12**, 76-78.
47. J. E. Gough, P. Christian, C. A. Scotchford, C. D. Rudd and I. A. Jones, *Journal of Biomedical Materials Research*, 2002, **59**, 481-489.
48. M. Bitar, V. Salih, V. Mudera, J. C. Knowles and M. P. Lewis, *Biomaterials*, 2004, **25**, 2283-2292.
49. M. Bitar, J. C. Knowles, M. P. Lewis and V. Salih, *Journal of Materials Science-Materials in Medicine*, 2005, **16**, 1131-1136.
50. V. Salih, A. Patel and J. C. Knowles, *Biomedical Materials*, 2007, **2**, 11-20.
51. N. J. Lakhkar, J.-H. Park, N. J. Mordan, V. Salih, I. B. Wall, H.-W. Kim, S. P. King, J. V. Hanna, R. A. Martin, O. Addison, J. F. W. Mosselmans and J. C. Knowles, *Acta Biomaterialia*, 2012, **8**, 4181-4190.
52. M. Uo, M. Mizuno, Y. Kuboki, A. Makishima and F. Watari, *Biomaterials*, 1998, **19**, 2277-2284.
53. H.-J. Seo, Y.-E. Cho, T. Kim, H.-I. Shin and I.-S. Kwun, *Nutrition Research and Practice*, 2010, **4**, 356-361.

54. M. Navarro, M. P. Ginebra and J. A. Planell, *Journal of Biomedical Materials Research Part A*, 2003, **67A**, 1009-1015.

55. A. J. Parsons, L. D. Burling, C. A. Scotchford, G. S. Walker and C. D. Rudd, *Journal of Non-Crystalline Solids*, 2006, **352**, 5309-5317.

56. E. A. A. Neel, I. Ahmed, J. Pratten, S. N. Nazhat and J. C. Knowles, *Biomaterials*, 2005, **26**, 2247-2254.

57. L. Yang, S. Perez-Amodio, F. Y. F. Barrere-de Groot, V. Everts, C. A. van Blitterswijk and P. Habibovic, *Biomaterials*, 2010, **31**, 2976-2989.

58. N. Lakhkar, E. A. Abou Neel, V. Salih and J. C. Knowles, *Journal of Biomaterials Applications*, 2011, **25**, 877-893.

59. S. P. Valappil, D. Ready, E. A. Abou Neel, D. M. Pickup, W. Chrzanowski, L. A. O'Dell, R. J. Newport, M. E. Smith, M. Wilson and J. C. Knowles, *Advanced Functional Materials*, 2008, **18**, 732-741.

60. J. J. Blaker, J. Pratten, D. Ready, J. C. Knowles, A. Forbes and R. M. Day, *Alimentary Pharmacology & Therapeutics*, 2008, **28**, 614-622.

61. A. A. Ahmed, A. A. Ali, D. A. R. Mahmoud and A. M. El-Fiqi, *Solid State Sciences*, 2011, **13**, 981-992.

62. A. M. Mulligan, M. Wilson and J. C. Knowles, *Journal of Biomedical Materials Research Part A*, 2003, **67A**, 401-412.

63. E. A. Abou Neel, I. Ahmed, J. Pratten, S. N. Nazhat and J. C. Knowles, *Biomaterials*, 2005, **26**, 2247-2254.

64. H. W. Kim, E. J. Lee, I. K. Jun, H. E. Kim and J. C. Knowles, *Journal of Biomedical Materials Research Part B-Applied Biomaterials*, 2005, **75B**, 34-41.

65. R. Shah, A. C. M. Sinanan, J. C. Knowles, N. P. Hunt and M. P. Lewis, *Biomaterials*, 2005, **26**, 1497-1505.

66. T. Alekseeva, E. A. Abou Neel, J. C. Knowles and R. A. Brown, *Journal of Biomaterials Applications*, 2012, **26**, 733-744.

67. I. Ahmed, I. A. Jones, A. J. Parsons, J. Bernard, J. Farmer, C. A. Scotchford, G. S. Walker and C. D. Rudd, *Journal of Materials Science-Materials in Medicine*, 2011, **22**, 1825-1834.

68. R. L. Prabhakar, S. Brocchini and J. C. Knowles, *Biomaterials*, 2005, **26**, 2209-2218.

69. I. Ahmed, A. J. Parsons, G. Palmer, J. C. Knowles, G. S. Walkers and C. D. Rudd, *Acta Biomaterialia*, 2008, **4**, 1307-1314.

70. I. Ahmed, P. S. Cronin, E. A. Abou Neel, A. J. Parsons, J. C. Knowles and C. D. Rudd, *Journal of Biomedical Materials Research Part B-Applied Biomaterials*, 2009, **89B**, 18-27.

71. Glocker and Winfrid, *Glass Technology*, Deutches Museum, Germany, 1992.

72. W. Vogel, *Chemistry of Glass*, The American Ceramic Society, Ohio, USA, 1985.

73. R. H. Doremus, *Glass Science*, John Wiley & Sons, New York, Chichester, Brisbane, Torornto, 1973.

74. J. E. Shelby, *Introduction to Glass Science and Technology*, The Royal Society of Chemistry, Cambridge, UK, 2005.

75. S. R. Elliot, *Physics of Amorphous Materials*, Longman Scientific and Technical, Essex, England, 1983.

76. J. J. Hudgens and S. W. Martin, *Journal of the American Ceramic Society*, 1993, **76**, 1691-1696.

77. U. Hoppe, G. Walter, A. Barz, D. Stachel and A. C. Hannon, *Journal of Physics-Condensed Matter*, 1998, **10**, 261-270.

78. D. Stachel, I. Svoboda and H. Fuess, *Acta Crystallographica Section C-Crystal Structure Communications*, 1995, **51**, 1049-1050.

79. I. Abrahams, Queen Mary University of London.

80. J. R. v. Wazer, *Phosphorus and its compounds*, Interscience, New York, 1958.

81. U. Hoppe, R. Kranold, A. Barz, D. Stachel and J. Neuefeind, *Solid State Communications*, 2000, **115**, 559-562.

82. U. Hoppe, *Journal of Physics-Condensed Matter*, 2000, **12**, 8809-8818.

83. K. Suzuya, D. L. Price, C. K. Loong and S. W. Martin, *Journal of Non-Crystalline Solids*, 1998, **232**, 650-657.

84. R. K. Brow, D. R. Tallant, J. J. Hudgens, S. W. Martin and A. D. Irwin, *Journal of Non-Crystalline Solids*, 1994, **177**, 221-228.

85. S. Prabakar, R. M. Wenslow and K. T. Mueller, *Journal of Non-Crystalline Solids*, 2000, **263**, 82-93.

86. R. J. Kirkpatrick and R. K. Brow, *Solid State Nuclear Magnetic Resonance*, 1995, **5**, 9-21.

87. P. Y. Shih, S. W. Yung and T. S. Chin, *Journal of Non-Crystalline Solids*, 1999, **244**, 211-222.

88. K. Meyer, *Physics and Chemistry of Glasses*, 1998, **39**, 108-117.

89. R. K. Brow, *Journal of Non-Crystalline Solids*, 2000, **263**, 1-28.

90. K. Meyer, *Journal of Non-Crystalline Solids*, 1997, **209**, 227-239.

91. G. Walter, U. Hoppe, R. Kranold and D. Stachel, *Physics and Chemistry of Glasses*, 1995, **36**, 154-154.

92. U. Hoppe, G. Walter, R. Kranold, D. Stachel and A. Barz, *Journal of Non-Crystalline Solids*, 1995, **193**, 28-31.

93. T. Kasuga, A. Ichino and Y. Abe, *Nippon Seramikkusu Kyokai Gakujutsu Ronbunshi-Journal of the Ceramic Society of Japan*, 1992, **100**, 1088-1089.

94. K. Meyer, A. Barz and D. Stachel, *Journal of Non-Crystalline Solids*, 1995, **191**, 71-78.

95. E. J. Griffith, *Phosphate Fibers.*, Plenum Publishing Corporation., New York, 1995.

96. R. K. Brow, C. C. Phifer, G. L. Turner and R. J. Kirkpatrick, *Journal of the American Ceramic Society*, 1991, **74**, 1287-1290.

97. G. Walter, U. Hoppe, T. Baade, R. Kranold and D. Stachel, *Berichte Der Bunsen-Gesellschaft-Physical Chemistry Chemical Physics*, 1996, **100**, 1631-1634.

98. J. Swenson, A. Matic, L. Borjesson and W. S. Howells, *Solid State Ionics*, 2000, **136**, 1055-1060.

99. R. K. Brow, *Journal of Non-Crystalline Solids*, 2000, **263**, 1-28.

100. F. Fayon, C. Roiland, L. Emsley and D. Massiot, *Journal of Magnetic Resonance*, 2006, **179**, 49-57.

101. R. Witter, P. Hartmann, J. Vogel and C. Jager, *Solid State Nuclear Magnetic Resonance*, 1998, **13**, 189-200.

102. M. Feike, C. Jager and H. W. Spiess, *Journal of Non-Crystalline Solids*, 1998, **223**, 200-206.

103. F. Fayon, C. Bessada, J. P. Coutures and D. Massiot, *Inorganic Chemistry*, 1999, **38**, 5212-5218.

104. C. Roiland, F. Fayon, P. Simon and D. Massiot, *Journal of Non-Crystalline Solids*, 2011, **357**, 1636-1646.

105. R. Witter, P. Hartmann, J. Vogel and C. Jager, *Solid State Nuclear Magnetic Resonance*, 1998, **13**.

106. R. Gresch, W. Mullerwarmuth and H. Dutz, *Journal of Non-Crystalline Solids*, 1979, **34**, 127-136.

107. M. Crobu, A. Rossi, F. Mangolini and N. D. Spencer, *Analytical and Bioanalytical Chemistry*, 2012, **403**, 1415-1432.

108. U. Hoppe, M. Karabulut, E. Metwalli, R. K. Brow and P. Jovari, *Journal of Physics-Condensed Matter*, 2003, **15**, 6143-6153.

109. R. K. Brow, D. R. Tallant, S. T. Myers and C. C. Phifer, *Journal of Non-Crystalline Solids*, 1995, **191**, 45-55.

110. G. Walter, J. Vogel, U. Hoppe and P. Hartmann, *Journal of Non-Crystalline Solids*, 2003, **320**, 210-222.

111. R. Pires, T. G. Nunes, I. Abrahams, G. E. Hawkes, C. M. Morais and C. Fernandez, *Journal of Materials Science-Materials in Medicine*, 2004, **15**, 201-208.

112. J. F. McCabe and A. W. G. Walls, *Applied Dental Materials*, Blackwell science, Oxford, 1998.

113. A. D. Wilson, 1968, **47**, 1133.

114. B. E. K. A. D. Wilson, 1972**, 132,** 133., *Br. Dent. J.*, 1972, **132**, 133.

115. A. D. Wilson, S. Crisp and A. J. Fermer, 5**5,** 489, *J. Dent. Res*, 1976, **55**, 489.

116. A. D. Wilson and B. E. Kent, *British Dental Journal*, 1972, **132**, 133-&.

117. A. D. Wilson, *The International journal of prosthodontics*, 1990, **3**, 425-429.

118. J. Rusz, J. Antonucci, F. Eichmiller and M. Anderson, *Journal of Dental Research*, 1990, **69**, 366-366.

119. J. W. McLean, J. W. Nicholson and A. D. Wilson, *Quintessence international (Berlin, Germany : 1985)*, 1994, **25**, 587-589.

120. A. Kakaboura, G. Eliades and G. Palaghias, *Dental Materials*, 1996, **12**, 173-178.

121. A. D. W. J. and W. McLean, *Glass Ionomer Cement*, Quintessence books, Chicago, 1988.

122. R. G. Hill and A. D. Wilson, *Glass Technology*, 1988, **29**, 150-158.

123. G. J. Mount, *Colour atlas of glass ionomer cements*, Martin Dunitz, London, 2002.

124. A. D. Wilson and B. E. Kent, *Br. Dent. J.*, 1972, **132**, 133.

125. A. D. Wilson, *Dental Materials*, 1996, **12**, 25-29.

126. H. J. Prosser, S. M. Jerome and A. D. Wilson, *Journal of Dental Research*, 1982, **61**, 1195-1198.

127. A. D. Neve, V. Piddock and E. C. Combe, *Clinical materials*, 1992, **9**, 7-12.

128. A. D. Neve, V. Piddock and E. C. Combe, *Clinical materials*, 1992, **9**, 13-20.

129. A. D. Neve, V. Piddock and E. C. Combe, *Clinical materials*, 1993, **12**, 113-115.

130. M. Darling and R. Hill, *Biomaterials*, 1994, **15**, 299-306.

131. J. A. Williams and R. W. Billington, *Journal of Oral Rehabilitation*, 1991, **18**, 163-168.

132. G. J. Pearson and A. S. Atkinson, *Biomaterials*, 1991, **12**, 658-660.

133. S. Crisp, M. A. Pringuer, Wardlewo.D and A. D. Wilson, *Journal of Dental Research*, 1974, **53**, 1414-1419.

134. H. J. Prosser, C. P. Richards and A. D. Wilson, *Journal of Biomedical Materials Research*, 1982, **16**, 431-445.

135. S. Matsuya, A. Stamboulis, R. G. Hill and R. V. Law, *Journal of Non-Crystalline Solids*, 2007, **353**, 237-243.

136. N. Zainuddin, N. Karpukhina, R. G. Hill and R. V. Law, *Dental Materials*, 2009, **25**, 290-295.

137. R. A. Pires, I. Abrahams, T. G. Nunes and G. E. Hawkes, *Journal of Materials Chemistry*, 2009, **19**, 3652-3660.

138. E. A. Wasson and J. W. Nicholson, *Journal of Dentistry*, 1993, **21**, 122-126.

139. T. I. Barry, D. J. Clinton and A. D. Wilson, *Journal of Dental Research*, 1979, **58**, 1072-1079.

140. P. V. Hatton and I. M. Brook, *British Dental Journal*, 1992, **173**, 275-277.

141. W. D. Cook, *Biomaterials*, 1982, **3**, 232-236.

142. E. A. Wasson and J. W. Nicholson, *British Polymer Journal*, 1990, **23**, 179-183.

143. E. A. Wasson and J. W. Nicholson, *Clin. Mater*, 1991, **7**, 289-293.

144. E. A. Wasson and J. W. Nicholson, *Journal of Dental Research*, 1993, **72**, 481-483.

145. R. A. Pires, T. G. Nunes, I. Abrahams and G. E. Hawkes, *Journal of Materials Science-Materials in Medicine*, 2008, **19**, 1687-1692.

146. S. G. Griffin and R. G. Hill, *Biomaterials*, 1999, **20**, 1579-1586.

147. B. E. Kent, B. G. Lewis and A. D. Wilson, *Journal of Dental Research*, 1979, **58**, 1607-1619.

148. S. Crisp and A. D. Wilson, *Journal of Dental Research*, 1974, **53**, 1408-1413.

149. R. E. Connick and R. E. Poulson., *J Am Chem Soc*, 1957, **79**, 5153.

150. J. Emsley, O. P. A. Hoyte, and R. E. Overill, *Journal of Chemical Society, Chemical Communications*, 1977, 225-226.

151. S. Crisp and A. D. Wilson, *Journal of Dental Research*, 1976, **55**, 1023-1031.

152. S. Crisp, B. G. Lewis and A. D. Wilson, *Journal of Dentistry*, 1979, **7**, 304-312.

153. S. Crisp, A. J. Ferner, B. G. Lewis and A. D. Wilson, *Journal of dentistry*, 1975, **3**, 125-130.

154. J. W. Nicholson, P. J. Brookman and O. M. Lacy, *Journal of Dental Research*, 1988, **67**, 1451-1454.

155. M. R. Towler, C. M. Crowley, D. Murphy and A. M. C. O'Callaghan, *Journal of Materials Science Letters*, 2002, **21**, 1123-1126.

156. M. R. Towler, S. Kenny, D. Boyd, T. Pembroke, M. Buggy and R. G. Hill, *Bio-Medical Materials and Engineering*, 2004, **14**, 565-572.

157. D. Boyd and M. R. Towler, *Journal of Materials Science-Materials in Medicine*, 2005, **16**, 843-850.

158. D. Xie, D. S. Feng, I. D. Chung and A. W. Eberhardt, *Biomaterials*, 2003, **24**, 2749-2757.

159. D. Boyd, M. R. Towler, R. V. Law and R. G. Hill, *Journal of Materials Science-Materials in Medicine*, 2006, **17**, 397-402.

160. D. Boyd, O. M. Clarkin, A. W. Wren and M. R. Towler, *Acta Biomaterialia*, 2008, **4**, 425-431.

161. A. W. Wren, D. Boyd, R. Thornton, J. C. Cooney and M. R. Towler, *Journal of Biomedical Materials Research Part B-Applied Biomaterials*, 2009, **90B**, 700-709.

162. D. Boyd, M. R. Towler, S. Watts, R. G. Hill, A. W. Wren and O. M. Clarkin, *Journal of Materials Science-Materials in Medicine*, 2008, **19**, 953-957.

Chapter 2

General Experimental Methods and Characterisation Techniques

2.0 Introduction

This chapter deals with the theory and brief description of characterisation techniques used in this work and general synthetic methods.

2.1 Characterisation Techniques

Unlike for crystalline materials, characterisation of glasses is not straightforward due to the absence of long range order. Combinations of techniques have been used to successfully understand the short and long range order of glasses as described in chapter 1. Techniques used in the present work include thermal analysis, solid state NMR spectroscopy, FTIR spectroscopy, X–ray diffraction and neutron diffraction. These techniques are discussed briefly in this chapter.

2.1.1 Nuclear Magnetic Resonance (NMR) Spectroscopy

2.1.1.1 Theory

All stable nuclei that contain an odd number of protons and/or neutrons possess nuclear spin and therefore have an associated magnetic moment and angular momentum. The angular momentum of a particle with spin is a vector quantity and in the absence of a magnetic field may be orientated in any possible direction. The direction of the spin angular momentum is called the spin polarization axis. This magnetic property can be investigated by studying the way these nuclei interact with an externally applied magnetic field B_0, which induces net magnetization. In the absence of an external magnetic field, the distribution of magnetic moments is isotropic and the nuclei are randomly arranged. When an external magnetic field is

applied the magnetic moment of the spin moves around the field. The spin moves in a cone keeping the angle constant between spin magnetic moment and the field. This is called precession. The frequency of precession ω_0 is given by

$$\omega_0 = -\gamma B_0 \qquad (2.1)$$

where γ is the gyromagnetic ratio, which is dependent on the type of nucleus and the applied field, B_0. ω_0 is known as the Larmor Frequency and as seen in Eqn 2.1 is proportional to B_0.

According to quantum mechanics, a nucleus of spin quantum number *I* will have (2*I* +1) possible orientations. Thus, nuclei with spin quantum number ½ will have two possible orientations as shown in Fig. 2.1. Nuclei exhibit a Boltzman distribution over these two states such that nuclei with the spin component of magnetic moment parallel to B_0 adopt a lower energy state (α), while those that are anti-parallel adopt a higher energy configuration (β). This interaction of the magnetic moment with the applied field is known as the Zeeman interaction.

The energy gap between the two states is given by:

$$\Delta E = \gamma(h/2\pi)B_0 \qquad (2.2)$$

where *h* is Planck's constant. The Boltzman distribution between the two states is given by:

$$n_\beta/n_\alpha = e^{(-\Delta E/kT)} \qquad (2.3)$$

where k is the Boltzman constant, T is the absolute temperature and n_β/n_α is the ratio of populations of the two states α and β. The difference in population between these two states depends on the applied magnetic field and the nuclei under observation.

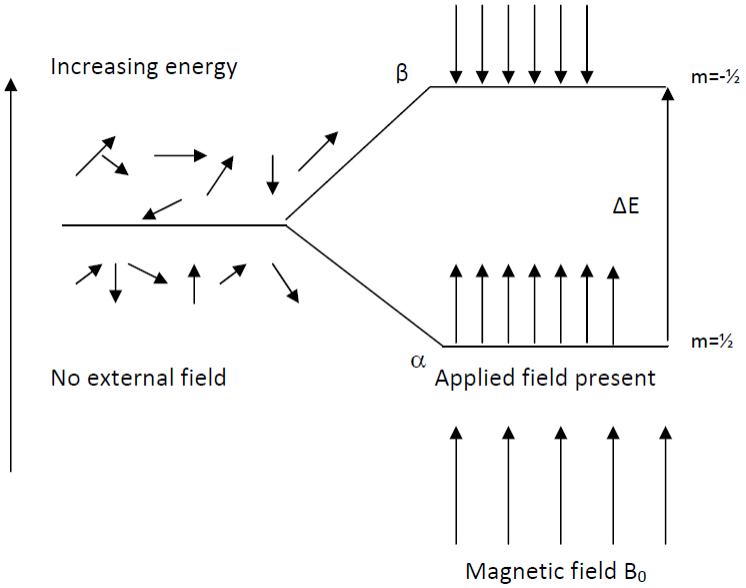

Fig.2. 1. In the absence of B_0 the magnetic nuclei all have the same energy. When B_0 is applied the aligned and opposed orientations correspond to m = ½ and m = -½ for a spin ½ nucleus.

At equilibrium, the net magnetization vector lies along the direction of the applied magnetic field and is called the equilibrium magnetization, M_0. When the system is perturbed from equilibrium (Boltzman distribution) with a second magnetic field (B_1), which oscillates at a radio frequency, similar to the magnetic energy gap between the nuclear energy levels, a torque is applied on the magnetization and causes the net magnetisation vector to precess perpendicular to B_0 at a constant frequency. The precessing magnetization induces current in the coil of a detector, which is detected as an NMR signal called a free induction decay (FID). The signal decays away after excitation[1-3].

2.1.1.2 Spin – Lattice Relaxation (T_1)

If we define the magnetization in the direction of the applied magnetic field as M_z, then at equilibrium $M_z = M_0$. If a radio frequency pulse of energy, equal to the energy difference between two spin states is supplied to the system, the net magnetization moves perpendicular to the applied field (y- direction) and $M_z \rightarrow 0$ (is equal to 0 if enough energy is provided). The time constant which describes how

quickly M_z returns to its equilibrium value is called the spin lattice relaxation time (T_1). T_1 depends on the interaction between the spins and the lattice[4].

2.1.1.3 Spin – Spin Relaxation (T_2)

When a radio frequency pulse is applied and the net magnetization, M_0, in the z- axis is rotated by $\pi/2$ (such that $M_0 = M_y$) the result will be spin polarization in the y axis. The net magnetic moment perpendicular to the applied magnetic field is called the transverse magnetization. When the pulse is removed, the transverse magnetization decays as polarization of the spins diminishes. This occurs because each spin experiences the magnetic field differently and rotates at its own Larmour frequency, due to different spin environments. T_2 or the transverse relaxation time constant is the homogenous decay of the transverse magnetization (Fig. 2.2). T_2 is always less than or equal to T_1 and depends on molecular interactions and variations in B_0[5-7].

The combined T_2 due to molecular interactions and inhomogenities in the applied magnetic field, called T_2*, can be represented as follows:

$$1/T_2^* = 1/T_{2(\text{mol int})} + 1/T_{2(\text{inhomo})} \qquad (2.4)$$

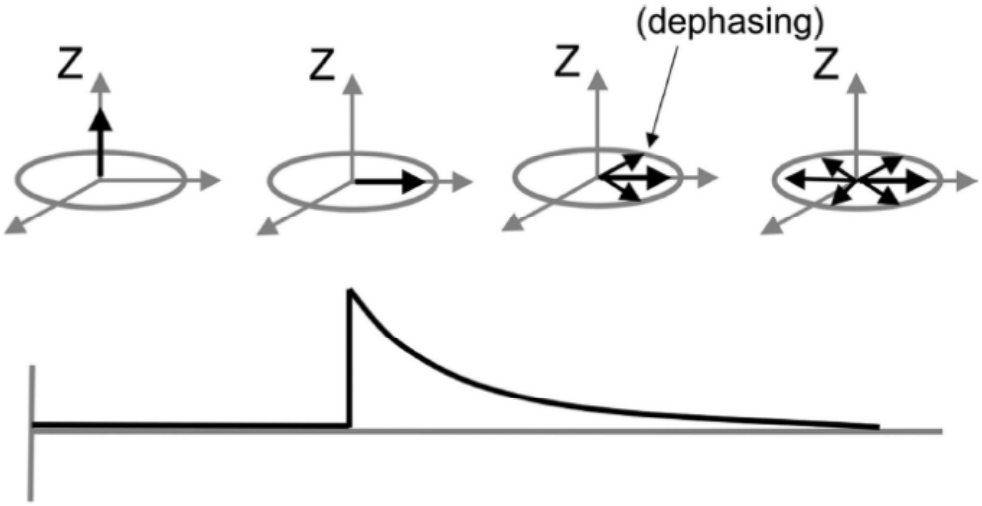

Fig.2. 2. Schematic illustration of spin – spin or transverse magnetization[5].

2.1.1.4 Chemical Shift

The applied magnetic field induces electronic currents around nuclei (Fig. 2.3). These induced currents will produce a small magnetic field which will either oppose the applied magnetic field or enhance it and gives rise to nuclear shielding or deshielding effects. Thus the exact Larmour frequency absorbed by a nucleus is modified by the interaction between its surrounding electron density and the applied magnetic field. Different chemical environments give rise to different absorption frequencies, and are the origin of chemical shift. The chemical shift of a specific nucleus, recorded in units of parts per million (ppm) in an NMR spectrum, is the resonance frequency of that nucleus in an applied field (ν_i), relative to that of a standard sample (ν_{ref}).

$$\delta_i = \frac{(\nu_i - \nu_{ref})\times 10^6}{\nu_{ref}} \qquad (2.5)$$

The interaction between the applied magnetic field, B_0 and electron density results in the nucleus experiencing an effective magnetic field, B_{eff}

$$B_{eff} = B_0 (1-\delta_c) \qquad (2.6)$$

where δ_c is the shielding constant[2, 8, 9].The resonance or absorption frequency is given by:

$$\nu = \gamma B_0/2\pi(1-\delta_c) \qquad (2.7)$$

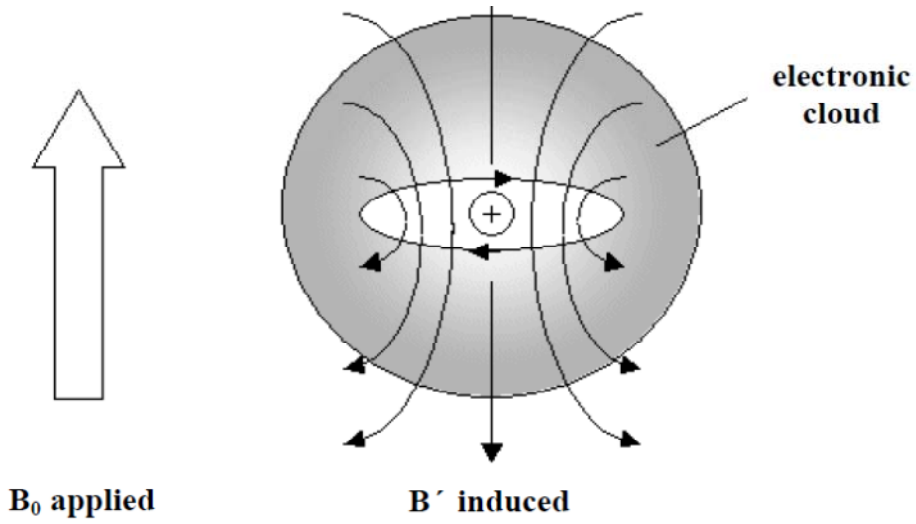

Fig.2. 3. Induced magnetic field (B') produced by electronic currents generated by applied magnetic field B_0[10]

2.1.1.5 Solid State Nuclear Magnetic Resonance

In liquid state (solution state) NMR experiments, rapid tumbling of molecules occurs which averages out a number of interactions such as dipole-dipole coupling, yielding spectra with sharp resonance peaks, with the chemical shifts of individual resonances relatively well resolved. In solid state NMR experiments these interactions are no longer averaged out and result in significantly broadened resonance peaks. In order to extract information from solid state spectra it is important to consider these interactions and these are discussed below.

2.1.1.6 Chemical Shift Tensor and Chemical Shift Anisotropy

The distribution of electrons around the nucleus is usually non-spherical therefore the shielding experienced by the nucleus depends on the relative orientation of the nucleus with respect to the applied magnetic field B_0. Therefore, in solids the chemical shift is anisotropic and is defined by a second rank tensor, σ. This tensor can be represented as a matrix

$$\sigma = \begin{pmatrix} \delta_{xx} & \delta_{xy} & \delta_{xz} \\ \delta_{yx} & \delta_{yy} & \delta_{yz} \\ \delta_{zx} & \delta_{zy} & \delta_{zz} \end{pmatrix}$$

Which can be diagonalised to give:

$$\delta = \begin{pmatrix} \delta_{xx} & 0 & 0 \\ 0 & \delta_{yy} & 0 \\ 0 & 0 & \delta_{zz} \end{pmatrix}$$

where δ_{ii} are the principal components of the chemical shift tensor. The isotropic chemical shift is then given by:

$$\delta_{iso} = 1/3\ (\delta_{xx} + \delta_{yy} + \delta_{zz}) \qquad (2.8)$$

In the present work the principal components of the chemical shift tensor were ordered according to the Haeberlen convention[11], i.e.

$$|\delta_{zz} - \delta_{iso}| > |\delta_{xx} - \delta_{iso}| > |\delta_{yy} - \delta_{iso}|$$

The chemical shift anisotropy ($\Delta\delta$) and asymmetry (η) are given by:

$$\Delta\delta = \delta_{zz} - \delta_{xx} \qquad (2.9)$$

$$\eta = (\delta_{xx} - \delta_{yy})/\ \delta_{zz} \qquad (2.10)$$

Schematic solid state static powder patterns with different values of asymmetry are shown in Fig. 2.4.

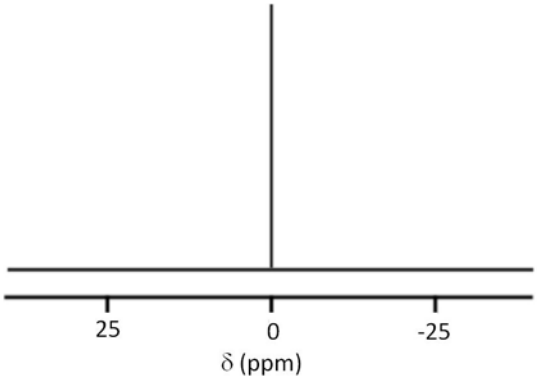

Cubic

($\delta_{xx} = \delta_{yy} = \delta_{zz}$)

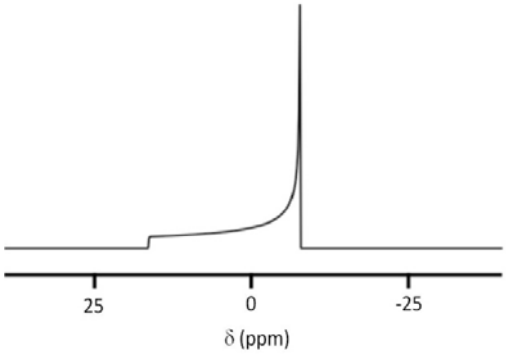

Axially symmetric

($\eta = 0$)

($\delta_{xx} = \delta_{yy} \neq \delta_{zz}$)

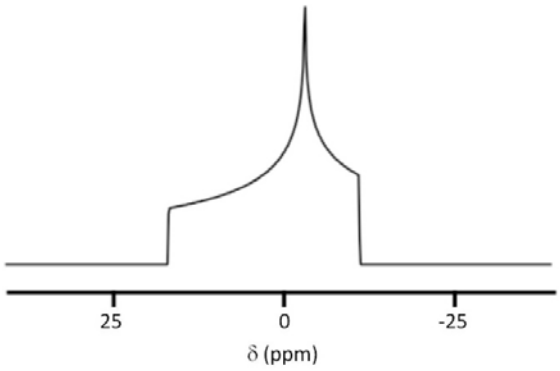

Axially asymmetric (η= 0.5)

($\delta_{xx} \neq \delta_{yy} \neq \delta_{zz}$)

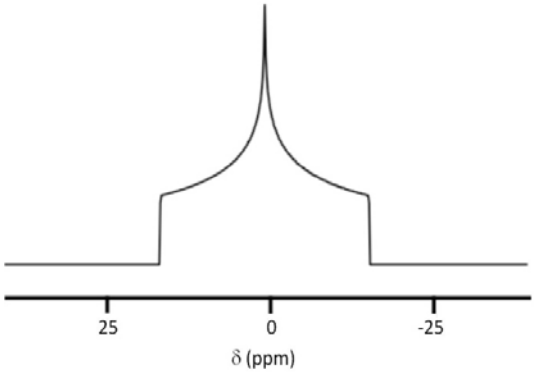

Axially asymmetric (η = 1)

($\delta_{xx} \neq \delta_{yy} \neq \delta_{zz}$)

Fig.2. 4. Powder line shapes with different values of chemical shift asymmetry (adapted from ref[12])

Thus by analyzing chemical shift anisotropy one can reveal details of the local electronic environment of the nucleus. e.g. for an axially symmetric environment $\delta_{xx} = \sigma_{yy}$ and $\eta = 0$ [13].

2.1.1.7 Dipole – Dipole Coupling

In solids, dipolar coupling is the major cause of line broadening. The magnetic moments created as a result of nuclear spin, interact with each other through space, like bar magnets (Fig. 2.5). This interaction is called dipole – dipole or dipolar coupling. The strength of the interaction depends on the internuclear distance, r, and the orientation of the molecule. The applied magnetic field B_0 causes the relative disposition of the two spins in space, hence the field presented by each nuclear magnetic dipole depends on the orientation of the molecular fragment they are held within, relative to B_0. The effective field, B_{eff}, at a nucleus A generated by nucleus B is given by

$$B_{eff} = \pm\mu_B r_{AB}^{-3}(3\cos^2\theta - 1) \qquad (2.11)$$

where μ_B is the magnetic moment of B, r_{AB} is the internuclear distance and θ is the angle between the internuclear vector and the magnetic field B_0.

Dipolar coupling can provide information about internuclear distances and hence the geometry and conformation of molecules due to its dependence on the magnitude of r_{AB}. Several recoupling techniques such as DRAMA, C7 etc. are applied to measure the dipolar couplings in both homonuclear and hetronuclear spin ½ and quadrupolar spin systems[13,14,15].

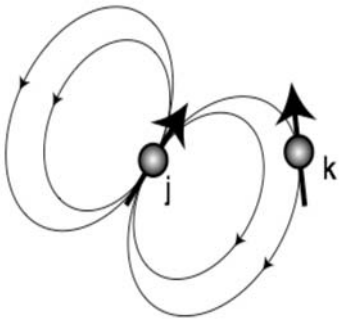

Fig.2. 5. schematic illustration of dipolar interaction between spins j and k[12].

2.1.1.8 Quadrupolar Coupling

Nuclei with spin greater than ½ are termed quadrupolar. They possess electric quadrupole moment due to charge distribution (Fig. 2.6). The electric quadrupole moment, *eQ*, (where e is the charge of nucleus and *Q* is the quadrupole coupling), interacts with any electric field gradient (V) which arises due to other nuclei and electrons in their vicinity. This interaction affects the nuclear spin energy levels (Fig. 2.7).

The quadrupole Hamiltonian describing the interaction between electric quadrupole moment and electric field gradient is[16]

$$H_Q = \vec{I} \cdot \hat{Q} \cdot \vec{I} \tag{2.12}$$

where $\vec{I}$ is the spin vector and $\hat{Q}$ is given by

$$\hat{Q} = \frac{eQ}{(2I(2I-1)h)}\hat{V} \tag{2.13}$$

where $\hat{V}$ is the electric field gradient tensor at the nucleus.

The nuclear electric quadrupole interaction is described by the quadrupolar coupling constant (C_Q) and the asymmetry parameter (η_Q).

$$C_Q = \frac{e^2 Q q_{zz}}{h} \tag{2.14}$$

$$\eta_Q = (V_{11} - V_{22})/V_{33} \tag{2.15}$$

where *q* is the largest component of the EFG at the nucleus and V_{11}, V_{22}, V_{33} are the diagonal elements of the electric field gradient in the principal axis system.

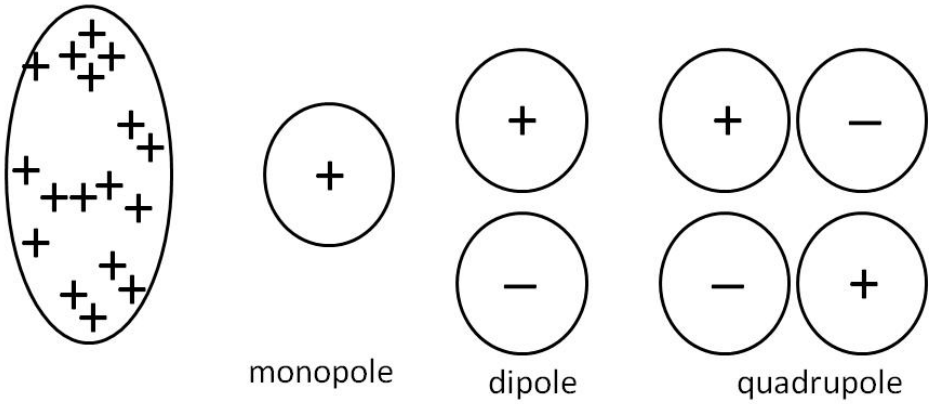

Fig.2. 6 . Schematic illustration of charge distribution on a nucleus.

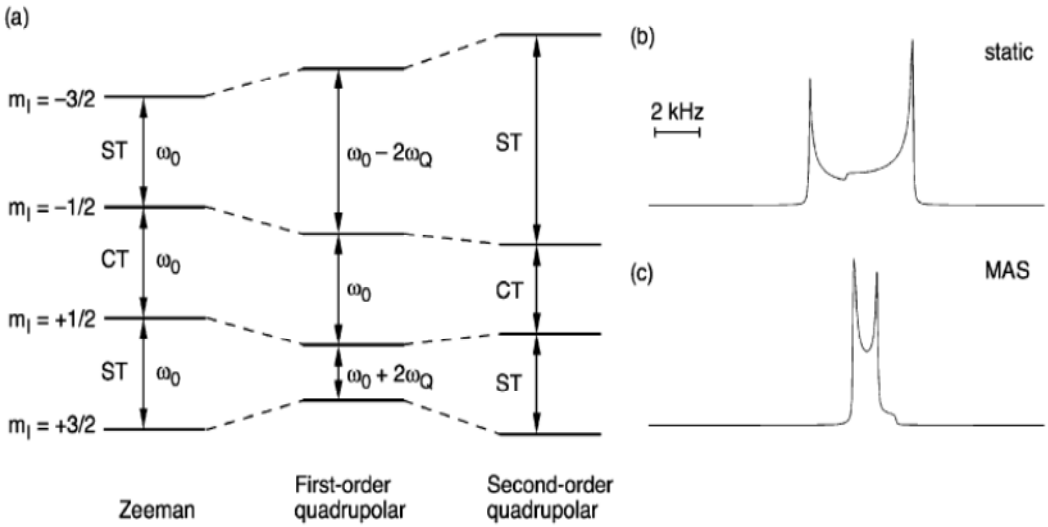

Fig.2. 7. (a) schematic energy level diagram for spin I = 3/2 showing the effect of first order and second order quadrupolar interactions (b) static (c) MAS line shape simulated with Cq = 2kHz[17]

Several pulse sequences are currently available for signal enhancement of low γ and low sensitivity quadrupolar nuclei such as QCPMG, Hahn echo, Solid echo etc.

2.1.1.9 Spin–Spin or J – Coupling

J-coupling is an indirect dipole-dipole coupling between two nuclear spins which arises due to hyperfine interaction between the nuclei and local electrons. It can provide information on bond lengths and angles. The *J*-coupling of two spins can be measured if they are linked though a small number of chemical bonds.

The Hamiltonian describing spin-spin coupling between spins *i* and *j* is given by

$$H_J = \vec{I}_i \cdot \hat{J}_{ij} \cdot \hat{I}_j \qquad (2.16)$$

J-coupling depends on molecular orientation, but is independent of the strength of the applied magnetic field. Solids have *J*-coupling anisotropy, however, it is usually very small and is often ignored[7].

2.1.1.10 Magic Angle Spinning

In order to reduce the broadening caused by the effects described above, several techniques are used to achieve high resolution NMR spectra. The most routinely used technique is magic angle spinning originally introduced by Raymond Andrew in 1958[18]. This technique is mainly used to overcome the effect of chemical shift anisotropy. It also helps to reduce the broadening of lines from quadrupolar nuclei and that due to homonuclear dipolar coupling. The magic angle spinning experiment is shown in Fig. 2.8.

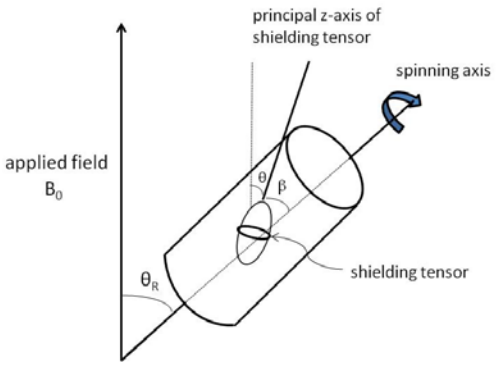

Fig.2. 8. A rotor inclined at magic angle with respect to magnetic field B_0. θ_R is the magic angle (54.74°). θ is the angle between principal z-axis of shielding tensor and B_0, β is the angle between principal z-axis and spinning axis.

The molecular orientation dependence of the nuclear spin interaction is of the form $3\cos^2\theta - 1$, θ is an angle which describes the orientation of the spin interaction tensor, (including shielding, dipole coupling and quadrupolar coupling components) and takes all possible values in a powder sample. All molecular orientations are therefore represented in a static NMR spectrum of a powder sample. If the sample is spun at an angle θ_R to the applied field as shown in Fig. 2.8 the angle θ changes with the time, due the change in orientation of the molecules with the spinning of the sample. The average orientation dependence of the nuclear spin interactions can be related to the spinning angle as follows

$$3\cos^2\theta - 1 = \tfrac{1}{2}(3\cos^2\theta_R - 1)(3\cos^2_{\beta} - 1) \qquad (2.17)$$

If θ_R is set to 54.7° then $3\cos^2\theta_R - 1$ becomes zero and hence $3\cos^2\theta - 1$ also becomes zero and therefore the interaction anisotropy averages to zero provided spinning is fast enough. If spinning is not fast enough to completely overcome anisotropic interactions, spinning side bands are observed at a distance equal to the spinning speed. Spinning side bands can be useful to extract important information about chemical shift anisotropy, which is averaged out during magic angle spinning[13].

Typically, spinning rates are in the order of 5 to 12 kHz. More recently solid state NMR probes have been developed for very fast spinning up to ca. 70 kHz. Small diameter rotors are required for spinning at these very high rates. Fig. 2.9 shows a range of typical rotor sizes as used in the present work.

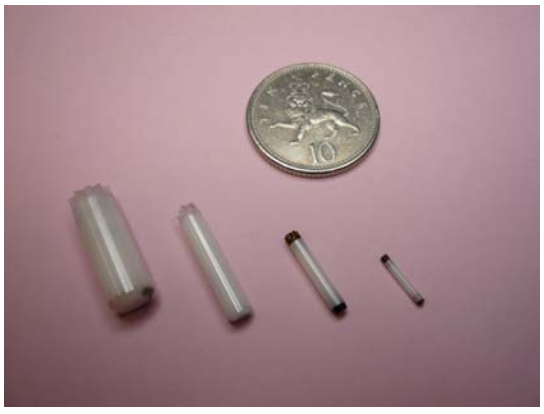

Fig.2. 9. Showing rotors of sizes 7mm, 4mm, 2.5mm, 1.3mm from left to right[12].

2.1.1.11 Multi-Dimensional Experiments

In the NMR experiment we do not observe the transition between energy states as in other forms of spectroscopy, instead NMR is the time evolution of coherences between the Zeeman levels of the spin system. The coherence between Zeeman levels i and j evolves as a function of $\exp(i\omega_{ij}t)$, where t is the time.

$$\omega_{ij} = (\mathrm{E}_i - \mathrm{E}_j)/h \qquad (2.18)$$

where E is the energy of a particular Zeeman level. We can only observe directly the evolution of the coherent superposition of Zeeman levels whose magnetic quantum number differs by -1. However, we can observe other orders of coherences indirectly using various pulse sequences. This is the basis of two-dimensional or multi-dimensional NMR experiments[13].

2.1.1.12 Pulse Sequences

A pulse sequence is a programme of radio frequency pulses and delays applied to the sample to acquire a free induction decay (FID) corresponding to the desired coherences. Pulse sequences can be divided into three components:

1) Preparation
2) Mixing
3) Acquisition

In preparation, the spin system is prepared to yield a specific type of information e.g transverse magnetization is achieved by a 90° pulse. Mixing may or may not be present depending on the type of experiment. During mixing coherence transfer is achieved in such a way that different frequencies can be correlated e.g in double quantum correlation experiments. The signal from the spin system is acquired during the acquisition time.

2.1.1.12.1 Basic 1D Pulse Sequence

Basic one dimensional NMR experiments for both solid state (static or MAS) and solution state utilise a very simple pulse sequence which is called a 90 degree pulse as shown in Fig. 2.10. When a 90 degree pulse (P_1) is applied to a spin system with equilibrium magnetization it rotates the magnetization in the x - y plane. An inter-pulse delay, also called a relaxation delay (D_1), allows the spin system to relax back to the equilibrium state. If an insufficient relaxation delay time is applied, the spin system will not relax completely and this will affect the intensity of the free induction decay (FID). D_1 is generally 4 – 5 times the longest T_1 value for the spin system under study. The acquisition time is the time during which signal from the spin system is recorded.

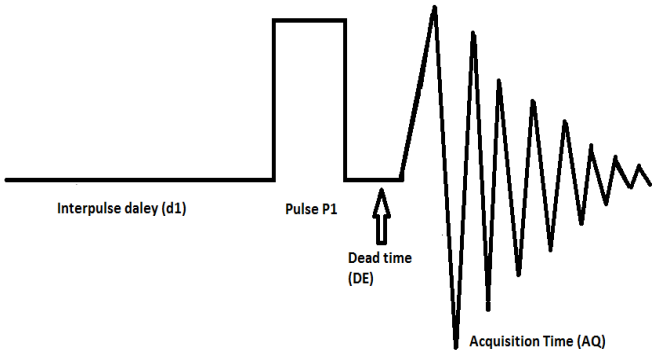

Fig.2. 10. Schematic representation of simple 1D pulse sequence.

2.1.1.12.2 Solid Echo Pulse Sequence

Solid echo is a 90°-90° pulse sequence which is a modification of the solid state spin echo method (90°- 180°) originally developed by Turner *et al* in 1986[19]. It is a useful pulse sequence for quadrupolar nuclei, where nuclei are split into multiple energy levels. Solid echo refocuses the transverse magnetisation to overcome the line broadening effect and loss of signal due to quadrupolar coupling. It involves a 90° pulse from the *x* plane followed by T_1 delay and another 90° pulse from the *y* plane before recording the FID after a T_2 delay. T_2 is kept shorter than T_1.

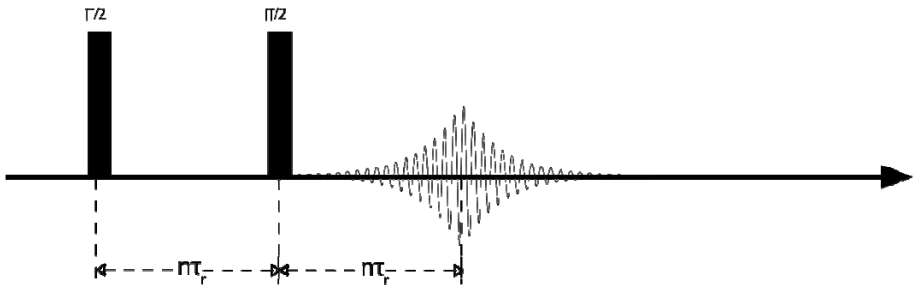

Fig.2. 11. A schematic illustration of solid echo pulse sequence.

2.1.1.12.3 Post C7 Pulse Sequence

The Post C7 pulse sequence written by Hohwy[15] is a modification of the C7 pulse sequence[20], which is applied to excite double quantum coherence under magic angle spinning for through space recoupling of spin interactions. C7 is a C_n^N pulse sequence, which represents a sequence of *n* rf pulse cycles C to fit into *N* periods of the sample rotations.

Both sequences consist of seven rf cycles C with two rotational periods. The overall phase of each consecutive cycle, ϕ, is incremented in steps of $2\pi/7$. The difference in C7 and Post-C7 lies in the construction of the basic pulse cycle C. In C7 cycle C consists of two rf pulses, each with a flip angle 2π. The phase of two pulses differs by x and $\bar{x}$, whereas cycle C in the POST-C7 pulse sequence consists of three rf pulses, with three different flip angles $\{\pi/2, 2\pi, 3\pi/2\}$ with phases $\{x, \bar{x}, x\}$

respectively[21] (Fig. 2.12). The Post-C7 sequence gives much more broad-band dipolar recoupling and enhanced radio frequency inhomogeneity compensation than C7.

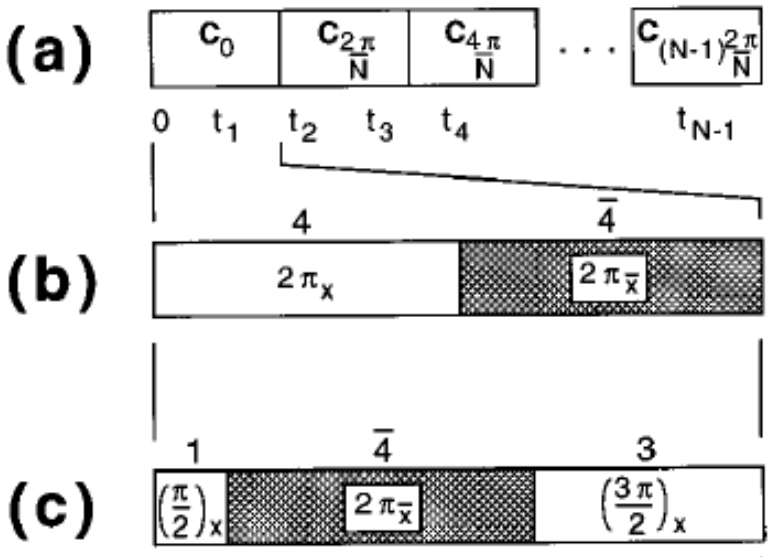

Fig.2. 12. a)Timing scheme for CN pulse sequence b) C7 c) post C7[15].

2.1.2 X–ray Diffraction

X–ray diffraction arising from the lattice planes within crystals is used as a fingerprint of crystal structure. No two crystals will have identical diffraction patterns as they are dependent on the symmetry and contents of the unit cell of the crystal. In the Bragg model, diffraction of X–rays is considered to arise from reflection of X–ray waves by the lattice planes in the crystal acting as semi-transparent mirrors. Consider parallel X–ray waves striking parallel crystallographic planes described by the Miller indices *hkl* and separated by an interplanar spacing d_{hkl} as shown in Fig 2.13.

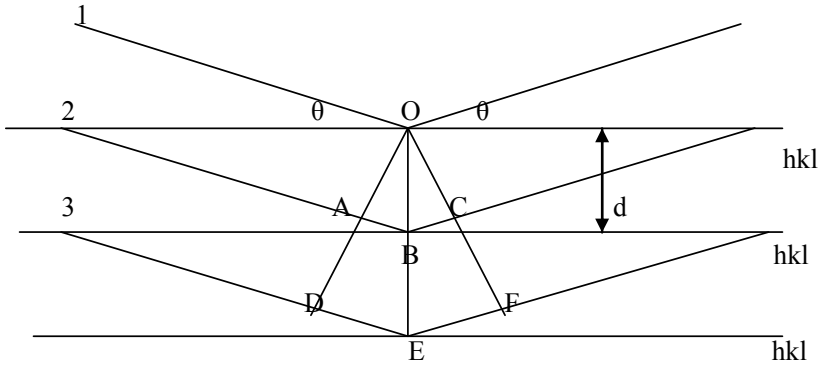

Fig.2. 13. Diffraction of X–rays from parallel planes in a crystal

The initial waves are in phase and reflect from each of the planes in the crystal. According to Snell's law, the angle of incidence must be equal to the angle of reflection. So in Fig 2.13, wave 2 must travel a distance ABC further than wave 1. Similarly, wave 3 must travel a distance DEF further than wave 2. Plane geometry shows that when the distance ABC is equal to one wavelength (λ), the distance DEF will be equal to 2λ. From the right angle triangle OAB

$$AB = d_{hkl} \sin \theta \qquad (2.19)$$

$$ABC = 2d_{hkl} \sin \theta \qquad (2.20)$$

For constructive interference of the waves ABC = λ , thus for diffraction

$$\lambda = 2d_{hkl} \sin \theta_{hkl} \qquad (2.21)$$

This is known as Bragg's law[22].

2.1.2.1 Powder X–ray Diffraction

When a powder with randomly oriented crystallites is placed in an X–ray beam, all the interatomic planes will be seen by the beam. However, the diffraction from each type of plane will only occur at its characteristic diffraction angle, θ. Thus if the

experimental angle 2θ is changed, all of the possible diffraction peaks that can be produced from the differently oriented crystallites in the powder will be observed (Fig. 2.14).

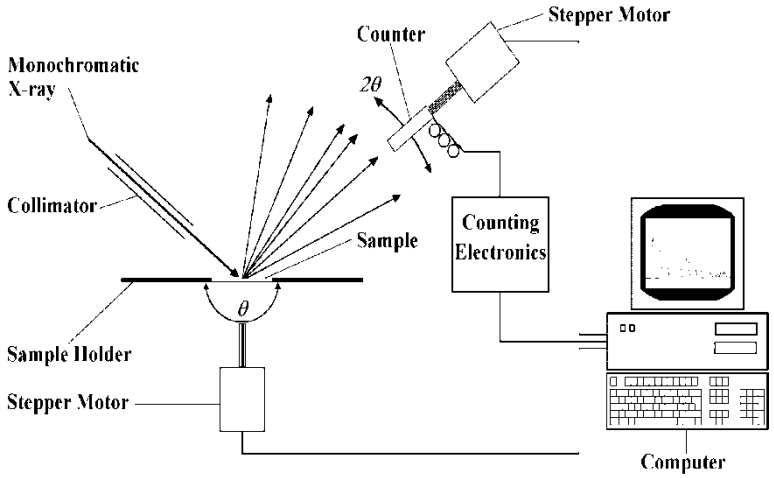

Fig.2. 14. Schematic Diagram of an X–ray powder diffractometer (θ/2θ) geometry[23].

For identification, the diffraction pattern of the solid is compared to diagrams of known substances until a match is obtained. Alternatively, *d* values calculated from the diffraction diagram of an unknown substance are compared with those of known substances. This information is contained in databases, the most comprehensive of which is the JCPDS powder diffraction file (PDF)[24]

2.1.3 Neutron Scattering

Like, X–ray diffraction, neutron scattering is a non-destructive technique for analysis of structure and utilizes neutrons of similar wavelength to the interatomic spacings in crystals. Neutrons have no charge and negligible electric dipole. They travel long distances without being absorbed or scattered and interact with nuclei via nuclear forces. Like other subatomic particles, neutrons show wave/particle duality. The wavelength of neutrons is often represented in terms of wave vector, *k.* The magnitude of the wave vector, which points in the direction of the neutron flight, can

be represented as $2\pi/\lambda$. The magnitude of the neutron wave vector *k* can be related to the neutron velocity *v* and mass m as follows[25]

$$k = 2\pi mv/h \tag{2.22}$$

The De Broglie equation is given by

$$\lambda = \frac{h}{mv} \tag{2.23}$$

Therefore

$$k = \frac{2\pi}{\lambda} \tag{2.24}$$

The effective area around the nucleus within which neutrons can hit the nucleus is called the neutron scattering cross section (σ) and is measured in barns (1 barn = 10^{-28} m^2). The amplitude of the scattered neutron wave depends on the strength of interaction between the nucleus and incident neutron wave. Since the nucleus is fixed the scattering is elastic, so the wave vector of the scattered beam is same as the incident beam. The cross section is given by

$$\sigma = 4\pi b^2 \tag{2.25}$$

where b is the scattering length of the nucleus. However, scattering by matter is different from that by a free nucleus. The scattering process can be inelastic, i.e. it can change the energy and momentum of both neutrons and matter. The neutron can transfer its momentum to the scatterer (nucleus). If k_i and k_s are the wave vectors of incident and elastically scattered neutron beams respectively.

The momentum transfer is given by

$$\frac{hQ}{2\pi} = \frac{h(k_i - k_s)}{2\pi} \tag{2.26}$$

Q is called the scattering vector and is equal to $k_i - k_s$. This can be represented schematically as a simple vector triangle, Fig.2.15.[26] Q is therefore given by

$$Q = 2k \sin\theta = \frac{4\pi \sin\theta}{\lambda} \tag{2.27}$$

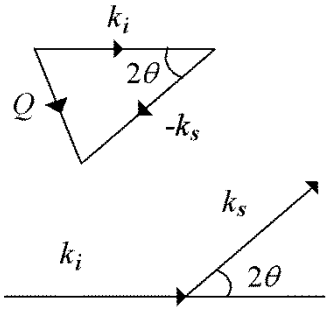

Fig.2. 15. Scattering triangle for elastically scattered beam.

In scattering experiments the scattering data can be represented as functions of wave vector, *k*, wave vector momentum transfer (*Q*) or energy (*E*), although the most commonly used term is (*Q*) which is a measure of reciprocal space.

The change in cross section with respect to the detector angle Ω is known as the differential cross section $\left(\frac{d\sigma}{d\Omega}\right)$ and is defined as:

$$\left(\frac{d\sigma}{d\Omega}\right) = \frac{\text{The number of quanta scattered per second into } d\Omega}{\Phi d\Omega} \tag{2.28}$$

In a scattering experiment the intensity as a function of *Q*, *I*(*Q*), is given by

$$I(Q) = \Phi\left(\frac{d\sigma}{d\Omega}\right)(Q)d\Omega \tag{2.29}$$

Where Φ is the neutron flux. The differential cross section $\left(\frac{d\sigma}{d\Omega}\right)$ has two basic components, distinct scattering and self scattering. Self scattering arises from individual nuclei, while distinct scattering is the scattering due to correlated pairs of nuclei. Typically self scattering is subtracted in during data processing.

$$\frac{d\sigma}{d\Omega} = \left(\frac{d\sigma}{d\Omega}(Q)\right)_{self} + \left(\frac{d\sigma}{d\Omega}(Q)\right)_{distinct} \tag{2.30}$$

Neutron scattering analysis is typically concerned with the distribution of one atom, α, around another, β. A total interference function *F*(*Q*) for this system is given by summing scattering over all pairs in the system according to their weighted proportion and scattering length.

$$F(Q) = \sum_{\alpha,\beta}^{n} c_\alpha c_\beta \overline{b_\alpha}\ \overline{b_\beta}\left[S_{\alpha\beta}(Q) - 1\right] \tag{2.31}$$

where $S_{\alpha\beta}$ is the partial structure factor relating to the atom pair α and β, c_α and c_β are the fractions of chemical species α and β and $\overline{b}_\alpha$ and $\overline{b}_\beta$ are the mean scattering lengths for atoms α and β. The partial structure factor is given by

$$S_{\alpha\beta} = S_{\beta\alpha} = 1 + \frac{1}{c_\alpha c_\beta N}\left\langle \sum_{i,j\neq i}^{N_\alpha, N_\beta} \frac{\sin(Qr_{ij})}{Qr_{ij}} \right\rangle \tag{2.32}$$

where r_{ij} is the radial distance between scatterers *i* and *j*, *N* is the total number of atoms in the system and the symbol $\langle\ \rangle$ denotes thermal average.

The partial pair distribution functions $g_{\alpha\beta}$ are obtained by Fourier transformation of $S_{\alpha\beta}$

$$S_{\alpha\beta}(Q)-1=\frac{4\pi\rho_0}{q}\int_0^\infty r\left[g_{\alpha\beta}(r)-1\right]\sin(Qr)\,dr \tag{2.33}$$

$$g_{\alpha\beta}(r)-1=\frac{1}{2\pi^2 r\rho_0}\int_0^\infty Q\left[S_{\alpha\beta}(Q)-1\right]\sin(Qr)\,dQ \tag{2.34}$$

where ρ_0 is the total number density of atoms = N/V (V = volume). The mean number of β atoms around α atoms in a spherical shell, $\bar{n}_\alpha^\beta$, i.e. the partial coordination number (is given by integration of the partial radial distribution function.

$$\bar{n}_\alpha^\beta = 4\pi\rho_0 c_\beta \int_{r_1}^{r_2} g_{\alpha\beta}(r) r^2\,dr \tag{2.35}$$

A number of total pair correlation functions are commonly used in scattering analysis of amorphous materials. The total pair correlation function, $G(r)$ is obtained by Fourier transformation of the total interference function:

$$G(r)=\frac{1}{2\pi^2 r\rho_0}\int_0^\infty qF(Q)\sin(Qr)\,dQ \tag{2.36}$$

The derived total correlation function $T(r)$, can be calculated as:

$$T(r)=4\pi r\rho_0\left[G(r)+\bar{b}^2\right] \tag{2.37}$$

where the mean scattering length $\bar{b}$ is given by

$$\bar{b}=\sum_\alpha^n c_\alpha \overline{b_\alpha} \tag{2.38}$$

Finally another correlation function that is often used is the differential correlation function $D(r)$, which is related to $G(r)$ by

$$D(r) = 4\pi\rho_0 G(r) \tag{2.39}$$

2.1.3.2 Instrumentation

2.1.3.2.1 Neutron Production

Neutrons are produced in two different ways, either by a nuclear reactor or a spallation processes. In a nuclear reactor, neutrons are produced through a neutron induced nuclear fission reaction, where a neutron hits a nucleus usually plutonium or uranium, which splits into daughter nuclei, with the release of at least two high energy neutrons and a large amount of energy. High energy neutrons are slowed down through a moderator. Controlled nuclear fission chain reactions are carried out to produce neutrons with energies much higher than those from a spallation source.

In the spallation process, high energy particles, usually protons, collide with a target nucleus, which produce highly excited nuclear states, which decay either immediately or with a delay and produce neutrons and other particles such as neutrinos as well as γ-rays. The energy of the neutrons produced through this process depends on the energy of the protons. If the target is uranium up to 30 neutrons per proton can be produced (Fig. 2.16).

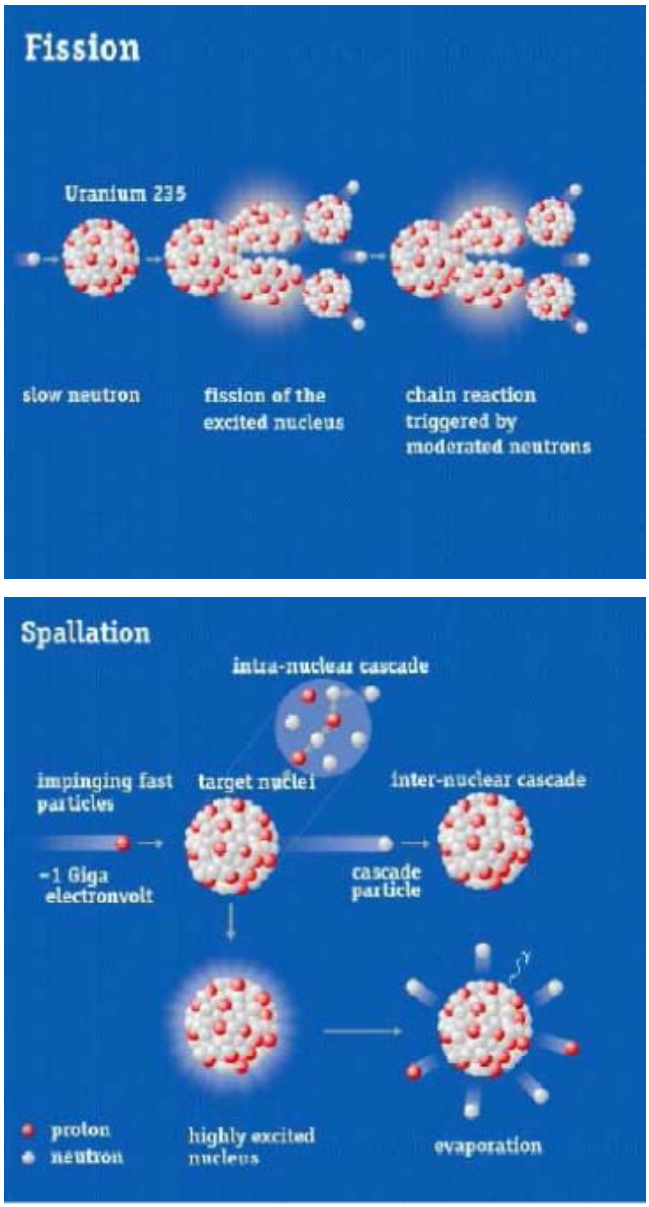

Fig.2. 16. Two different ways of neutron production[27].

2.1.3.2.5 Neutron Detection

All the work carried in the present study was performed using the spallation source at the ISIS facility, Rutherford Appleton Laboratory, UK. Measurements were recorded as counts per microsecond (i.e. per time of flight, the time taken for the neutron to leave the moderator and reach the detector after scattering from the sample).

The total flight path (L) is the distance from the moderator (used to broaden the spectrum of energies of the neutrons) to the sample (L_0) and from the sample to the detector (L_1).

$$L = L_0 + L_1 \tag{2.40}$$

Assuming no inelastic loss of energy then the time of flight t.o.f. is given by

$$t.o.f. = \frac{L}{v} \tag{2.41}$$

where *v* is the neutron velocity. From the de Broglie eqn (eqn 2.23)

$$t.o.f. = \frac{mL\lambda}{h} \tag{2.42}$$

From eqn 2.24

$$t.o.f. = \frac{mL2\pi}{hk} \tag{2.43}$$

From Eqn 2.27 $Q = 2k\sin\theta$, therefore

$$Q = \frac{4\pi mL\sin\theta}{ht} \tag{2.44}$$

Fig 2.17 shows a schematic diagram of the GEM diffractometer with its eight detector banks. Each detector bank is associated with a particular *Q* range and in data analysis these are summed to give the overall scattering pattern. Typically, the data from banks 1 and 2 are not used in data analysis due to excessive nosie. The maximum *Q* value for data analysis is typically between 50 and 60 $Å^{-1}$.

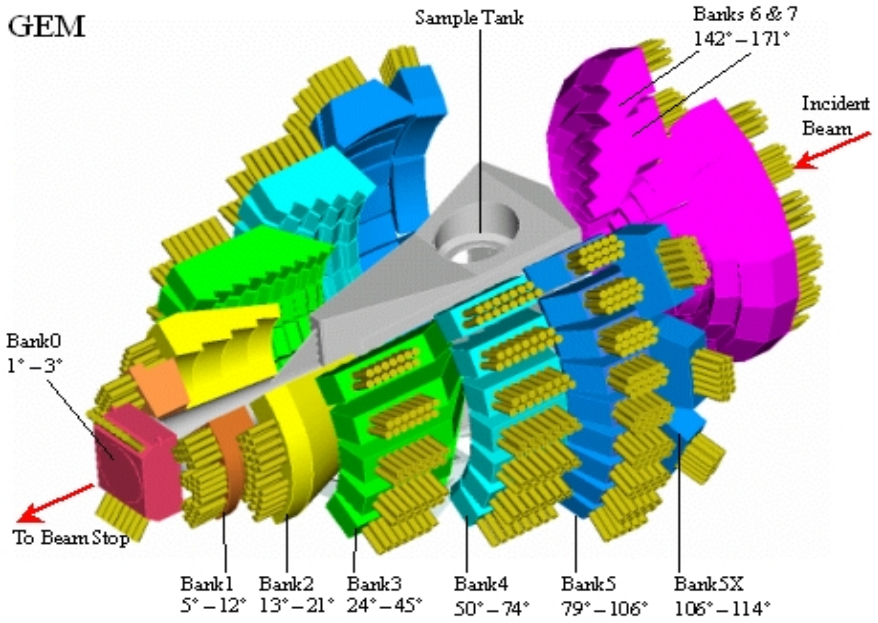

Fig.2. 17. Schematic diagram of the GEM diffractometer[28]

2.1.4 Fourier Transform Infrared Spectroscopy (FTIR)

Infrared spectroscopy makes use of the electromagnetic radiation from wave number 10 cm^{-1} to 4000 cm^{-1}. When molecules absorb IR radiation, changes in the vibrational and rotational energy levels take place. Molecules must undergo a change in dipole moment in order for a vibrational mode to be IR active. The alternating electric field of the electromagnetic radiation interacts with the changing dipole moment of the molecule and causes a change in amplitude of molecular vibration, if the frequency of the electromagnetic radiation matches the vibrational frequency of the molecule. In solids only vibrational transitions are seen. There are two types of vibrations *i.e.* stretching and bending. Stretching vibration involves a change in inter-atomic distance along the bond and can be symmetric or asymmetric. Bending vibrations are changes in angle between two bonds. Bending vibrations are twisting, rocking, wagging and scissoring. Thus the frequency of absorbed radiation can be associated with a particular bond type[29]. Table 2.1 summarises the main phosphate vibrations seen in IR spectra.

Table 2. 1 FTIR features frequently observed in phosphate glasses[30, 31]

Frequency cm^{-1}	Assignment
~ 1260	P=O vibration superposed with $(PO_2)_{as}$ mode in Q^2 units.
~ 1190	(P–O) vibration in Q^2 units
~ 1100-1140	Broad band for $(P–O^-)_{as}$ vibration in Q^2 units and/or P–O–Zn linkages
~ 1040	Vibration of PO_4^{3-} (Q^0) tetrahedra
~ 970	$(P–O)_{as}$ vibration in Q^1 units
~ 880-900	$(P–O–P)_{as}$ vibration of BOs
~ 720-780	$(P–O–P)_s$ vibration of BOs
~ 530	Deformation mode of P–O groups.

2.1.5 Differential Scanning Calorimetry (DSC)

Differential scanning calorimetry (DSC) is a thermo analytical technique, where an inert reference and a sample are subjected to a programmed temperature change. When an endothermic or exothermic physical or chemical change occurs in the sample, heat is added to either the sample or the reference container in order to maintain both the sample and the reference at the same temperature (Fig. 2.18). The plot of differential heat flow to the sample and the reference versus programmed temperature indicates the transition temperature and whether the transition is exothermic or endothermic[32].

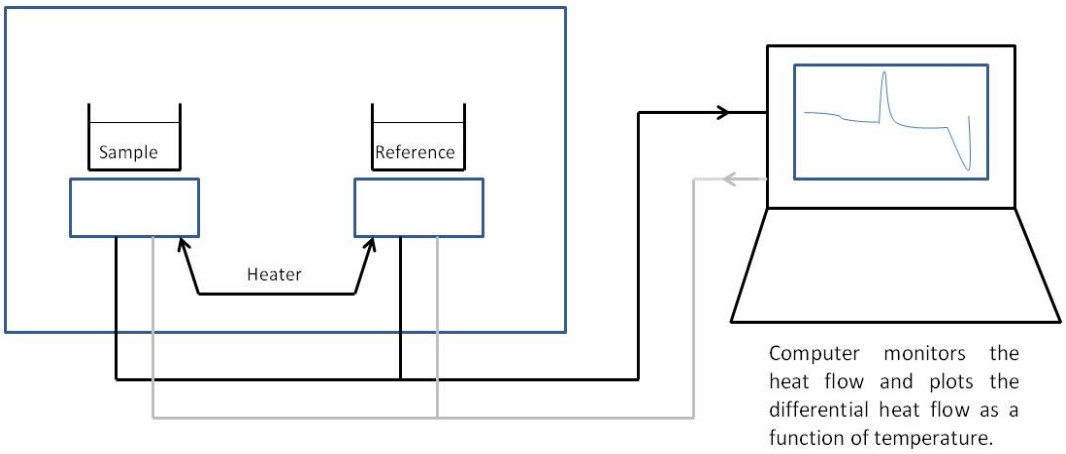

Fig.2. 18. Schematic illustration of DSC.

2.2 Experimental Methods

2.2.1 General Glass Preparation

Glasses were prepared by the melt quench method from $NH_4H_2PO_4$ (98-101%, BDH), ZnO (99.999%, KOCH Chemicals Ltd), Na_2CO_3 (99%, BDH), $CaCO_3$ (99% AnalaR Hopkin and Williams) and $SrCO_3$(99.9% Sigma–Aldrich). Stoichiometric amounts of starting materials were weighed and ground together for 15 min as a slurry in methylated spirits using an agate mortar and pestle and subsequently dried in air. The dry powder was transferred to a platinum crucible, which was then heated in an electric muffle furnace for 1 h at 300°C to decompose the phosphate, 1 h at 600°C to decompose the carbonate and 1 h at 1100°C to achieve the melt. The molten glass was quenched rapidly in air onto a stainless steel plate. Glass discs were prepared by pouring the molten product into a stainless steel mold to cast discs of 12 mm diameter and 2-3 mm thickness for solubility studies. Glass rods for neutron diffraction experiments were prepared from the molten glass, which was poured into a preheated graphite mould. This was placed into an electric muffle furnace, at a temperature about 20°C above glass transition temperature as measured by DSC, for 1 h. The sample and mould were then cooled slowly in air over a period of ca. 24 h.

Glass powder for cements was obtained by grinding bulk glass samples in a vibratory mill (Gyro mill, Glen Creston, London, UK) for two 7 min cycles. Powders were sieved through a 38 μm sieve to obtain particles with less than 38 μm diameter. All samples were stored under vacuum in desiccators over silica gel.

2.2.2 Cement Preparation

All cements were made by mixing glass powder with either poly acrylic acid (PAA) or (VPA-AA) copolymer and distilled water or tartaric acid solution (TA) in distilled water on a glass slab. Cements were prepared with different powder to liquid (P:L) ratio with an optimum ratio of 3:1, where 300 g of glass was mixed with 100 g of polymeric acid and 100 g of water/TA.

2.2.3 Setting Time Measurements

Samples were prepared using round plastic moulds of 6 mm diameter. Initial and final setting time was studied with the help of Gilmore needle apparatus HM-310 (Fig.2.19) with 1/4lb and 1lb needles for initial and final setting time respectively. The flat end of a cylindrical needle was placed onto the cement in the mould and indentation formation was measured visually. Absence of any mark or indentation upon placement of the needle was taken as setting time according to the respective needle.

Fig.2. 19. Gillmore needle apparatus used for measuring setting time.

2.2.4 Compressive Strength

Cylindrical samples of 4 mm diameter and 6 mm height were prepared by packing cement mixture into stainless steel moulds. Moulds were covered with acetate sheet, clamped between two steel plates and stored in an incubator at 37°C, until the compressive strength was measured. Compressive strength was tested using a hydraulic testing machine (Instron 5567, Instron Europe, High Wycombe, UK) with a 1 kN load cell and 1 mm s^{-1} testing speed.

2.2.5 Hydrolytic Stability

Hydrolytic stability was measured to check sample suitability for further investigation. A set cement (24 h setting time) was prepared in a cylindrical stainless steel mould to yield sample rods of 6 mm height and 4 mm diameter. The sample rod was immersed in distilled water at room temperature and visually inspected after 24 h immersion. If the sample remained intact it was considered to be hydrolytically stable.

2.2.6 Nuclear Magnetic Resonance (NMR)

2.2.6.1 Instrumentation

2.2.6.1.1 ^{31}P and ^{23}Na 1D MAS–NMR

Solid state ^{31}P and ^{23}Na MAS–NMR experiments were carried out on Bruker Avance 600 MHz NMR instrument. A 30° pulse (zg) with relaxation delays of 60 s and 5 s were used to acquire ^{31}P and ^{23}Na 1D spectra, respectively. Samples were contained in a 4 mm or 2.5 mm diameter zirconia rotor at spinning speeds of 8 kHz, 12 kHz and 21 KHz to acquire 16 or 32 ^{31}P and 64 for ^{23}Na spectra.. ^{31}P spectra were referenced to 85% phosphoric acid solution whereas ^{23}Na spectra were referenced to 1M aqueous solution of sodium chloride.

2.2.6.1.2 ^{31}P – ^{31}P Double Quantum – Single Quantum MAS-NMR

^{31}P–^{31}P double quantum–single quantum (DQ–SQ) MAS-NMR spectra were collected at a spinning speed of 21 kHz in a 2.5 mm o.d. zirconia rotor, using the Post C7 pulse sequence[15, 21, 33]. To avoid spinning side bands in the ω1 dimension, t_1 increments were rotor synchronized. A total of 96 or 128 t_1 increments were used, each slice was the sum of 16 transients using a recycle delay of 30 s. The pulse sequence and coherence pathway for Post C7 are presented in Fig. 2.20

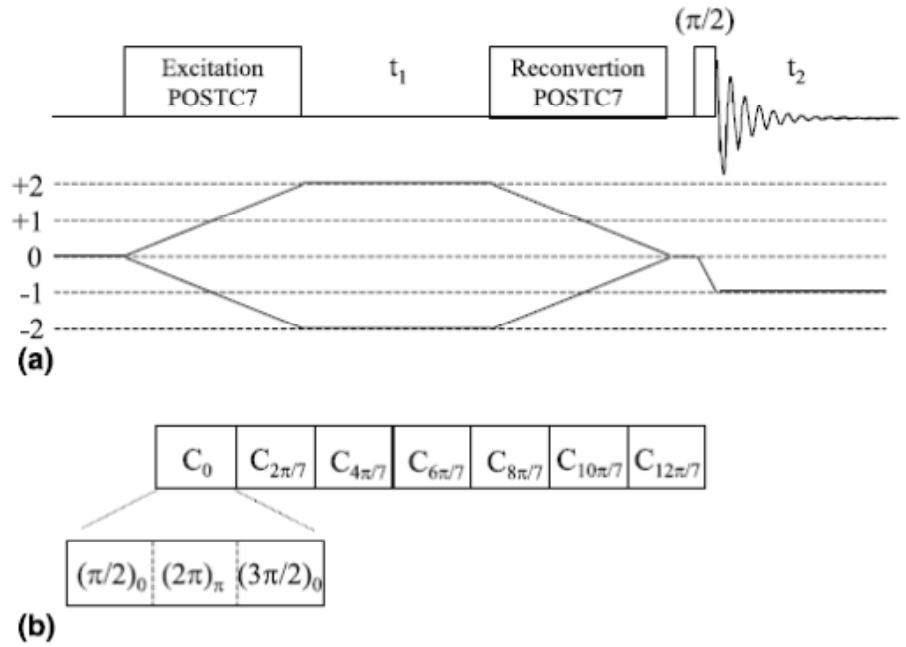

Fig.2. 20. (a) Pulse sequence schematic and coherence pathway used for the two-dimensional double quantum MAS-NMR experiment. (b) detail of the post C7 sequence[33].

2.2.6.1.3 Ultra High Field ^{67}Zn and ^{43}Ca NMR

^{67}Zn static and ^{43}Ca static and MAS—NMR experiments on glass samples were performed at 21.1 T on a 900 MHz Bruker Avance II spectrometer at the National Ultrahigh-field NMR Facility for Solids in Ottawa, Canada, operating at 56.4 MHz, and 60.56 MHz respectively. Sample powders were packed into 7 mm zirconia rotors. Spectra were acquired in a 7 mm home built probe for stationary samples, using the Solid Echo pulse sequence[34] with recycle delay of 0.5 s and 1 s for ^{67}Zn and ^{43}Ca respectively. ^{67}Zn and ^{43}Ca spectra were referenced to 1 M aqueous solutions of zinc nitrate (δ_{iso} = 0 ppm) and calcium chloride (δ_{iso} = 0 ppm) respectively.

2.2.6.2 Data Analysis

NMR spectra were deconvoluted and fitted using WINFIT DM 2011[35]. ^{31}P MAS-NMR whole spectra, including side bands, were fitted using the program NMRLSS[36]. Integrated intensities for all spinning side bands were analysed using the Herzfeld Berger[37] method, with the program HBA[38] to calculate the principal components of the

chemical shift shielding tensors (δ_{11}, δ_{22}, δ_{33}), chemical shift anisotropy ($\Delta\delta$) and asymmetry parameter (η). ^{67}Zn NMR spectra were simulated using Qstat ½ line shape in program DMFIT (dm2011vs)[35] and QUADFIT[39] to calculate peak width, quadrupolar coupling centre and quadrupolar asymmetry.

2.2.7 Neutron Diffraction

2.2.7.1 Instrumentation

Data were acquired on the General Materials diffractrometer (GEM) at the ISIS facility, Rutherford Appleton Laboratory UK[40]. The GEM diffractometer has a incident flight path L_i of 17.0m and detectors which cover a 10 m^2 area to optimise the high count rate. Glass rods of approximately 12 mm diameter and 70 mm height were used to collect data up to Q = 60 $Å^{-1}$.

2.2.7.2 Neutron Data Analysis

Neutron data were analysed and processed using software, GUDRUN[41], OpenGenie[42], Xsect[43] and Gemsqraw[43]. GUDRUN2 was used in combination with OpenGenie and Xsect to correct data and fit the total correlation function $T(r)$ to get pair distances and coordination numbers, whereas data were processed using GUDRUN4 for use in RMC calculations.

Before beginning data analysis the following information about each sample was noted.

Sample composition

Sample height

Sample weight

Sample diameter

Packing density if a powder

Accurate density (e.g. by pychnometry)

The .raw files for the samples and the normalisation, i.e. empty diffractometer, empty can, vanadium rod etc. were copied to the working folder for analysis. Full details of the data correction procedure are given in Appendix A1.

2.2.8 X- ray Diffraction

X–ray powder diffraction (XRD) data were collected on a PANalytical X'Pert Pro diffractometer using Ni filtered Cu-Kα radiation (λ = 1.5418 Å). Data were recorded in flat plate θ/θ geometry over the 2θ range 5 to 70°, at a step width of 0.0334°, with an effective count time of 200 s per step.

2.2.9 Differential Scanning Calorimetry (DSC)

A Stanton Redcroft DSC 1500 was used for thermal analysis of the glasses, with alumina as a reference material. Approximately 50 mg of sample and reference were placed in platinum pans and data recorded over the temperature range 50°C to 1000°C, at a heating rate of 20°C min^{-1}, under a flowing N_2 atmosphere.

2.2.10 FTIR

FTIR spectra were recorded on powdered samples using a Perkin Elmer Spectrum 65 spectrometer, with an ATR attachment. Spectra were recorded over the range 600 to 2000 cm^{-1} and air was subtracted as background.

2.2.11 Solubility Studies

2.2.11.1 Tris Buffer Preparation

Tris buffer was prepared by dissolving 15.090 g of Tris(hydroxylmethyl) aminomethane (Sigma Aldrich) in 800 mL of distilled water, followed by the addition of 44.2 ml of 1 M hydrochloric acid (HCl) (Sigma Aldrich). The solution was heated to 37°C overnight, after which the pH was adjusted to 7.30 using HCl and a pH meter (Orion 9609BNWP with Orion pH/ISE meter 710, both Thermo Scientific, Waltham, MA, USA) and the solution was made up to 2 litres using deionised water.

2.2.11.2 Solubility Tests

The solubility of glass discs was measured in deionised water and tris(hydroxymethyl)aminomethane/HCl buffer (tris). The starting pH of the tris buffer solutions was kept between 7.26 and 7.40. Discs were placed in 25 mL of solution and every seven days discs were removed from solution, washed with ethanol, dried in an incubator at 80°C for about 15 min, weighed and then immersed in fresh solution. Solutions collected at each time point were filtered through a 0.2 μm syringe filter. The pH of solutions was measured using a pH meter. Solutions were stabilised with 0.5 mL 5% HNO_3 and analysed using a Vista Pro CCD simultaneous ICP-OES. A second set of experiments was carried out, where discs were immersed in 25 mL of solution and left at 37°C for 28 days. The discs were then removed, dried in an incubator at 37°C and ground into a fine powder in an agate mortar.

2.3 References

1. C. H. Yoder and C. D. Schaeffer, *Introduction to multinuclear NMR*, The Benjman/Cummings publishing company, Inc, California, 1987.
2. J. W. Akitt, *NMR and chemistry : an introduction to modern NMR spectroscopy*, Chapman & Hall, London, UK, 1992.
3. W. Kemp, *NMR in chemistry : A multinuclear introduction*, Macmillan, 1986.
4. K. Jeremy, M. Sanders and K. Brian, *Modern NMR spectrscopy: a guide for chemists*, Oxford university press, 1993.
5. R. A. Pooley, *Radiographics*, 2005, **25**, 1087-1099.
6. D. E. Andrew, *Modern NMR Techniques for Chemistry Research*, Pergamon press, Oxford, New York, Seoul, Tokyo, 1993.
7. H. M. Levitt, *Spin dynamics : Basics of Nuclear Magnetic Resonance*, Wiley, 2008.
8. P. J. Hore, *Nuclear Magnetic Resonance*, Oxford University Press, Oxford, UK, 1995.
9. J. L. Thomas, Department of Pharmaceutical Chemistry, University of California, USA, Fundamentals of NMR.
10. P. G. Ioannis, T. Anastassios, E. Vassiliki and B. Klimentini, *Chemistry Education and Research Practice in Europe*, 2002, **3**, 229-252.
11. U. Haeberlen, *Advances in magnetic resonance*, Academic Press, New York, 1976.
12. S. Ashbrook, presented in part at the CASTEP Workshop, Oxford, UK, 2009.
13. M. J. Deur, *Introduction to Solid-State NMR Spectroscopy*, Blackwell Publishing Ltd, Oxford, UK, 2004.
14. R. Tycko and S. O. Smith, *Journal of Chemical Physics*, 1993, **98**, 932-943.
15. M. Hohwy, H. J. Jakobsen, M. Eden, M. H. Levitt and N. C. Nielsen, *Journal of Chemical Physics*, 1998, **108**, 2686-2694.
16. C. P. Slichter, *Principles of Magnetic Resonancce*, Springer-Verlag, Berlin, 1990.
17. S. E. Ashbrook, *Physical Chemistry Chemical Physics*, 2009, **11**, 6892-6905.
18. E. R. Andrew and R. G. Eades, *Nature*, 1958, **182**, 1659.
19. A. C. Kunwar, G. L. Turner and E. Oldfield, *Journal of Magnetic Resonance*, 1986, **69**, 124-127.
20. Y. K. Lee, N. D. Kurur, M. Helmle, O. G. Johannessen, N. C. Nielsen and M. H. Levitt, *Chemical Physics Letters*, 1995, **242**, 304-309.

21. T. Karlsson, J. M. Popham, J. R. Long, N. Oyler and G. P. Drobny, *Journal of the American Chemical Society*, 2003, **125**, 7394-7407.
22. *R. Jenkins* and *R. L. Snyder*, *X-Ray Powder Diffractometry*, *John Wiley & sons,* Inc, New York, 1996.
23. I. Abrahams, Queen Mary University of London, 2012.
24. PDF2, The International Centre for Diffraction Data, Pennsylvania, USA.
25. G. L. Squires, *Introduction to the Theory of Thermal Neutron Scattering*, Dover Publications, 1997.
26. R. Pynn, *Neutron Scattering: A Primer*, Los Alamos Science, 1990.
27. K. Lefmann, Neutron Scattering: Theory, Instrumentation, and Simulation
28. in '*http://www.isis.rl.ac.uk/disordered/gem/gem_home.htm*'.
29. J. H. V. Maas, *Basic Infrared Spectroscopy*, Heyden & Sons Ltd, London, 1972.
30. D. Muresan, M. Vasilescu, I. Balasz, C. Popa, W. Kiefer and S. Simon, *Journal of Optoelectronics and Advanced Materials*, 2006, **8**, 558-560.
31. J. Schwarz, H. Ticha, L. Tichy and R. Mertens, *Journal of Optoelectronics and Advanced Materials*, 2004, **6**, 737-746.
32. H. H. .Willard, L. L. Meritt, J. A. Dean and F. A. Settle, Wandsworth Publishing Company, California, 1998.
33. F. Fayon, D. Massiot, K. Suzuya and D. L. Price, *Journal of Non-Crystalline Solids*, 2001, **283**, 88-94.
34. J. T. Cheng and P. D. Ellis, *Journal of Physical Chemistry*, 1989, **93**, 2549-2555.
35. D. Massiot, F. Fayon, M. Capron, I. King, S. Le Calve, B. Alonso, J. O. Durand, B. Bujoli, Z. H. Gan and G. Hoatson, *Magnetic Resonance in Chemistry*, 2002, **40**, 70-76.
36. I. Abrahams, Queen Mary University of London., 2003.
37. J. Herzfeld and A. E. Berger, *Journal of Chemical Physics*, 1980, **73**, 6021-6030.
38. HBA, 1990.
39. T. F. Kemp and M. E. Smith, *Solid State Nuclear Magnetic Resonance*, 2009, **35**, 243-252.
40. A. C. Hannon, *Nuclear Instruments & Methods in Physics Research Section a-Accelerators Spectrometers Detectors and Associated Equipment*, 2005, **551**, 88-107.
41. http://www.disordmat.moonfruit.com/.
42. http://www.opengenie.org/Main_Page.

43. http://wwwisis2.isis.rl.ac.uk/disordered/ACH/Software/index.htm.

Chapter 3 Zinc Containing Metaphosphate Glasses

3.0 Introduction

This chapter deals with the structural investigation of metaphosphate glass systems of stoichiometry $Na_{1-x}Zn_{1+x/2}(PO_3)_3$ (i.e. $16.7(1-x)\%Na_2O{:}33.3(1+x/2)\%ZnO{:}50\%P_2O_5$; x = 0, 0.25, 0.5, 0.75, 1.0) and $NaZn_{1-x}M_x(PO_3)_3$ (i.e. $16.7\%Na_2O{:}33.3(1-x)\%ZnO{:}33.3x\%MO{:}50\%P_2O_5$; x = 0.25, 0.5, 0.75, 1.0; M = Ca and Sr). A variety of zinc oxide based cements are used widely in dentistry, e.g. zinc phosphate, zinc polycarboxylate, zinc eugenol and zinc imidazole cements. In glasses, zinc oxide is believed to play an intermediate role as both network former and modifier. When included in binary phosphate glass formulations it extends the glass forming region down to the invert phosphate composition region around 20 mol% P_2O_5[1]. This implies that the local environment of the zinc cations in glasses, even within a series of compositions, can change substantially. This is unsurprising, since it is known that the coordination number of zinc in crystalline zinc metaphosphate, $Zn(PO_3)_2$, is different in the high temperature and low temperature polymorphs, with values of 4 and 6 respectively[2, 3] (Fig. 3.1). Similarly, α–$Zn_2(P_2O_7)$ is reported to have 5 and 6 coordinated zinc sites[4]. In glasses, it is therefore assumed that zinc can show variable coordination numbers from six or five to four, in a similar way to aluminium in conventional glass–ionomer cements.

Sodium is often added to glasses to reduce glass transition temperature and make them more soluble. Calcium and strontium are other desired elements for biomaterials. The presence of calcium in phosphate glasses helps in precipitation of apatite or other bioactive calcium phosphates[5-7]. Strontium in dental cements imparts radio opaqueness to the material. Additionally, it helps in osteoblast differentiation and inhibits osteoclast activity[8]. It is shown to have the potential to reduce oxidative stress in therapeutic biomaterials[9].

(a)

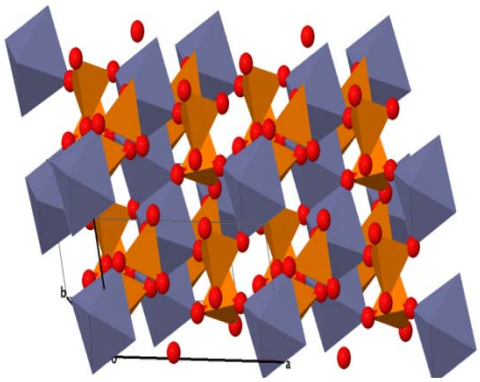

(b)

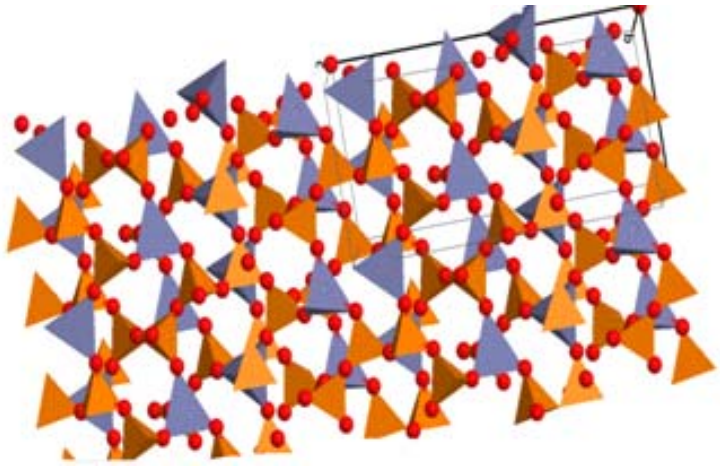

Fig. 3.1. (a) Low temperature (α) and (b) High temperature (β) polymorphs of crystalline $Zn(PO_3)_2$

The structures of zinc containing metaphosphate glasses in binary and ternary systems have been studied using several techniques such as FTIR, Raman[10-12] and ^{31}P MAS–NMR[12-15] spectroscopies, neutron diffraction[14, 16, 17], X–ray diffraction[18, 19], RMC modelling[20, 21] and Molecular Dynamics (MD) [22-25]. Brow *et al*.[11] studied the structure of zinc polyphosphate glasses using ^{31}P MAS–NMR and Raman spectroscopies and concluded the existence of tetrahedral zinc in both zinc metaphosphate and pyrophosphate. Hope *et al*.[26] have also studied the structure of zinc phosphate glasses from metaphosphate to invert phosphate with neutron diffraction and extended X–ray absorption fine structure (EXAFS). RMC modelling of these data revealed silica like

network for zinc phosphate glass with PO_4 units alternating with ZnO_4 units. They attributed the presence of only four coordinated zinc in the metaphosphate to the minimal packing density at this composition. Bionducci *et al.*[16] investigated the structure of binary zinc phosphate glass using X–ray diffraction, neutron diffraction, EXAFS and X–ray scattering. Using RMC modelling they found zinc atoms interposed between phosphate tetrahedra in a long range structure. Sourial[22] *et al*. performed MD calculations on $Zn(PO_3)_2$, $Mg(PO_3)_2$ and $Pb(PO_3)_2$ and found that the structures of $Zn(PO_3)_2$ and $Mg(PO_3)_2$ were very similar with a distorted tetrahedrally coordinated structure. Tischenderof *et al*. **[23]** used zinc force field calculations to calculate density, glass transition temperature and zinc coordination number in zinc phosphate glasses. Their calculated densities and glass transition temperatures showed good agreement with literature data. They predicted the presence of 3, 4 and 5 coordinated zinc and that this shows little change with changing zinc content over various glass compositions. They attributed coordination number to preparation method and quenching rate[23, 27]. The zinc metaphosphate glass structure model calculated by Tischendorf is presented in Fig. 3.2.

Hassan *et al.*[28] studied the structure of ternary barium zinc metaphosphates. They concluded the presence of denser structures with increased zinc content due to the shortened chain length. Wetherall *et al.*[29] studied the short and medium range structures of calcium metaphosphate glasses using neutron and X–ray diffraction, with RMC modelling of their data. They observed distorted polyhedral units of Ca–O with an average coordination number of 7 and bond distances of 2.35 to 2.86 Å.

Xiang *et al.*[30] studied the effect of strontium substitution in bioactive 45S5 glass and found preferential distribution of calcium and strontium around phosphorous, which affects the properties of the glass. They found an Sr–O bond length of about 2.59 Å and a Sr coordination number of 7. However, substitution of calcium with strontium did not change the overall Q^n speciation of the glass network.

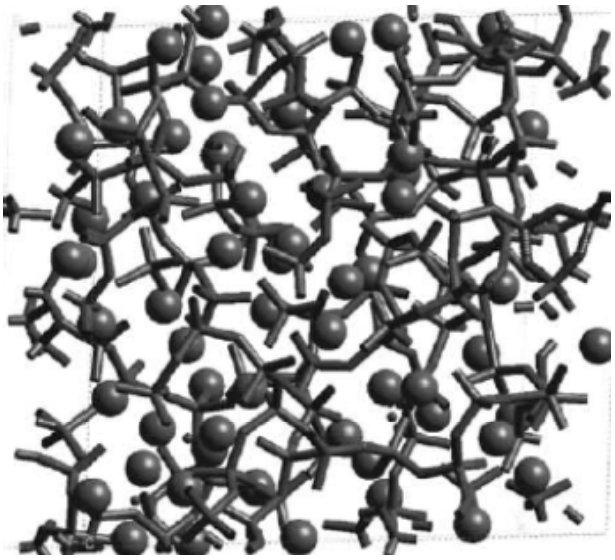

Fig. 3.2. Snapshot of equilibrated simulation cell for glass composition $50ZnO{:}50P_2O_5$[23]

3.1 Experimental

3.1.1 Synthesis

Metaphosphate glasses of general composition $Na_{1-x}Zn_{1+x/2}(PO_3)_3$ (i.e. $16.7(1-x)\%Na_2O{:}33.3(1+x/2)\%ZnO{:}50\%P_2O_5$; x = 0, 0.25, 0.5, 0.75, 1.0) and $NaZn_{1-x}M_x(PO_3)_3$ (i.e. $16.7\%Na_2O{:}33.3(1-x)\%ZnO{:}33.3x\%MO{:}50\%P_2O_5$; x = 0.25, 0.5, 0.75, 1.0; M = Ca and Sr) were prepared by melt quenching methods as described in Chapter 2. Molar compositions of the studied glasses are summarised in Table 3.1.

The high temperature polymorph of crystalline zinc metaphosphate was prepared according to the procedure described by Weil[2] with some modifications. A mixture of ZnO and $NH_4H_2PO_4$ was heated at 670°C for 20 h and then quenched in water.

The low temperature polymorph of zinc metaphosphate was prepared according to the procedure described by Averbuch–Pouchot *et al.*[3], with some modifications. 1 g of $ZnCO_3$ was dissolved in 10 cm^3 of 85% H_3PO_4. The mixture was heated in the furnace at 350°C for 1 week and then washed with excess boiling water.

Table 3.1 Molar compositions of the studied glass samples

Composition	*x*	P_2O_5	Na_2O	ZnO	CaO	SrO
$Na_{1-x}Zn_{1+x/2}(PO_3)_3$	0.00	50	16.6	33.4	0	0
	0.25	50	12.5	37.5	0	0
	0.50	50	8.3	41.7	0	0
	0.75	50	4.2	45.8	0	0
	1.00	50	0.0	50.0	0	0
$NaZn_{1-x}Ca_x(PO_3)_3$	0.25	50	16.7	25	8.3	0
	0.50	50	16.7	16.7	16.6	0
	0.75	50	16.7	8.1	25.2	0
	1.00	50	16.7	0	33.3	0
$NaZn_{1-x}Sr_x(PO_3)_3$	0.25	50	16.7	25	0	8.3
	0.50	50	16.7	16.7	0	16.6
	0.75	50	16.7	8.1	0	25.2
	1.00	50	16.7	0	0	33.3

3.1.2 NMR Spectroscopy

^{31}P, ^{23}Na and ^{43}Ca MAS–NMR and ^{67}Zn and ^{43}Ca static NMR spectra were acquired according to the procedures described in Chapter 2.

^{67}Zn NMR spectra of the two polymorphs of crystalline zinc metaphosphate were acquired at 20.0 T on 850 MHz Bruker Avance wide bore NMR spectrometer at the University of Warwick, UK, at a Larmour frequency of 53.191 MHz. Samples were ground into powder and packed into a 7 mm diameter zirconia rotor. Static ^{67}Zn NMR spectra were acquired using the DFS-WURST-QCPMG pulse sequence[31] with a 1 s relaxation delay. Spectra were referenced to 1 M aqueous $ZnCl_2$ solution (δ_{iso} = 0 ppm). The acquisition time for each echo was adjusted to obtain spikelet separations of 6 kHz and 2 kHz in the frequency spectrum for β–$Zn(PO_3)_2$ and α–$Zn(PO_3)_2$, respectively. The stepped–frequency piecewise acquisition technique[32] was employed to cover the full

width of spectra. Spectra were acquired by changing the transmitter offset frequency in steps of 20 kHz and 12313 scans were acquired for each step in the case of α—$Zn(PO_3)_2$, whereas 53048 scans were acquired for the central offset of sample β—$Zn(PO_3)_2$, with 6631 scans for each of the other steps. Spectra were then summed to give the final spectrum. For β—$Zn(PO_3)_2$ spectra with lesser numbers of scans were scaled up to match their intensity with the central spectrum of 53048 scans before summing them.

3.1.3. Neutron Diffraction

Neutron diffraction data for crystalline β–$Zn(PO_3)_2$ and glass compositions $Na_{1-x}Zn_{1+x/2}(PO_3)_3$ (*x* = 0.0, 0.5, 1.0), $NaZn_{1-x}M_x(PO_3)_3$ (*x* = 0.5, M = Ca and Sr) were collected on the GEM instrument at the ISIS facility, Rutherford, Appleton Laboratory. A powdered sample of β–$Zn(PO_3)_2$ was packed into a vanadium container of 8.3 mm diameter and 60 mm sample height and 5.9099 g sample weight, while glass compositions were cast into rods as described in Chapter 2. The dimensions of the glass rods are presented in Table 3.2. Densities were measured by Helium pychnometry. Data from 6 of the 8 data banks were normalised and summed and the effects of background scattering subtracted to give the normalised total scattering structure factors $S(Q)$ up to Q = 60 $Å^{-1}$ and the radial distribution function $D(r)$ via Fourier transformation using the program Gudrun[33].

Table 3.2 Dimensions of glass rods used to collect neutron data.

Composition	*x*	Diameter (cm)	Length (cm)	Weight (g)
$Na_{1-x}Zn_{1+x/2}(PO_3)_3$	1.0	1.195	6.357	18.85
$Na_{1-x}Zn_{1+x/2}(PO_3)_3$	0.5	1.200	6.975	21.55
$Na_{1-x}Zn_{1+x/2}(PO_3)_3$	0.0	1.164	6.780	20.33
$NaZn_{1-x}Ca_x(PO_3)_3$	0.5	1.200	6.780	19.47
$NaZn_{1-x}Sr_x(PO_3)_3$	0.5	1.175	6.889	21.35

3.1.4 RMC Calculations

The analysis of the neutron scattering data was carried out using the RMCProfile software[34]. An initial starting model based on the crystal structure of β–$Zn(PO_3)_2$ was used to generate a supercell configuration of 6 × 6 × 3 unit cells, containing a total of 5164 oxygen, 1728 phosphorus and 884 zinc atoms for $Na_{1-x}Zn_{1+x/2}(PO_3)_3$ (x = 1), which is a zinc metaphosphate ($ZnO:P_2O_5$) glass. For glass composition $Na_{1-x}Zn_{1+x/2}(PO_3)_3$ (x = 0), which is $NaZn(PO_3)_3$ glass, the $KBeP_3O_9$ crystal structure[35] was used to generate a supercell configuration of 7 × 7 × 5 unit cells containing a total of 8820 oxygen, 2940 phosphorus, 980 zinc and 980 sodium atoms. The crystal structure of $NaCaP_3O_9$[36] was used as an initial starting model for glass composition $NaZn_{1-x}M_x(PO_3)_3$ (x = 0.5, M = Ca). A super cell of configuration 8 × 8 × 8 unit cells, containing a total of 9216 oxygen, 3072 phosphorus, 1024 sodium, 512 zinc and 512 calcium atoms was generated. The size of configuration cells was adjusted to according to the measured glass density. Fitting was carried out against the reciprocal space data, $S(Q)$ and the real space data, $D(r)$. The former was broadened by convolution with a box function to reflect the finite size of the simulation box:

$$S_{\text{box}}(Q) = \frac{1}{\pi}\int_{-\infty}^{\infty} S_{\text{expt}}(Q')\frac{\sin L(Q-Q')/2}{Q-Q'}\,dQ' \qquad (3.1)$$

where L is the smallest dimension of the RMC configuration and, as such, defines the upper limit of $G(r)$. Minimum distance constraints were applied in calculations.

3.2 Results and Discussion

3.2.1 Crystalline $Zn(PO_3)_2$

Fig. 3.3 shows the X–ray powder diffraction patterns of crystalline α and β polymorphs of $Zn(PO_3)_2$. The patterns are in good agreement with the structures described by Averbuch–Pouchot *et al*[3] and Weil[2], respectively. Fig. 3.4 shows the Rietveld fit to the neutron diffraction pattern of β–$Zn(PO_3)_2$, with the corresponding

crystal and refinement data in Table 3.3. The unit cell contents are shown in Fig. 3.5, with refined structural parameters and selected contact distances and angles in Tables 3.4 and 3.5, respectively. A polyhedral representation of the structure of β–$Zn(PO_3)_2$ is shown in Fig. 3.6 and consists of infinite metaphosphate chains linked together by ZnO_4 tetrahedra. The structure is in good agreement with that presented by Weil[2]. The structure possess two zinc and four phosphorous sites in the asymmetric unit with average Zn–O and P–O bond lengths of 1.943 and 1.532 Å, respectively, compared to the respective values of 1.929 and 1.530 Å determined by Weil[2] for β–$Zn(PO_3)_2$ and 2.094 and 1.540 Å for α–$Zn(PO_3)_2$ determined by Averbuch–Pouchot *et al*.[3] (note the later value for Zn–O is for octahedrally coordinated zinc).

(a)

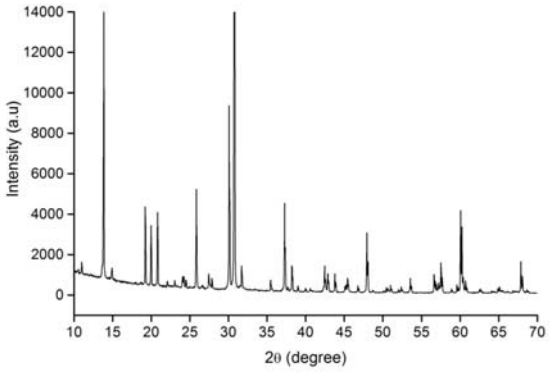

(b)

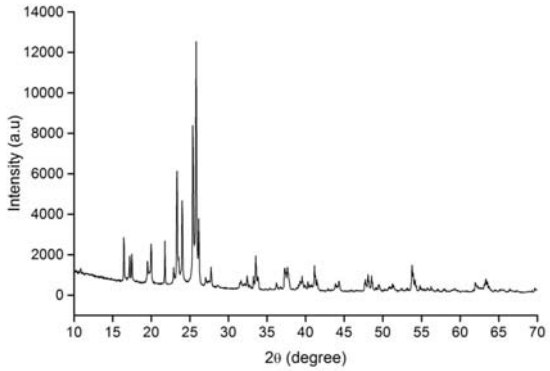

Fig. 3.3. XRD patterns of polymorphs of crystalline $Zn(PO_3)_2$. (a) α–$Zn(PO_3)_2$ (b) β–$Zn(PO_3)_2$

Table 3.3 Crystal, data collection and structure refinement data for β–$Zn(PO_3)_2$

(a) Crystal data	
Name	zinc metaphosphate
Empirical formula	O_6P_2Zn
Structural formula	$Zn(P_2O_6)$
Formula weight	223.32 g mol^{-1}
Crystal system	Monoclinic
Space group	*Cc*
Unit cell dimensions	*a* = 7.6526(4) Å, *b* = 7.6316(4) Å, *c* = 16.3845(9) Å, β = 92.190(2)°
Volume	956.19(15) $Å^3$
Z	8
Density (calculated)	3.103 g cm^{-3}
Sample description	Colourless powder
Synthesis	Solid state synthesis from ZnO, and $NH_4H_2PO_4$ at 670 °C
(b) Data collection	
Diffractometer	GEM
Sample holder	8.3 mm diameter vanadium can
Temperature	293 K
Scan time	1110 μA h
Sample height	60 mm
Sample weight	5.9099 g
(c) Refinement	
Refinement software	GSAS (Larson and Von Dreele, 1986)
Initial model source	M. Weil, Acta Crystallogr. Sect. C, 60 (2004) i20–i22
t.o.f. range refined	4.074 to 16.07 msec
Excluded regions	None
Data corrections	None
Secondary phases	None
No. of observations/restraints/parameters	1161/0/102
Total no. of reflections used	3982
Independent reflections due to 1° phase	3982
Peak shape	Pseudo–Voigt
Final R–factors	R_p = 0.0136, R_{wp} = 0.0145 R_{ex} = 0.0056, χ^2 = 7.304 R_F2 = 0.0178
Maximum atomic shift/esd	0.01

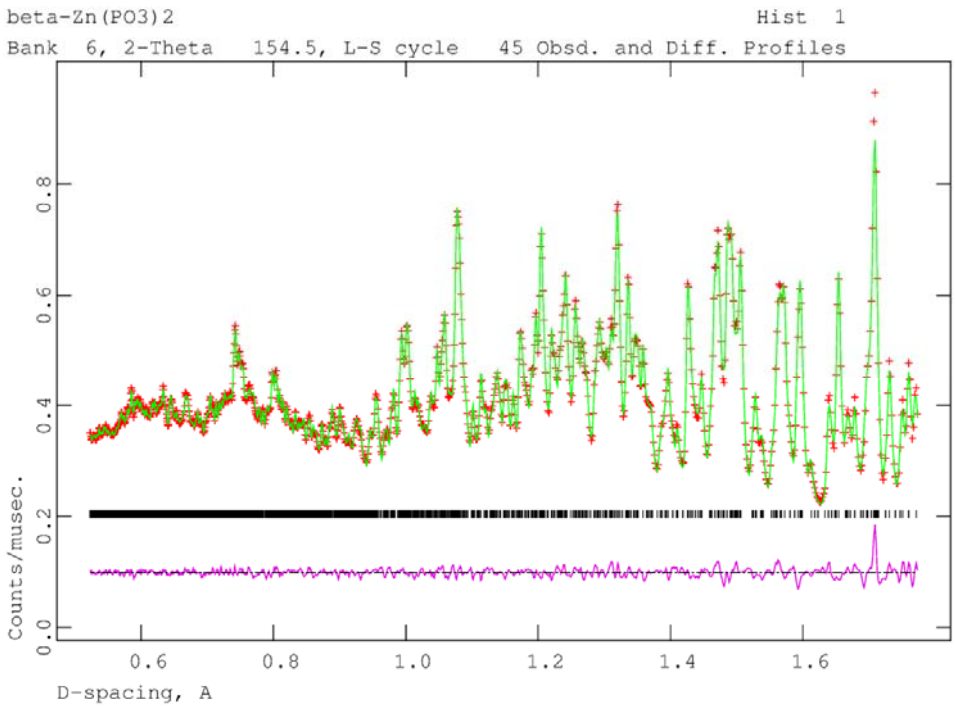

Fig. 3.4. Rietveld fit to neutron diffraction data for β–$Zn(PO_3)_2$, showing observed (+ symbols), calculated (green) and difference (mauve) profiles. Reflection positions are indicated by markers.

Table 3.4 Atomic Coordinates and Isotropic Thermal Parameters for β–$Zn(PO_3)_2$

Atom	Site	*x*	*y*	*Z*	Occ.	U_{iso} (Å^2)
Zn1	4a	0.5438(8)	0.6045(7)	0.4049(4)	1.0	0.0089(13)
Zn2	4a	0.6299(9)	0.3068(8)	0.1213(4)	1.0	0.0134(12)
P1	4a	0.2214(8)	0.2136(8)	0.1458(4)	1.0	0.0107(12)
P2	4a	0.2274(8)	0.5229(8)	0.2586(4)	1.0	0.0089(13)
P3	4a	–0.0487(8)	0.5148(8)	0.37602(34)	1.0	0.0071(12)
P4	4a	–0.0367(8)	0.7721(7)	0.5124(4)	1.0	0.0024(10)
O1	4a	–0.0045(8)	0.9596(8)	0.4979(4)	1.0	0.0171(12)
O2	4a	0.0083(9)	0.3473(9)	0.4094(4)	1.0	0.0217(14)
O3	4a	0.0782(9)	0.3008(8)	0.0877(4)	1.0	0.0265(16)
O4	4a	0.1609(7)	0.0394(8)	0.1664(4)	1.0	0.0129(12)
O5	4a	0.1918(8)	0.3283(8)	0.2257(4)	1.0	0.0148(12)
O6	4a	0.2615(9)	0.6391(10)	0.1928(4)	1.0	0.0190(15)
O7	4a	–0.2331(9)	0.5452(8)	0.3593(4)	1.0	0.0175(14)
O8	4a	–0.2221(8)	0.7116(11)	0.5213(4)	1.0	0.0165(12)
O9	4a	0.3642(8)	0.5018(8)	0.3266(4)	1.0	0.0114(12)
O10	4a	0.3975(9)	0.2427(10)	0.1151(4)	1.0	0.0219(15)
O11	4a	0.0382(8)	0.6666(8)	0.4361(4)	1.0	0.0157(13)
O12	4a	0.0482(8)	0.5719(7)	0.2959(4)	1.0	0.0147(13)

Table 3.5 Significant Contact Distances (Å) and Angles (°) for β–$Zn(PO_3)_2$

Zn1–O1	1.929(9)	Zn2–O4	1.933(10)
Zn1–O2	1.875(8)	Zn2–O6	1.984(10)
Zn1–O7	1.943(9)	Zn2–O8	2.032(10)
Zn1–O9	2.004(8)	Zn2–O10	1.844(11)
P1–O3	1.572(10)	P2–O5	1.600(9)
P1–O4	1.451(9)	P2–O6	1.427(11)
P1–O5	1.597(10)	P2–O9	1.508(9)
P1–O10	1.473(11)	P2–O12	1.568(9)
P3–O2	1.451(9)	P4–O1	1.473(8)
P3–O7	1.446(9)	P4–O3	1.589(10)
P3–O11	1.645(10)	P4–O8	1.505(8)
P3–O12	1.593(9)	P4–O11	1.611(9)
P1..P4	2.892(8)	P2..P3	2.912(9)
O1–Zn1–O2	120.2(4)	O4–Zn2–O6	108.3(4)
O1–Zn1–O7	111.6(4)	O4–Zn2–O8	107.9(4)
O1–Zn1–O9	97.73(34)	O4–Zn2–O10	111.7(4)
O2–Zn1–O7	112.1(4)	O6–Zn2–O8	98.4(4)
O2–Zn1–O9	108.4(5)	O6–Zn2–O10	109.2(4)
O7–Zn1–O9	104.7(4)	O8–Zn2–O10	120.2(5)
O3–P1–O4	107.9(5)	O5–P2–O6	110.9(6)
O3–P1–O5	98.4(5)	O5–P2–O9	104.8(5)
O3–P1–O10	110.8(5)	O5–P2–O12	102.3(4)
O4–P1–O5	104.8(5)	O6–P2–O9	118.8(5)
O4–P1–O10	121.4(6)	O6–P2–O12	109.5(5)
O5–P1–O10	110.9(5)	O9–P2–O12	109.3(5)
O2–P3–O7	119.3(6)	O1–P4–O3	112.0(5)
O2–P3–O11	106.6(5)	O1–P4–O8	118.6(5)
O2–P3–O12	114.2(5)	O1–P4–O11	107.1(5)
O7–P3–O11	111.7(5)	O3–P4–O8	108.2(5)
O7–P3–O12	106.4(5)	O3–P4–O11	103.0(5)
O11–P3–O12	96.3(4)	O8–P4–O11	106.7(5)

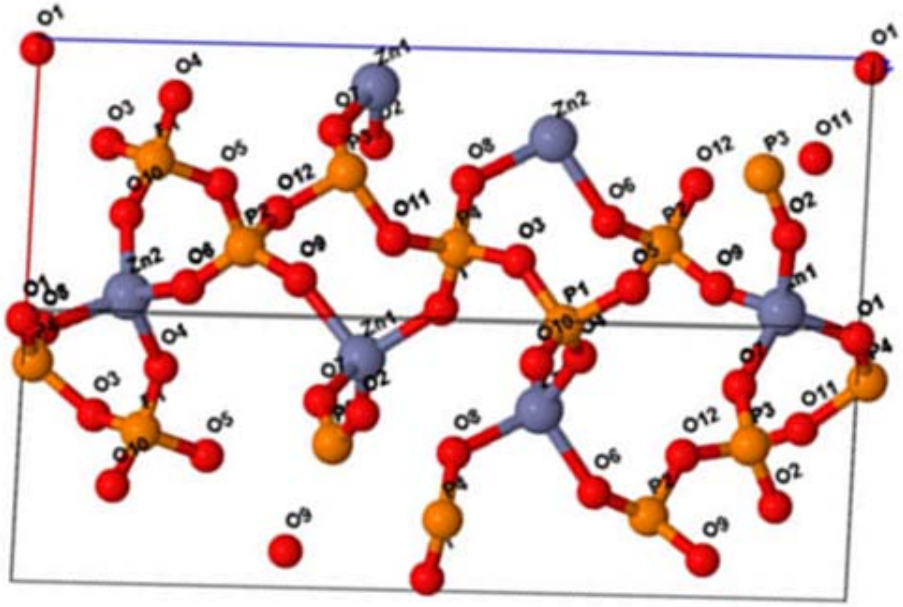

Fig. 3.5. Unit cell contents of β–$Zn(PO_3)_2$ calculated from neutron diffraction data.

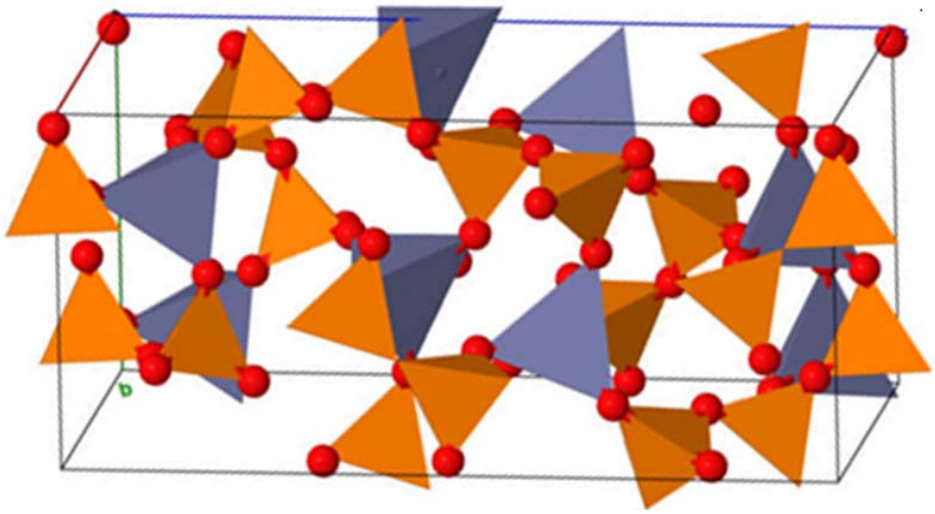

Fig. 3.6. Polyhedral representation of structure of β–$Zn(PO_3)_2$ calculated from neutron diffraction data. PO_4 tetrahedra= orange ZnO_4 tetrahedra= purple.

The level of distortion of the tetrahedral coordination polyhedra can be described using a distortion index as in Eqns 3.2 and 3.3.

$$D_1 = \frac{\sum_{i=1}^{i=6}(\theta_i - 109.47)^2}{6} \tag{3.2}$$

$$D_2 = \frac{\sum_{i=1}^{i=6}|\theta_i - 109.47|}{6} \tag{3.3}$$

where θ_i is the O–M–O angle. Higher values indicate greater level of distortion. The calculated distortion indices for β–$Zn(PO_3)_2$ are given in Table 3.6. and reveal significant distortion for both zincate and two of the four phosphate tetrahedra.

Table 3.6 Distortion indices for tetrahedral sites in β–$Zn(PO_3)_2$

Central Atom	D_1	D_2
Zn1	48.052	5.512
Zn2	41.093	4.507
P1	48.826	5.555
P2	27.057	3.800
P3	52.514	5.983
P4	24.420	4.090

Natural abundance static ^{67}Zn DFS-WURST-QCPMG NMR spectra of the two polymorphs of zinc metaphosphate are presented in Fig. 3.7 together with simulated spectra. ^{67}Zn NMR parameters derived from simulations of the experimental spectra are presented in Table 3.7. The crystal structure described in the literature for α–$Zn(PO_3)_2$ shows that it is monoclinic, with space group *C*2/*c*. There is only one Zn site in the asymmetric unit of α–$Zn(PO_3)_2$ and zinc exhibits an octahedral coordination (Fig. 3.1a). The spectrum of α–$Zn(PO_3)_2$ exhibits a typical quadrupolar line shape, which is

well fitted using one set of EFG parameters, with a non–axially symmetric EFG tensor (C_Q = 9.26 MHz and η = 0.1). No chemical shift tensors were considered while fitting the line due to lack of second NMR field strength data and large C_Q value. The isotropic chemical shift value falls within the range reported for other six coordinated zinc environments[37].

(a)

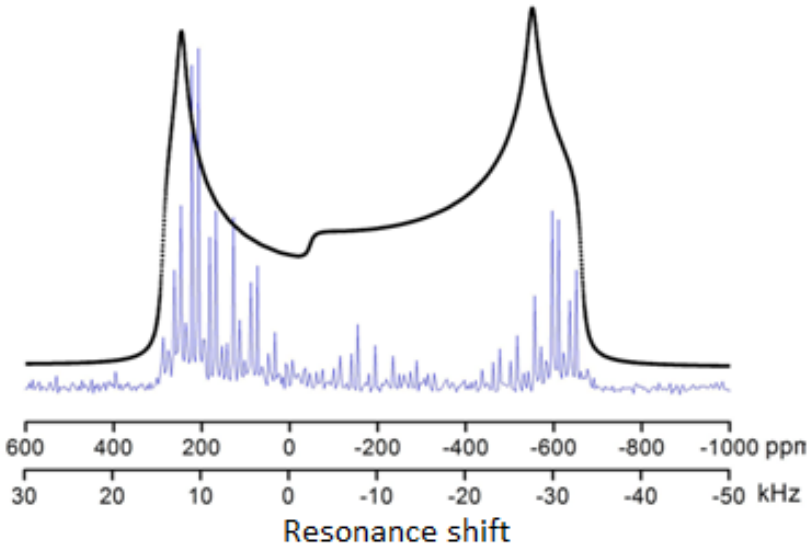

(b)

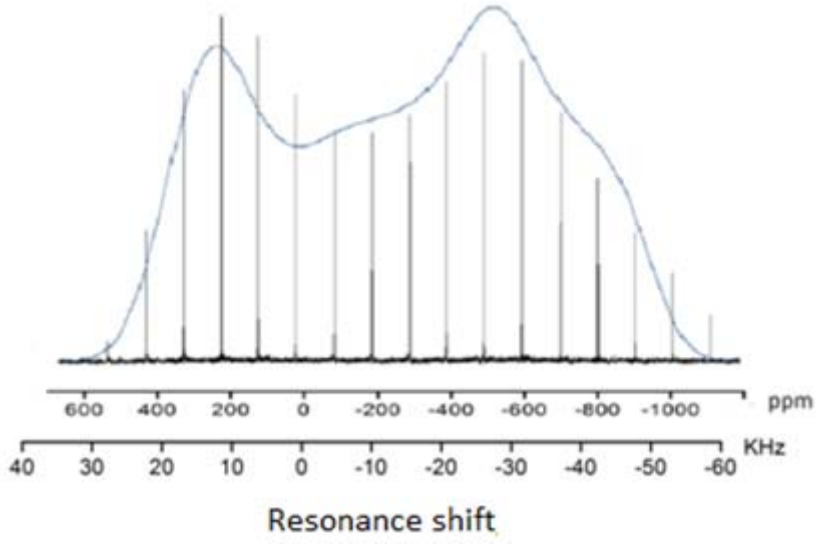

Fig. 3.7. Natural abundance static ^{67}Zn DFS–WURST–QCPMG NMR spectra of (a) α–$Zn(PO_3)_2$ (b) β–$Zn(PO_3)_2$

The crystal structure of β–$Zn(PO_3)_2$ shows that it has monoclinic space group *Cc* with two crystallographically non–equivalent Zn sites in tetrahedral coordination, with bond lengths ranging from 1.87 Å to 2.00 Å and bond angle from 97.7°–120.2°. The natural abundance static co–added ^{67}Zn DFS-WURST-QCPMG NMR spectrum for this sample is also described by a typical quadrupolar solid state line shape. Despite the presence of two crystallographically distinct zinc sites, the large width of the static line pattern and very similar chemical environments of the two sites prohibits their resolution in the ^{67}Zn NMR spectrum. Hence line shape was again fitted with a single set of EFG parameters (C_Q = 10.97 MHz and η = 0.31). The isotropic chemical shift corresponds to tetrahedrally coordinated zinc[38]. ^{67}Zn NMR parameters for crystalline zinc metaphosphates as calculated from simulations of the experimental spectra are presented in Table 3.7.

Numerical simulations using a program such as CASTEP[39] can be performed in future in order to validate the experimental results.

Table 3.7 ^{67}Zn NMR parameters for crystalline zinc metaphosphates as calculated from simulations of the experimental spectra.

Sample	C_Q (MHz)	η_Q	δ_{iso} (ppm)
β–$Zn(PO_3)_2$	10.97	0.31	8.7
α–$Zn(PO_3)_2$	9.26	0.1	–20

3.2.2 Glass Compositions $Na_{1-x}Zn_{1+x/2}(PO_3)_3$

The powder X–ray diffraction patterns for glasses of composition $Na_{1-x}Zn_{1+x/2}(PO_3)_3$ show no Bragg peaks, confirming all samples were pure glasses with no crystallised phase (Fig. 3.8). Fig. 3.9 shows the thermo analytical data as measured using differential scanning calorimetry (DSC). The data show an increase in T_g with increasing value of *x*. This indicates that the network strengthens with increasing zinc

content. This can be explained by considering the nature of the Zn–O bond in comparison to the Na–O interaction which is considerably more ionic. Replacing sodium with zinc increases the glass stability to crystallisation, which is the difference between T_c and T_g. Fig. 3.10 shows the measured density for glass compositions x = 0.0, 0.5 and 1.0. There is no obvious trend with composition in this system with little difference observed in the density of different glass compositions.

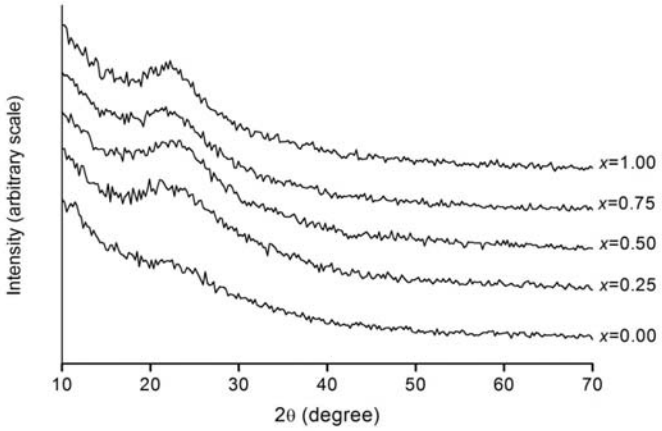

Fig. 3.8. X–ray diffraction patterns for $Na_{1-x}Zn_{1+x/2}(PO_3)_3$ glass compositions

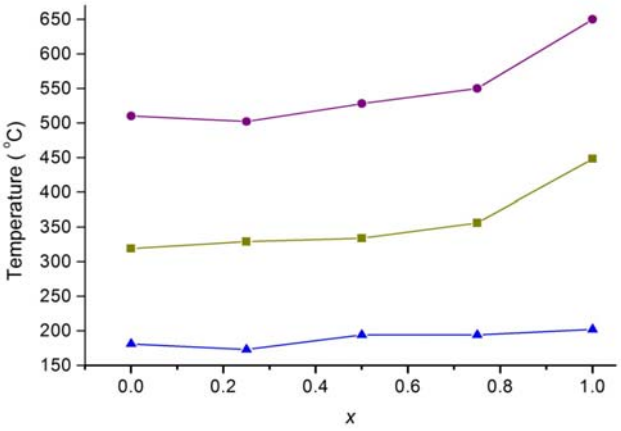

Fig. 3.9. Compositional variation of T_c (circles), T_g (squares) and $T_c - T_g$ (triangles) for $Na_{1-x}Zn_{1+x/2}(PO_3)_3$ glass compositions. (esd = ±20°C)

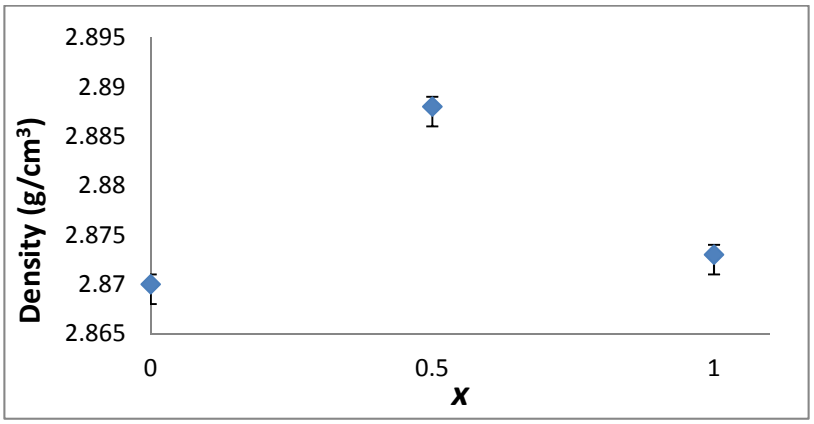

Fig. 3.10. Compositional variation of density of $Na_{1-x}Zn_{1+x/2}(PO_3)_3$ glass composition. (error bars = ±SD)

Fig. 3.11 shows the IR spectra for the studied glass compositions. All glass compositions show peaks at about 1280 cm^{-1} and 900 cm^{-1} characteristic of $(PO_2)^-$ (Q^2 species) and the P–O–P asymmetric stretch respectively. A weak band at about 1100 cm^{-1} is attributed to $(PO_3)^{2-}$ (Q^1 species). Peaks become broader with decreasing value of *x* (addition of more Na_2O), which reflects the multi–cation effect on the disorder of the system. A broad band at about 780 cm^{-1} corresponds to (P–O–P) symmetric vibration of BOs[40, 41].

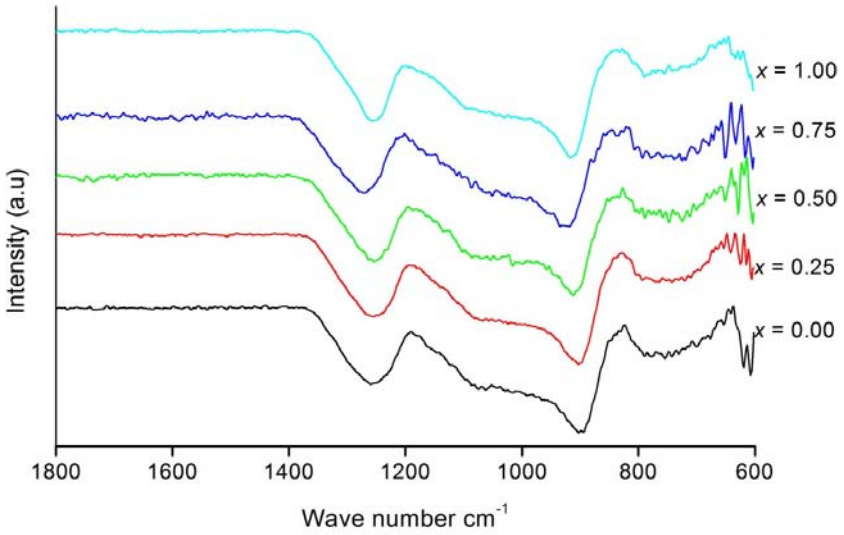

Fig. 3.11. IR spectra of $Na_{1-x}Zn_{1+x/2}(PO_3)_3$ glass compositions

^{23}Na MAS–NMR spectra of all the studied glass samples showed a single resonance, Fig. 3.12. The isotropic shift moves slightly towards more negative values with increasing amount of zinc in the studied glass series. This can be explained, by considering that with increasing zinc content, less oxygen atoms will find a cationic neighbour, as zinc has a lower coordination number than sodium, so there is more clustering of metal cations. This moves the chemical shift towards more negative values due to increased shielding.

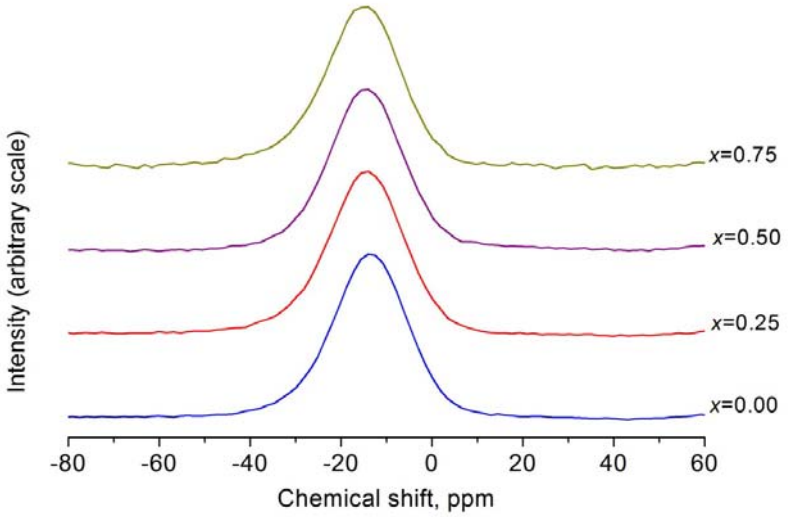

Fig. 3.12. ^{23}Na MAS–NMR spectra of $Na_{1-x}Zn_{1+x/2}(PO_3)_3$ glass compositions

Fig.3.13 shows the ^{31}P MAS–NMR spectra of the studied glass compositions. All glass samples have two peaks associated with Q^1 at ca. –8 ppm to –14 ppm and Q^2 at –25.80 to –30.4 ppm respectively. However, the predominant peak in all glass samples is Q^2. This is in agreement with the fact that glasses with 50 mol% P_2O_5 are predominantly metaphosphate glasses[42-44]. The ratios of the integrated intensities in the spectra show Q^1 *ca*. 1 to 10 % and Q^2 *ca*. 90 to 99 %. A small proportion of Q^1 species is known to occur in metaphosphate glass compositions which is attributed to surface hydrolysis[45]. Spectral parameters of all compositions are presented in Table 3.8. The large chemical shift anisotropy, at –187 to –202 ppm, is typical of metaphosphate glasses[46]. The chemical shift becomes more negative with increasing zinc content. This is again in agreement with previous studies and indicates the more

covalent nature of Zn–O bond and hence more shielding[47]. ^{31}P MAS-NMR parametres derived from simulations of experimental spectra are presented in Table 3.8.

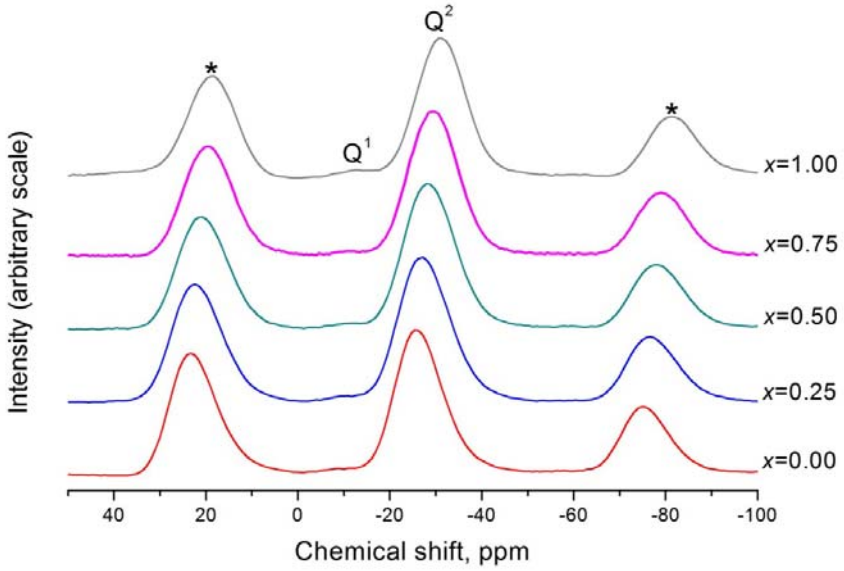

Fig. 3.13. ^{31}P MAS–NMR spectra of $Na_{1-x}Zn_{1+x/2}(PO_3)_3$ glass compositions

Table 3.8 Derived ^{31}P spectral parameters of glasses of compositions $Na_{1-x}Zn_{1+x/2}(PO_3)_3$

X	δ_{iso}/ppm	δ_{11}/ppm	δ_{22}/ppm	δ_{33}/ppm	Δδ/ppm	η	χ^2	%int
0.00	–25.80(4) –7.11(2)	60.55 48.39	7.42 –32.86	–157.00 –36.86	–197.00 83.24	0.40 0.07	0.00 0.12	100 0.44
0.25	–27.4(2) –8.00(3)	65.74 26.29	6.00 25.15	–154.00 –25.15	–189.00 51.44	0.47 0.00	0.001 0.088	100 0.36
0.50	–29.20(1) –6.97(1)	67.00 128.34	–0.42 25.15	–154.00 –122.71	–187.00 202	–0.54 0.71	0.00 0.11	100 11.62
0.75	–30.40(2) –42.85(1)	35.58 23.03	35.58 23.03	–162.00 –174.61	–198.00 –197.00	0.00 0.00	0.005 0.07	100 16.22
1.00	–30.4(1) –13.00(1)	61.9 136.36	–1.08 36.36	–151.00 –111.73	–182.00 148.10	0.518 0.00	0.002 0.014	100 7.88

Fig. 3.14 shows ^{67}Zn NMR spectra for $Na_{1-x}Zn_{1+x/2}(PO_3)_3$ glass compositions (x = 1.0 and 0.0) which correspond to pure zinc metaphosphate $Zn(PO_3)_2$ and sodium zinc metaphosphate $NaZn(PO_3)_3$ glasses, respectively. Line shapes for both glass compositions are not characteristic of either of the crystalline polymorphs of zinc

metaphosphate due to the disordered structure of these glasses. Disordered bonds around the metal atom cause the disordering of magnetic resonance parameters[48]. Both spectra were fitted with two isotropic peaks at about 200 ppm and 100 ppm, which can be attributed to tetrahedral and octahedral zinc coordinations, respectively, based on the ^{67}Zn NMR parameters of other compounds containing zinc in different coordinations with oxygen[49, 50]. Lines are broader than those observed for crystalline polymorphs of zinc metaphosphate. The line for amorphous $NaZn(PO_3)_3$ is slightly broader than that for amorphous zinc metaphosphate, which indicates the presence of more randomness in the network with more cations. However overall there is no effect on zinc coordination with the addition of sodium oxide. Derived spectral parameters are presented in Table 3.9.

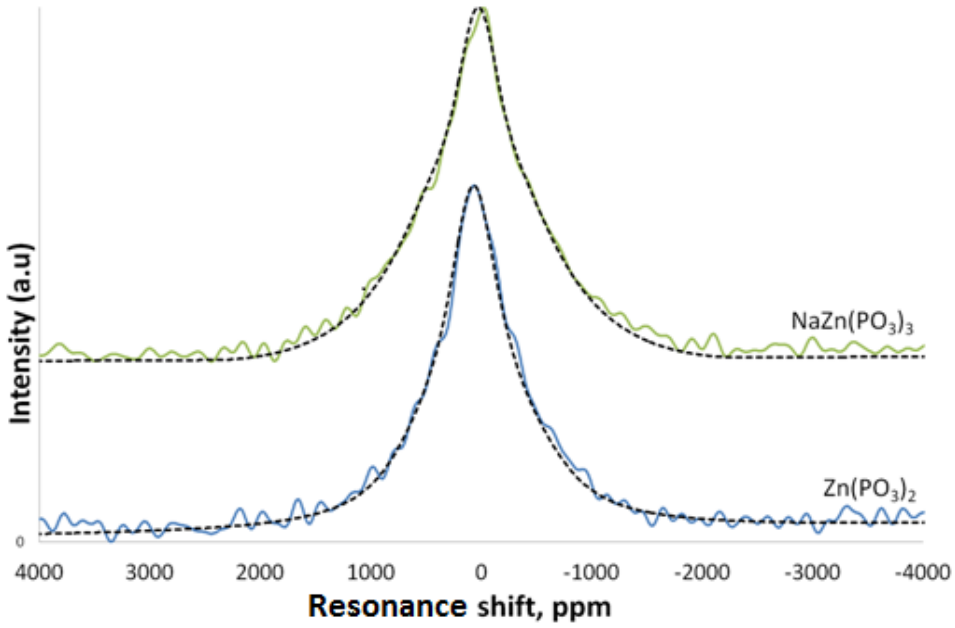

Fig. 3.14. Natural abundance static ^{67}Zn NMR spectra of glass compositions $Na_{1-x}Zn_{1+x/2}(PO_3)_3$ (x = 0.0 and 1.0) with dotted lines showing fits

Table 3.9 ^{67}Zn NMR parameters derived from simulations of experimental spectra.

Composition (x)	δ (ppm)	C_Q (MHz)	η_Q	% intensity
1.0	212 105	9.4 5.4	0.55 0.67	85 15
0.0	185 96	8.0 5.9	0.11 0.38	85 15

Fig. 3.15 show the Q space interference functions $i(Q)$ derived from neutron diffraction data for glass compositions x = 0.0, 0.5 and 1.0. $i(Q)$ of all glass samples show an intermediate range order (IRO) peak between 1.1 $Å^{-1}$ and 2.0 $Å^{-1}$, with a main peak at *ca*. 1.6 $Å^{-1}$ and a shoulder at 1.1 $Å^{-1}$, corresponding to non–bridging and bridging P–O correlations respectively.

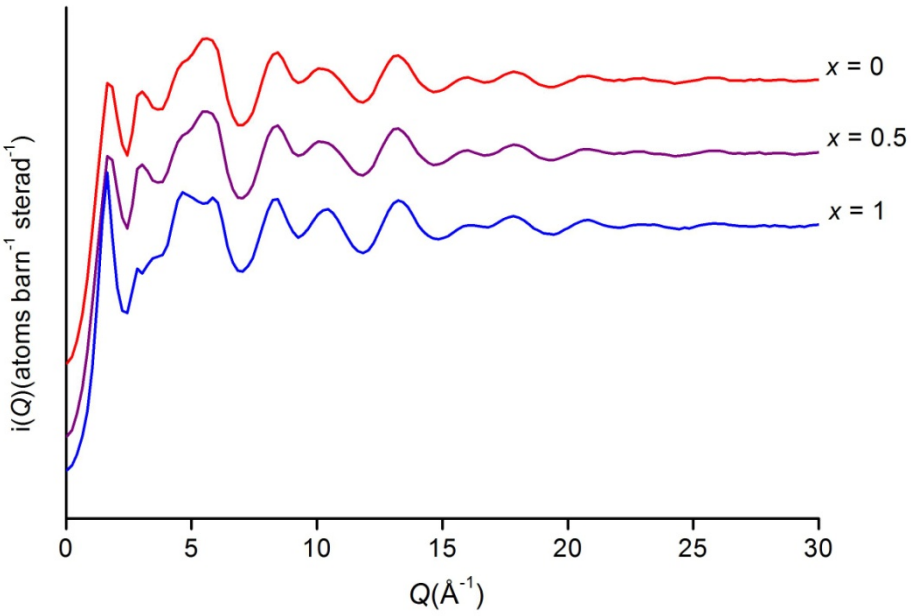

Fig. 3.15. Q space interference functions $i(Q)$ for $Na_{1-x}Zn_{1+x/2}(PO_3)_3$ glass compositions

The total correlation functions *T(r)* obtained by Fourier transformation of the corresponding structure function $S(Q)$ using the Lorch modification function and a Q range of 0–60 $Å^{-1}$ together with fits are presented in Fig. 3.16. Details of the fits are given in Figs 3.17, with the fits to the P–O correlations given in Fig. 3.18. The shorter correlation peak at about 1.5 Å corresponds to P–NBO, whereas the one at about 1.6 Å is attributed to P–BO[51-53].

Correlation distances and coordination numbers extracted from the fits are presented in Table 3.10. The peak observed at about 1.9 Å, is attributed to Zn–O in tetrahedral coordination[14, 17, 26]. A weak shoulder is observed at a distance of about 2.1 Å in the x = 1.0 (i.e. $Zn(PO_3)_2$) glass composition, which probably indicates the presence

of some six coordinate zinc. The peak at 2.5 Å is a combination of O–O, Na–O and P–P correlations[54].

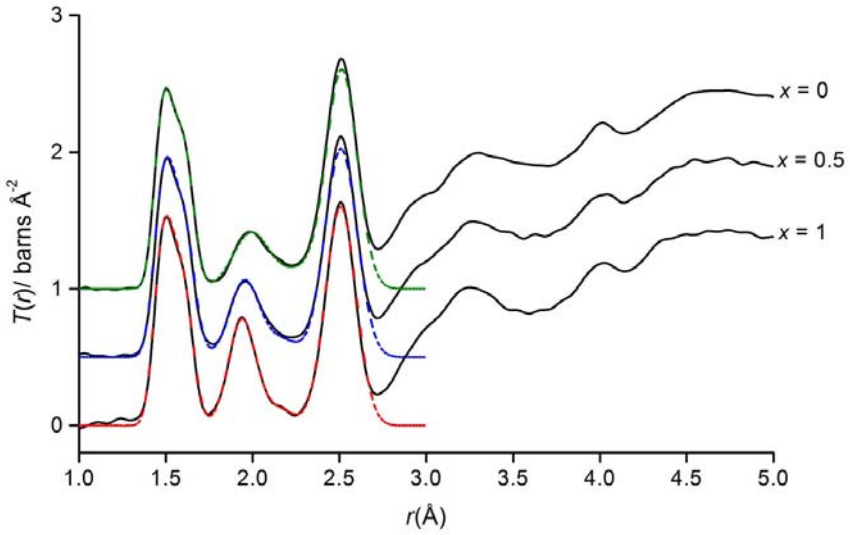

Fig. 3.16. Real space data for the total diffraction patterns *T*(*r*) for glass compositions $Na_{1-x}Zn_{1+x/2}(PO_3)_3$.Coloured lines showing fits.

Table 3.10 Structural parameters (r_{i-j} interatomic distance and N_{i-j} coordination number) derived from fitted T(*r*).

x	1.0		0.5		0.0	
Density (g cm^{-3})	2.873		2.888		2.870	
	r_{i-j}	N_{i-j}	r_{i-j}	N_{i-j}	r_{i-j}	N_{i-j}
P –NBO	1.48(1)	1.9(2)	1.49(1)	1.9(1)	1.48(0)	1.9(3)
P –BO	1.60(1)	1.9(2)	1.60(1)	1.9(1)	1.60(1)	1.9(1)
P –O (Total)		3.8		3.8		3.8
Zn –O(1)	1.93(1)	4.0(2)	1.95(1)	3.8(1)	1.98(1)	4.3(0)
Na –O			2.16(0)	4.3(3)	2.28(1)	3.8(1)
O – O	2.51(1)	3.9(3)	2.51(1)	4.0(1)	2.51(1)	4.0(1)

The P–NBO or P–BO correlation distances show almost no variation with glass composition. The coordination numbers of about 4 are as expected for the phosphate tetrahedra. Similarly, average coordination numbers of about four for both Zn–O and Na–O are found. The values for the *x* = 1.0 composition are in reasonable agreement with those found by Navarra *et al*. [20, 21] of 1.54, 1.94 and 2.49 Å for P–O, Zn–O and O–O pair correlations and those of Hoppe *et al*.[14, 55, 56], with P–NBO of 1.51 Å, P–BO of 1.57 Å, Zn–O of 1.94 Å and O–O of 2.51 Å.

(a)

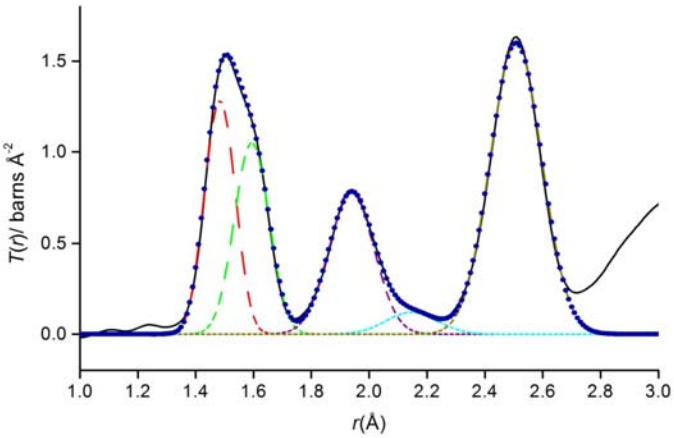

(b)

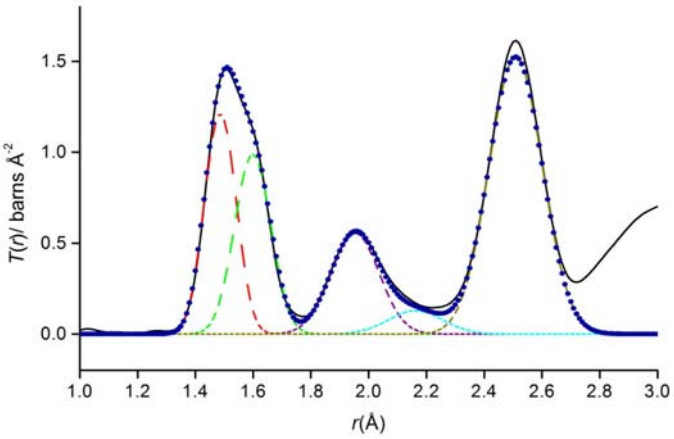

(c)

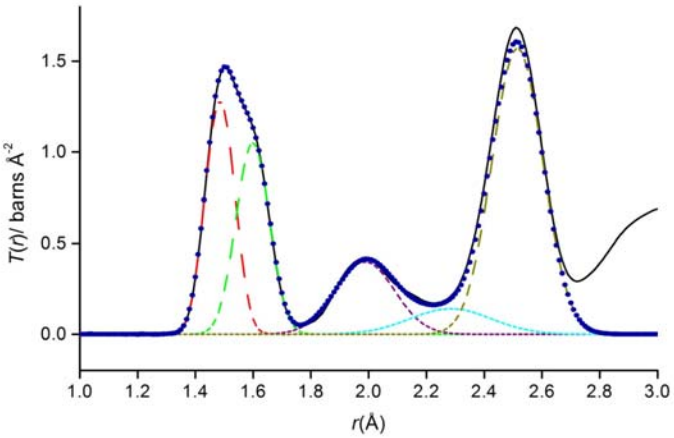

Fig. 3.17. Fit to correlation function *T*(*r*) for the studied glass compositions (a) *x* = 1.0, (b) *x* =0. 5, (c) *x* = 0.0

(a)

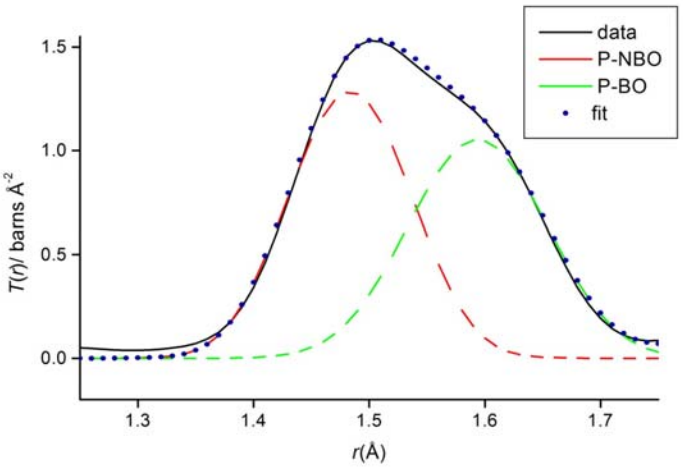

(b)

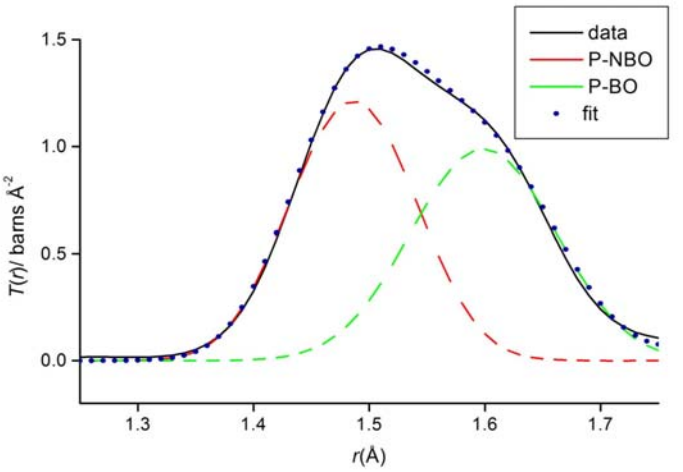

(c)

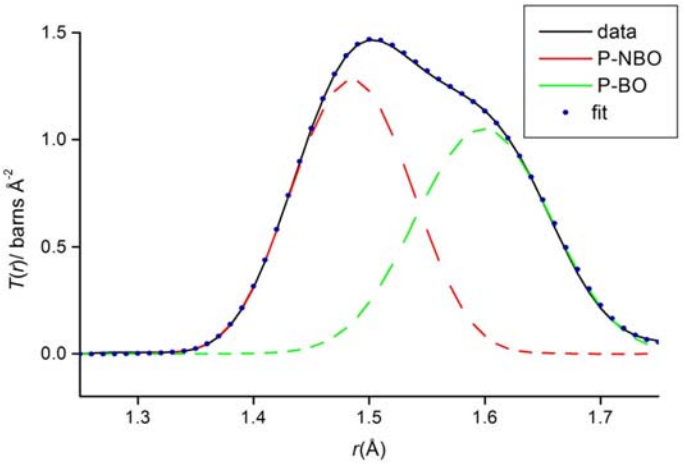

18. Fit to correlation function *T*(*r*) in the range of P–O 1st coordination correlation for the studied glass compositions. (a) *x* = 1.0, (b) *x* =0. 5, (c) *x* = 0.0

The compositional variation of the Zn–O correlation distance is plotted in Fig. 3.19. The average Zn–O correlation distance is seen to become shorter with increasing ZnO content.

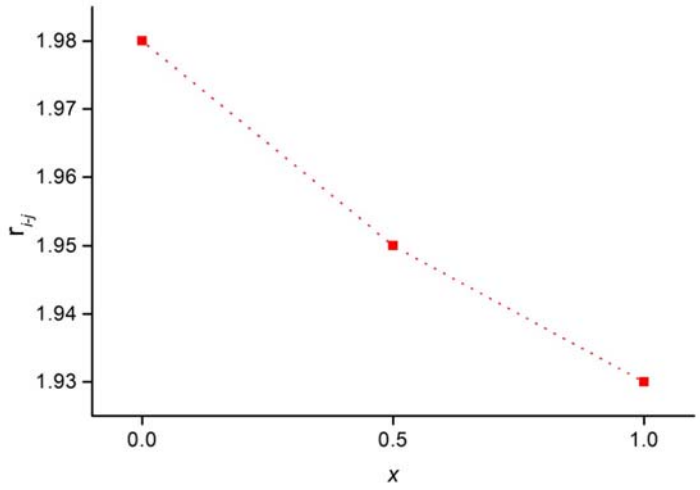

Fig. 3.19. Compositional variation of Zn–O bond length. The dotted line is a guide to the eye.

The final RMC fits to the $S_{box}(Q)$ and $G(r)$ data for x = 0.0 and x = 1.0 glass compositions at room temperature are shown in Figs. 3.20 and 3.21.

(a)

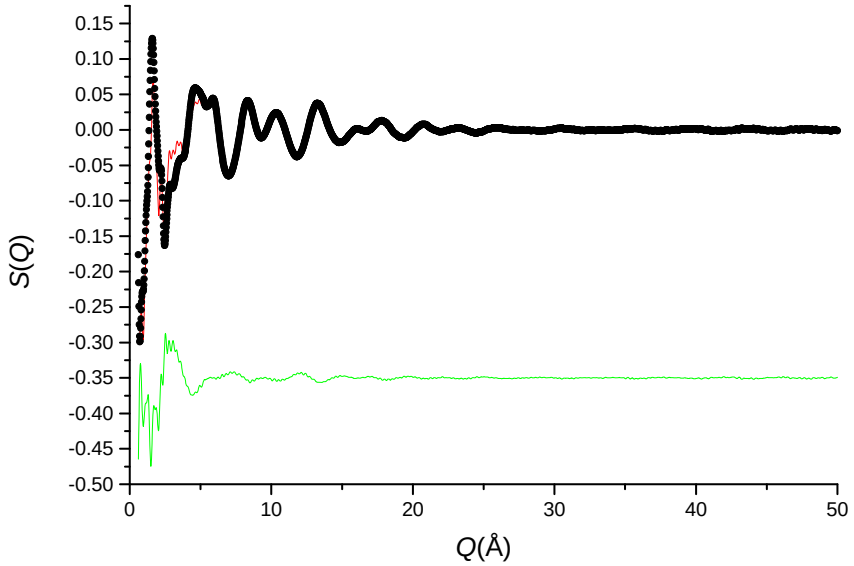

(b)

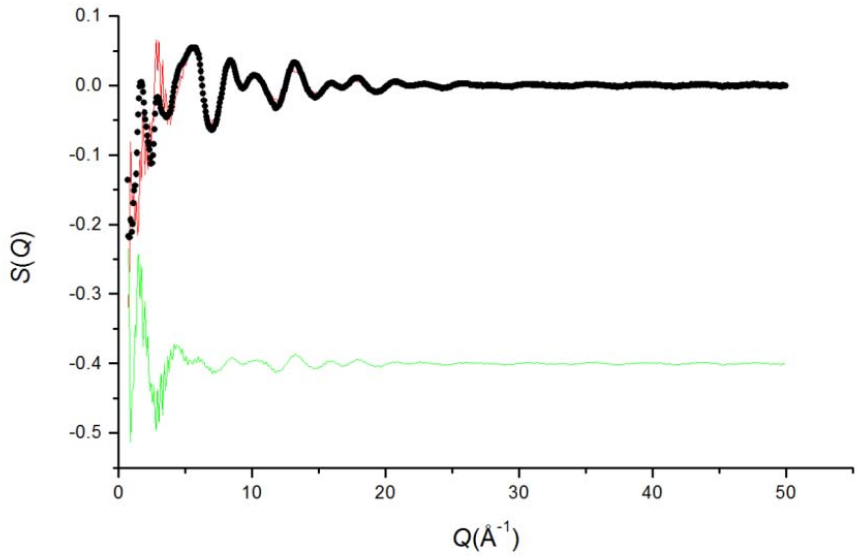

Fig. 3.20. Fitted reciprocal space neutron scattering data $S_{box}(Q)$ for $Na_{1-x}Zn_{1+x/2}(PO_3)_3$ (a) x = 1 and (b) x = 0 glass compositions at room temperature, showing observed (points), calculated (red line) and difference (green line), patterns.

(a)

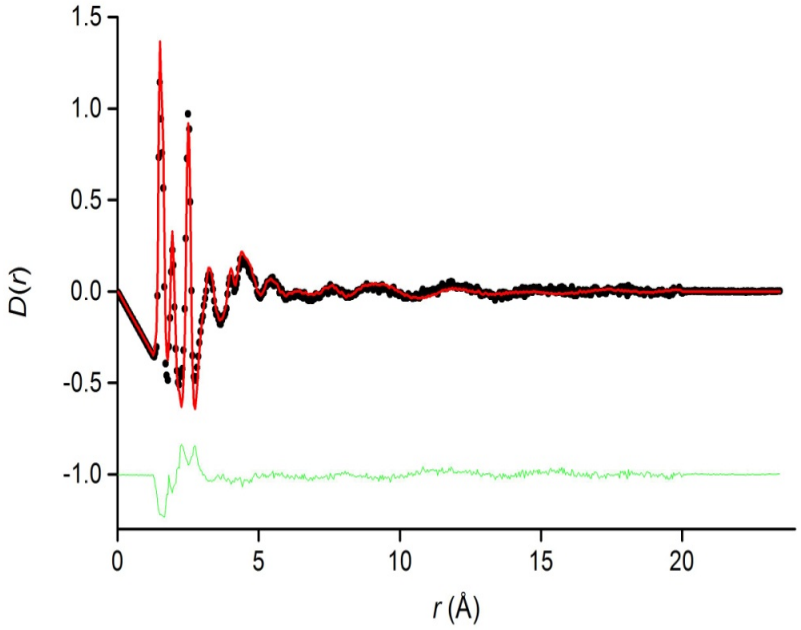

(b)

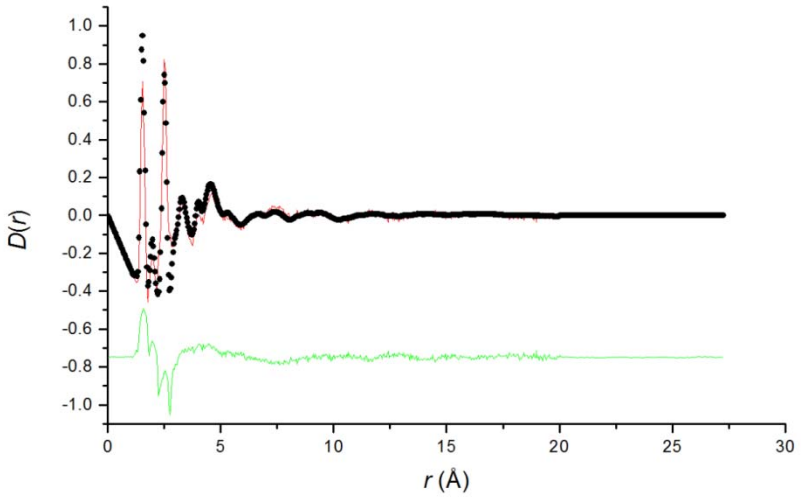

Fig. 3.21. Fitted real space neutron scattering data *D*(*r*) for $Na_{1-x}Zn_{1+x/2}(PO_3)_3$ (a) *x* = 1 and (b) *x* = 0 glass at room temperature, showing observed (points), calculated (red line) and difference (green line), patterns.

The corresponding partial distribution functions $g_{ij}(r)$ are shown in Fig. 3.22 with the corresponding correlation distances and coordination numbers shown in Table 3.11.

(a)

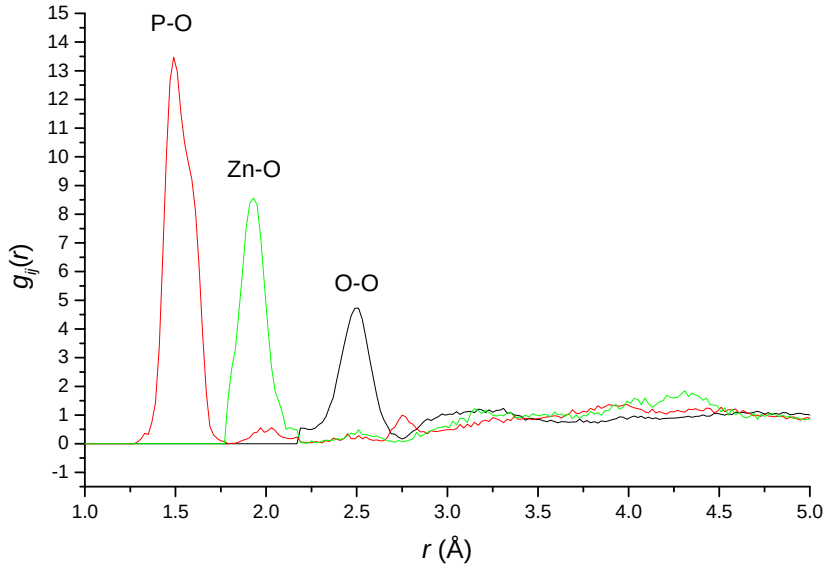

(b)

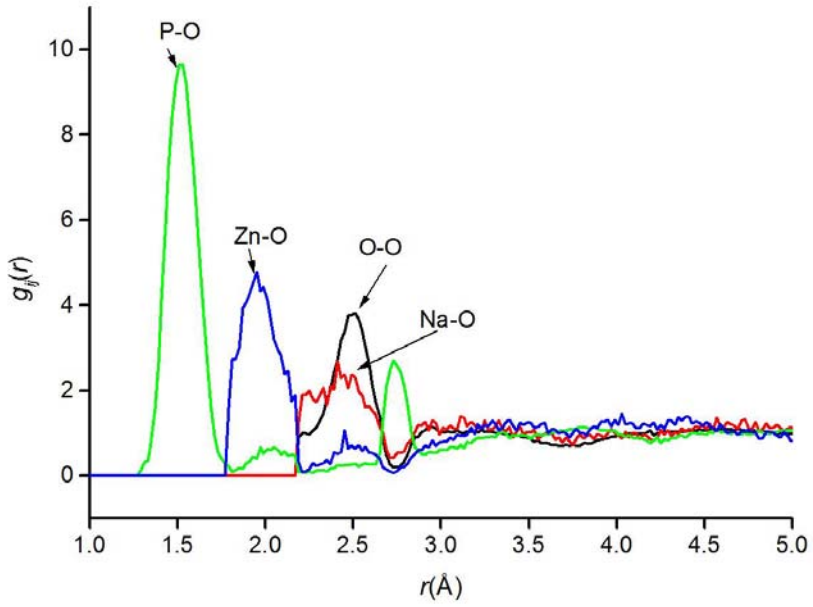

Fig. 3.22. Selected pair correlation functions for glass compositions $Na_{1-x}Zn_{1+x/2}(PO_3)_3$ (a) *x* = 1 and (b) x = 0 at room temperature.

Table 3.11 Pair correlation distances and coordination numbers from RMC analysis of neutron scattering data for $Na_{1-x}Zn_{1+x/2}(PO_3)_3$ (*x* = 1.0 and 0.0) glass at room temperature

Composition (*x*)	1		0		
Pair	P–O	Zn–O	P–O	Zn–O	Na–O
Distance	1.497	1.888	1.507	1.924	2.565
Coordination number	3.432	3.398	3.021	3.171	3.576

The distances observed in the RMC analysis are lower than the mean distances from the Rietveld analysis of β–$Zn(PO_3)_2$ of 1.943 Å and 1.530 Å for Zn–O and P–O respectively and are also lower than the corresponding values from the simple curve fitting to *T*(*r*). This difference might be accounted for by the fact that the distances from the RMC analysis correspond to the median value in the corresponding g_{ij} curve up to the first deep minimum in the curve, rather than a mean value. The coordination numbers also appear to be slightly lower than expected. This is believed to be due to small errors in the data correction procedure. It is noted that the simple curve fits to the *T*(*r*) data yielded more plausible coordination numbers. Hoppe *et al*.[26] observed coordination numbers of 3.85 and 4.25 for P–O and Zn–O, respectively in their RMC modelling of neutron and X–ray diffraction data for a composition close to zinc metaphophate.

The final configuration cell is shown in Fig. 3.23.It can be seen that the layers present in the crystalline β–$Zn(PO_3)_2$ are to some extent preserved in the glass as noted previously by Hoppe *et al*[26]. However, bearing in mind the quality of the fits and the possible data correction errors, this conclusion remains very tentative.

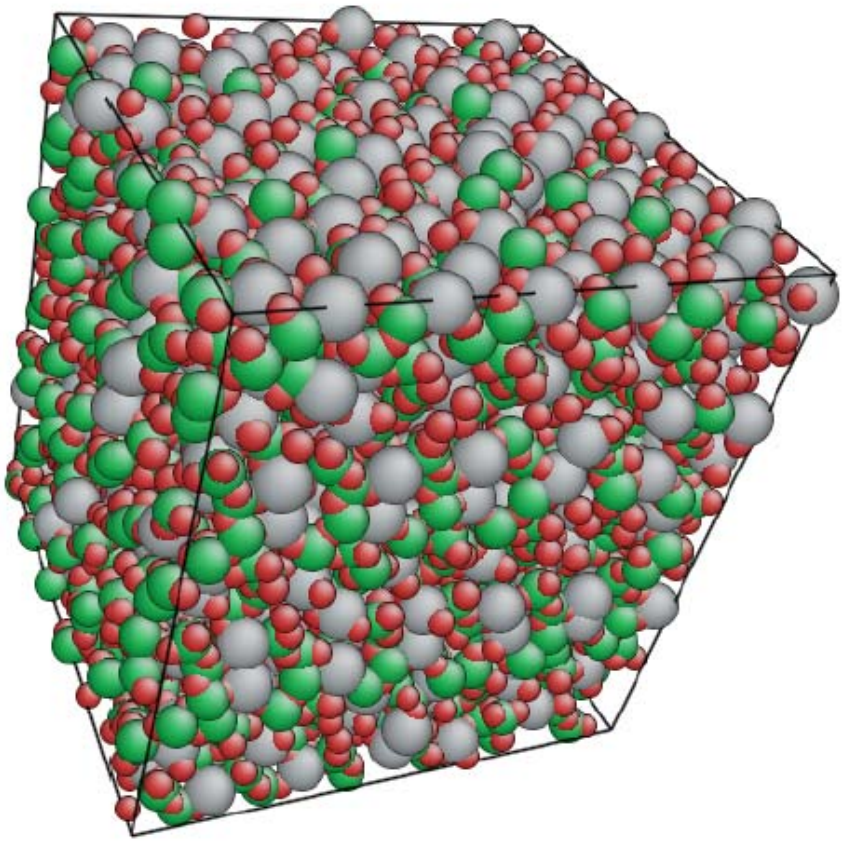

Fig. 3.23. Final RMC configuration cell for $Na_{1-x}Zn_{1+x/2}(PO_3)_3$ (x = 1) showing Zn (grey) P (green) and O (red) atoms.

3.2.3 Glass Compositions $NaZn_{1-x}M_x(PO_3)_3$ (M = Ca and Sr)

Fig. 3.24 shows X–ray diffraction patterns for the studied glass compositions in the series $NaZn_{1-x}M_x(PO_3)_3$ (M = Ca and Sr). The absence of Bragg peaks indicates the amorphous nature of glasses. Fig. 3.25 shows the compositional variation of thermoanalytical parameters for these glasses. T_g increases with increasing Ca/Sr content in the two series of glass compositions as observed by Ping *et al*[12] in zinc strontium metaphosphate glasses. This is contrary to expectation, since theoretically the Zn–O bond should be stronger and T_g would therefore be expected to decrease as the Zn–O bond is replaced by more ionic Ca–O and Sr–O interactions. Table 3.12 shows the M–O bonding energies of sodium and some divalent metals. The Zn–O bond has been reported to have the lowest bonding energy in the divalent metal oxide series[57].

This weak bond energy may explain the increase in T_g. Another possible explanation is that zinc is four coordinate whereas Ca and Sr are typically six coordinate or higher. This means that there is an increase in the number of phosphate groups cross–linked on substitution of Zn by Ca or Sr.

(a)

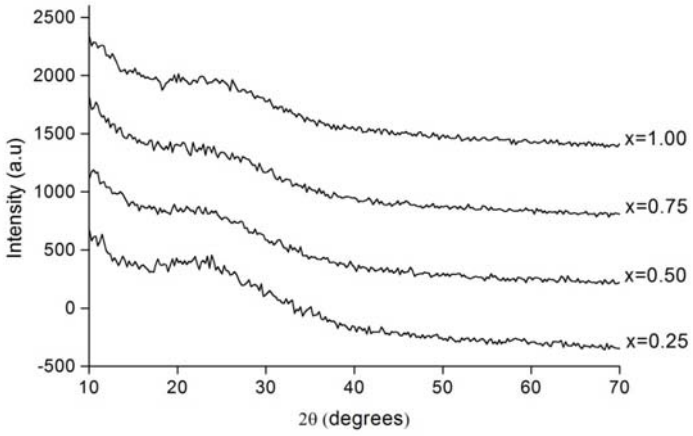

(b)

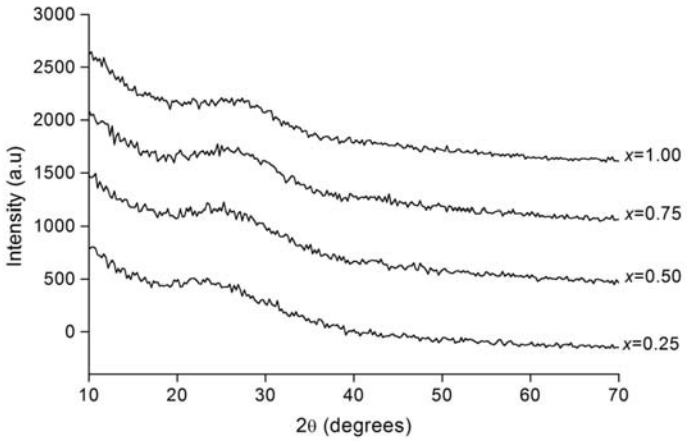

Fig. 3.24. X–ray diffraction patterns for $NaZn_{1-x}M_x(PO_3)_3$ glass compositions. (a) M = Ca, (b) M = Sr.

(a)

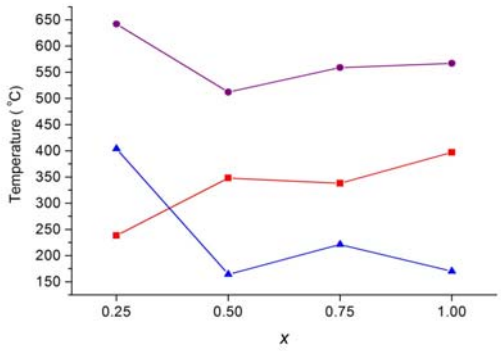

(b)

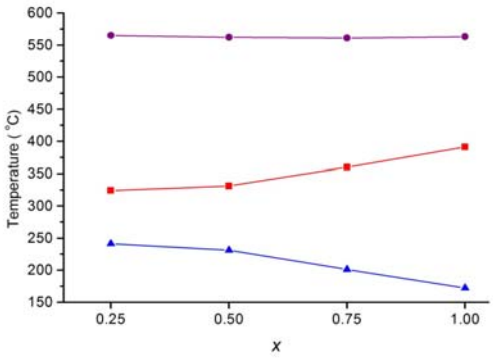

Fig. 3.25. Compositional variation of T_c (circles), T_g (squares) and $T_c - T_g$ (triangles) for glass compositions $NaZn_{1-x}M_x(PO_3)_3$.(a) M = Ca (b) M = Sr. Lines are guides to the eye. (esd = ±20°C)

Table 3.12 Selected M–O bond strengths[57]

Bond	Strength at 298K kJ/mol
Na–O	256.5
Mg–O	362.3
Ca–O	385.0
Sr–O	415.9
Ba–O	545.6
Mn–O	360.0
Fe–O	408.8
Zn–O	284.1

(a)

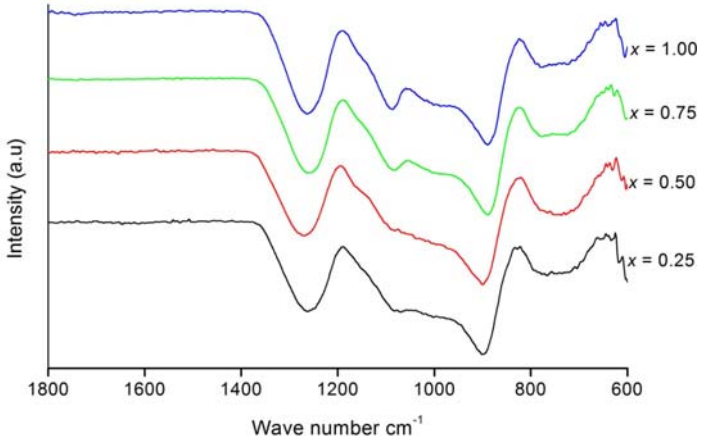

(b)

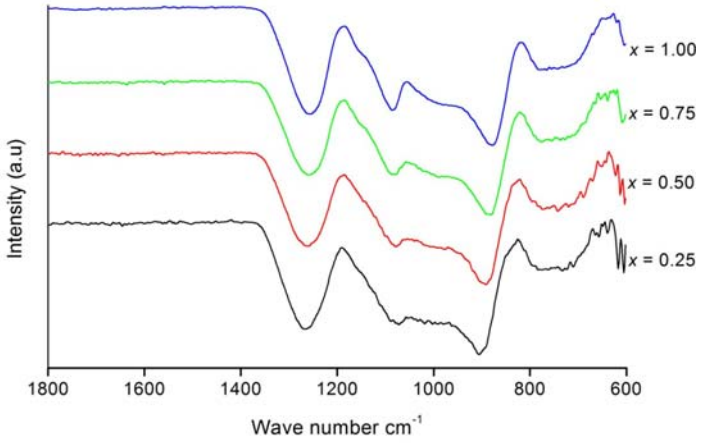

Fig. 3.26. IR spectra for the studied glass compositions $NaZn_{1-x}M_X(PO_3)_3$.(a) M = Ca, (b) M = Sr

Fig. 3.26 shows the IR spectra for the studied glass compositions. All glass compositions again show peaks characteristic of metaphophate glasses at about 1280 cm^{-1} and 900 cm^{-1} for $(PO_2)^-_{as}$ (Q^2 species) and P–O–P asymmetric stretch, respectively. No difference in peak shape is observed with the substitution of ZnO with CaO or SrO. However, the band at about 900 cm^{-1} moves toward lower frequency, with increasing CaO/SrO content in both series of glasses. This is explained by an increase in the P–O–P bond angle, which increases with the decrease in field strength of cation[10]. Since Ca^{2+} and strontium Sr^{2+} have lower field strengths than Zn^{2+}, the in-chain P–O–P bond angle increases. $(PO_2)^-_{as}$ moves towards higher frequency value with increaseing CaO/SrO content. This is again due to the greater ionic nature of the Ca–O

and Sr–O bonds compared to the Zn–O bond, due to the higher electronegativity of Zn compared to Ca or Sr. Hence the P–O–Ca/Sr bond is more ionic than P–O–Zn. These results are similar to those obtained previously in the strontium[12] substituted system and also where zinc is substituted with barium[28, 58].

Fig. 3.27 shows ^{23}Na MAS–NMR spectra of the two studied glass compositional series. In both cases, isotropic chemical shift moves towards less negative values with decreasing zinc oxide content. However, no difference in line broadness or shape is observed.

(a)

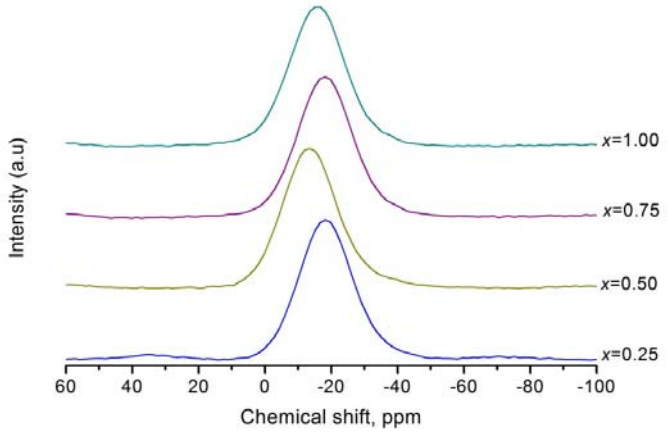

(b)

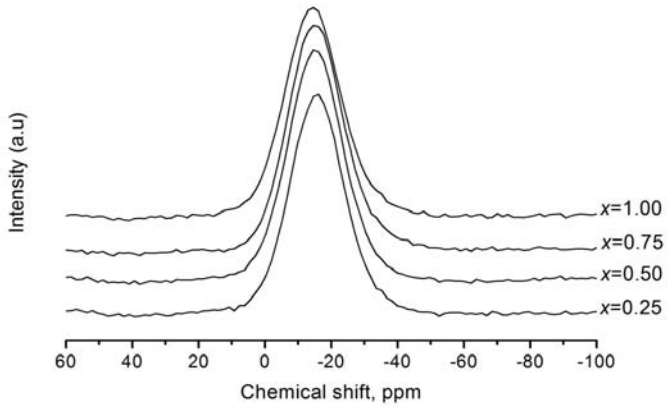

Fig. 3.27. ^{23}Na MAS–NMR spectra of glass compositions $NaZn_{1-x}M_X(PO_3)_3$.(a) M = Ca, (b) M = Sr

Fig. 3.28 shows the ^{31}P MAS–NMR spectra of the studied glass compositions. All the glass samples have two peaks associated with Q^1 at ca. –8 ppm to –14 ppm and Q^2 at –25.80 to –30.4 ppm respectively. However, the predominant peak in all glass samples is Q^2. This is in agreement with the fact that glasses with 50 mol% P_2O_5 are predominantly metaphosphate glasses. The ratios of the integrated intensities in the spectra show Q^1 *ca*. 1 to 4 % and Q^2 *ca*. 96 to 99 %. Spectral parameters of all compositions for the main resonance (Q^2 species) are presented in Table 3.13. The large chemical shift anisotropy, at –187 to –202 ppm, is typical of metaphosphate glasses. The chemical shift becomes more negative with increasing zinc content. This can be explained in terms of charge to radius ratio. Zinc has larger cation potential than calcium which in turn has a larger cation potential than strontium.

(a)

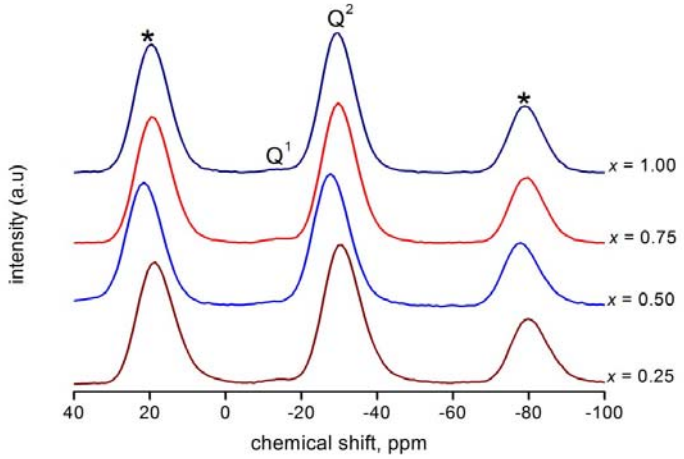

(b)

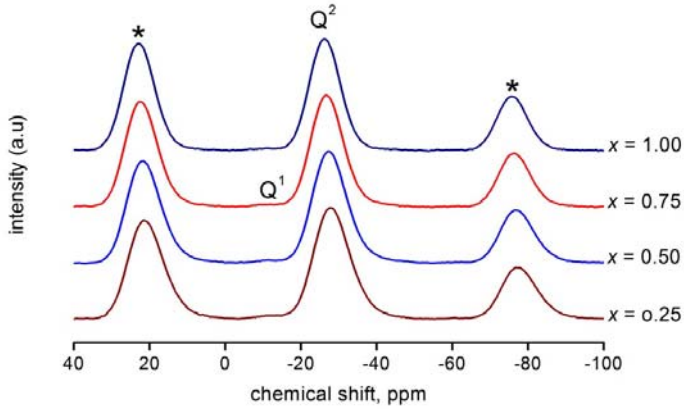

Fig. 3.28. ^{31}P MAS–NMR spectra for studied glass compositions $NaZn_{1-x}M_x(PO_3)_3$.(a) M = Ca (b) M = Sr. * represents spinning side bands.

Table 3.13 Spectral parameters derived from fitted ^{31}P MAS–NMR spectra of glass compositions $NaZn_{1-x}M_x(PO_3)_3$ (M = Ca, Sr) (x = 0.25. 0.5, 0.75, 1.00) (χ^2 = 0.001 – 0.01)

M	x	δ_{iso}/ppm	δ_{11}/ppm	δ_{22}/ppm	δ_{33}/ppm	Δδ/ppm	η
Ca	0.25	–30.07(1)	35.00	35.00	–161.00	–196.00	0.00
	0.50	–25.27(2)	74.00	13.00	–163.00	–207.00	0.44
	0.75	–29.53(1)	36.60	36.60	–162.00	–197.00	0.00
	1.00	–29.63(1)	69.00	4.90	–162.00	–199.00	0.48
Sr	0.25	–27.70(2)	38.20	38.20	–159.00	–197.00	0.00
	0.50	–27.10(1)	38.94	38.94	–159.00	–198.00	0.00
	0.75	–26.59(1)	71.30	9.90	–160.00	–201.50	0.45
	1.00	–26.20(2)	72.12	10.80	–161.52	–202.00	0.45

^{67}Zn NMR static spectra for the glass composition $NaZn_{1-x}M_x(PO_3)_3$ (x = 0.5) are presented in Fig. 3.29. Spectra were again fitted to two quadrupolar static resonance shifts using the program DMFIT[59]. No difference in line shape is observed on substitution of ZnO either with CaO or SrO (compare with Fig. 3.14), which is an indication that the presence of different cations in the system does not change the chemical environment of zinc significantly. Spectral parameters derived from simulations of the experimental spectra are presented in Table 3.14.

(a)

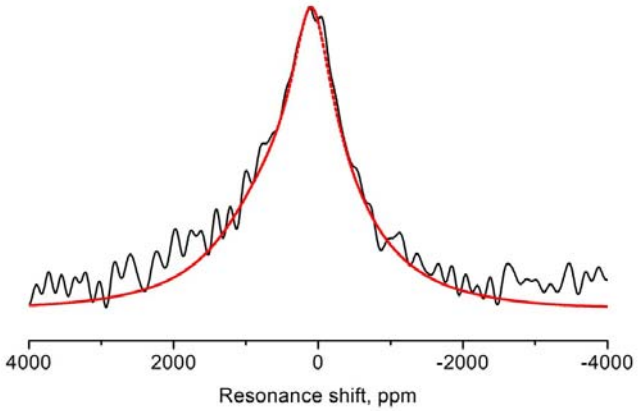

(b)

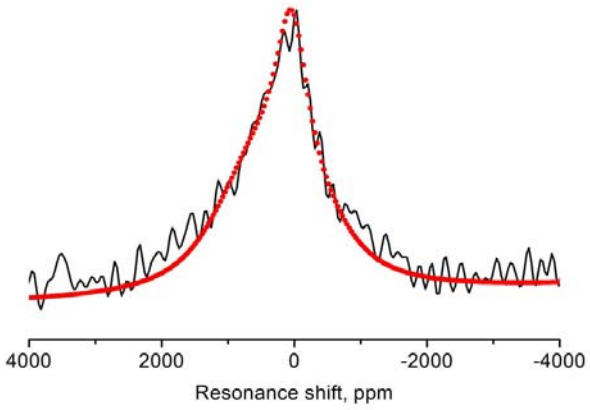

Fig. 3.29. Fitted natural abundance static ^{67}Zn NMR spectra of glass compositions $NaZn_{1-x}M_x(PO_3)_3$ (x = 0.5) (a) M = Ca (b) M = Sr. Red line indicates fit.

Table 3.14 ^{67}Zn NMR parameters for glass compositions $NaZn_{1-x}M_x(PO_3)_3$ (x = 0.5)derived from simulations of experimental spectra.

composition (M)	δ (ppm)	C_Q (MHz)	η_Q	% intensity
Ca	212 105	9.4 5.4	0.55 0.67	85 15
Sr	438 92	9.3 4.7	0.62 0.01	83 17

Fig. 3.30 shows ^{43}Ca static and MAS NMR spectra of glass composition $NaZn_{1-x}M_x(PO_3)_3$ (x = 0.5, M = Ca) acquired at ultra high field (21.1 T). A single resonance is observed under both conditions at about 4.12 ppm. Line broadness does not change under MAS conditions. According to chemical shift and bond length correlations established for calcium silicate compounds[60, 61] the observed chemical shift in the present system can be correlated to a Ca–O mean distance of 2.3 Å – 2.4 Å.

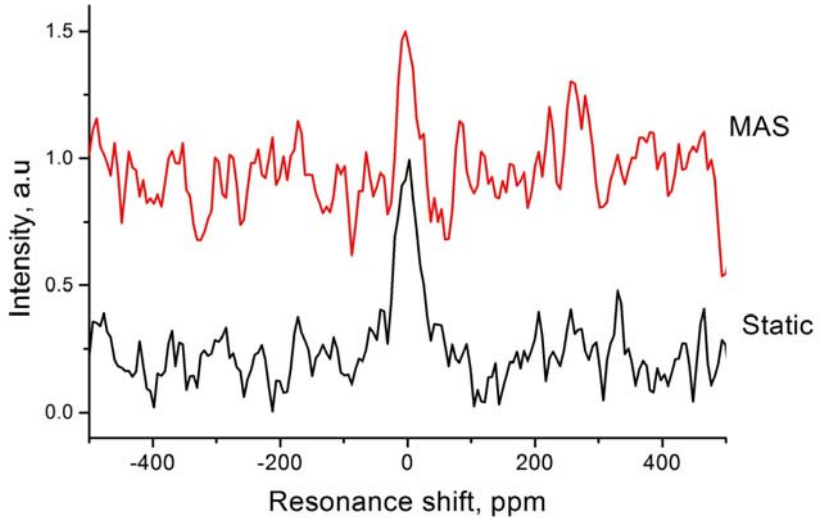

Fig. 3.30. ^{43}Ca NMR of glass composition $NaZn_{1-x}M_x(PO_3)_3$ (x = 0.5, M = Ca)

Neutron coherent scattering intensity $i(Q)$ obtained by background correction and subtraction of self scattering from neutron diffraction data are plotted in Fig. 3.31. The corresponding $T(r)$ functions produced by Fourier transform using a Lorch modifiction function are presented in Fig. 3.32. The $T(r)$ function was simulated up to 3 Å to fit the 1st coordination pair correlations to give bond distances and coordination numbers and hence the short range order of the glass structure. Fig. 3.33 shows the fitted $T(r)$ functions with detail of the fits in Fig. 3.34. The P–O peak is resolved into two separate peaks at 1.5 Å and 1.6 Å due to contributions from P–NBO and P–BO, respectively. The P–O peak for glass composition M = Sr is less well resolved as compared to that for M = Ca, which indicates the effect of different cations on P–O bonding. Further structural details were obtained by fitting Zn–O, Na–O, Ca–O/Sr–O and O–O first neighbour peaks. Assumptions were made to fit the real space correlation functions of such complex systems, since peaks due to Na–O, Ca–O/Sr–O and O–O are overlapped in the range 2 Å to 3 Å. The O–O coordination number for each glass composition was assumed to be 4 according to the formula $24/(5 + y)$[62] where y is the mole ratio between mole fraction of modifier and phosphate content. The $T(r)$ peak at about 2.5 Å was fitted to an O–O coordination number of 4 and then subtracted from rest of the $T(r)$. The residual $T(r)$ was fitted to a Zn–O pair correlation at about 1.9 Å. The fit of the residual area between 2.0 Å to 2.75 Å gives the coordination numbers for Na–O and Ca–O/Sr–O. Fitted parameters are presented in Table 3.15. The number of P–NBO and P–O is same as expected based on composition. The total P–O coordination number is about 4 (within the measurement errors) as expected for (PO_4) tetrahedra. The Zn–O coordination number is about 4 as observed in other glass compositions and the literature[14]. Na–O coordination is also 4, which is consistent with results obtained by Pickup *et al*[63] in their studies of sodium calcium metaphosphate glasses. The Ca–O coordination number is 3 and Sr–O coordination number is about 5, which are lower than those observed in literature[29, 55]. This can be attributed to errors in fitting.

(a)

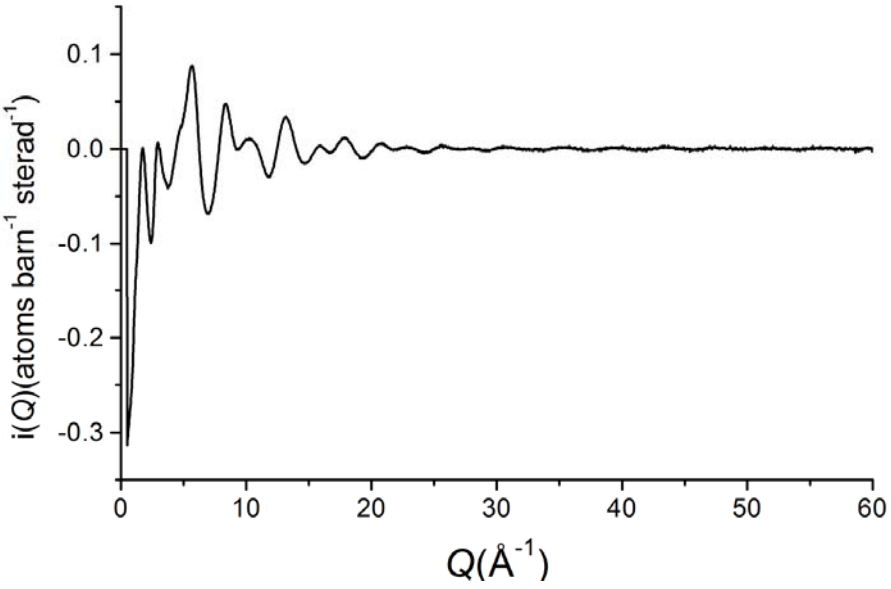

(b)

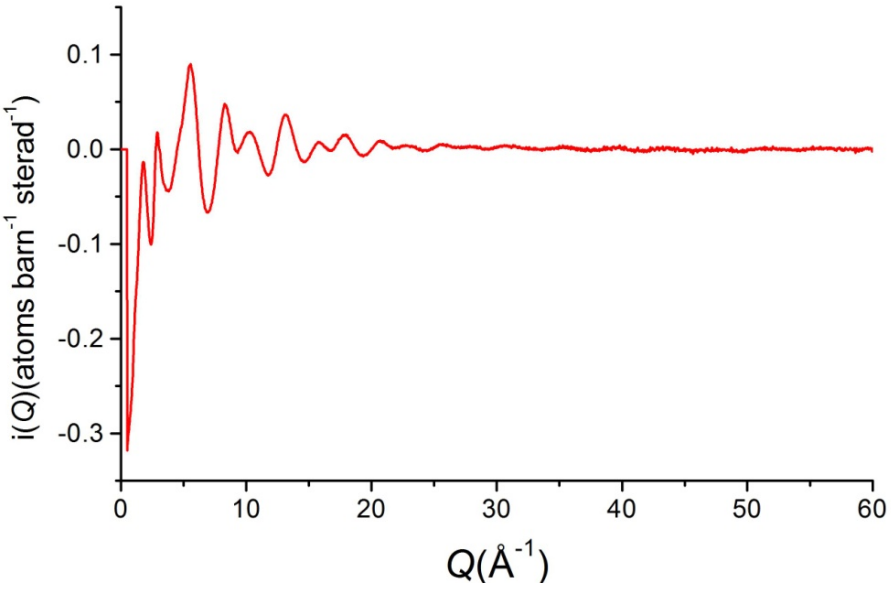

Fig. 3.31. Q space interference functions $i(Q)$ for glass compositions $NaZn_{1-x}M_x(PO_3)_3$ (x = 0.5) (a) M = Ca (b) M = Sr

(a)

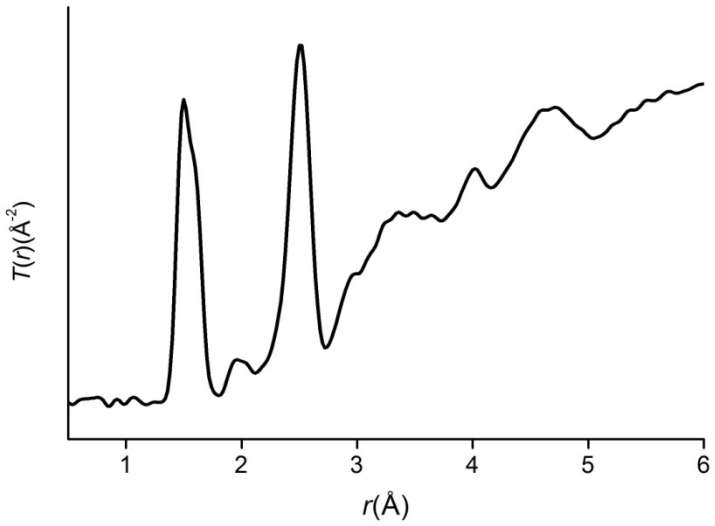

(b)

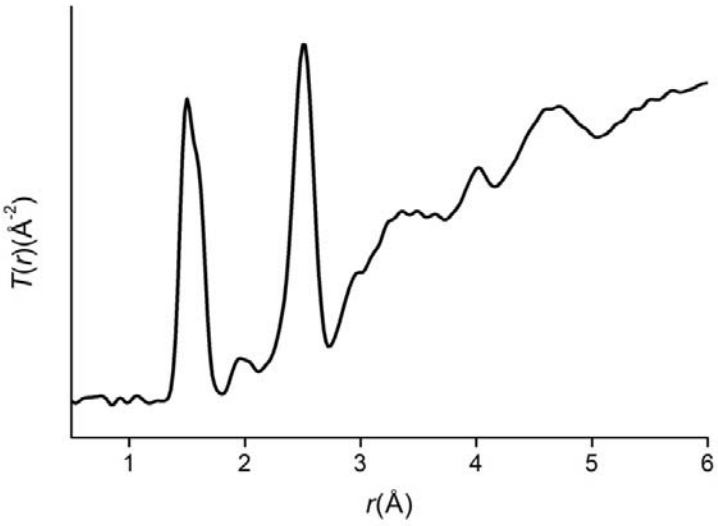

Fig. 3.32. The real space data for the total diffraction pattern *T*(*r*) for glass compositions $NaZn_{1-x}M_x(PO_3)_3$ (*x* = 0.5) (a) M=Ca (b) M=Sr.

(a)

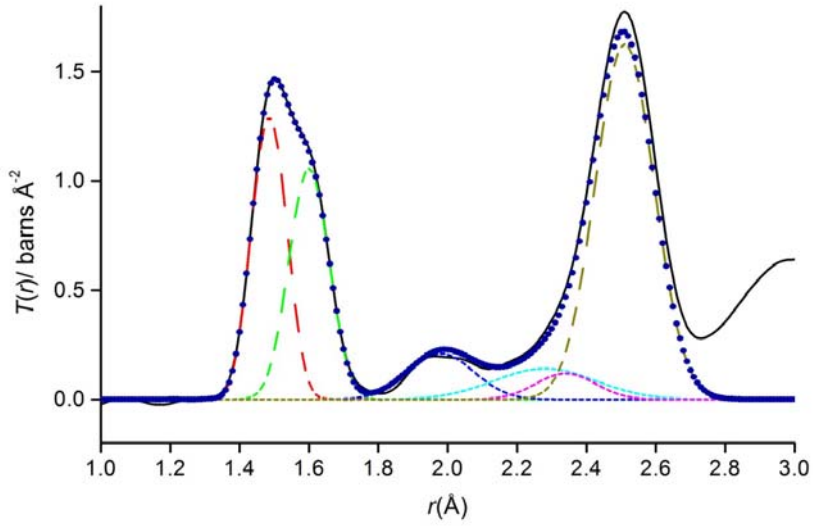

(b)

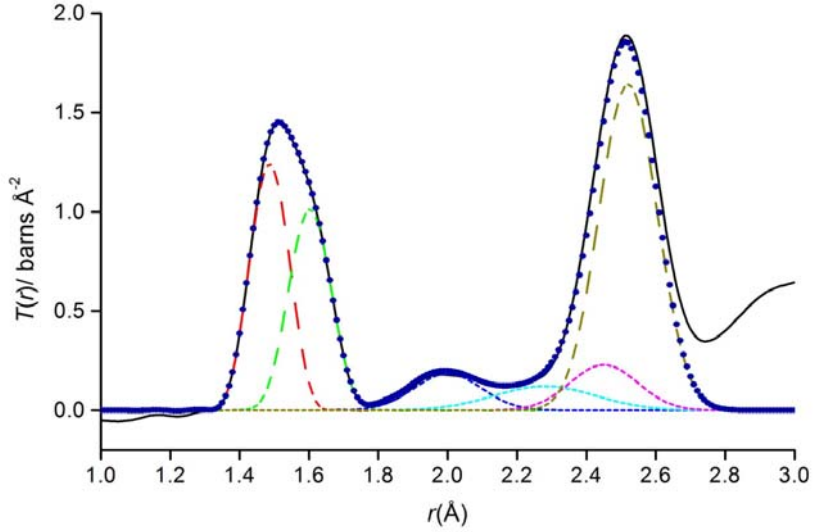

Fig. 3.33. The total pair distribution function *T*(*r*) (solid black lines) together with fits (dotted blue line for the glass compositions $NaZn_{1-x}M_x(PO_3)_3$ (*x* = 0.5) (a) M = Ca, (b) M = Sr

(a)

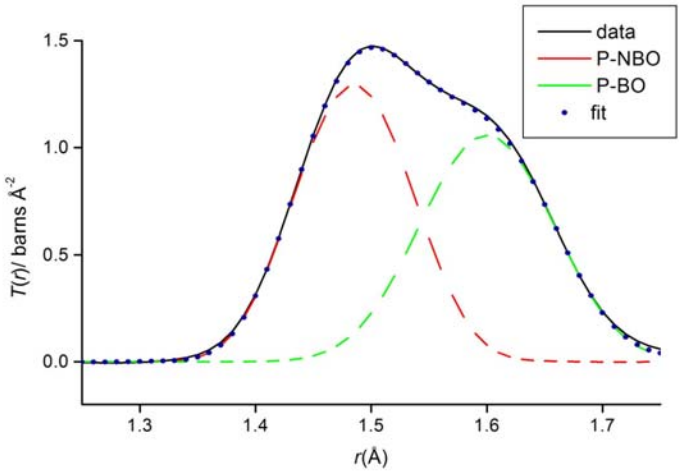

(b)

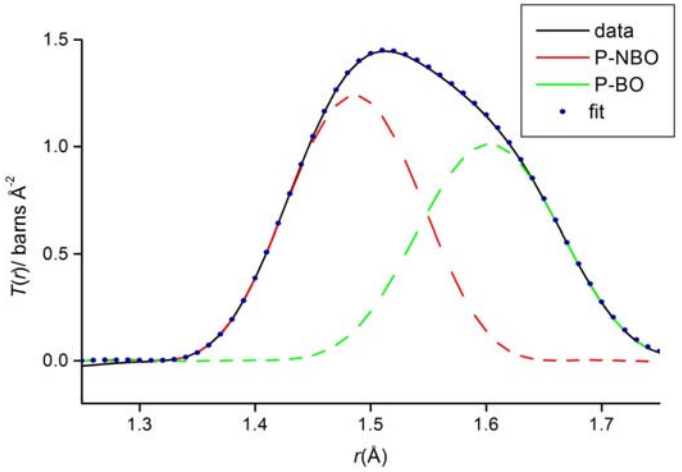

Fig. 3.34. Fits to correlation function *T*(*r*) in the range of P– O 1st coordination correlation for glass compositions $NaZn_{1-x}M_x(PO_3)_3$ (*x* = 0.5) (a) M=Ca (b) M=Sr

Table 3.15 Structural parameters (r_{i-j} interatomic distance and N_{i-j} coordination number) derived from fitted $T(r)$ for glass compositions $NaZn_{1-x}M_x(PO_3)_3$ (x = 0.5) (a) M = Ca, (b) M = Sr.

Sample	Correlation	$r_{(i-j)}$ /Å (±0.02)	$N_{(i-j)}$ (±0.2)
$NaZn_{1-x}M_x(PO_3)_3$ (x = 0.5, M = Ca)	P – O (NB)	1.48	1.9
	P – O (B)	1.6	1.9
	Zn – O	1.98	4.2
	Na – O	2.28	3.9
	Ca – O	2.34	3.0
	O – O	2.51	4.0
$NaZn_{1-x}M_x(PO_3)_3$ (x = 0.5, M = Sr)	P – O (NB)	1.48	2.0
	P – O (B)	1.6	1.9
	Zn – O	2.0	3.8
	Na – O	2.28	3.8
	Sr – O	2.45	4.7
	O – O	2.52	4.0

The final fits to the $S_{box}(Q)$ and $D(r)$ data derived from neutron diffraction data for $NaZn_{1-x}M_x(PO_3)_3$ (x = 0.5, M = Ca) glass at room temperature are shown in Figs. 3.35 and 3.36, respectively. The corresponding partial distribution functions $g_{ij}(r)$ are shown in Fig. 3.37, with the corresponding correlation distances and coordination numbers shown in Table 3.16. The pair correlation distances observed in the RMC analysis are higher than those derived from the RMC analysis of $ZnO:P_2O_5$ glass. The Zn–O correlation is longer than in the other glasses examined and may well reflect a greater degree of network modifying role for zinc in this glass. The derived coordination numbers for phosphorous and sodium are closer to expected levels, but that for zinc is significantly lower. As can be seen in Figs. 3.36 and 3.37, the analysis struggled to model the Zn–O correlation, and is reflected in the significant differences seen in the $D(r)$ and $S(Q)$ fits. This problem might be addressed using an improved starting model (after energy minimisation) and using stronger constraints in the analysis.

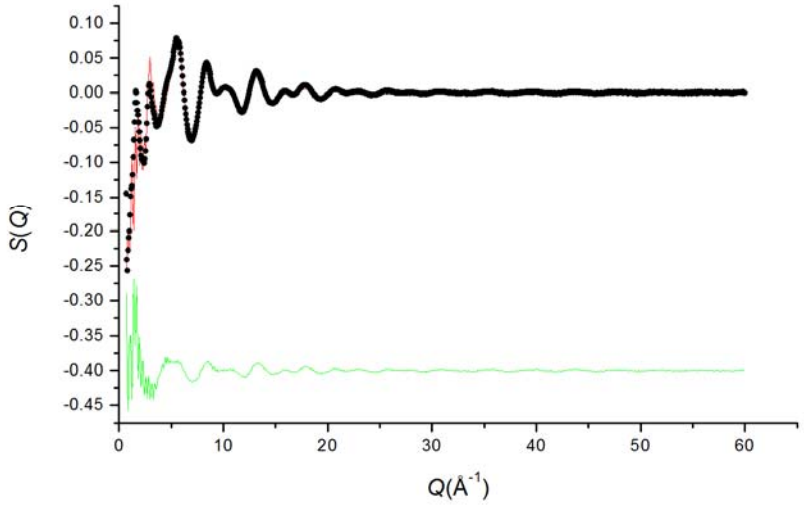

Fig. 3.35. Fitted reciprocal space neutron scattering data $S_{box}(Q)$ for $NaZn_{1-x}M_x(PO_3)_3$ (x = 0.5) glass at room temperature, showing observed (points), calculated (red line) and difference (green line), patterns.

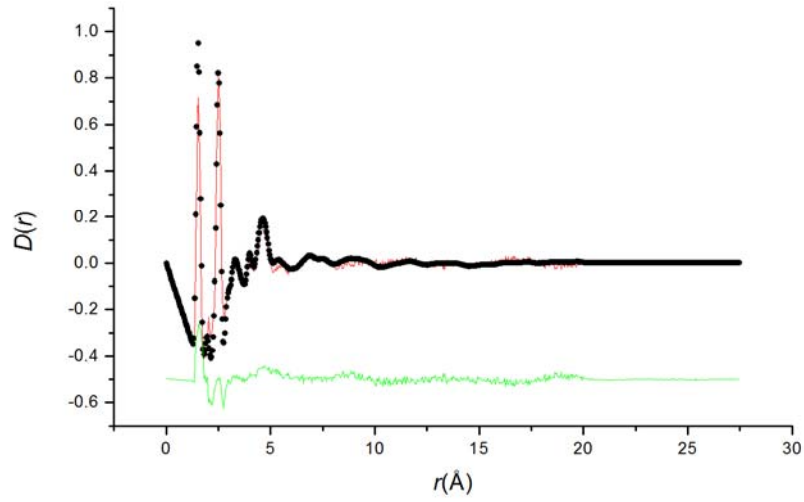

Fig. 3.36. Fitted real space neutron scattering data $D(r)$ for $NaZn_{1-x}M_x(PO_3)_3$ (x = 0.5) glass at room temperature, showing observed (points), calculated (red line) and difference (green line), patterns.

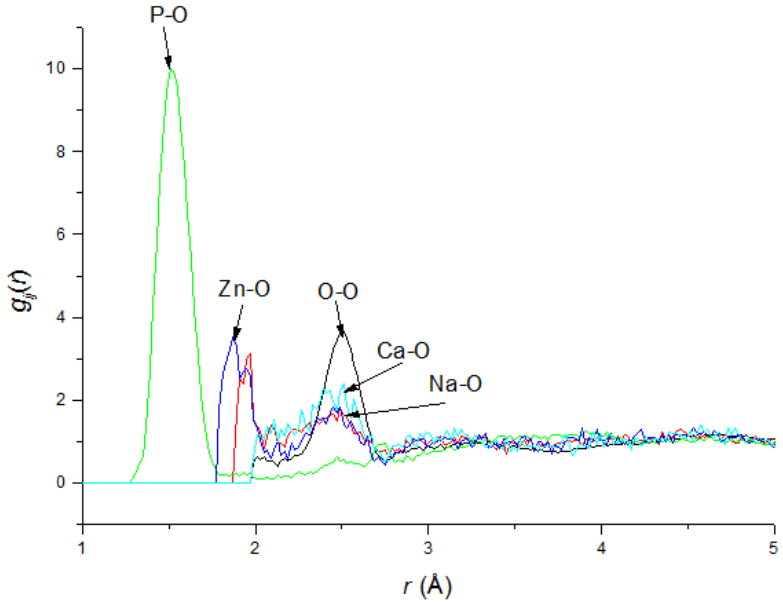

Fig. 3.37. Selected pair correlation functions for $NaZn_{1-x}M_x(PO_3)_3$ (x = 0.5) glass at room temperature.

Table 3.16 Pair correlation distances and coordination numbers from RMC analysis of neutron scattering data for $NaZn_{1-x}M_x(PO_3)_3$ (x = 0.5) glass at room temperature

Pair	**P–O**	**Zn–O**	**Na–O**	**Ca–O**
Distance	1.515	2.116	2.943	2.496
Coordination number	3.54	1.64	3.9	3.8

3.3 Conclusions

The short range structure of metaphosphate glasses has been investigated to characterize the structural role of zinc in these glass compositions. To this end structure investigation started from zinc metaphosphate glass and its isocompositional crystalline polymorphs. In β–$Zn(PO_3)_2$, zinc is seen to adopt a distorted tetrahedral coordination with oxygen. The zincate tetrahedra bridge metaphosphate chains, yielding the three dimensional structure. In zinc metaphosphate glass, zinc is seen to be predominantly tetrahedral with average Zn–O bonds very similar to those observed in the crystalline analogue. There is evidence for a small proportion of the zinc

adopting six–coordinate geometry in the glass. The Zn–O bond length varies little with composition in the glass system $Na_{1-x}Zn_{1+x/2}(PO_3)_3$. Increasing zinc content is seen to decrease glass transition temperature in the $Na_{1-x}Zn_{1+x/2}(PO_3)_3$ series, but in the $NaZn_{1-x}M_X(PO_3)_3$ series, T_g in general shows a decrease with decreasing Zn content, when Zn is substituted by Sr or Ca. This trend in T_g is attributed to differences in the relative bond strengths of the Zn–O, Sr–O and Ca–O bonds. ^{31}P MAS–NMR spectra showed that isotropic chemical shift moved to more positive values with decreasing zinc content, due to the lower electronegativity and hence lower shielding of sodium, calcium and strontium compared to zinc.

^{67}Zn NMR spectra of α and β forms of zinc metaphosphate show typical quadrupolar static line shapes, with isotropic chemical shifts corresponding to 4 and 6 coordinated for β–$Zn(PO_3)_2$ and α–$Zn(PO_3)_2$ respectively. C_Q is about 10 MHz which is comparable to the values obtained for glass compositions, though the line shape for the glasses is typical of disordered materials. ^{67}Zn NMR spectra of all glass compositions indicate the presence of zinc mainly in tetrahedral coordination with about 10–17% in octahedral coordination. Analysis of real space neutron diffraction data in the range of 1 Å to 2.75 Å gives distinct bond lengths for P–NBO and P–BO. Both zinc and sodium are seen to have coordination numbers around 4, consistent with previous studies. A model for the long range structure of $Zn(PO_3)_2$ glass shows that the layered structure is preserved. However, these results must be tentative and require further study, to eliminate bias from the starting model.

3.4 References

1. U. Hoppe, Y. Dimitriev and P. Jovari, *Zeitschrift Fur Naturforschung Section a-a Journal of Physical Sciences*, 2005, **60**, 517-526.
2. M. Weil, *Acta Crystallographica Section C-Crystal Structure Communications*, 2004, **60**, I20-I22.
3. Avrbuch-Pouchot, A. Durif and M. Bagieu Beucher, *Acta Crystallographica*, 1983, **39**, 25-26.
4. B. E. Robertson and C. Calvo, *Journal of Solid state Chemistry*, 1970, **1**, 120.
5. M. Bitar, V. Salih, V. Mudera, C. J. Knowles and P. M. Lewis, *Biomaterials*, 2004, **25**, 2283-2292.
6. D. S. Brauer, C. Russel, W. Li and S. Habelitz, *Journal of Biomedical Materials Research Part A*, 2006, **77A**, 213-219.
7. M. Navarro, M. P. Ginebra and J. A. Planell, *Journal of Biomedical Materials Research Part A*, 2003, **67A**, 1009-1015.
8. E. Gentleman, Y. C. Fredholm, G. Jell, N. Lotfibakhshaiesh, M. D. O'Donnell, R. G. Hill and M. M. Stevens, *Biomaterials*, 2010, **31**, 3949-3956.
9. S. Jebahi, H. Oudadesse, H. el Feki, T. Rebai, H. Keskes, P. Pellen and A. el Feki, *Journal of Applied Biomedicine*, 2012, **10**, 195-209.
10. K. Meyer, *Journal of Non-Crystalline Solids*, 1997, **209**, 227-239.
11. R. K. Brow, D. R. Tallant, S. T. Myers and C. C. Phifer, *Journal of Non-Crystalline Solids*, 1995, **191**, 45-55.
12. P. Y. Shih and H.-M. Shiu, *Materials Chemistry and Physics*, 2007, **106**, 222-226.
13. T. M. Alam, J. McLaughlin, C. C. Click, S. Conzone, R. K. Brow, T. J. Boyle and J. W. Zwanziger, *Journal of Physical Chemistry B*, 2000, **104**, 1464-1472.
14. G. Walter, U. Hoppe, J. Vogel, G. Carl and P. Hartmann, *Journal of Non-Crystalline Solids*, 2004, **333**, 252-262.
15. B. Tischendorf, J. U. Otaigbe, J. W. Wiench, M. Pruski and B. C. Sales, *Journal of Non-Crystalline Solids*, 2001, **282**, 147-158.
16. M. Bionducci, G. Licheri, A. Musinu, G. Navarra, G. Piccaluga and G. Pinna, *Zeitschrift Fur Naturforschung Section a-a Journal of Physical Sciences*, 1996, **51**, 1209-1215.

17. K. Suzuya, K. Itoh, A. Kajinami and C. K. Loong, *Journal of Non-Crystalline Solids*, 2004, **345**, 80-87.

18. U. Hoppe, G. Walter, R. Kranold, D. Stachel and A. Barz, *Journal of Non-Crystalline Solids*, 1995, **193**, 28-31.

19. G. Walter, G. Goerigk and C. Ruessel, *Journal of Non-Crystalline Solids*, 2006, **352**, 4051-4061.

20. G. Walter, U. Hoppe, A. Barz, R. Kranold and D. Stachel, *Journal of Non-Crystalline Solids*, 2000, **263**, 48-60.

21. G. Navarra, A. Falqui, G. Piccaluga and G. Pinna, *Physical Chemistry Chemical Physics*, 2002, **4**, 4817-4822.

22. E. Sourial, T. Peres, J. A. Capobianco, A. Speghini and M. Bettinelli, *Physical Chemistry Chemical Physics*, 1999, **1**, 2013-2018.

23. B. C. Tischendorf, T. M. Alam, R. T. Cygan and J. U. Otaigbe, *Journal of Non-Crystalline Solids*, 2003, **316**, 261-272.

24. G. G. Boiko, N. S. Andreev and A. V. Parkachev, *Journal of Non-Crystalline Solids*, 1998, **238**, 175-185.

25. A. J. Parsons, I. Ahmed, C. D. Rudd, G. J. Cuello, E. Pellegrini, D. Richard and M. R. Johnson, *Journal of Physics-Condensed Matter*, 2010, **22**, 485403-485411.

26. U. Hoppe, G. Walter, G. Carl, J. Neuefeind and A. C. Hannon, *Journal of Non-Crystalline Solids*, 2005, **351**, 1020-1031.

27. M. Uo, M. Mizuno, Y. Kuboki, A. Makishima and F. Watari, *Biomaterials*, 1998, **19**, 2277-2284.

28. J. S. Hassan and M. Hafid, *Materials Research Bulletin*, 2004, **39**, 1123-1130.

29. K. M. Wetherall, D. M. Pickup, R. J. Newport and G. Mountjoy, *Journal of Physics-Condensed Matter*, 2009, **21**, 035109-003518.

30. Y. Xiang and J. Du, *Chemistry of Materials*, 2011, **23**, 2703-2717.

31. C. Bonhomme, C. Gervais, N. Folliet, F. Pourpoint, C. C. Diogo, J. Lao, E. Jallot, J. Lacroix, J.-M. Nedelec, D. Iuga, J. V. Hanna, M. E. Smith, Y. Xiang, J. Du and D. Laurencin, *Journal of the American Chemical Society*, 2012, **134**, 12611-12628.

32. M. A. Kennedy, R. L. Vold and R. R. Vold, *Journal of Magnetic Resonance*, 1991, **92**, 320-331.

33. S.E. McLain, D. T. Bowron, A. C. Hannon and A. K. Soper, *GUDRUN: A computer program developed for analysis of neutrondiffraction data*, ISIS Facility, Rutherford Appleton LaboratoryChilton, Didcot, OXON, United Kingdom.
34. J. D. Wicks and R. L. McGreevy, *Journal of Non-Crystalline Solids*, 1995, **193**, 23-27.
35. A. Durif, M.T. Averbuch-Pouchot and J. C.Guitel, *J.C. Z. Kristallogr. Kristallgeom. Kristallphys*, 1986, **177**, 139-142.
36. I. Abrahams, G. E. Hawkes, A. Ahmed, T. Di Cristina, D. Z. Demetriou and G. I. Ivanova, *Magnetic Resonance in Chemistry*, 2008, **46**, 316-322.
37. T. Vosegaard, U. Andersen and H. J. Jakobsen, *Journal of the American Chemical Society*, 1999, **121**, 1970-1971.
38. Y. Zhang, S. Mukherjee and E. Oldfield, *Journal of the American Chemical Society*, 2005, **127**, 2370-2371.
39. M. D. Segall, P. J. D. Lindan, M. J. Probert, C. J. Pickard, P. J. Hasnip, S. J. Clark and M. C. Payne, *Journal of Physics-Condensed Matter*, 2002, **14**, 2717-2744.
40. J. Schwarz, H. Ticha, L. Tichy and R. Mertens, *Journal of Optoelectronics and Advanced Materials*, 2004, **6**, 737-746.
41. D. Muresan, M. Vasilescu, I. Balasz, C. Popa, W. Kiefer and S. Simon, *Journal of Optoelectronics and Advanced Materials*, 2006, **8**, 558-560.
42. R. J. Kirkpatrick and R. K. Brow, *Solid State Nuclear Magnetic Resonance*, 1995, **5**, 9-21.
43. R. K. Brow, R. J. Kirkpatrick and G. L. Turner, *Journal of Non-Crystalline Solids*, 1990, **116**, 39-45.
44. D. M. Pickup, P. Guerry, R. M. Moss, J. C. Knowles, M. E. Smith and R. J. Newport, *Journal of Materials Chemistry*, 2007, **17**, 4777-4784.
45. R. K. Brow, *Journal of Non-Crystalline Solids*, 2000, **263**, 1-28.
46. R. Pires, I. Abrahams, T. G. Nunes and G. E. Hawkes, *Journal of Non-Crystalline Solids*, 2004, **337**, 1-8.
47. E. A. Abou Neel, L. A. O'Dell, M. E. Smith and J. C. Knowles, *Journal of Materials Science-Materials in Medicine*, 2008, **19**, 1669-1679.
48. A. S. Lipton, R. W. Heck, G. R. Staeheli, M. Valiev, W. A. De Jong and P. D. Ellis, *Journal of the American Chemical Society*, 2008, **130**, 6224-6230.
49. A. SuTrisno, L. Liu, J. Xu and Y. Huang, *Physical Chemistry Chemical Physics*, 2011, **13**, 16606-16617.

50. S. Sham and G. Wu, *Canadian Journal of Chemistry-Revue Canadienne De Chimie*, 1999, **77**, 1782-1787.

51. U. Hoppe, R. Kranold, D. Stachel, A. Barz and A. C. Hannon, *Zeitschrift Fur Naturforschung Section a-a Journal of Physical Sciences*, 2000, **55**, 369-380.

52. U. Hoppe, G. Walter, R. Kranold and D. Stachel, *Zeitschrift Fur Naturforschung Section a-a Journal of Physical Sciences*, 1998, **53**, 93-104.

53. U. Hoppe, G. Walter, R. Kranold, D. Stachel and A. Barz, *Journal of Non-Crystalline Solids*, 1998, **224**, 153-162.

54. R. M. Moss, E. A. Abou Neel, D. M. Pickup, H. L. Twyman, R. A. Martin, M. D. Henson, E. R. Barney, A. C. Hannon, J. C. Knowles and R. J. Newport, *Journal of Non-Crystalline Solids*, 2010, **356**, 1319-1324.

55. U. Hoppe, G. Walter, R. Kranold and D. Stachel, *Journal of Non-Crystalline Solids*, 2000, **263**, 29-47.

56. U. Hoppe, R. Kranold, A. Barz, D. Stachel, J. Neuefeind and D. A. Keen, *Journal of Non-Crystalline Solids*, 2001, **293**, 158-168.

57. R. C. Weast, *CRC Handbook of Chemistry and Physics*, CRC Press, Cleveland, Ohio, 1978.

58. T. Jermoumi, S. Hassan and M. Hafid, *Vibrational Spectroscopy*, 2003, **32**, 207-213.

59. D. Massiot, F. Fayon, M. Capron, I. King, S. Le Calve, B. Alonso, J. O. Durand, B. Bujoli, Z. H. Gan and G. Hoatson, *Magnetic Resonance in Chemistry*, 2002, **40**, 70-76.

60. D. L. Bryce, *Dalton Transactions*, 2010, **39**, 8593-8602.

61. F. Angeli, M. Gaillard, P. Jollivet and T. Charpentier, *Chemical Physics Letters*, 2007, **440**, 324-328.

62. U. Hoppe, *Journal of Non-Crystalline Solids*, 1996, **195**, 138-147.

63. D. M. Pickup, I. Ahmed, P. Guerry, J. C. Knowles, M. E. Smith and R. J. Newport, *Journal of Physics-Condensed Matter*, 2007, **19**, 415116-415124.

Chapter 4 Metaphosphate to Invert Phosphate Glasses

4.0. Introduction

As reviewed in Chapter 1, the properties of phosphate glasses can be tailored according to the desired end applications. Different glass compositions can be used for various applications e.g. significantly soluble glasses with no precipitate formed in solution are used for the controlled release of beneficial ions[1]. Calcium phosphate glasses are shown to precipitate into apatite on immersion in physiological solution and have potential for bone attachment and differentiation of human osteoblasts[2-6]. Zinc substituted metaphosphate glasses are shown to be suitable for tissue engineering applications[7]. Phosphate glass composites with different biodegradable polymers have been shown to be suitable for application as bone scaffolds[8-12]. In contrast, highly soluble phosphate glasses are also reported deleterious for cells[2, 13]. Glass degradation rate, corresponding ion release and pH are the factors which determine the cytocompatibility of the glass[14], whereas glass composition and reaction medium are the factors which determine the mechanism and rate of degradation of phosphate glasses[15, 16]. Based on the general method of silicate based bioactive glass dissolution proposed by Hench[17], Gao *et al.*[15] described phosphate glass dissolution as follows (Fig. 4.1).

(1) Ion exchange of Na^+ cations with H^+ or H_3O^+

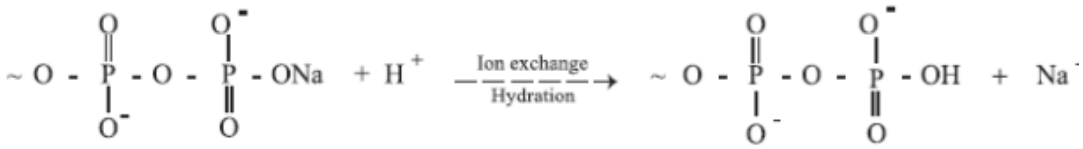

(2) Breakage of P – O – P bond.

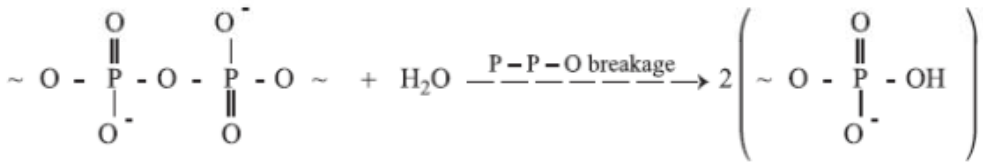

Fig. 4. 1. Mechanism of phosphate glass dissolution as described by Gao *et al.*[15]

According to Bunker *et al.*[18] ion exchange of Na^+ ions with H^+ is the dominating process in glass dissolution and which is a uniform process, with the composition of products in solution the same as in the bulk glass. Conversely Liu *et al.*[19] proposed that network breakage is the principal process in glass dissolution, whereas Na–H ion exchange initiates the network breakage process.

In this chapter the structure of zinc containing metaphosphate to invert phosphate glasses in the system $10Na_2O:(20 + x/2)ZnO:(20 + x/2)CaO:(50 - x)\ P_2O_5$. ($x$ = 0, 5, 10, 15, 20) have been studied through FTIR spectroscopy, ^{31}P single pulse and double quantum (DQ) MAS-NMR spectroscopy, solid state ^{67}Zn static and ^{43}Ca static and MAS-NMR spectroscopy and X–ray and neutron diffraction methods. Glass structure has been related to its dissolution behavior in different media. Since the coordination environment of the divalent cation is another important factor which determines the dissolution of phosphate glasses and zinc shows an anomalous behaviour in phosphate glasses, the Ca:Zn ratio is kept constant throughout the series and the mol% of Na_2O is also constant in these glass compositions.

The structure of phosphate glasses has been studied extensively using various techniques such as FTIR spectroscopy, Raman spectroscopy, NMR spectroscopy, XPS and X–ray and neutron diffraction as reviewed in Chapter 1. It has been shown that incorporation of metal oxide into phosphate glasses shortens the chain length and changes the properties of the glasses according to the amount and type of modifier cations.

Ahmed *et al.*[20] studied the copmositions in the system $Na_2O:CaO:P_2O_5$ with 45 mol%, 50 mol% and 55 mol% P_2O_5 content, with varying amounts of calcium and sodium in each series. They studied the structure, dissolution and pH and observed a decrease in the solubility of glasses with increasing calcium content and decreasing phosphate content. A steady increase in pH with time was attributed to the release of Na^+ and Ca^{2+} cations in solution. In another study by Pickup *et al.*[21] the structure of metaphosphate glass in the above system with varying calcium and sodium content was studied using neutron diffraction and ^{31}P NMR spectroscopy and related to the dissolution behaviour of the glasses. It was explained that substitution of Na^+ with Ca^{2+}

results in an increase in covalency of the M – NBO bond due to the increase in field strength of the cation. Similar work was carried out by Knowles *et al*.[22], where they studied the effect of addition of zinc in sodium calcium metaphosphate glasses on structure and biocompatibility. No significant structural change was observed with the substitution of calcium by zinc, apart from an increase in local disorder of phosphate Q^2 species. Glass compositions with ZnO content 10 mol% or above were shown to be cytotoxic to MG60 cells. This cytotoxicity was attributed to the increased release of Zn^{2+} and increase in pH. More recently, Raluca *et al.*[6] studied the structure and in vitro dissolution of calcium zinc phosphate glasses in the system $ZnO:CaO:P_2O_5$. They observed that higher amounts of zinc increased the aqueous stability of glasses and reduced apatite formation in solution on immersion of the glasses in simulated body fluid (SBF).

To our knowledge no work has been done so far on structure and solubility correlation with changing phosphate content in zinc containing phosphate glasses.

4.1 Experimental

4.1.1 Glass Synthesis

Glass samples of general composition $10Na_2O:(20 + x/2)ZnO:(20 + x/2)CaO:(50 - x)P_2O_5$ (x = 0,5,10,15,20) were prepared by melt quench methods as described in Chapter 2. Table 1 summaries the glass compositions studied.

Table 4. 1 Summary of compositions studied in the system $10Na_2O:(20 + x/2)ZnO:(20 + x/2)CaO: (50 - x)P_2O_5$

x	P_2O_5	Na_2O	ZnO	CaO
0	50.0	10.0	20.0	20.0
5	45.0	10.0	22.5	22.5
10	40.0	10.0	25.0	25.0
15	35.0	10.0	27.5	27.5
20	30.0	10.0	30.0	30.0

4.1.2 Characterisation

Glasses were characterised by DSC, XRD, FTIR, ^{23}Na, ^{31}P, ^{43}Ca and ^{67}Zn NMR and neutron diffraction techniques as described in Chapter 2.

4.1.3 Degradation Studies

The degradation behavior of prepared glass compositions in tris(hydroxymethyl)aminomethane /HCl buffer (tris) and deionised water was studied according to the procedure described in Chapter 2.

4.2 Results and Discussion

4.2.1 X–ray Diffraction

The X-ray diffraction patterns for the synthesised glasses are shown in Fig. 4.2 and reveal that all glasses were amorphous with no evidence of crystallisation. This contrasts to the situation in the ternary system NaO:CaO:P_2O_5[14], where crystallisation readily occurred in compositions containing 33% P_2O_5 or less. The present results appear to confirm the ability of zinc oxide to aid glass formation in these systems. The scattering maximum appears to shift to higher 2θ values (lower d values) with increasing *x*-value. This is consistent with a densification of the glass system with increasing *x*.

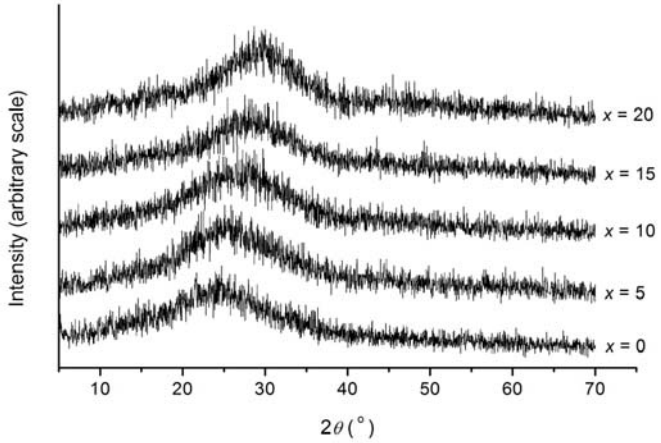

Fig. 4. 2. X–ray diffraction patterns for glasses of composition $10Na_2O$:(20 + x/2)ZnO:(20 + x/2)CaO:(50 – x) P_2O_5.

4.2.2 Density

Fig. 4.3 shows density of the glass compositions studied. It shows a linear increase with the decrease in phosphate content. It increases from 2.79 to 3.23 g cm^{-3} from glass composition x = 0 to x = 20. This suggests that glass structure becomes more compact and packed with increasing metal oxide content. The density values are consistent with the known density ranges for phosphate glasses[22].

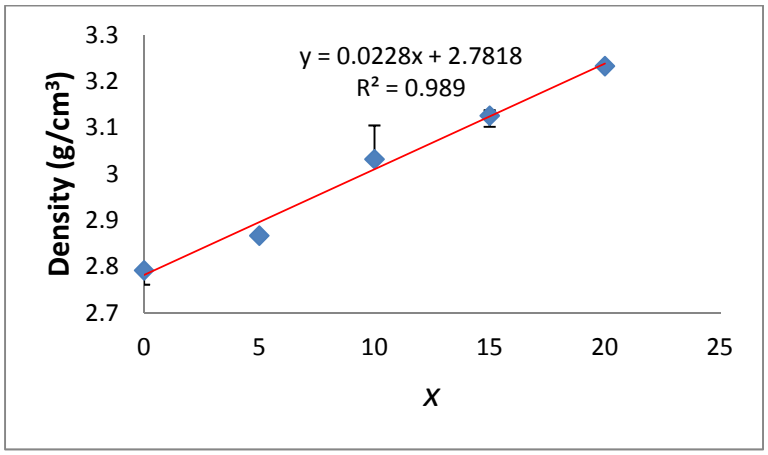

Fig. 4. 3. Density plotted as a function of value of x for the studied glass compositions. (error bars = ± SD)

4.2.3 Thermal Analysis

The compositional variation of glass transition temperature (T_g), crystallisation temperature (T_c) and glass forming window ($T_c - T_g$) are presented in Fig. 4.4. T_g increases linearly with increasing *x*-value, indicating a strengthening of the network with increasing cation: phosphate ratio. This is consistent with observations in sodium and magnesium containing binary phosphate systems where T_g was also seen to increase with decreasing P_2O_5 content[14, 23]. However, it is different to the trend observed by Walter *et al.*[24] in binary zinc polyphosphate glasses with nominal ZnO content between 50 to 75 mol%, where a minimum in T_g was observed at 60 mol% ZnO[24]. The glass stability to crystallisation as measured by $T_c - T_g$ shows a workable range in excess of 100°C for all studied compositions.

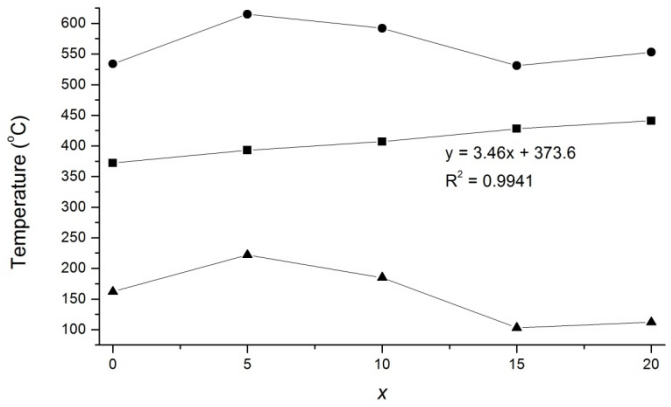

Fig. 4. 4. Compositional variation of T_c (circles), T_g (squares) and $T_c - T_g$ (triangles) for glass compositions in the system $10Na_2O:(20 + x/2)ZnO:(20 + x/2)CaO:(50 - x)P_2O_5$. The linear equation is for T_g.

4.2.4 FTIR Spectroscopy

The IR spectra for the synthesised glasses are displayed in Fig. 4.5 and confirm the depolymerisation of the phosphate network with increasing cation: phosphate ratio. The prominent band at about 1250 cm^{-1}, in the $x = 0$ composition is attributed to asymmetric stretching of the P=O bond in Q^2 species[6, 25-27]. This band is seen to loose

intensity with increasing *x*-value and at *x* = 20 is absent. Another strong band at about 900 cm^{-1}, attributed to the P–O–P asymmetric stretch, shifts toward higher wave number values. The bands at around 750 cm^{-1} and 780 cm^{-1} are characteristic of the P–O–P symmetric stretch and P–O–M stretch, respectively[28]. The latter band is seen to become sharper and more prominent in the spectra of higher *x*-value compositions, consistent with the higher proportion of P–O–M linkages. A small band at 1020 cm^{-1} appears in the spectrum of the *x* = 20 composition, which corresponds to the stretching vibration of the Q^0 PO_4^{3-} unit[29, 30]. A weak band observed at 1080 cm^{-1} is related to the asymmetric stretching vibration of $(PO_3)^{2-}$ species[31].

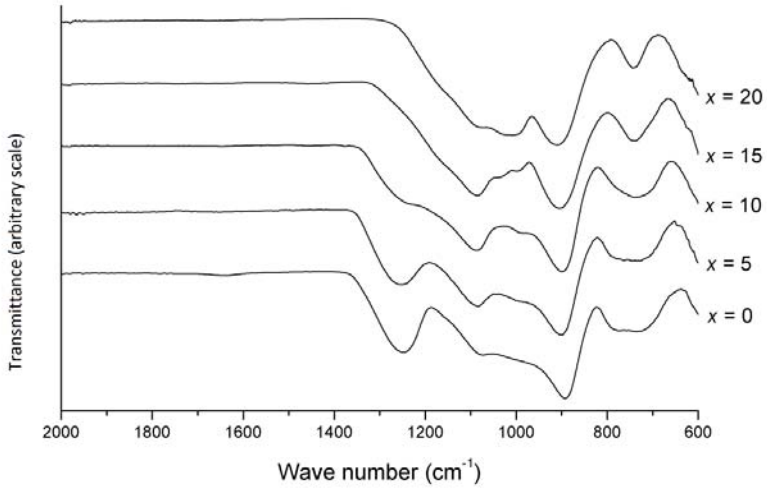

Fig. 4. 5. FTIR spectra for the studied glass compositions.

4.2.5 NMR

4.2.5.1 ^{31}P MAS-NMR

The ^{31}P MAS-NMR spectra for the studied glass compositions, recorded at two spinning speeds, 21 kHz and 12 kHz, are shown in Fig. 4.6 and 4.7 respectively. ^{31}P MAS-NMR spectra show the depolymerisation of the network and formation of shorter chains with the addition of metal oxide and is consistent with previous studies[32-36]. The

spectral parameters presented in Table 4.2 are derived from fitting the data collected at 12 kHz, since fast spinning averages out chemical shift anisotropy (CSA) and reduces the intensity of side bands. Resonances with chemical shifts around -25 ppm and a chemical shift anisotropy, Δδ, of *ca*. -150 ppm were assigned to Q^2 phosphate species [32, 33, 36-39], while those at around -8 ppm with Δδ values around 130 ppm were assigned to Q^1 species[37, 40]. The third type of resonance at around 5 ppm was assigned to Q^0 species[41]. The NMR results are consistent with depolymerisation of the glass with increasing cation: phosphate ratio. The observation of a small amount of Q^0 phosphate as well as Q^1 and Q^2 species in the spectrum for the x = 15 composition suggests a small degree of disproportionation, consistent with Van Wazer's reorganization theory[42]. Isotropic chemical shift (δ) for both Q^2 and Q^1 species (Fig. 4.8) shifts toward less negative values with increasing value of x, which is an indication of a decrease in chain length.

Fig. 4.9 shows $\%Q^n$ intensities calculated from ^{31}P MAS-NMR spectra (12 kHz data) compared with theoretical values based on composition. The observed relative intensities of the phosphate species differ from those calculated assuming ZnO acting in an entirely network modifying role (Table 4.3). For all compositions above x = 0, the observed amount of the more condensed species is greater than that expected for ZnO acting exclusively as a network modifier. This suggests that a proportion of the ZnO in each case must act as a network former. Only the x = 0 sample deviates from this in having a small amount of the less condensed species above that expected for a pure metaphosphate. This deviation from the predicted speciation is often seen in metaphosphate systems and is associated with a small degree of surface hydrolysis, which generates a small fraction of Q^1.

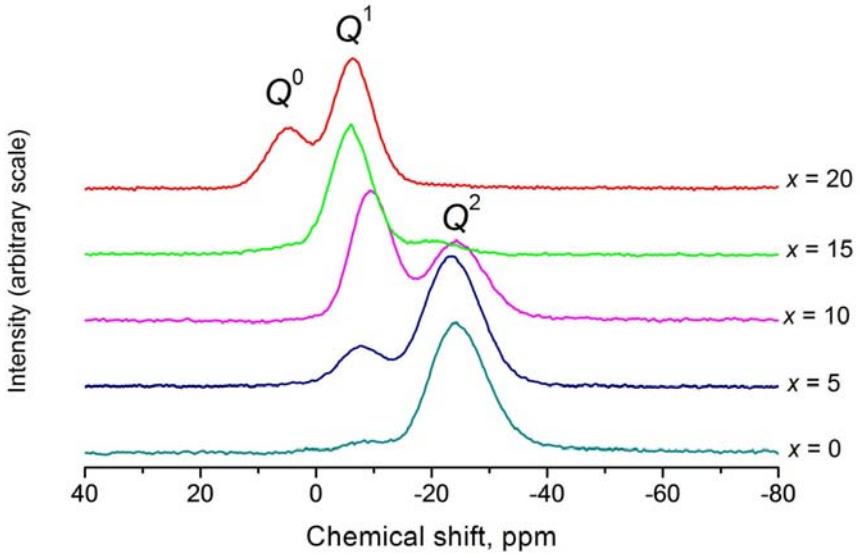

Fig. 4. 6. ^{31}P MAS-NMR spectra of glasses of composition $10Na_2O$:(20 + x/2)ZnO:(20 + x/2)CaO:(50 – x) P_2O_5 measured at 21 kHz spinning speed.

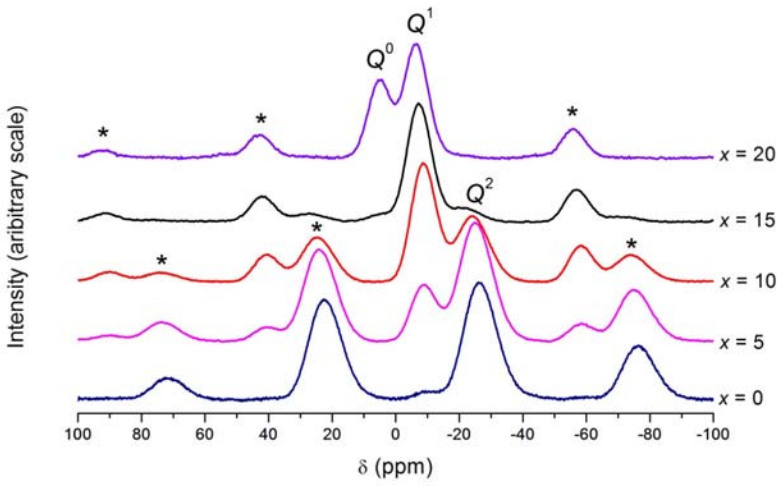

Fig. 4. 7. ^{31}P MAS-NMR spectra of glasses of composition $10Na_2O$:(20 + x/2)ZnO:(20 + x/2)CaO:(50 – x) P_2O_5 meaured at 12 kHz spinning speed. * marks spinning side bands.

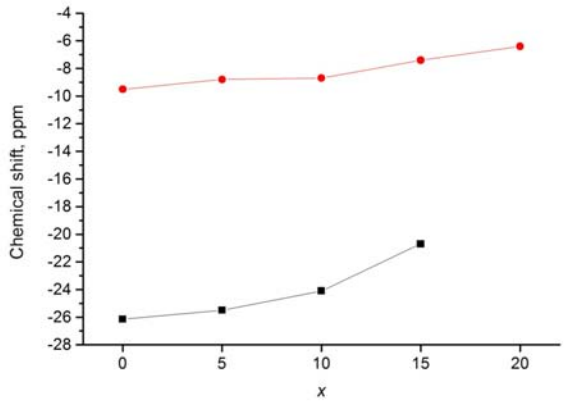

Fig. 4. 8. Change in isotropic chemical shift of Q^n species with the value of *x*, for the studied glass compsitions. Q^2 (squares) Q^1 (circles). Lines are guides for eyes only.

Table 4. 2 ^{31}P MAS-NMR parameters derived from the fitting of spectra acquired at 12 kHz (Fig. 4.7), for glasses in the system $10Na_2O:(20 + x/2)ZnO:(20 + x/2)CaO:(50 – x) P_2O_5$. (Rel. Int. corresponds to % relative intensity)

x	Q^n	δ_{iso} (ppm)	δ_{11} (ppm)	δ_{22} (ppm)	δ_{33} (ppm)	$\Delta\delta$ (ppm)	η	Rel. Int. (%)
0	Q^1	-9.52(12)	80.0	-31.3	-77.2	134.3	0.51	3.2
	Q^2	-26.15(1)	66.9	9.2	-154.6	-192.7	0.45	75.8
	Q^2	-34.45(1)	91.3	16.4	-178.3	-215.7	0.75	21.0
5	Q^1	-8.85(1)	78.1	-27.8	-76.8	130.4	0.59	17.9
	Q^2	-25.54(1)	69.0	4.7	-150.2	-187.1	0.52	82.1
10	Q^1	-8.78(1)	76.2	-26.7	-75.8	127.5	0.58	46.6
	Q^2	-24.14(1)	66.2	3.2	-141.8	-176.5	0.54	53.4
15	Q^0	5.17(1)	38.9	38.9	-62.3	-101.2	0.00	3.2
	Q^1	-7.39(1)	74.6	-22.8	-74.0	123.0	0.63	76.8
	Q^2	-20.75(8)	75.2	-18.3	-119.1	-147.5	0.95	20.0
20	Q^0	5.20(2)	22.7	22.7	-29.7	-52.4	0.00	26.2
	Q^1	-6.36(4)	73.8	-20.7	-72.0	120.3	0.64	73.8

Table 4. 3 Phosphate speciation (%) observed from ^{31}P MAS-NMR spectra and given in Table 4.2 for glasses of composition 10Na_2O: (20 + *x*/2)ZnO:(20 + *x*/2)CaO:(50 – *x*) P_2O_5 compared to theoretical values calculated assuming ZnO acting as a purely network modifier.

x	Q^0_{obs}	Q^1_{obs}	Q^2_{obs}	Q^0_{theor}	Q^1_{theor}	Q^2_{theor}
0	0.0	3.2	96.8	0.0	0.0	100.0
5	0.0	18.3	81.7	0.0	22.2	77.8
10	0.0	44.9	55.1	0.0	50.0	50.0
15	6.8	77.6	15.6	0.0	85.7	14.3
20	26.9	73.1	0.0	33.3	66.7	0.0

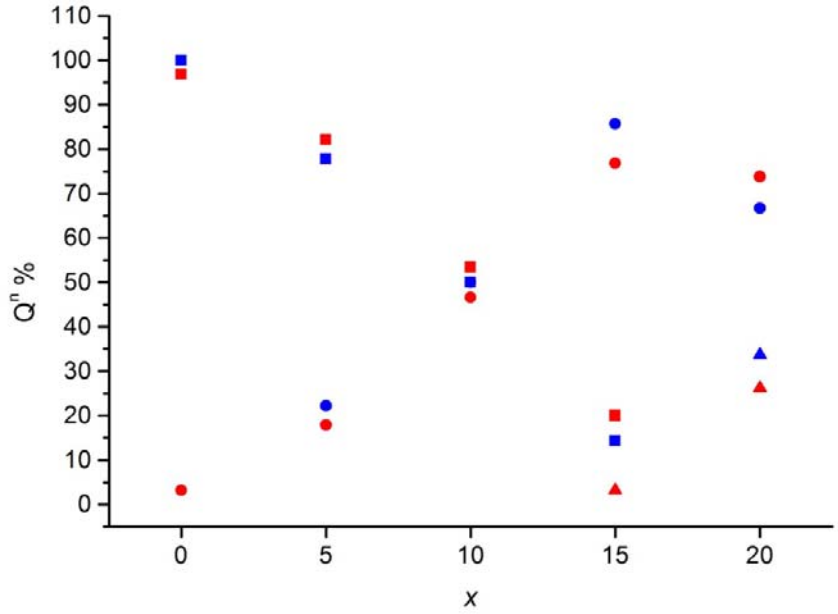

Fig. 4. 9. Showing Q^n (%) observed (red) and theoretical (blue) plotted as a function of *x* value. (Squares Q^2, Circles Q^1 and Triangles Q^0) The numbers for each fraction are also given in Tabel 4.3.

Fig 4.10 shows two-dimensional ^{31}P – ^{31}P DQ–SQ MAS-NMR spectra acquired with the Post C7 pulse sequence for the studied glass compositions. DQ–SQ spectra are shown as contour plots. The lowest contour levels are set to 10% and levels increase in steps of 10%. Double quantum experiments under MAS allow for determination of through space connectivities between two neighboring Q^n species

which have dipole-dipole coupling[43-47]. Peaks on the diagonal (auto-correlated peaks) represent DQ coherences between adjacent units of the same kind, whereas off-diagonal pairs (cross-correlated) correspond to DQ coherences between chemically different groups[47, 48]. For the *x* = 0 glass composition, a single broad auto-correlated peak at *ca*. -25 ppm on the f_2 dimension is attributed to Q^2–Q'^2 correlation, according to the convention used by Witter *et al.*[45]. This correlation is consistent with metaphosphate chains or rings[49]. In addition to the diagonal peak at -25 ppm on the f_2 dimension for Q^2–Q'^2 correlation, the spectra of the *x* = 5 and *x* = 10 glass compositions show another diagonal peak at about -10 ppm. This latter diagonal correlation corresponds to Q^1–Q'^1 connectivities. Off-diagonal peak pairs observed in *x* = 5 and 10 at *ca*. -9 ppm and -27 ppm along the f_2 axis located at about -35 ppm on the DQ axis, f_1, are associated with Q^1–Q^2 correlations [50]. Q^2 coherence in this correlation shows a split which could correspond to different Q^2 sites in this glass composition. A resonance located downfield could correspond to Q^2 species connected to only Q^1 as in a trimer, whereas an upfield (more negative) shoulder could correspod to Q^2 species connected to a long chain. The spectrum for the *x* = 15 composition shows an auto correlated Q^1 peak at about -6 ppm on f_2 and chain ending Q^1 units correlated with Q^2 units at around -8 ppm and -20 ppm on f_2 and -28 ppm on the f_1 axis. For the *x* = 20 glass composition, diagonal correlations for Q^1–Q^1 and Q^0–Q^0 coherences are observed at about -7 ppm and 5 ppm, respectively, on the f_2 axis. Q^1–Q^1 being the dominant coherence is an indication of $P_2O_7^{4-}$ as the prevailing species in this glass composition. In addition, an off diagonal correlation pair between Q^0–Q^1 is also observed at about 7 ppm and -8 ppm along the f_2 axis. Similar coherence has been observed by Wiench *et al*.[51] in zinc polyphosphate glasses. ^{31}P chemical shift is sensitive to structural changes up to the fourth coordination sphere of phosphorus[45, 49, 52]. The presence of Q^0–Q^0 and Q^0–Q^1 correlations could be an indication of insertion of ZnO_4 tetrahedra into the phosphate chain.

Quantitative measurement of the different species detected in the DQ experiment is not straight forward. However, this can be achieved by quantitative fitting of 1D MAS-NMR spectra with chemical shift and line width for each of the correlating species, determined from the DQ MAS spectra[45]. Table 4.4 presents the

proportion of each of the correlated species calculated by fitting the 21 kHz 1D spectra. The *x* = 5 glass composition has 69.3% infinitely long chains or rings, whereas the rest of the 15% Q^2 species are terminated by 15% Q^1 units. Q^1-Q^1 correlation in *x* = 5 is not quantified due to very small proportion and hence low resolution of internal projection slices for this peak. The *x* = 10 glass composition, with 40 mol% P_2O_5, has a distribution of three different kinds of species. Quantitative analysis of the DQ spectrum shows the presence of 26.8% pyrophosphate units and 22.1% Q^2–Q^2 long chain or rings, whereas 25% of Q^2 species are terminated by 25% Q^1 species. The *x* = 15 glass composition has 56.9% dimer units with 21.7% to 21.4% chain ending Q^1 and Q^2, respectively. This is within ±10% of results studied in the literature[50].

Slight differences in the peak intensities are found between the DQ projections and 1D experiment (Fig.4.7). Relatively smaller Q^1 intensity from DQ projections could be due to the fact that Q^1 is directly connected to only one PO_4 unit and a lower intensity of Q^0 compared to Q^1 in glass composition x = 20 is due to the fact that Q^0 species are coupled through weak intermolecular dipolar interactions[48]. Overall Q^n intensities calculated from fitting of 1D data acquired at 21 kHz spinning speed, with slices from DQ are within 5% of intensities calculated from central resonance and side band fitting of the 12 kHz data.

(a)

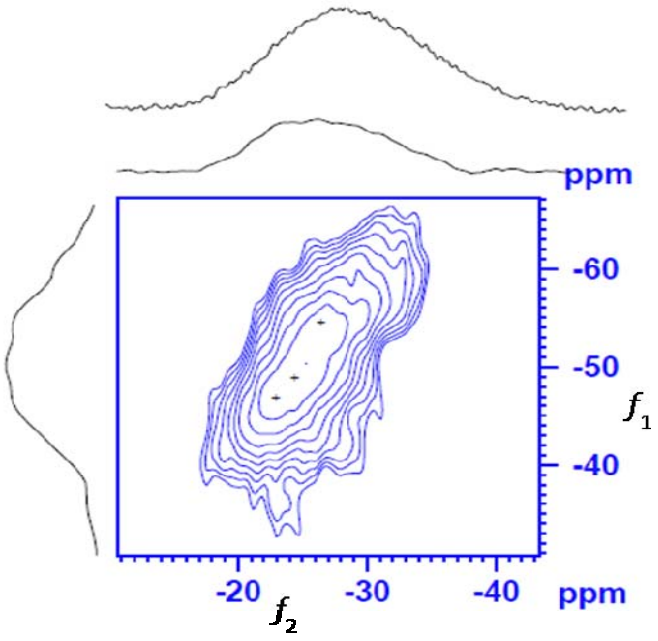

(b)

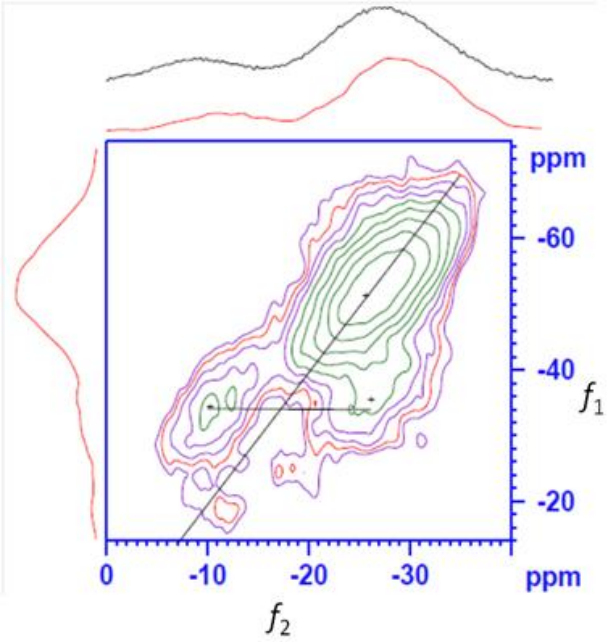
ppm
-60
-40
-20
f_1
0
-10
-20
-30
ppm
f_2

(c)

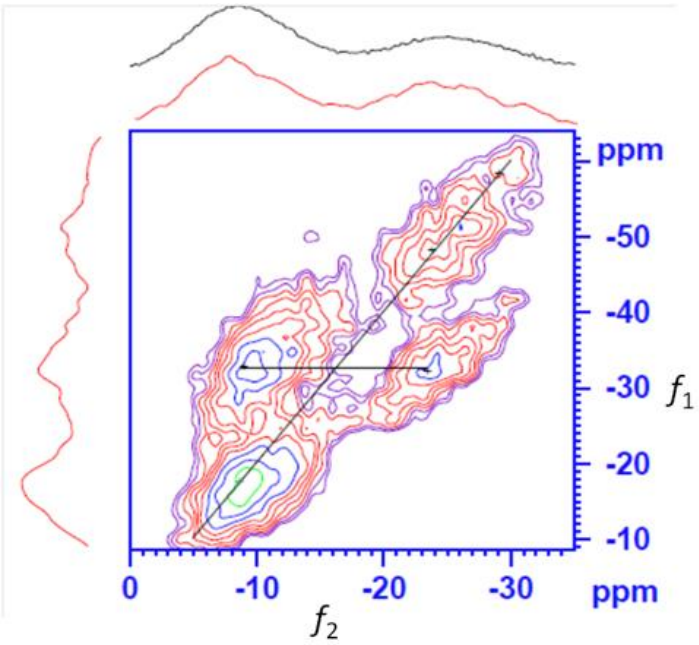
ppm
-50
-40
-30
-20
-10
f_1
0
-10
-20
-30
ppm
f_2

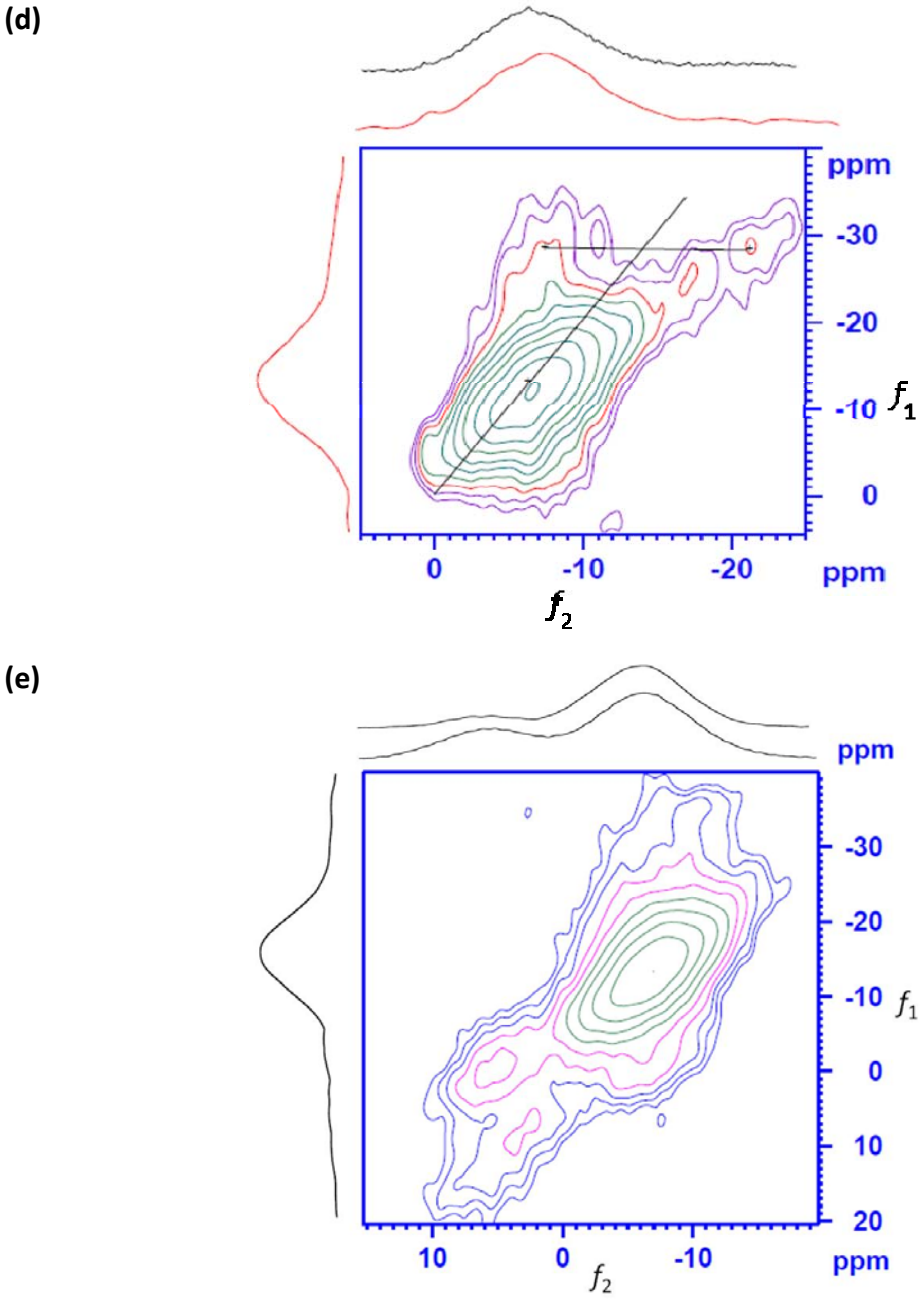

Fig. 4. 10. Two-dimensional ^{31}P-^{31}P DQ MAS-NMR spectra of studied glass compositions $10Na_2O$:(20+x/2)ZnO:(20+x/2)CaO:(50-x) P_2O_5. (a) x = 0, (b) x = 5, (c) x = 10, (d) x = 15. (e) x = 20. Different colors of contours are to highlight contour levels and intensity of each peak. Projections on top are sum of all horizontal internal projections and 1D spectrum (bottom to top), whereas projection on right is the sum of all vertical internal projections. All projections and contours are positive.

Table 4. 4 %Intensity of different species in studied glass compositions. (Fwhm corresponds to Full width at half maximum whereas %I is % intensity)

x	$Q^{1,1}$			$Q^{1,2}$		
	δ	Fwhm	%I	δ	Fwhm	%I
5				-9.7	8.0	15.6
10	-9.9	8.0	26.8	-10.5	10.5	25.4
15	-7.3	9.0	56.9	-8.0	9.0	21.7
	$Q^{2,1}$			$Q^{2,2}$		
	δ	Fwhm	%I	δ	Fwhm	%I
5	-24.7	10.5	15.0	-26.8	11.0	69.3
10	-24.3	10.0	25.7	-28.0	10.0	22.1
15	-21.5	12.5	21.4			

4.2.4.2 ^{67}Zn NMR

Fited ^{67}Zn NMR spectra are presented in Fig. 4.11. Each spectrum was fitted to two peaks with isotropic chemical shifts between 260 ppm to 400 ppm and 50-80 ppm, assumed to correspond to tetrahedral and octahedral zinc coordinations respectively. Since no work has been done on ^{67}Zn NMR spectroscopy of zinc containing condensed phosphates either crystalline or amorphous, assignment has been made according to the ^{67}Zn NMR literature for zinc oxide, zinc halide and zinc coordinations in inorganic complexes[53-58]. Fitted parameters are presented in Table 4.5. Changes in chemical shift are not very significant, compared to the line broadness. The quadrupolar coupling constant, C_Q, decreases with the increase in degree of depolymerisation. Low values for η_Q indicate that zinc coordination in this system is relatively symmetric. Relative intensities between the types of zinc coordination show that octahedral zinc is present only in a very small proportion.

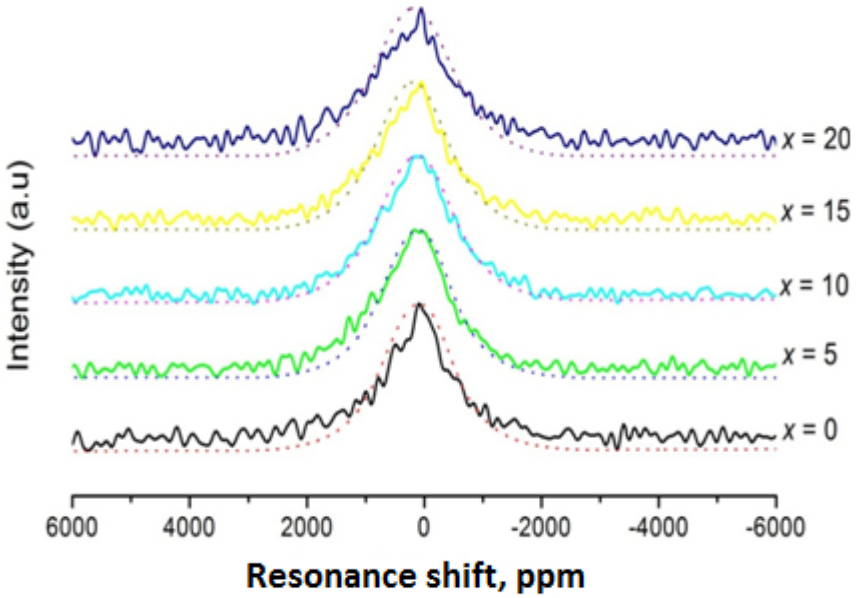

Fig. 4. 11. ^{67}Zn static NMR spectra for the studied glass compositions acquired at 56.3MHz NMR with dotted lines showing fits.

Table 4. 5 ^{67}Zn NMR parameters derived from fitting of spectra shown in Fig. 4.11

composition	δ (ppm)	C_Q(MHz)	η_Q	% intensity
0	260	9.1	0.5	87
	74	5.0	0.8	13
5	365	8.7	0.1	94
	96	4.2	0.3	6
10	278	8.8	0.0	97
	121	3.7	0.1	3
15	375	8.4	0.0	95
	131	3.9	0.0	5
20	407	9.4	0.3	96
	57	4.8	0.4	4

4.2.4.3 ^{43}Ca NMR

^{43}Ca static and MAS-NMR spectra for glass composition x = 15 are presented in Fig.4.12. The line shape of the static spectrum is a typical of a disordered structure. Line width decreases when the sample is spun at 5 kHz, as compared to the static spectrum. Spinning of the sample at 5 kHz does not resolve the line into more than one resonance. This indicates the presence of chemical shift distribution and hence chemical shift anisotropy.

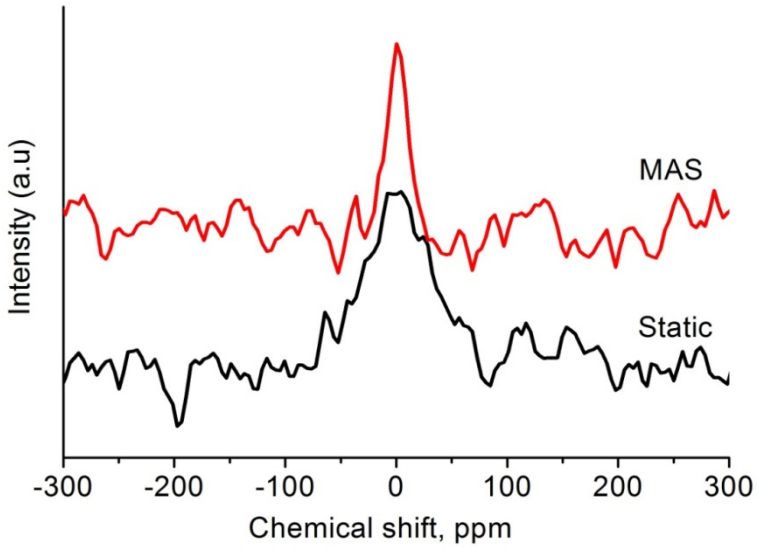

Fig. 4. 12. ^{43}Ca static and MAS-NMR spectra of the glass composition x = 15 acquired at 60.6 MHz.

4.2.5 Neutron Diffraction

The total neutron interference functions $i(Q)$ for the studied glass compositions are shown in Fig. 4.13(a) with detail of the patterns at low Q presented in Fig. 4.13 (b). The patterns of all glass samples shows an intermediate range order (IRO) peak between 1.1 Å $^{-1}$ and 2.0 Å $^{-1}$. For the metaphosphate glass composition x = 0, the main peak is at 1.6 Å $^{-1}$, with a shoulder at 1.1 Å $^{-1}$. With decreasing phosphate

content and increasing cation content, the IRO peak decreases in intensity and shifts towards higher Q value. This implies a transition from a more open structure to a more compact structure, with increasing cation content due to the increase in P – O_T – M linkages. This is consistent with the previous neutron diffraction studies of binary phosphate systems[59] and the observed compositional variation of density (Fig. 4.3).

(a)

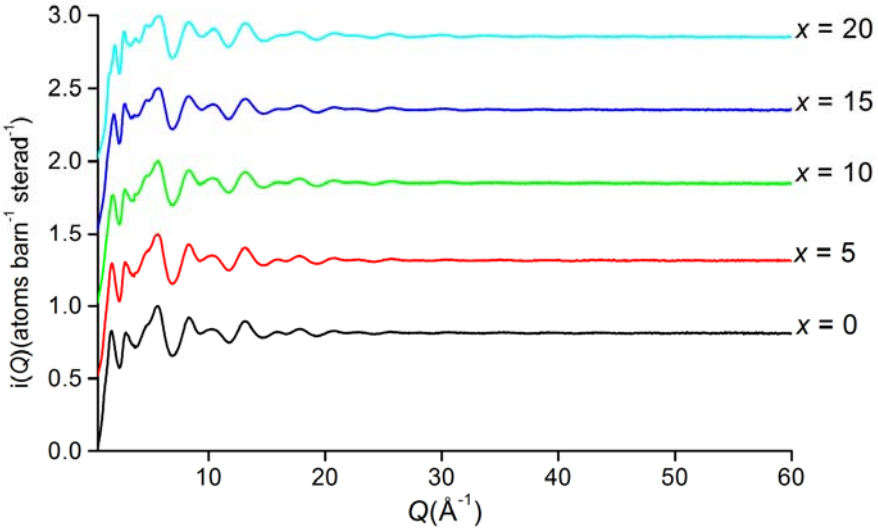

(b)

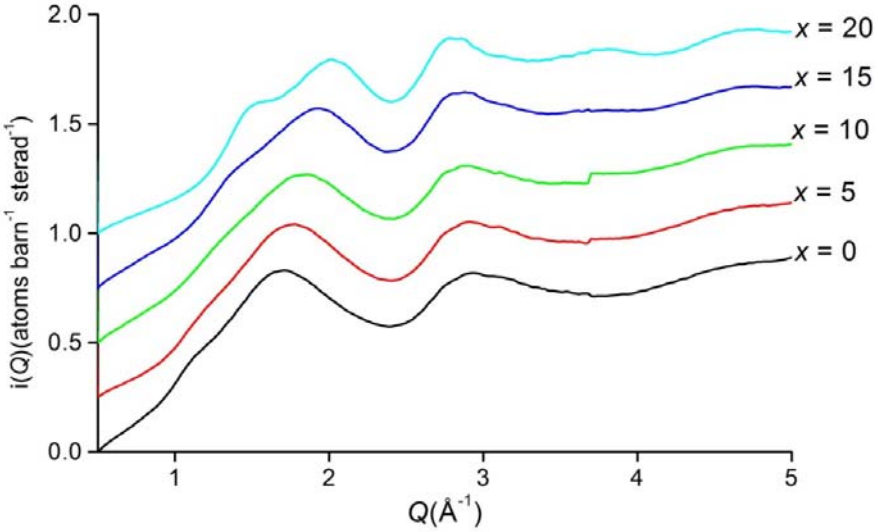

Fig. 4. 13. (a) Q space interference functions $i(Q)$ for the studied glass compositions. (b) Q space interference functions $i(Q)$ in the low-Q region.

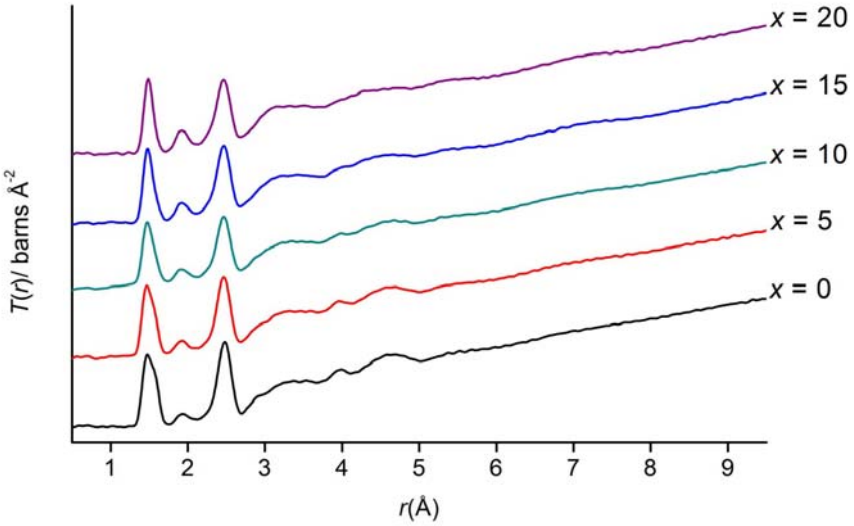

Fig. 4. 14. Total correlation functions *T*(*r*) for the studied glass compositions.

The total correlation functions *T(r),* obtained by Fourier transformation of the structure function *S*(*Q*), using the Lorch modification function and a Q range (Q_{max}) of 0 – 60 $Å^{-1}$ for the studied glasses are presented in Fig. 4.14. Gaussian fits to the *T*(*r*) functions in the range of the P–O bond length are presented in Fig. 4.15. Two P–O peaks are are resolved. The peak at about 1.5 Å corresponds to P–NBO whereas the one at about 1.6 Å is attributed to P–BO. P–O distances are plotted as a function of composition in Fig 4.16. The P–NBO bond length increases with increasing cation content. The P–O bond length is seen to decrease from x = 0 to *x* = 5, but then shows a small but steady increase above *x* = 5. The P–BO peak becomes broader and decreases in intensity, indicative of the change in level of condensation with increasing metal oxide content[60]. The ratio between P–NBO and P–BO depends on composition according to the relationship proposed by Van Wazer (3 – *y*)/(1 + *y*) where *y* is the molar ratio between network modifier content and P_2O_5. The fitted total correlation function for each of the studied glass compositions is presented in Fig. 4.17, whereas bond length and coordination numbers extracted from fits are presented in Table 4.6.

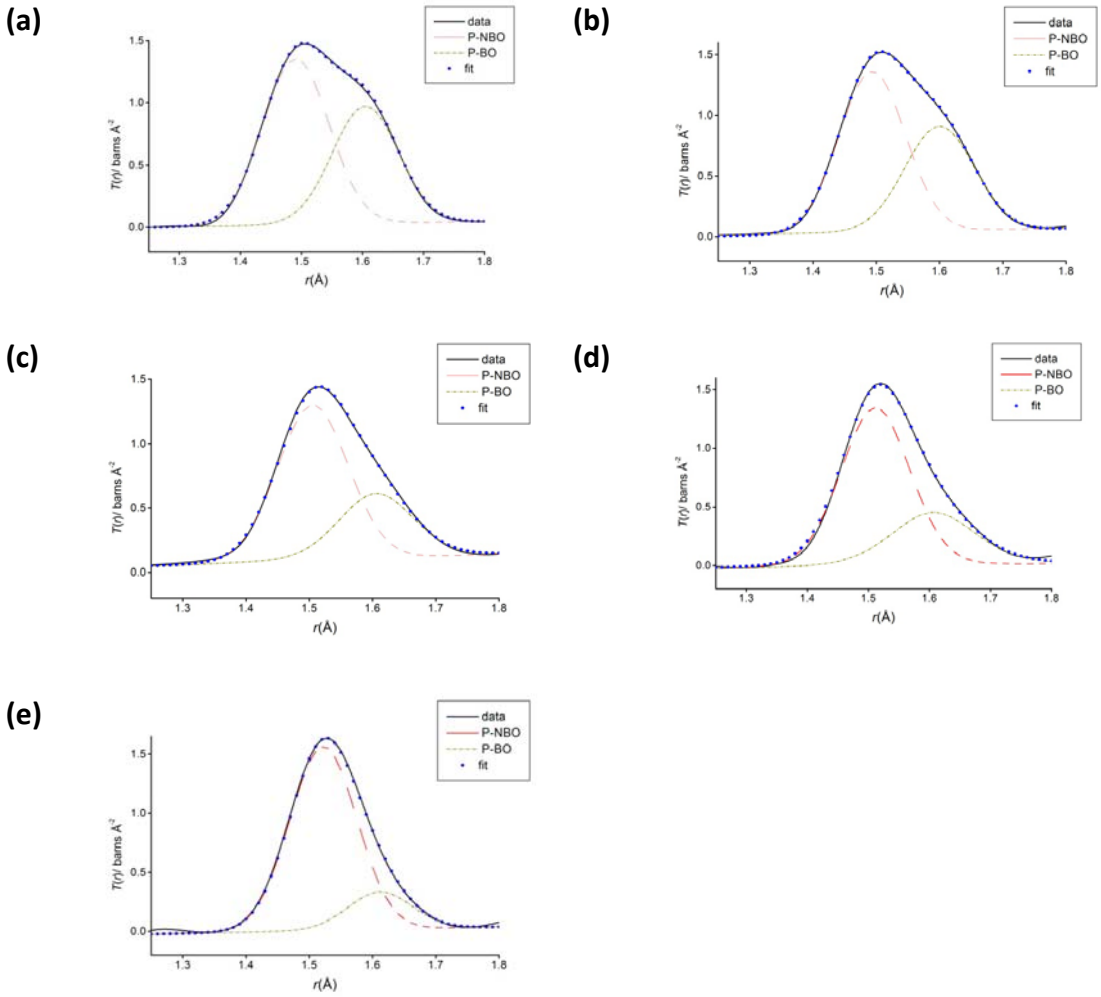

Fig. 4. 15. Fit to correlation function *T*(*r*) in the range of P- O 1st coordination correlation for the studied glass compositions . (a) *x* = 0, (b) *x* = 5, (c) *x* = 10, (d) *x* = 15 (e) *x* = 20.

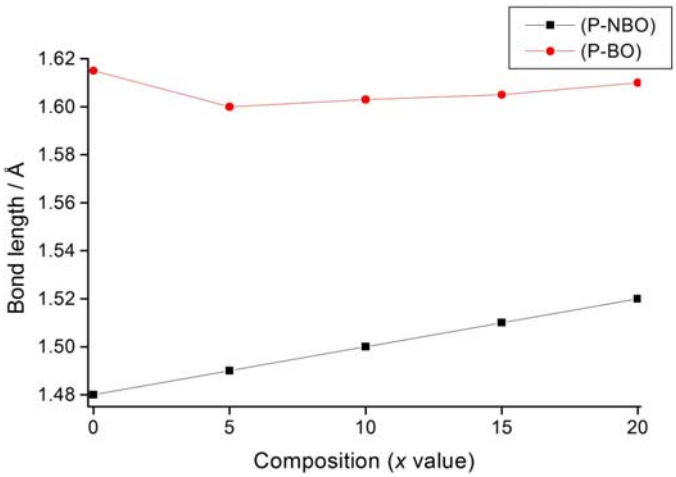

Fig. 4. 16. Variation in P–NBO and P–BO bond length as a function of composition in studied glasses. (esd ±0.02)

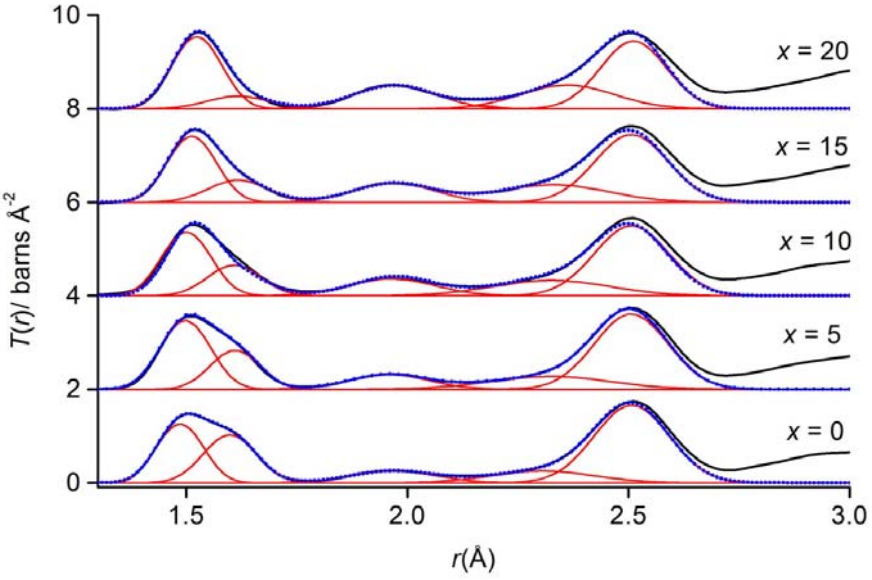

Fig. 4. 17. Fitted total correlation functions *T* (*r*) for the studied glass compositions. Observed total (solid black lines), fitted total (blue line) and individual pair (red lines) correlations are shown.

Table 4. 6 Structural parameters, r_{i-j} interatomic distance (Å) and N_{i-j} coordination number derived from fitted $T(r)$ for studied glass compositions.

X	0		5		10		15		20	
	r_{i-j}	N_{i-j}	r_{i-j}	N_{i-j}	r_{i-j}	N_{i-j}	r_{i-j}	N_{i-j}	r_{i-j}	N_{i-j}
P–NBO	1.48(1)	1.88(4)	1.49(1)	2.49(10)	1.50(1)	2.4(3)	1.51(1)	2.71(1)	1.52(1)	3.30(1)
P–BO	1.60(1)	1.88(4)	1.61(1)	1.50(10)	1.61(1)	1.35(1)	1.61(1)	1.17(1)	1.61(1)	0.75(1)
P–O (Total)		3.76		3.99		3.75		4.05		4.05
Zn–O(1)	1.97(1)	4.15(6)	1.96(1)	4.0(6)	1.96(1)	4.32(6)	1.97(1)	3.9(4)	1.97(1)	4.14(5)
Zn–O(2)									2.16(7)	0.23(6)
Ca–O /Na–O (ave)	2.31(1)	7.00(10)	2.32(1)	7.5(11)	2.33(1)	7.52(10)	2.33(1)	6.84(10)	2.36(1)	6.84(12)
O–O	2.51(1)	4.01(1)	2.51(1)	3.87(1)	2.51(1)	3.70(1)	2.51(1)	3.57(1)	2.51(1)	3.28(1)

The O–O coordination number for each glass composition is calculated according to the formula $24/(5 + y)$[61] where y is the mole ratio between mole fraction of modifier and phosphate content. The $T(r)$ peak at about 2.5 Å was fitted according to the calculated coordination number and subtracted from rest of the $T(r)$. The fit of the residual area between 1.75 Å to 2.75 Å gives the coordination numbers for Zn–O and Ca–O/Na–O. A prominent peak at ~1.9 Å is observed in the $T(r)$ of all compositions which increases in intensity with increase in x value, due to increase in ZnO content. The Zn–O coordination calculated from the fitted peak is between 3.9 to 4.3. This could be considered as an average coordination of four within experimental errors and fitting uncertainty as observed in other studies of zinc phosphate glasses[24, 62, 63], or it could be an indication of a small proportion of zinc in coordination higher than four in agreement with the results obtained through X–ray and neutron diffraction of zinc phosphate systems by Suzuya *et al.*[59]. In addition an average coordination of 7 is observed for the unresolved Na–O /Ca–O peak area calculated assuming (r_{i-j}) equal to Ca–O. This also gives an indication that sodium and calcium environment also remains unchanged in all glass compositions.

4.2.6 Solubility

Changes in pH values in tris buffer and deionised water are plotted as a function of time in Fig 4.18. In tris buffer, all samples showed a minimum in pH after two weeks immersion. Only the x = 0 glass composition showed significant deviation away from pH = 7 to lower pH, reaching a minimum value of pH = 6.5. In deionised water, the x = 0 and x = 5 compositions show an initial decrease in pH over the first week, remaining fairly constant to week 3 and showing a small increase in week 4. For the less condensed samples x = 10 to x = 20 an initial increase in pH is observed after immersion for a week. For the x = 10 composition, the pH is seen to show a small but steady decrease for the duration of the experiment. In contrast the pH for composition x = 15 is steady until week 3, showing a small decrease between weeks 3 and 4, while that for the x = 20 samples remains almost constant after week 1. The observed changes in pH reflect the corresponding weight loss profiles shown in Fig. 4.19, which

reveal decreasing weight loss with a decreasing level of condensation, indicating that the *x* = 0 composition is the most soluble, while the *x* = 15 and *x* = 20 compositions show very limited solubility.

Ion release profiles in tris buffer, and deionised water for constituent ions in all studied glass compositions, as a function of time are shown in Fig. 4.20 as a 3D plot. It is clearly evident from the figures that the amount of ions released upon dissolution of discs in both tris buffer and distilled water decreased with decreasing phosphate content and increasing cation content, reflecting the weight loss and pH measurements. In the most soluble glass composition, *x* = 0, for each ion studied, a large initial release of ions is observed at week 1 which decreases to a near steady state after week 1 up to week 3 and then increases again in week 4 in deionised water. For this glass composition tris buffer, a steady decrease is observed for all ions except Zn^{2+}, which remains steady for three weeks and then decreases in week 4. Glass compositions *x* =5 and 10 show nearly the same behavior in both studied media, with an initial increase and then decrease in weight loss of all constituent ions. For the two highly cross linked compositions there is very little ion release in deionised water and tris buffer, however, a higher weight loss and ion release are observed for glass compositions *x* = 10, 15 and 20 in tris buffer than in deionised water, while the reverse is true for glass compositions *x* = 0 and 5.

(a)

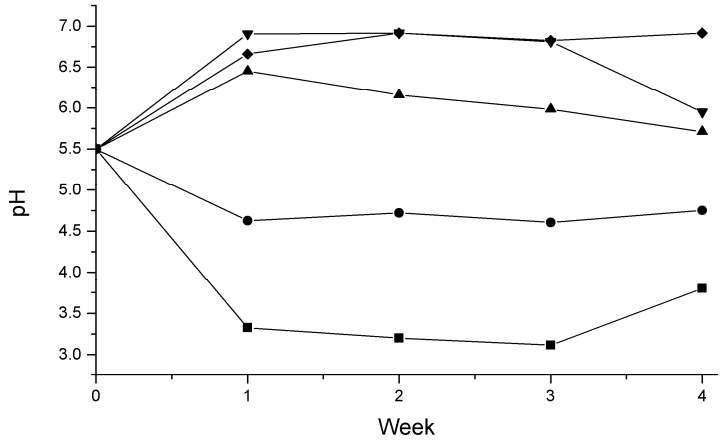

(b)

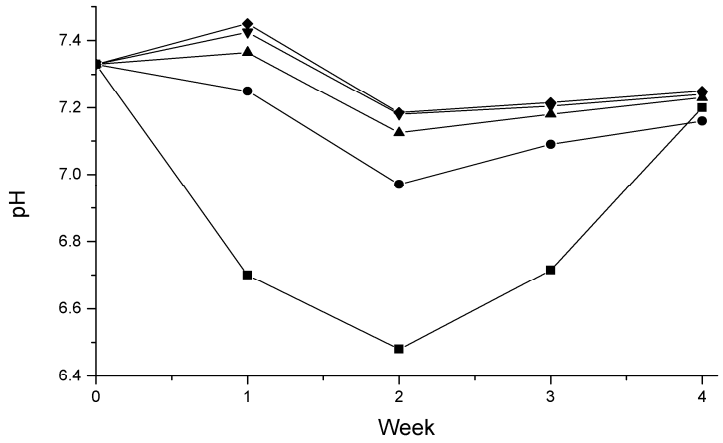

Fig. 4. 18. Change in pH of solution as a function of time for the studied glass compositions on immersion in (a) deionised water (b) tris buffer, showing *x* = 0 (squares), *x* = 5 (circles), *x* = 10 (up triangles), *x* = 15 (down triangles) and *x* = 20 (diamonds) compositions.

(a)

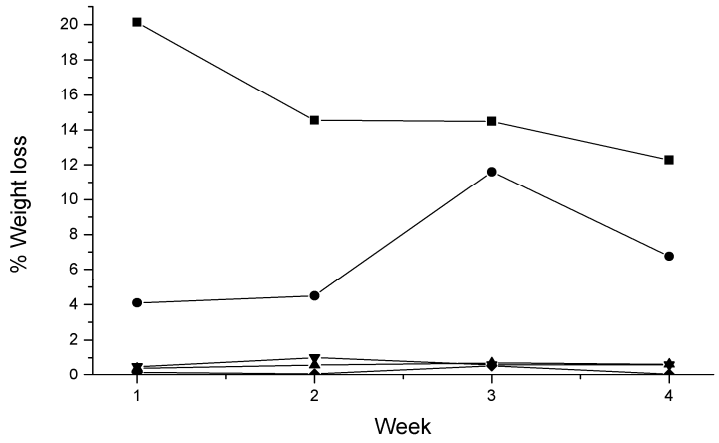

(b)

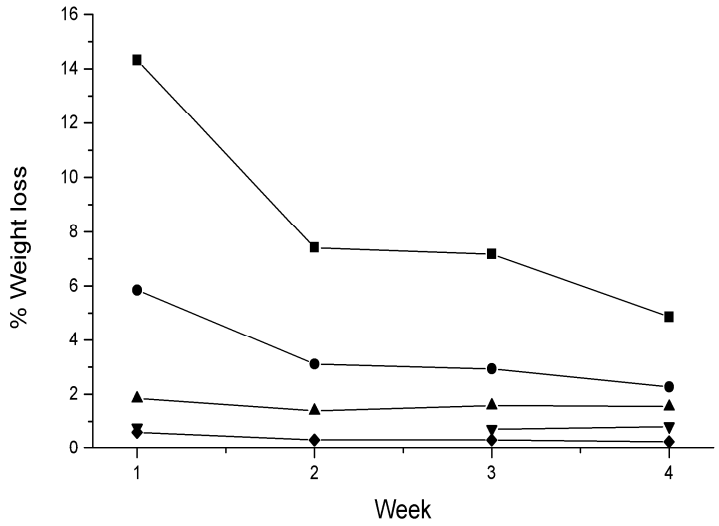

Fig. 4. 19. Percentage weight loss of glass discs as a function of time in (a) de-ionized water and (b) tris buffer, showing *x* = 0 (squares), *x* = 5 (circles), *x* = 10 (up triangles), *x* = 15 (down triangles) and *x* = 20 (diamonds) compositions.

(a)

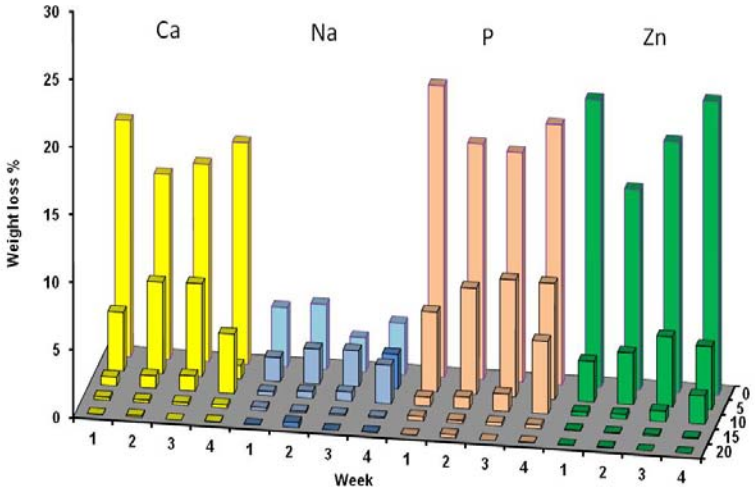

(b)

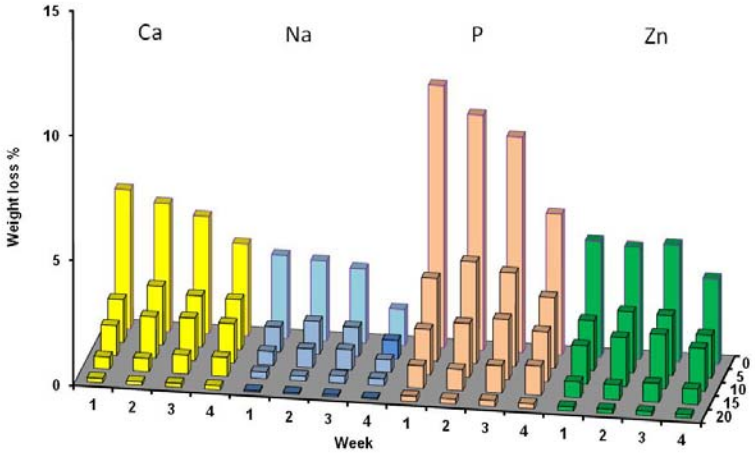

Fig. 4. 20. Ion release profiles for studied glasses immersed in (a) deionised water and (b) tris buffer. Values are presented as percentage weight loss normalized to the ion content in the parent glass.

X–ray diffraction patterns for the glass discs after immersion in tris buffer for 28 days are presented in Fig. 4.21. Sharp Bragg peaks are only observed in the glass composition x = 0, whereas the absence of any sharp peaks in the patterns of the other compositions confirms their amorphous nature. The diffraction peaks in the pattern for the x = 0 composition are consistent with a mixture of hydrated zinc and calcium pyrophosphates ($Zn_2P_2O_7.3H_2O$, JCPDS 11-22; $Ca_3H_2(P_2O_7)_2.4H_2O$, JCPDS 44-810).

^{31}P MAS-NMR spectra of glass discs after immersion in tris buffer for 28 days are presented in Fig.4.22. The presence of sharp peaks at about -4 ppm and -7 ppm for glass composition x = 0 indicates the precipitation of crystalline pyrophosphates with some residual amorphous metaphosphate phase. Glass composition x = 5 shows a significant increase in Q^1 species and decrease in Q^2 species, with the formation of an additional amorphous Q^0 species. For all other glass compositions, no major change is observed compared to spectra of the glasses before immersion.

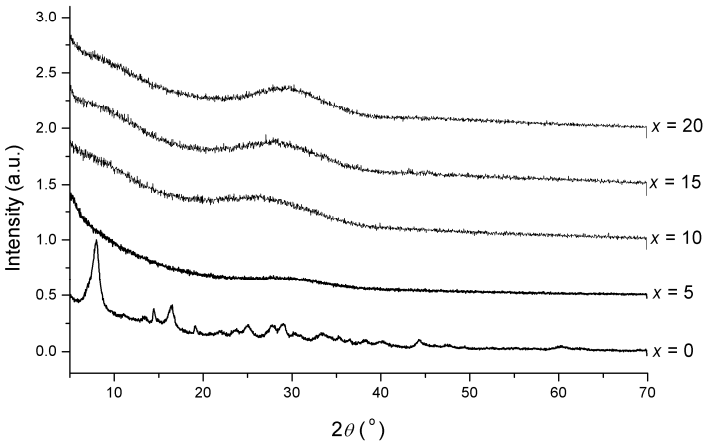

Fig. 4. 21. X–ray diffraction patterns of glasses after immersion in tris buffer for 28 days.

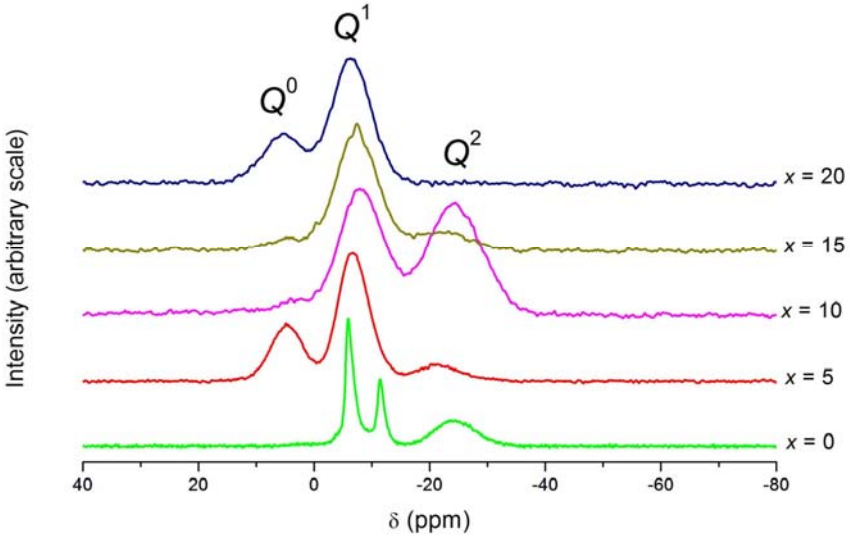

Fig. 4. 22. ^{31}P MAS-NMR spectra of glasses of composition 10Na_2O:(20 + *x*/2)ZnO:(20 + *x*/2)CaO:(50 - *x*) P_2O_5 after immersion for 28 days in tris buffer. Spectra were measured at 21 kHz spinning speed.

As expected based on the glass transition temperatures and density measurements glass dissolution rate and weight loss decreases with decreasing phosphate content in both media. Ion release profiles shows that the glass composition with *x* = 0 is the most soluble glass, whereas the *x* = 20 composition, with the lowest phosphate content is the most stable glass composition on immersion. 1D and DQ ^{31}P MAS-NMR spectrospy show that the structure of the *x* = 0 glass consists of infinitely long –P–O–P– chains or rings, with a low degree of P=O...M cross-linkages, which is also evidenced by the equal quantities of NBO and BO calculated from the neutron diffraction data . P–O–P linkages are more susceptible to hydrolysis in aqueous media producing protonated phosphate $(HPO_4)^{2-}$ units. It also explains the decrease in pH. The *x* = 5 glass composition releases half of the amount of phosphate ions in tris buffer compared to the *x* = 0 composition, which again agrees with the structure determined from MAS-NMR spectroscopy which showed long chains, short chains and a very small proportion of dimer units. So there are more P=O...M linkages and the structure is more compact than that for *x* = 0. A higher release of ions in deionised water than in tris buffer for glass compositions *x* =0 and 5 can be explained by Gao's hydration theory. The P-O-P linkage is very sensitive to attack by protons (H^+), decreasing the pH of a solution which could increase dissolution. In addition breakage of P-O-P linkages releases additional H^+ ions which results in a further decrease of pH in deionised water. However tris buffer tends to buffer released H^+ ions and hence slows down the dissolution rate. The *x* = 10 glass releases phosphate ions about 2.4 times less than the *x* = 5 glass due to the higher degree of depolymerisation, more compact structure and presence of a large proportion of dimer units (pyrophosphate). The *x* = 15 glass composition releases phosphate ions only 1.5 times less than the *x* = 10 composition. This can be attributed to the presence of highly soluble Q^2 units as a result of disproportion reactions. The *x* = 20 glass compositionis the least soluble, as it consists of Q^0 and Q^1 units. It has the most compact structure with the highest degree of cross-linking. These results suggest that the decrease in solubility is solely related to P–O–P chain length for at least glass compositions close to metaphosphate, since there is no difference in the coordination environment of sodium or calcium throughout the range of composition as obsereved from neutron

diffraction data. The ion release profiles show the amount of zinc relased is higher than calcium in glasses with low or no Q^2 species (i.e. *x* = 10, 15 and 20), when immersed in distilled water, however, in tris buffer the concentration of calcium released is always higher than zinc for all glass compositions. This indicates that zinc is released more in lower pH which is in agreement with other studies carried out in our group on zinc containing silicate glasses. A higher degradation of compositions *x* = 10, 15 and 20 in tris buffer than in deionised water is opposite to the behavior of compositions with *x* =0 and 5 and can be explained by Bunker's[18] theory. The degradation of phosphate glass occurs by the uptake of both H^+ and OH^- ions from the solution and for pH below 6.5 uptake of H^+ is higher, whereas at pH values above 6.5, OH^- is consumed more. For these glass compositions where P–O–P bonds are not available for H^+ uptake in deionised water there is more uptake of OH^- ions in tris buffer and hence more dissolution. This is also indicated from an increase in pH of the solution for these compositions. In addition the degradation of small cyclic rings of trimetaphosphate and tetrametaphosphate decreases in lower pH medium and increases in basic solution, which explains the lower dissolution of *x* = 10 and 15, due to a presence of such short chains as observed from ^{31}P DQ NMR experiments.

Fig. 4.23 shows changes in pH of deionised water after immersion of glass discs with fixed P_2O_5 content (50 and 45 mol%) and varying amounts of Na_2O and CaO, as observed by Ahmed *et al.*[20]. The change in pH of solutions with the 50 mol% P_2O_5 glass compositions is consistent with our observations. However, for glass compositions with 45 mol% lower pH is observed in our studies. This might be attributed to the presence of zinc in our glass compositions.

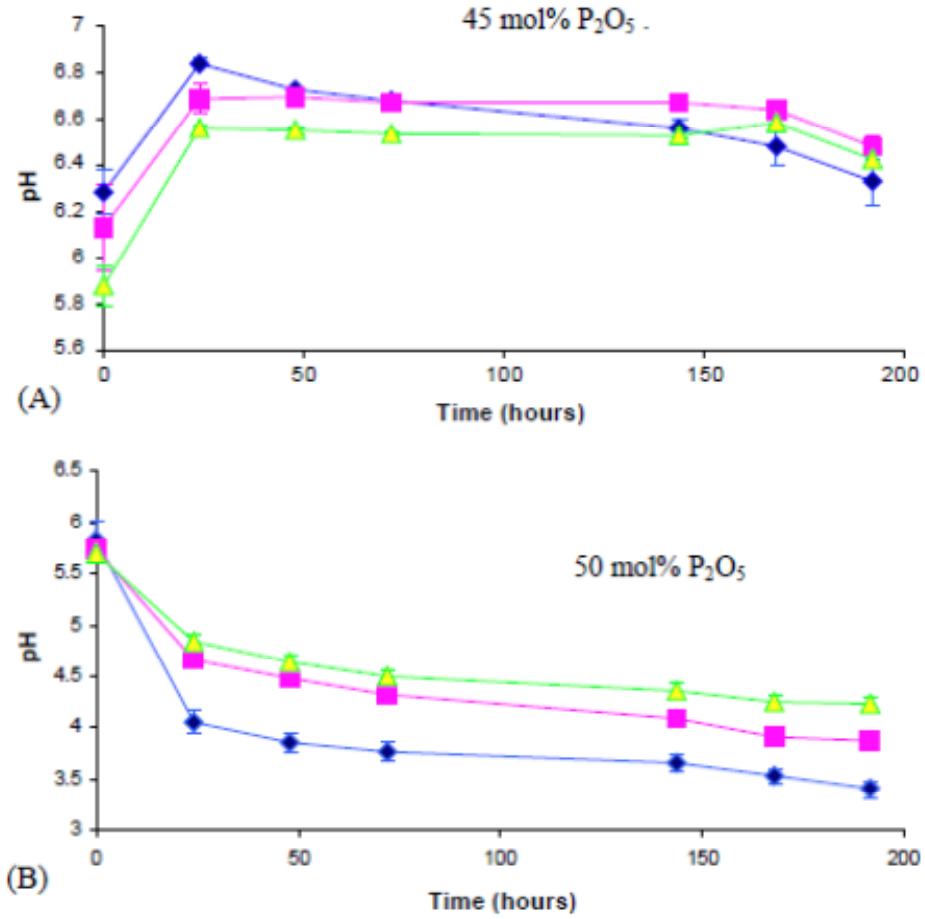

Fig. 4. 23. Change in pH of deionised water after immersion of glass discs. (A) $45P_2O_5$: (40-x)CaO: (15+x)Na_2O x = 0, 5 and 10 (B) $50P_2O_5$: (40-*x*)CaO: (10+*x*)Na_2O x = 0, 5 and 10. (Adapted from ref[20]).

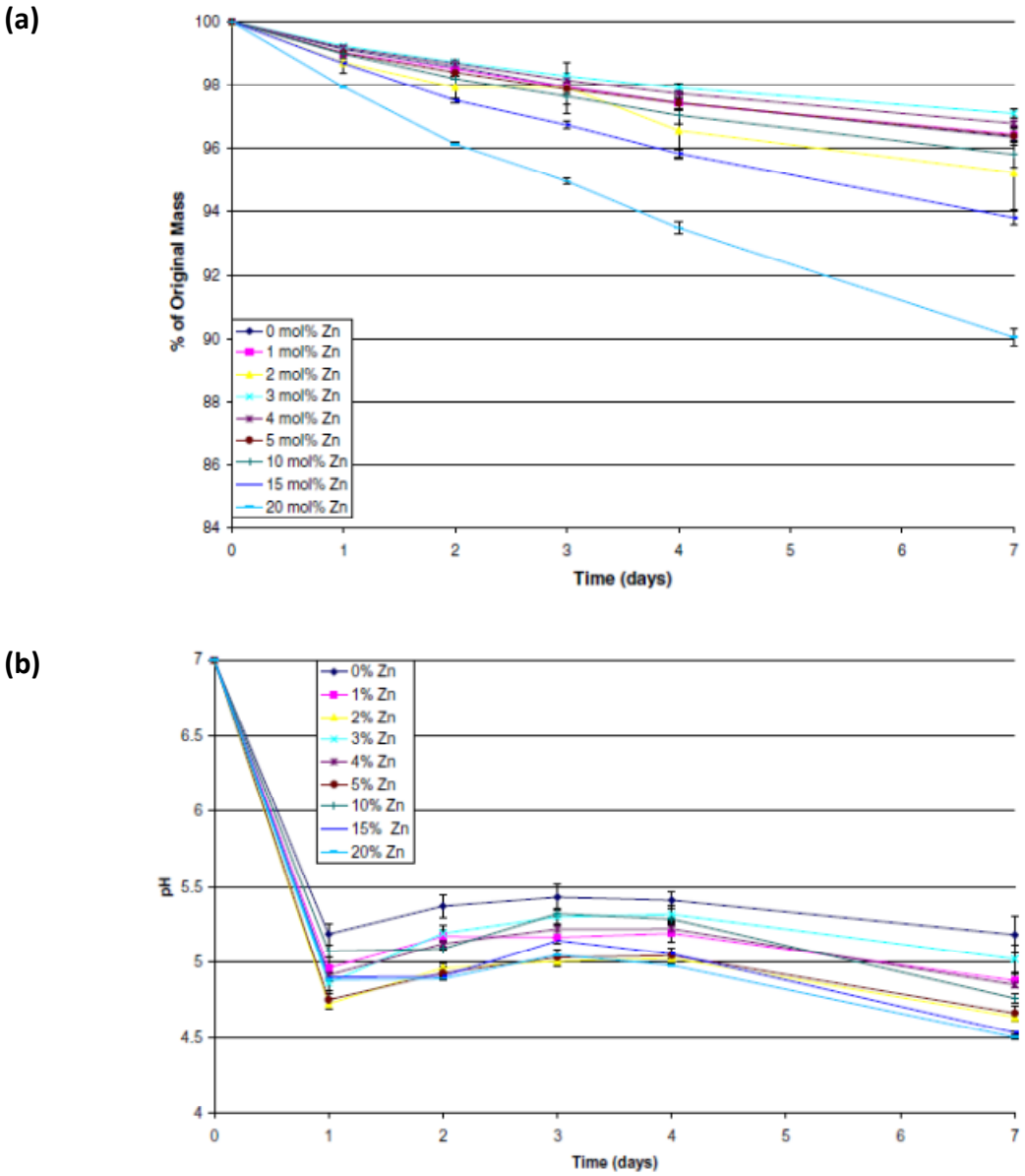

Fig. 4. 24. (a) Dissolution of glass discs at 37 °C (b) Effect of glass discs on the pH of water at 37 °C. for glass compositions $50P_2O_5$: (40-*x*)CaO: *x*ZnO: $10Na_2O$ where *x* = 0, 1, 2, 3, 4, 5, 10, 15 and 20 mol%. (adapted from ref[7]).

Salih *et al.* have also observed a higher degradation rate and lowest pH for glass compositions with the highest amount of zinc, in zinc substituted sodium calcium metaphosphate glasses (Fig. 4.24). This decrease in pH of solution with after immersion of zinc containing phosphate glasses compared to calcium phosphate can

be explained in terms of the structural role of zinc as observed by ^{31}P DQ NMR and neutron diffraction in our studies. Neutron diffraction data and ^{67}Zn NMR show that zinc adopts mainly a tetrahedral coordination and observation of Q^0–Q^0 and Q^0–Q^1 correlations in the ^{31}P DQ NMR spectrum of the *x* = 20 composition, appears to confirm that ZnO_4 tetrahedra occur between PO_4 tetrahedra in glass compositions with higher zinc content. Hence degradation of Zn–O–P linkages occurs in a similar way to the degradation of P–O–P, thus increasing the degradation rate and decreasing pH.

4.3 Conclusions

The short and intermediate range structure of different phosphate based glasses within the composition range $10Na_2O:(20+x/2)ZnO:(20+x/2)CaO:(50-x)P_2O_5$ ($0 \leq x \leq 20$) were investigated using different techniques. The structure, solubility and pH of glasses are affected by the cation content. Metaphosphate glass (*x* = 0) is the most soluble glass and shows the greatest decrease in pH in tris buffer, which could have a detrimental effect on surrounding tissue. Due to cross-linking by divalent Ca^{2+} and Zn^{2+}, Invert phosphate glasses have more compact structures, so dissolution in both tris buffer and deionised water of the x = 15 and 20 compositions is slower. On dissolution, the invert compositions maintain pH within the physiological pH range. Glass compositions with *x* = 5 and 10, with intermediate levels of cross-linking are not very soluble and able to maintain the pH within the physiological pH range. They therefore have potential to be used as biomaterials. These studies show that probing ^{31}P–^{31}P correlations via DQ MAS-NMR experiments can be used to predict solubility behavior and pH change in phosphate glasses. These are important considerations when designing a glass for biomedical applications.

4.4 References

1. C. Curless, J. Baclaski and R. Sachdev, *Biotechnology Progress*, 1996, **12**, 728-728.
2. M. Bitar, V. Salih, V. Mudera, J. C. Knowles and M. P. Lewis, *Biomaterials*, 2004, **25**, 2283-2292.
3. L. J. Jha, J. D. Santos and J. C. Knowles, *Journal of Biomedical Materials Research*, 1996, **31**, 481-486.
4. M. Bitar, J. C. Knowles, M. P. Lewis and V. Salih, *Journal of Materials Science-Materials in Medicine*, 2005, **16**, 1131-1136.
5. V. Salih, K. Franks, M. James, G. W. Hastings, J. C. Knowles and I. Olsen, *Journal of Materials Science-Materials in Medicine*, 2000, **11**, 615-620.
6. R. C. Lucacel, O. Ponta and V. Simon, *Journal of Non-Crystalline Solids*, 2012, **358**, 2803-2809.
7. V. Salih, A. Patel and J. C. Knowles, *Biomedical Materials*, 2007, **2**, 11-20.
8. I. Ahmed, A. J. Parsons, G. Palmer, J. C. Knowles, G. S. Walkers and C. D. Rudd, *Acta Biomaterialia*, 2008, **4**, 1307-1314.
9. I. Ahmed, P. S. Cronin, E. A. Abou Neel, A. J. Parsons, J. C. Knowles and C. D. Rudd, *Journal of Biomedical Materials Research Part B-Applied Biomaterials*, 2009, **89B**, 18-27.
10. R. M. Felfel, I. Ahmed, A. J. Parsons and C. D. Rudd, *Journal of the Mechanical Behavior of Biomedical Materials*, 2013, **17**, 76-88.
11. E. A. Abou Neel, I. Ahmed, J. J. Blaker, A. Bismarck, A. R. Boccaccini, M. P. Lewis, S. N. Nazhat and J. C. Knowles, *Acta Biomaterialia*, 2005, **1**, 553-563.
12. D. S. Brauer, C. Ruessel, S. Vogt, J. Weisser and M. Schnabelrauch, *Journal of Biomedical Materials Research Part A*, 2007, **80A**, 410-420.
13. J. E. Gough, P. Christian, C. A. Scotchford, C. D. Rudd and I. A. Jones, *Journal of Biomedical Materials Research*, 2002, **59**, 481-489.
14. M. Uo, M. Mizuno, Y. Kuboki, A. Makishima and F. Watari, *Biomaterials*, 1998, **19**, 2277-2284.
15. H. S. Gao, T. N. Tan and D. H. Wang, *Journal of Controlled Release*, 2004, **96**, 29-36.
16. H. S. Gao, T. N. Tan and D. H. Wang, *Journal of Controlled Release*, 2004, **96**, 21-28.

17. L. L. Hench, *Journal of Non-Crystalline Solids*, 1977, **25**, 343-369.
18. G. W. A. B.C. Bunker, J.A. Wilder, *Journal of Non crystalline solids*, 1984, **64**, 291.
19. Q. X. Liu, X. M. Chen and X. Li, *Journal of Wuhan University of Technology*, 1996, **18**, 26-29.
20. I. Ahmed, M. Lewis, I. Olsen and J. C. Knowles, *Biomaterials*, 2004, **25**, 491-499.
21. D. M. Pickup, I. Ahmed, P. Guerry, J. C. Knowles, M. E. Smith and R. J. Newport, *Journal of Physics-Condensed Matter*, 2007, **19**, 415116-415124.
22. E. A. Abou Neel, L. A. O'Dell, M. E. Smith and J. C. Knowles, *Journal of Materials Science-Materials in Medicine*, 2008, **19**, 1669-1679.
23. G. Walter, J. Vogel, U. Hoppe and P. Hartmann, *Journal of Non-Crystalline Solids*, 2003, **320**, 210-222.
24. G. Walter, U. Hoppe, J. Vogel, G. Carl and P. Hartmann, *Journal of Non-Crystalline Solids*, 2004, **333**, 252-262.
25. G. Le Saout, P. Simon, F. Fayon, A. Blin and Y. Vaills, *Journal of Raman Spectroscopy*, 2002, **33**, 740-746.
26. A. Saranti, I. Koutselas and M. A. Karakassides, *Journal of Non-Crystalline Solids*, 2006, **352**, 390-398.
27. E. Metwalli and R. K. Brow, *Journal of Non-Crystalline Solids*, 2001, **289**, 113-122.
28. D. Boudlich, L. Bih, M. E. Archidi, M. Haddad, A. Yacoubi, A. Nadiri and B. Elouadi, *Journal of the American Ceramic Society*, 2002, **85**, 623-630.
29. P. Subbalakshmi, D. K. Durga, B. A. Kumari and K. Srilatha, Dielectric dispersion and certain other physical properties of ZnO-Ga2O3-P2O5 glass system, Acharya Nagarjuna Univ, Guntur, INDIA, 2009.
30. D. Muresan, M. D. Bularda, C. Popa, L. Baiai and S. Simon, *Romanain Journal of Physics*, 2006, **51**, 231-237.
31. G. Le Saout, P. Simon, F. Fayon, A. Blin and Y. Vaills, *Journal of Raman Spectroscopy*, 2009, **40**, 522-526.
32. R. K. Brow, *Journal of Non-Crystalline Solids*, 2000, **263**, 1-28.
33. R. J. Kirkpatrick and R. K. Brow, *Solid State Nuclear Magnetic Resonance*, 1995, **5**, 9-21.
34. R. K. Brow, E. Metwalli and D. L. Sidebottom, in *Inorganic Optical Materials Ii*, eds. A. J. Marker and E. G. Arthurs, 2000, vol. 4102, pp. 88-94.

35. R. K. Brow, R. J. Kirkpatrick and G. L. Turner, *Journal of Non-Crystalline Solids*, 1990, **116**, 39-45.

36. R. K. Brow, D. R. Tallant, S. T. Myers and C. C. Phifer, *Journal of Non-Crystalline Solids*, 1995, **191**, 45-55.

37. R. K. Brow, C. C. Phifer, G. L. Turner and R. J. Kirkpatrick, *Journal of the American Ceramic Society*, 1991, **74**, 1287-1290.

38. I. Abrahams, K. Franks, G. E. Hawkes, G. Philippou, J. Knowles, P. Bodart and T. Nunes, *Journal of Materials Chemistry*, 1997, **7**, 1573-1580.

39. F. Fayon, D. Massiot, K. Suzuya and D. L. Price, *Journal of Non-Crystalline Solids*, 2001, **283**, 88-94.

40. G. Walter, J. Vogel, U. Hoppe and P. Hartmann, *Journal of Non-Crystalline Solids*, 2001, **296**, 212-223.

41. L. Montagne, G. Palavit and R. Delaval, *Journal of Non-Crystalline Solids*, 1997, **215**, 1-10.

42. J. R. v. Wazer, *Phosphorus and its compounds*, Interscience, New York, 1958.

43. H. Geen, J. Gottwald, R. Graf, I. Schnell, H. W. Spiess and J. J. Titman, *Journal of Magnetic Resonance*, 1997, **125**, 224-227.

44. M. Feike, C. Jager and H. W. Spiess, *Journal of Non-Crystalline Solids*, 1998, **223**, 200-206.

45. R. Witter, P. Hartmann, J. Vogel and C. Jager, *Solid State Nuclear Magnetic Resonance*, 1998, **13**, 189-200.

46. C. Jager, P. Hartmann, G. KunathFandrei, O. Hirsch, P. Rehak, J. Vogel, M. Feike, H. W. Spiess, K. Herzog and B. Thomas, *Berichte Der Bunsen-Gesellschaft-Physical Chemistry Chemical Physics*, 1996, **100**, 1560-1562.

47. M. Feike, R. Graf, I. Schnell, C. Jager and H. W. Spiess, *Journal of the American Chemical Society*, 1996, **118**, 9631-9634.

48. J. W. Wiench, B. Tischendorf, J. U. Otaigbe and M. Pruski, *Journal of Molecular Structure*, 2002, **602**, 145-157.

49. F. Fayon, C. Bessada, J. P. Coutures and D. Massiot, *Inorganic Chemistry*, 1999, **38**, 5212-5218.

50. C. Roiland, F. Fayon, P. Simon and D. Massiot, *Journal of Non-Crystalline Solids*, 2011, **357**, 1636-1646.

51. J. W. Wiench, M. Pruski, B. Tischendorf, J. U. Otaigbe and B. C. Sales, *Journal of Non-Crystalline Solids*, 2000, **263**, 101-110.

52. F. Fayon, C. Roiland, L. Emsley and D. Massiot, *Journal of Magnetic Resonance*, 2006, **179**, 49-57.

53. Y. Zhang, S. Mukherjee and E. Oldfield, *Journal of the American Chemical Society*, 2005, **127**, 2370-2371.

54. Y.-I. Kim, S. Cadars, R. Shayib, T. Proffen, C. S. Feigerle, B. F. Chmelka and R. Seshadri, *Physical Review B*, 2008, **78**, 195205-195217.

55. K. H. Mroue and W. P. Power, *Journal of Physical Chemistry A*, 2010, **114**, 324-335.

56. A. S. Lipton, M. D. Smith, R. D. Adams and P. D. Ellis, *Journal of the American Chemical Society*, 2002, **124**, 410-414.

57. S. Sham and G. Wu, *Canadian Journal of Chemistry-Revue Canadienne De Chimie*, 1999, **77**, 1782-1787.

58. A. Sutrisno, L. Liu, J. Xu and Y. Huang, *Physical Chemistry Chemical Physics*, 2011, **13**, 16606-16617.

59. K. Suzuya, K. Itoh, A. Kajinami and C. K. Loong, *Journal of Non-Crystalline Solids*, 2004, **345**, 80-87.

60. U. Hoppe, R. Kranold, D. Stachel, A. Barz and A. C. Hannon, *Zeitschrift Fur Naturforschung Section a-a Journal of Physical Sciences*, 2000, **55**, 369-380.

61. U. Hoppe, *Journal of Non-Crystalline Solids*, 1996, **195**, 138-147.

62. S. Bruni, F. Cariati, A. Corrias, P. H. Gaskell, A. Lai, A. Musinu and G. Piccaluga, *Journal of Physical Chemistry*, 1995, **99**, 15229-15235.

63. G. Navarra, A. Falqui, G. Piccaluga and G. Pinna, *Physical Chemistry Chemical Physics*, 2002, **4**, 4817-4822.

Chapter 5 Invert Phosphate Glasses

5.0 Introduction

As has been described in previous chapters, the properties of phosphate glasses depend on the phosphate content and the type of modifier cations. Different compositions of phosphate glasses with varying degrees of dissolution in aqueous media are used for various applications[1, 2]. Invert phosphate glasses (i.e. those with a P_2O_5 content ≤ 40 mole%) dissolve slowly in aqueous media as compared to metaphosphate and ultraphosphate glasses. Their processing is difficult due to their high affinity to crystallisation. However, by the addition of different cations, processing has been improved and various compositions have been designed for a number of applications[3, 4]. Kasuga *et al*.[5] have studied titanium containing invert phosphate glasses for bioactive glass coatings of titanium alloys. They observed the formation of apatite like crystals in glasses of composition $60CaO{:}10TiO_2{:}30P_2O_5$, whereas calcium metaphosphate glasses are reported as unable to form apatite in simulated body fluid (SBF)[6]. This difference was attributed to no change in pH, compared to the situation in metaphosphate glasses. In this chapter we discuss the structure of invert phosphate glasses with a constant phosphate content and variable amounts of calcium oxide and zinc oxide. The effect of varying modifier cation content can therefore be studied independently of the phosphate content as the latter is not a variable parameter.

Brow *et al*.[7] studied zinc polyphosphate glasses with zinc oxide content varying from 50 mol% to 71 mol%. They compared the molar volume of glass with the corresponding crystal structure and found the molar volume of the glass was greater than that of the corresponding crystal structure. They related this to the tetrahedral environment in all glass compositions, which leads to a more open network. Hoppe *et al*.[8] also studied the structure of zinc phosphate glasses from metaphosphate to invert phosphate, using neutron and X–ray diffraction techniques including RMC modelling of their data. They suggested the existence of tetrahedral Zn for all compositions from metaphosphate and below and observed that at ZnO contents of 60 mol% and 70 mol%, ZnO_4 tetrahedra break the long phosphate chains resulting in the dominance of

loose PO_4 units. With increasing ZnO content, two or three ZnO_4 tetrahedra share corners with PO_4 units (Fig. 5.1). Boiko et al.[9] studied the structure of sodium and zinc containing pyrophosphate glasses using molecular dynamics. In pure zinc pyrophosphate they found zinc cations irregularly located between chain fragments with an average zinc oxygen co-ordination of 4.3 distributed as three (8%), four (58.7%), five (29.3%) and six fold (4%) coordinated zinc. They concluded the role of zinc oxide in zinc pyrophosphate glasses was entirely modifying. In a glass composition with equimolar amounts of sodium and zinc they found a zinc oxygen co-ordination number of 3.92 with most of the ZnO_4 tetrahedra connected through PO_4 tetrahedra (Fig. 5.2), i.e that zinc in this glass composition acted entirely as a network former.

(a)

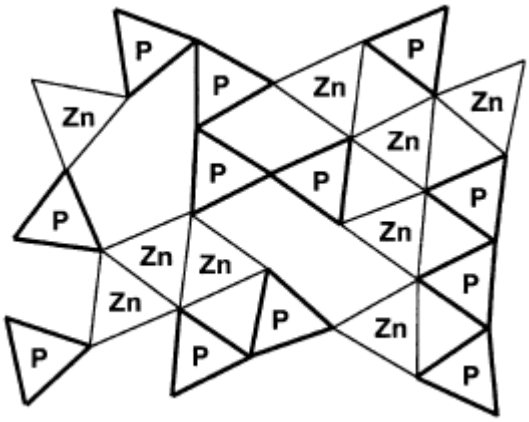

(b)

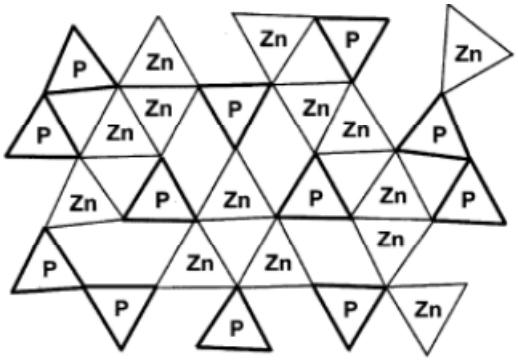

Fig. 5. 1. Illustration of network change of zinc polyphosphate glasses as proposed by Hoppe[8]. (a) 60 mol% ZnO and (b) 70 mol% ZnO.

(a)

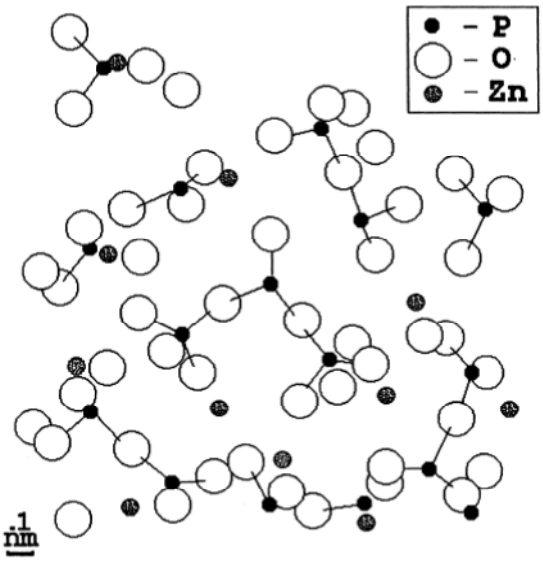

(b)

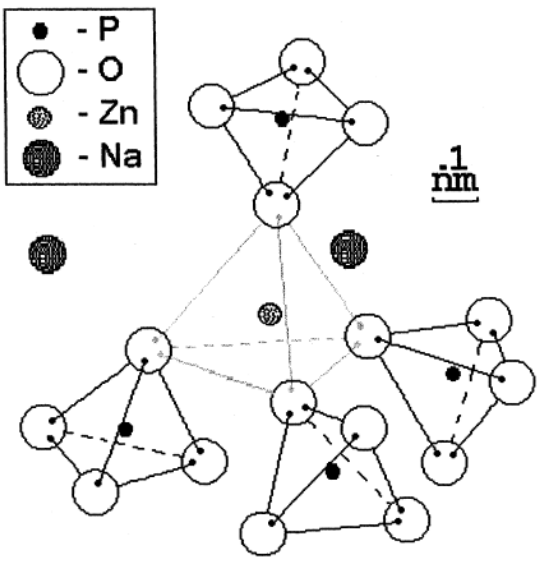

Fig. 5. 2. Fragment of snapshot structure of (a) $ZnO:P_2O_5$ pyrophosphate glass and (b) $Na_2O:ZnO:P_2O_5$ at 300 K from Molecular Dynamics[9].

5.1 Experimental

5.1.1 Glass Preparation

Glasses of general compositions $10Na_2O:(60–x)ZnO:xCaO:30P_2O_5$ and $10Na_2O:(50–x)ZnO:xCaO:40P_2O_5$ (x = 0, 10, 20 and 30) were prepared by the melt quench method (as described in Chapter 2) at temperatures between 1200°C to 1350°C. Melts for the glass compositions $10Na_2O:(60–x)ZnO:xCaO:30P_2O_5$ were quenched by the splat quench method, where melts were poured onto a stainless steel plate and covered by another stainless steel plate for about 5 minutes.

5.1.2 Glass Characterisation

Glasses were characterised by differential scanning calorimetry (DSC), X – ray diffraction, FTIR spectroscopy, ^{31}P, ^{67}Zn and ^{23}Na NMR spectroscopy, and neutron diffraction. All experiments were carried out according to the details given in Chapter 2.

5.2 Results and Discussion

5.2.1 Glass compositions

$10Na_2O:(60–x)ZnO:xCaO:30P_2O_5$ (x = 0, 10, 20, 30)

X–ray powder diffraction patterns for the studied compositions are presented in Fig 5.3. All patterns show the absence of Bragg peaks, with a broad “hump” characteristic of amorphous systems, confirming that no crystallization occurred, within the detection limits of this technique.

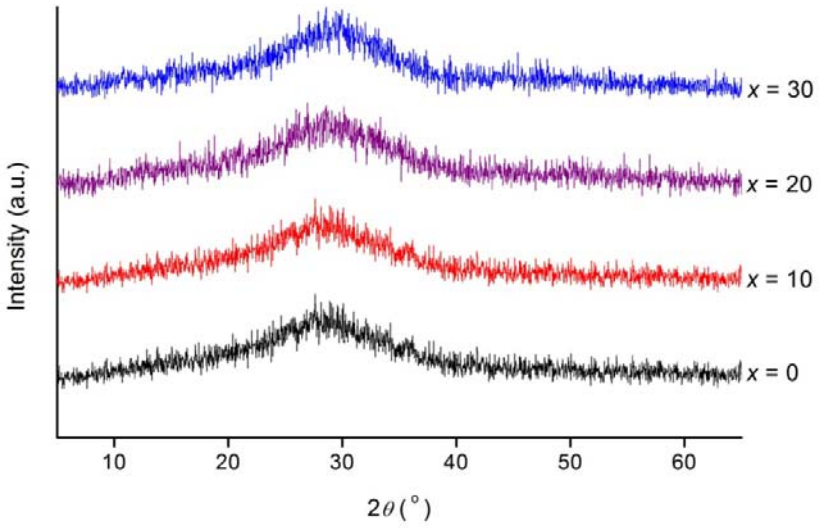

Fig. 5. 3. X–ray diffraction patterns for the $10Na_2O$:(60–*x*)ZnO:*x*CaO:$30P_2O_5$ glass compositions.

Fig. 5.4 shows DSC thermograms for the studied compositions. Generally all thermograms show a weak exotherm at temperatures from 300°C to 450°C, which corresponds to the glass transition temperature. This is followed by a significant exotherm between 500°C to 560°C, which corresponds to the crystallization temperature T_C. This exothermic peak becomes broader with increasing value of *x*, suggesting the formation of different crystalline phases. This thermal event is followed by two or more endothermic peaks at temperatures up to 760°C. These several small enotherms may correspond to eutectics or phase transitions of the crystalline phases present. No sharp endotherm is observed within the heating range 800°C to 1000°C, this is because melting temperature of glass compositions was above the maximum temperature used in the DSC experiments. A summary of the thermal events, glass transition temperature T_g, crystallisation temperature T_C and glass forming window $T_C - T_g$ are presented in Table 5.1. Variation of T_g and T_C and $T_C - T_g$ with composition are presented in Fig 5.5. Glass transition and crystallisation temperature increase with the decrease in zinc oxide content. The glass forming window decreases with decrease in zinc oxide content, which indicates that zinc oxide aids in glass formation.

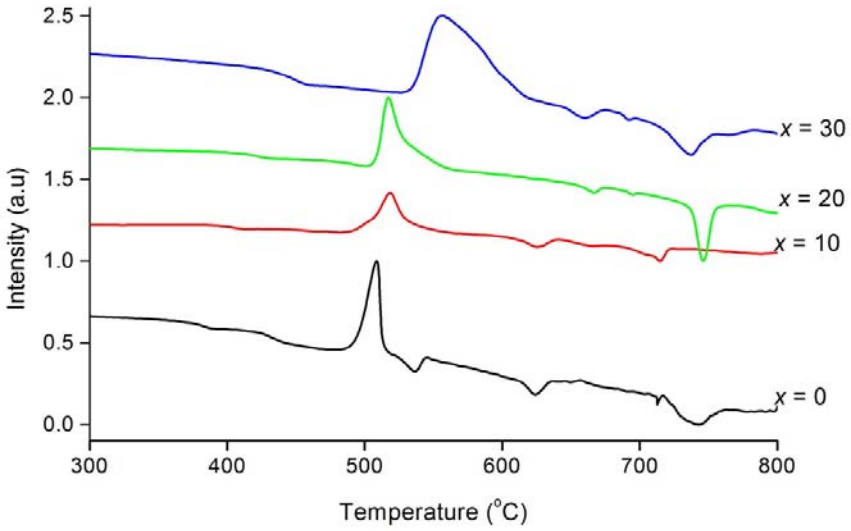

Fig. 5. 4. DSC traces for the studied glass compositions.

Table 5. 1 Summary of thermal events (°C) on heating glasses in the system $10Na_2O:(60–x)ZnO:xCaO:30P_2O_5$

X	T_g	TC	$T_C – T_g$
0	377	507	130
10	398	517	119
20	409	517	108
30	441	554	113

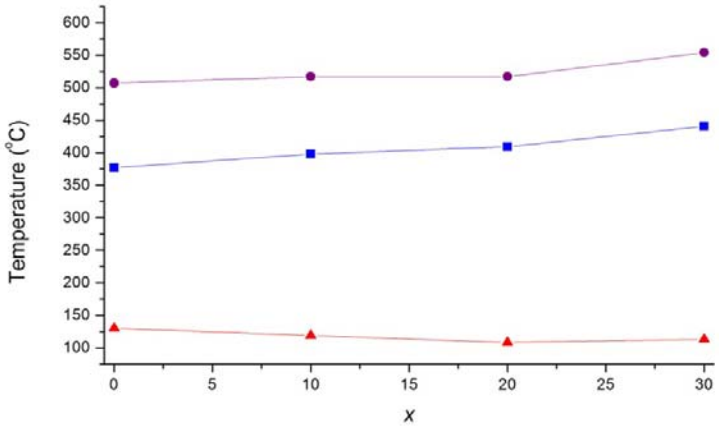

Fig. 5. 5. Compositional variation of T (circles), T_g (squares) and $T_c - T_g$ (triangles) for glass compositions in the system $10Na_2O:(60–x)ZnO:xCaO:30P_2O_5$.

^{31}P MAS–NMR spectra acquired at 12 kHz spinning speed are presented in Fig. 5.6. Two significant peaks are observed for all spectra at about –6.5 and 6.0 ppm, which correspond to Q^1 and Q^0 speciation, respectively[7, 10-12]. All spectra show prominent spinning side bands for Q^1, whereas very small or no side bands are observed for Q^0 peaks. This is related to the higher symmetry of Q^0 species. Analysis of the obtained spectra was carried out by whole spectral fitting using DMfit [13, 14] and NMRLSS [14]. The refined spectral parameters are summarized in Table 5.2. $\Delta\delta$ values for Q^1 species vary between 119 to 121 ppm, whereas those for Q^0 species lie between –49 to –55 ppm and are within the expected limits for Q^1 and Q^0 species, as reported in the literature[7, 11]. Equal values of chemical shift tensors, δ_{11} and δ_{22} with unequal δ_{33} for Q^0 species suggest that this species is axially symmetric. A zero value for the asymmetry parameter further confirms the symmetric environment of this phosphate group, whereas unequal δ_{11}, δ_{22}, and δ_{33} and a non zero asymmetry parameter for the Q^1 species is an indication of the axially asymmetric structure of this species.

Table 5. 2 Fitted and derived ^{31}P MAS–NMR parameters for glasses in the system $10Na_2O:(60–x)ZnO:xCaO:30P_2O_5$(Rel. Int. corresponds to % relative intensity)

x	Q^n	δ_{iso} (ppm)	δ_{11} (ppm)	δ_{22} (ppm)	δ_{33} (ppm)	$\Delta\delta$ (ppm)	η	Rel Int %
0	Q^0	6.81(1)	24.9	24.9	–29.3	–54.2	0.00	26.2
	Q^1	–6.57(2)	73.2	–21.7	–71.2	119.6	0.62	73.8
10	Q^0	5.96(1)	22.3	22.3	–26.8	–49.1	0.04	27.6
	Q^1	–6.87(1)	73.3	–19.9	–74.0	120.1	0.68	72.4
20	Q^0	5.52(1)	23.7	23.7	–30.9	–54.5	0.00	31.7
	Q^1	–6.58(1)	74.1	–19.3	–74.6	121.1	0.684	68.3
30	Q^0	5.20(1)	22.7	22.7	–29.7	–52.4	0.00	26.2
	Q^1	–6.36(1)	73.8	–20.7	–72.0	120.3	0.64	73.8

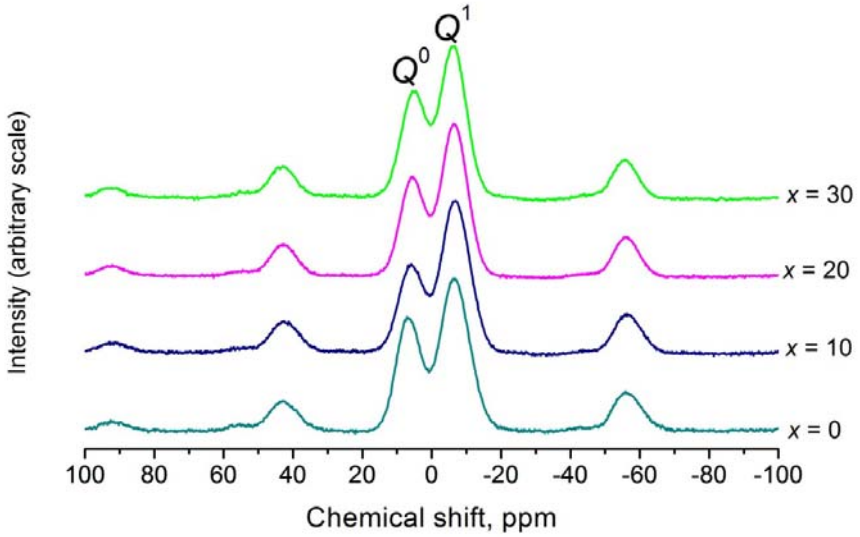

Fig. 5. 6. Central resonances in ^{31}P MAS–NMR spectra of glasses of composition $10Na_2O:(60–x)ZnO:xCaO:30P_2O_510Na_2O$ measured at 12 kHz spinning speed.

(a)

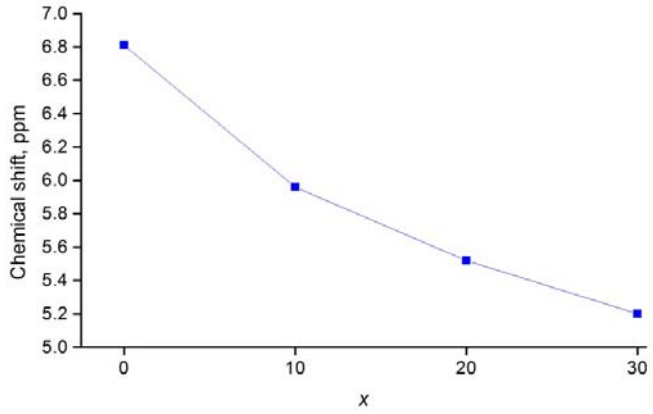

(b)

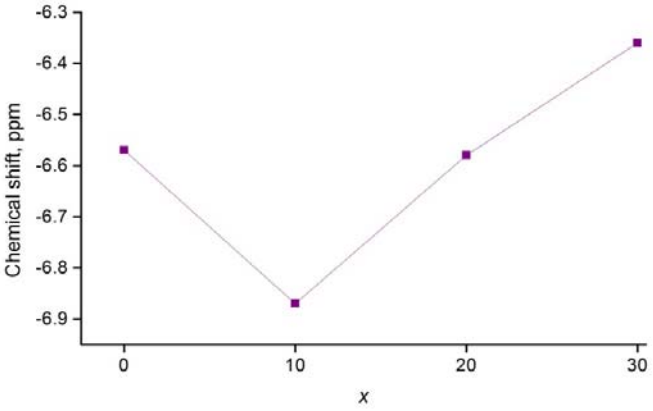

Fig. 5. 7. Variation of ^{31}P chemical shift with composition in $10Na_2O:(60–x)ZnO:xCaO:30P_2O_5$ glasses for (a) Q^0 and (b) Q^1 species. (esd±1 ppm)

The variations of chemical shift with composition for both Q^0 and Q^1 species are presented in Figs. 5.7.(a) and 5.7(b), respectively. The isotropic chemical shift for Q^0 species decreases linearly with decreasing zinc oxide content, while chemical shift for the Q^1 species initially decreases on going from x = 0 to x = 10, followed by an increase in chemical shift from x = 10 to x = 30.

Fig. 5.8 shows the $^{31}P - {}^{31}P$ double quantum (DQ) correlation spectra of the glass compositions x = 10 and x = 30, while Fig. 5.9 shows fits to the sum of the internal projections of the DQ spectra. Fitted parameters of the internal projections are presented in Table 5.3. The diagonal peaks at about –10 ppm on f_2 and –20 ppm on f_1 dimensions correspond to Q^1–Q^1 correlations, whereas cross correlated peaks at about 5 ppm on f_1 and –5 ppm on f_2 dimensions represent coherence between Q^0 and Q^1 species. Another auto-correlated coherence at 5 ppm and 10 ppm on f_2 and f_1 axes, respectively, corresponding to Q^0–Q^0 correlation is observed in the x = 30 glass composition. Although Q^0 species are nominally isolated PO_4^{3-} units and do not have any through bond correlation with any other phosphate species, the existence of Q^0–Q^0 and Q^0–Q^1 correlations suggests the presence of ZnO_4 tetrahedra between PO_4 tetrahedra, since the POST–C7 pulse sequence measures dipolar couplings through space[15-17] and it is sensitive up to the fourth coordination sphere.

^{67}Zn NMR spectra for glass compositions x = 0 to x = 20 are presented in Fig. 5.10. All spectra are broad since they were acquired under static conditions. However, line shapes are not specific to static powder line shapes due to the amorphous nature of sample. The data were fitted using DMfit with the “Qstatic1/2” peak function based on evidence from the neutron diffraction results. Each spectrum was modelled as two resonances between 250 ppm to 450 ppm and 117 ppm to 168 ppm. According to the literature[18] the more positive chemical shift corresponds to 4–coordinated zinc, whereas the less positive values can be attributed to 6–coordinated zinc.

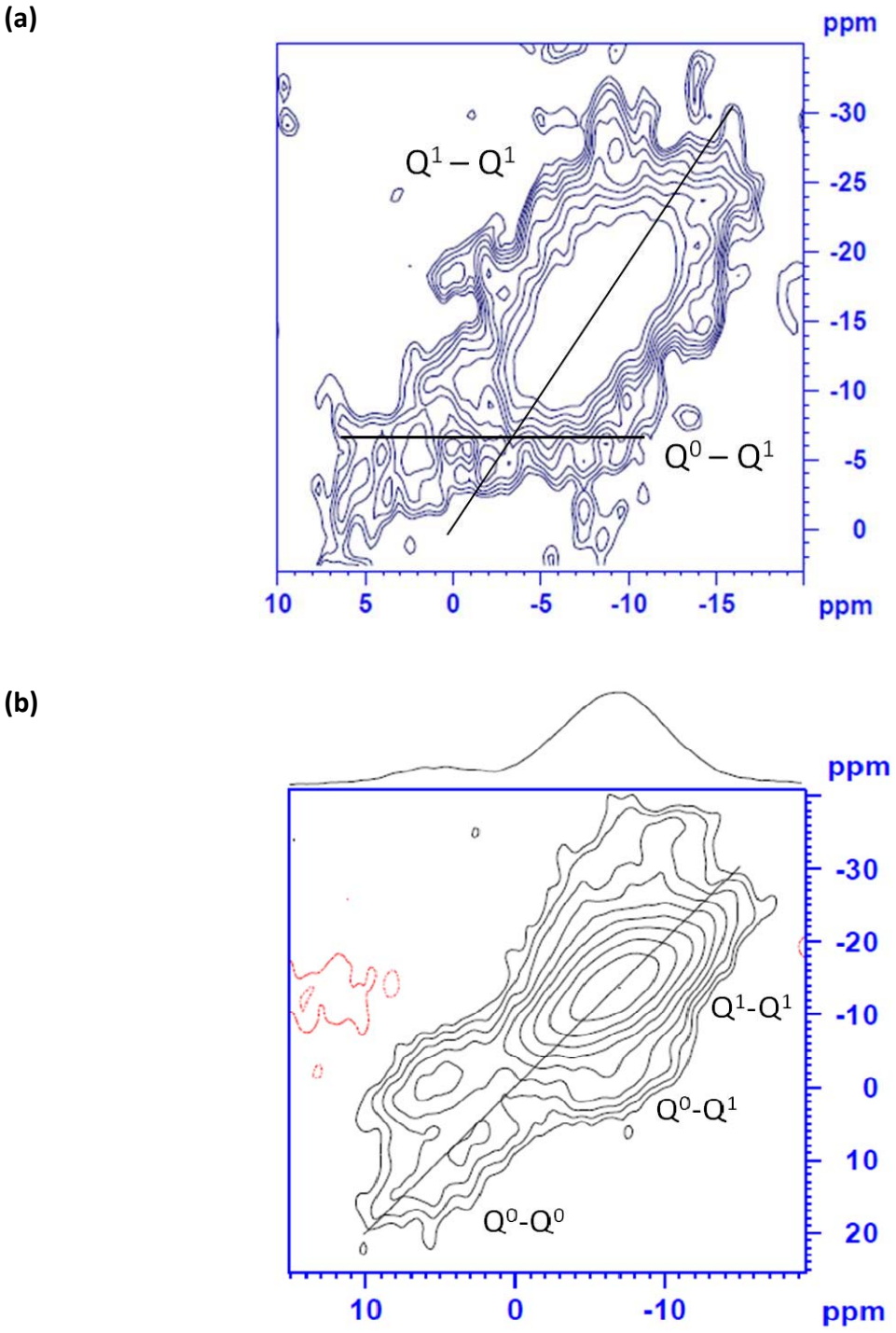

Fig. 5. 8. ^{31}P–^{31}P double quantum–single quantum (DQ–SQ) correlation spectra of $10Na_2O:(60–x)ZnO:xCaO:30P_2O_5$ glass compositions (a) *x* = 0 and (b) *x* = 30.

(a)

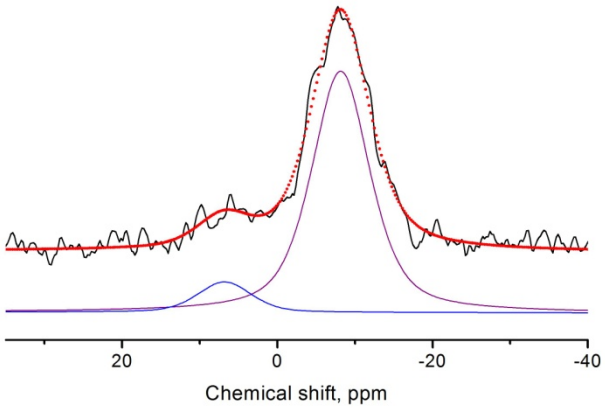

(b)

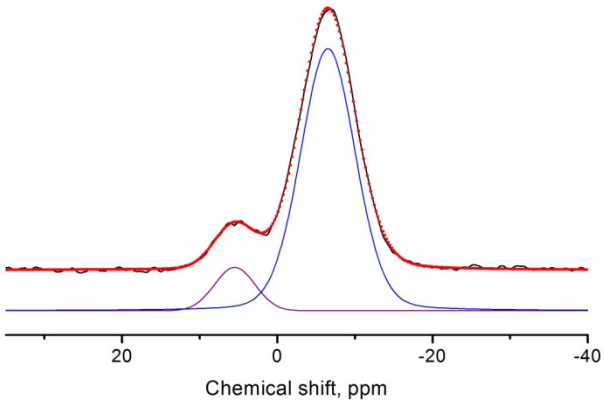

Fig. 5. 9. Fit to the sum of al internal projections of DQ spectra for $10Na_2O:(60–x)ZnO:xCaO:30P_2O_5$ glass composition (a) x = 0 and (b) x = 30.

Table 5. 3 ^{31}P chemical shift and % intensity derived from the fit of sum of internal projections of DQ spectra.

x	Q^n	δ_{iso} ppm	% Intensity
0	Q^0	5.49	10
	Q^1	–6.51	90
30	Q^0	6.80	10
	Q^1	–8.15	90

(a)

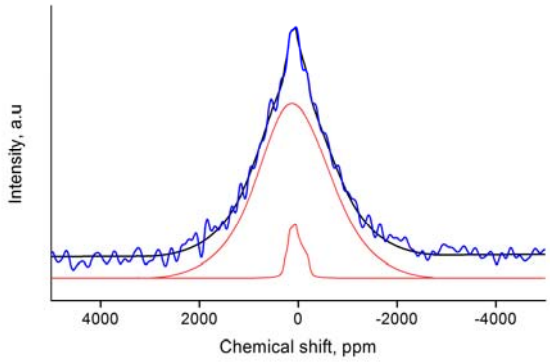

(b)

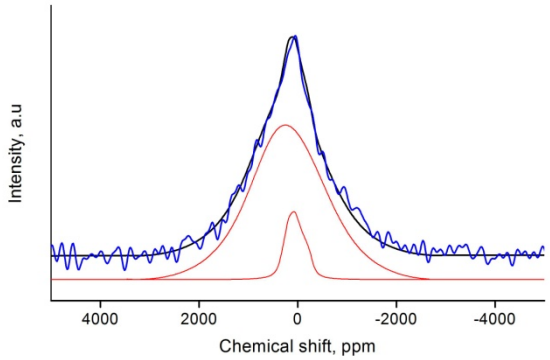

(c)

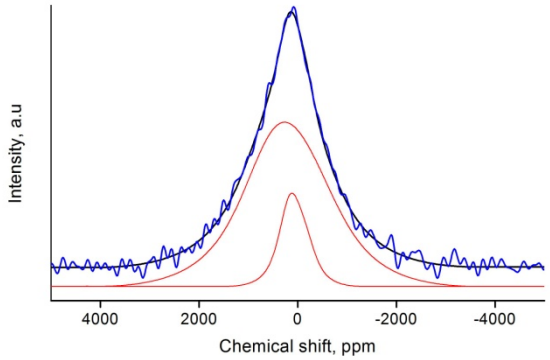

Fig. 5. 10. Fitted ^{67}Zn static NMR spectra for glass compositions (a) *x* = 0, (b) *x* = 10 and (c) *x* = 20. Solid blue lines represent the acquired spectra, solid black lines represent the sum of all fitted peaks and red lines represent the fits to individual peaks. The latter is lowered on the intensity scale for clarity.

The derived NMR parameters from these fits are presented in Table 5.4. From these initial results it is seen that tetrahedral zinc has a higher quadrupolar coupling constant C_Q and quadrupolar asymmetry than octahedral zinc with values for C_Q of about 9 MHz and 6 MHz and for η_Q of about 0.9 and 0.7 for tetrahedral and octahedral zinc respectively.

Table 5. 4. Fitted and derived ^{67}Zn NMR parameters for glasses in the system $10Na_2O:(60–x)ZnO:xCaO:30P_2O_5$.

x	δ, ppm	C_Q, MHz	η_Q	%Intensity
0	273 117	9.3 5.7	0.92 0.69	94 6
10	412 137	9.0 6.3	0.95 0.67	89 11
20	441 168	10.1 6.1	0.76 0.99	90 10

Fig. 5.11 shows the Q–space distinct neutron scattering iQ $\left(Q_{\max} = 60\right)$ for glass composition x = 0, which is calcium free and has the maximum amount of zinc oxide (60 mol%). Fig. 5.12 shows the corresponding real space correlation function $T(r)$, which is the Fourier transform of iQ with background subtracted.

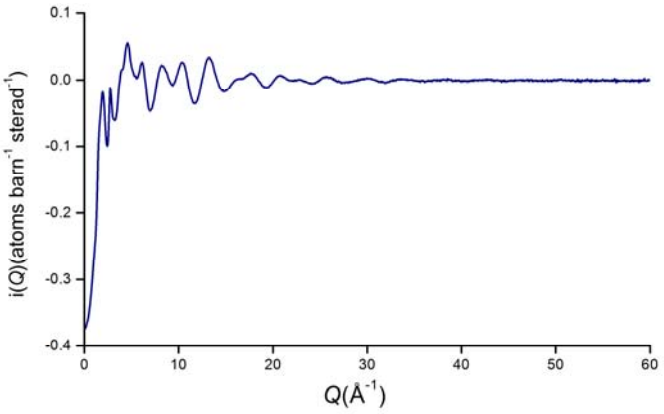

Fig. 5. 11. The Q–space interference function iQ for glass composition $10Na_2O:60ZnO:30P_2O_5$

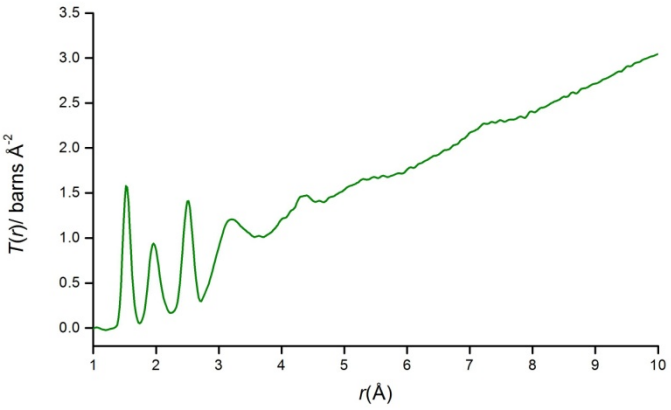

Fig. 5. 12. Real space total correlation function *T*(*r*) for glass composition $10Na_2O:60ZnO:30P_2O_5$

The fit to *T*(*r*) is shown in Fig 5.13(a), while Fig. 5.13(b) shows the fit to the P–O correlation pair. The real space correlation function shows distinct peaks corresponding to pair correlations in the glass system. The distance assignment was made according to the literature[10, 19, 20]. The fitted parameters are summarised in Table 5.5. The first pair correlation at a distance about 1.55 Å relates to the P–O bond. In metaphosphates and other phosphates with lower numbers of NBOs, this correlation is clearly split into into shorter bonds to non–bridging oxygens atoms (P–NBO) and longer bonds to bridging oxygens (P–BO). In the studied invert phosphate glass composition, this correlation is not well resolved due to the higher proportion of the P–NBO, compared to P–BO. However, asymmetry is seen at higher *r*. The P–O pair correlation was fitted according to Van Wazer's relationship $(3-y)/(1+y)$, where y is the ratio between mole fraction of modifier oxide (M_2O or MO) and P_2O_5. The observed ratio between NBO and BO is in good agreement with the calculated ratio based on composition as well as with neutron difftaction results of other invert phosphate glasses[10] . The second shortest correlation pair is observed at a distance of 1.96 Å, which is assigned to Zn–O, according to previous studies on zinc phosphates[8, 19, 21, 22]. The peak for the Zn–O correlation is asymmetric towards higher *r*. Considering the ^{67}Zn NMR results, where fitting of the line with one resonance was not possible and a good fit was obtained by the introduction of second resonance for octahedral

zinc, an additional Zn–O correlation is introduced at a distance of 2.1 Å, corresponding to octahedral zinc. Thus the total oxygen co-ordination number for zinc is found to be 4.17, which indicates the presence of about 8% 6–coordinated zinc, with 92% in 4–coordinated geometry. The characterisation of the Na–O correlation pair is difficult, since it is overlapped by the O–O correlation. In order to resolve the Na–O correlation, the area of the O–O correlation peak was fixed at a value corresponding to a co-ordination number of 3.275 calculated according to the formula 24/(5 + y) given by Hoppe[23] and subtracted from the rest of the $T(r)$. The residual area was fitted as the Na–O correlation at a distance r = 2.48 Å, which giving a co-ordination number of about 4.

(a)

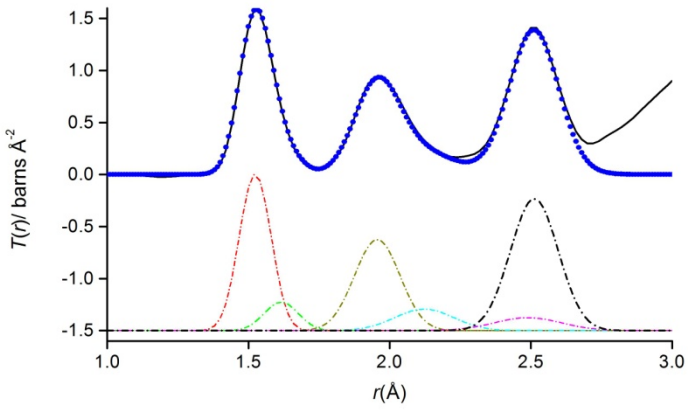

(b)

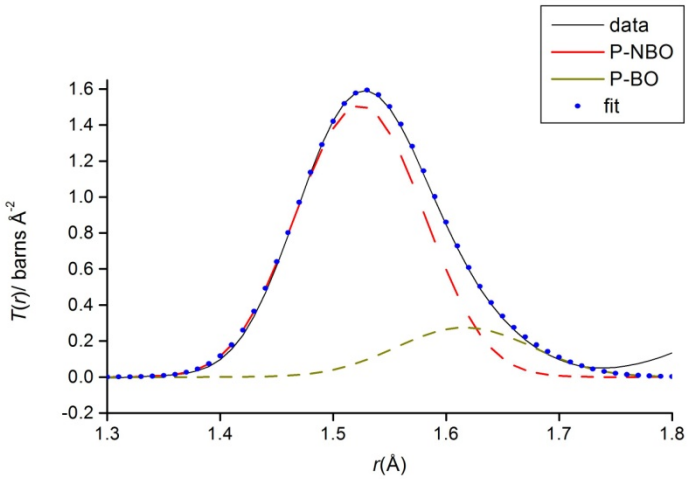

Fig. 5. 13. (a) Real space correlation function $T(r)$ (solid back line) together with fit (dotted blue line). Fit to individual pair distribution functions are dotted coloured lines, shown offset –1.5 for clarity. (b) Detail of fit of P–O correlation pair.

Table 5. 5 Co-ordination numbers (N_{i-j}) and correlation distances (r_{i-j}) derived from the fit of $T(r)$ for glass composition $10Na_2O$:(60-x)ZnO:xCaO$30P_2O_5$. (x = 0 and 30)

x	0		30	
Correlation	r_{i-j} **(Å)**	N_{i-j}	r_{i-j} **(Å)**	N_{i-j}
P–NBO	1.52	3.22	1.52	3.30
P–BO	1.61	0.67	1.61	0.75
P–O(tot)	1.55	3.89		4.05
Zn–O(1)	1.96	3.13	1.97	4.14
Zn–O(2)	2.12	1.04	2.16	0.23
Zn– O(tot)	2.00	4.17		4.37
M–O	2.48	3.97	2.36	6.84
O–O	2.51	3.28	2.51	3.28

5.2.2 Glass Compositions

$10Na_2O$: (50–x)ZnO: xCaO: $40P_2O_5$ (x = 0, 10, 20, 30)

Fig. 5.14 shows X–ray diffraction patterns for the studied glass compositions in the $10Na_2O$: (50–x)ZnO: xCaO: $40P_2O_5$ system. The absence of sharp Bragg peak confirms the amorphous nature of prepared glass compositions.

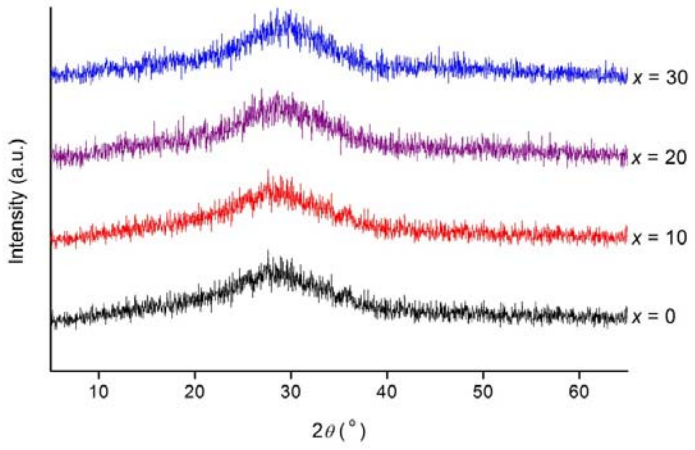

Fig. 5. 14. X–ray diffraction patterns of studied glass compositions in the $10Na_2O$: (50–x)ZnO: xCaO: $40P_2O_5$ system.

Thermal events, in this system are summarised in Table 5.6 and plotted in Fig. 5.15. T_g increases linearly with the decrease in zinc oxide content. An increase in T_c and the decrease in $T_c - T_g$ is observed with decreasing zinc oxide content. Therefore the glass forming window decreases with decreasing zinc oxide content and explains why the *x* = 40 glass composition (i.e 10 mole% ZnO) did not produce glass and readily crystallised after splat quenching at room temperature.

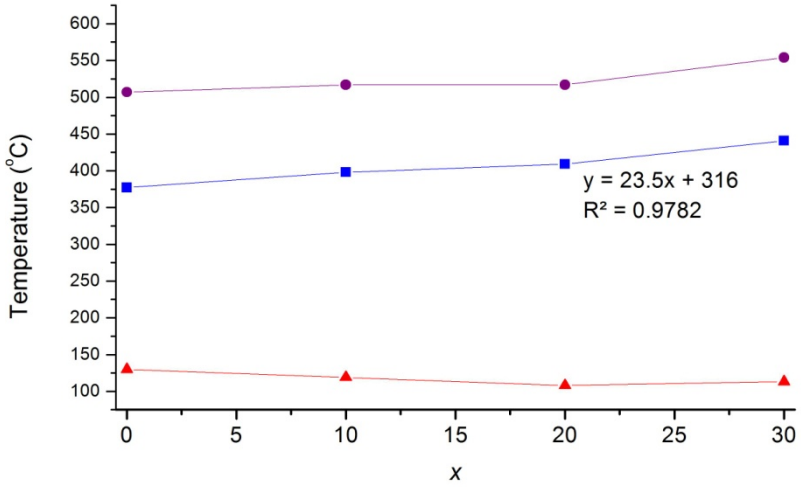

Fig. 5. 15. Compositional variation of T_c (circles), T_g (squares) and $T_c - T_g$ (triangles) in the $10Na_2O$: (50–x)ZnO: xCaO: $40P_2O_5$ system. Linear equation is for T_g.

Table 5. 6 Thermal events in the $10Na_2O$: (50–x)ZnO: xCaO: $40P_2O_5$ system

x	T_g	Tc	$Tc - T_g$
0	344	522	178
10	357	592	235
20	388	573	185
30	412	560	148

^{31}P MAS–NMR spectra for the studied compositions, together with fits to central resonances and side bands are presented in Fig. 5.16. Two major peaks are observed for each spectrum, with isotropic chemical shifts at about –23 ppm and –8 ppm, which correspond to Q^2 and Q^1 phosphate species[7, 10, 12, 24-27]. The isotropic chemical shift moves toward less negative values (Fig. 5.17) with increasing value of *x*,

which indicates the greater shielding effect of Zn^{2+} compared to Ca^{2+}, due to its higher electronegativity and ion potential. As expected, based on the symmetry of Q^2 and Q^1 species, prominent side bands are observed in each spectrum. Parameters derived from DMfit and NMRLSS fits of of the whole spectra are presented in Table 5.7. $\Delta\delta$ values for the Q^2 species vary between –169 to –175 ppm, whereas the Q^1 species have $\Delta\delta$ values between 129 to 142 ppm. $\delta_{11} \neq \delta_{22} \neq \delta_{33}$ and η values are near 0.5 for both species and indicates that they are both axially asymmetric. The relative intensity between the two species deviates from the theoretically calculated values based on composition (50% Q^2, 50% Q^1), however no trend is observed in proportion of two species.

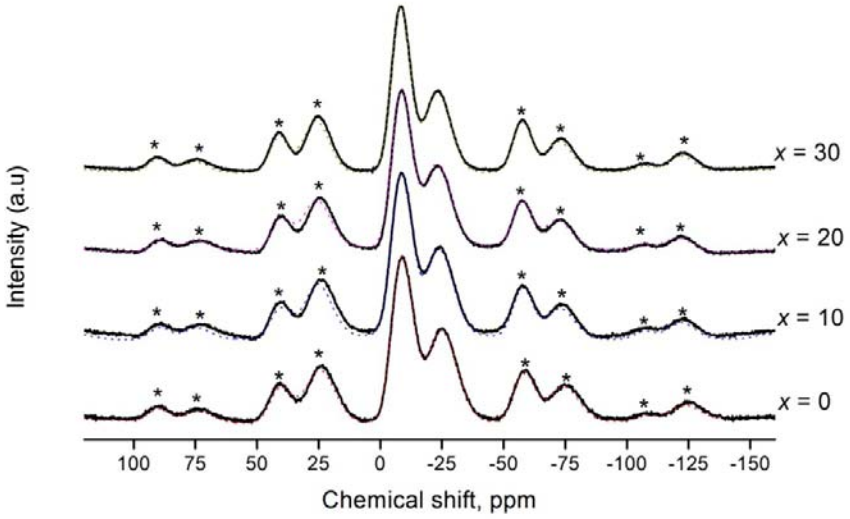

Fig. 5. 16. ^{31}P MAS–NMR spectra for glass compositions in the $10Na_2O$: (50–x)ZnO: xCaO: $40P_2O_5$ system, acquired at 12 kHz spinning speed (* symbols represent spinning side bands).

(a)

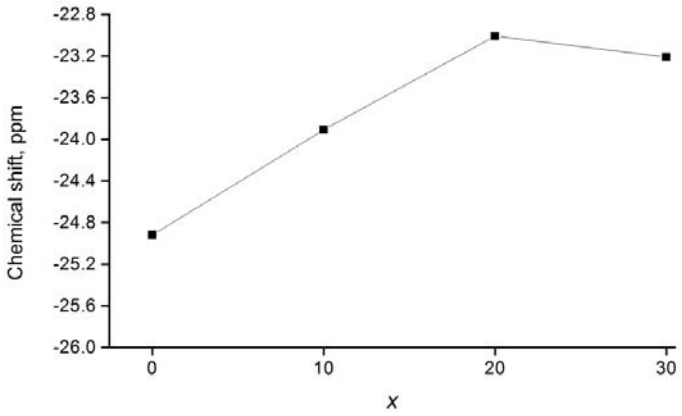

(b)

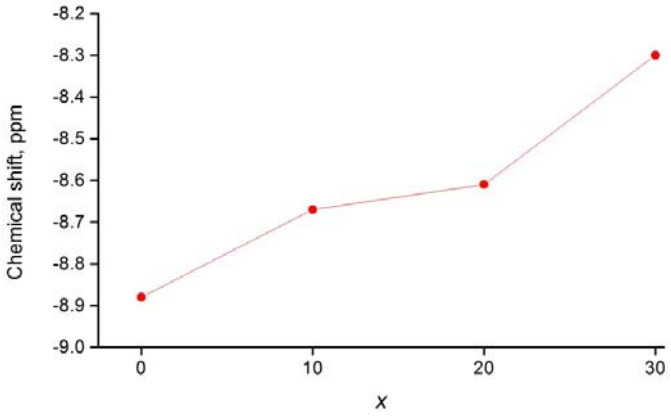

Fig. 5. 17. Variation in isotropic chemical shift of (a) Q^2 and (b) Q^1 species with composition.

Table 5. 7 ^{31}P MAS–NMR parameters for compoistions in the $10Na_2O$: (50–x)ZnO: xCaO: $40P_2O_5$ system derived from the fitting of spectra acquired at 12 kHz (Fig. 5.16). (Rel. Int. corresponds to % relative intensity)

x	Q^n	δ_{iso} (ppm)	δ_{11} (ppm)	δ_{22} (ppm)	δ_{33} (ppm)	$\Delta\delta$ (ppm)	η	Rel Int %
0	Q^1	–8.82	77.7(1)	–31.6(5)	–72.8(1)	129.9(1)	0.48(1)	42.0
	Q^2	–24.92	87.4(12)	–20.7(6)	141.5(10)	–174.8(5)	0.92(14)	58.0
10	Q^1	–8.67	78.5(1)	–37.0(7)	–67.5(1)	130.8(2)	0.35(2)	43.5
	Q^2	–23.91	63.8(3)	3.7(17)	–139.2(2)	–172.9(4)	0.52(3)	56.5
20	Q^1	–8.61	77.9(1)	–37.3(6)	–66.4(0.7)	129.7(1)	0.34(1)	40.8
	Q^2	–23.01	64.1(2)	1.4(1)	–314.5(2)	–167.2(3)	0.56(2)	59.3
30	Q^1	–8.30	85.9(3)	–39.5(2)	–71.3(3)	141.4(5)	0.34(1)	49.0
	Q^2	–23.21	67.1(2)	3.3(1)	–140(1)	–175.1(2)	0.55(2)	51.0

Fig. 5.18 shows the ^{31}P DQ MAS–NMR spectrum for glass composition x = 0 which shows two diagonal peaks at about –10 ppm and –27 ppm on the f_2 dimension for Q^1— Q^1 and Q^2— Q^2 correlations, respectively. Two off diagonal (cross-correlating) resonances at –10 ppm and –25 ppm on the f_2 dimension correspond to Q^1— Q^2 correlations. Correlating peaks show more significant splitting, with more negative chemical shift values at about –31 ppm and –33 ppm for Q^2 peaks in Q^1— Q^2 and Q^2— Q^2 correlations, respectively in this spectrum compared to the spectrum of glass composition x = 25 (Fig. 4.10c, corresponding to x = 10 in the system $10Na_2O$:(20+x/2)ZnO:(20+x/2)CaO:(50-x)P_2O_5). The gretater splitting indicates that higher amounts of ZnO break the —P—O—P—chains and ZnO_4 tetrahedra are inserted between these chains forming —P—O—Zn— type chains with a distribution of lengths.

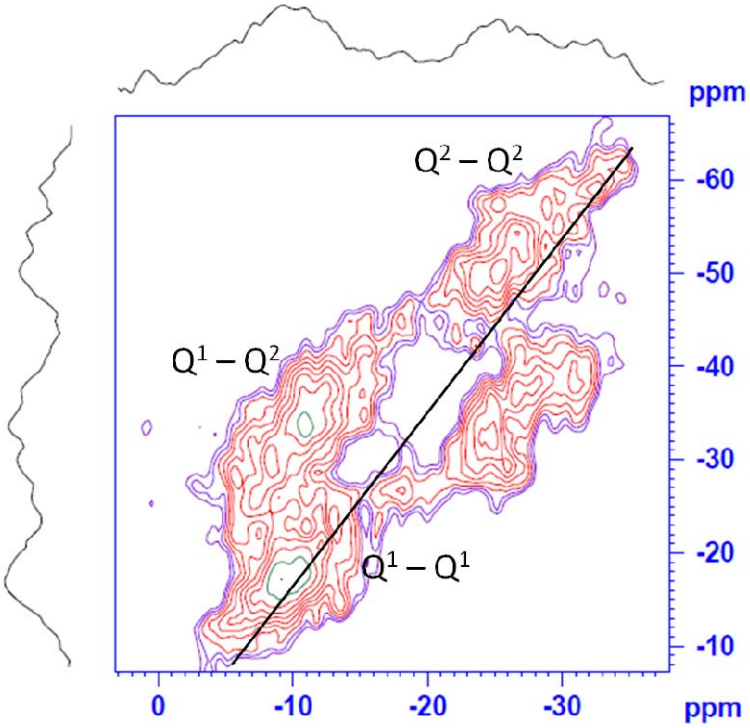

Fig. 5. 18. ^{31}P DQ MAS–NMR spectrum for the glass composition 10Na_2O:50ZnO:40P_2O_5 (*x* = 0). Different colors of contours are to highlight contour levels and intensity of each peak. Projection on top is the sum of all horizontal internal projections, whereas projection on right is the sum of all vertical internal projections.

Fig. 5.19 shows the fitted ^{67}Zn NMR spectrum of glass composition 10Na_2O:50ZnO:40P_2O_5 (*x* = 0), with the derived spectral parameters presented in Table 5.8. The spectrum was fitted to two peaks with chemical shifts at 231 ppm and 119 ppm. According to the literature for the zinc oxide environment in different organic and inorganic complexes[28-30], these chemical shift values are assigned to tetrahedral and octahedral co-ordination for zinc, though the relative intensity of the octahedral zinc (ZnO_6) is only 6%. C_Q values for both sites are slightly lower than those observed for the 30 mol% P_2O_5 series (section 5.2.1).

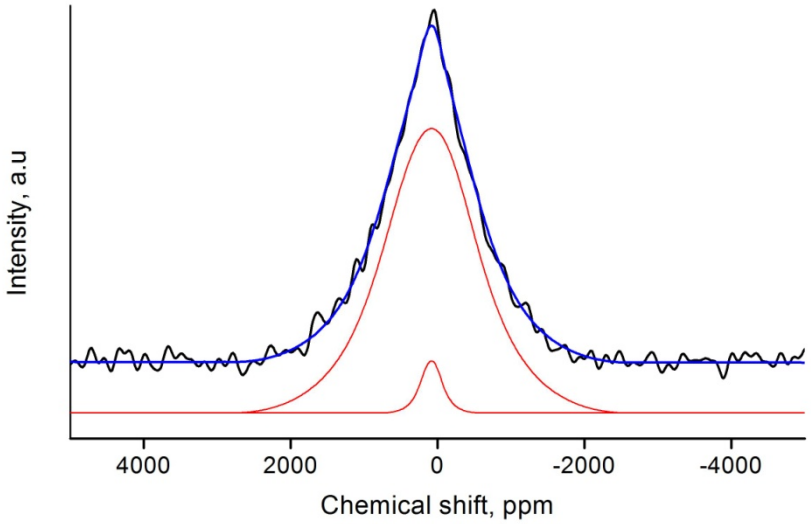

Fig. 5. 19. Fitted ^{67}Zn static NMR spectrum for glass composition 10Na_2O:50ZnO: 40P_2O_5 (*x* = 0). Solid black line represents the acquired spectrum, solid blue line represents the calculated spectrum and the red lines represent the fits to individual resonances. The latter are lowered on the intensity scale for clarity.

Table 5. 8 ^{67}Zn NMR derived parameters for glass composition 10Na_2O:50ZnO:40P_2O_5 (*x* = 0)

δ, ppm	CQ, MHz	η_Q	%Intensity
231	8.4	0	94
119	4.2	0	6

Fig. 5.20 shows the Q—space distinct neutron scattering iQ Q_{max} = 60 for glass compositions *x* = 0 and *x* = 30 and Fig. 5.21 shows the corresponding real space correlation function *T*(*r*). The shortest correlation is for the P–O pair at a distance of about 1.55 Å, characteristic of PO_4 tetrahedra in phosphates. The second shortest distance peak at about 1.9 Å corresponds to the 4 coordinated Zn–O correlation, which decreases in intensity in glass composition *x* = 30 due to the decrease in ZnO content. Another very prominent peak for the O–O pair corrleation is observed at a distance of 2.5 Å.

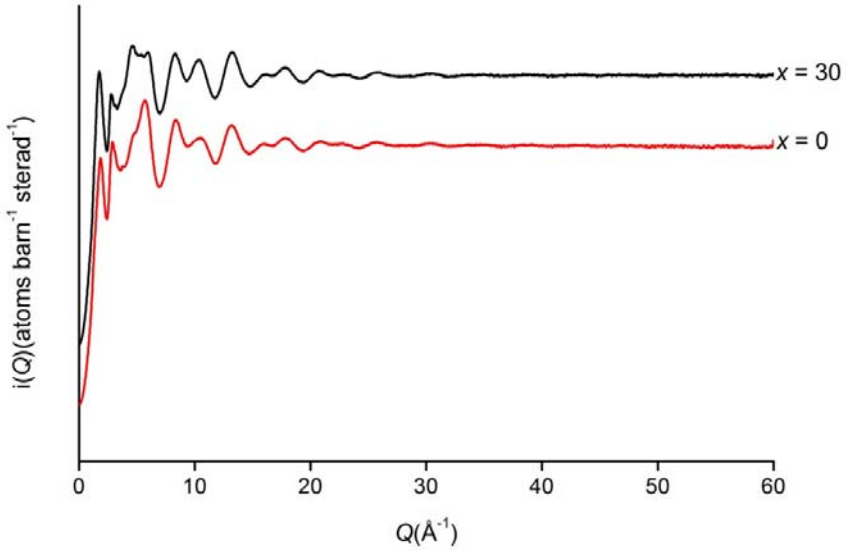

Fig. 5. 20. The *Q*–space interference function *iQ* for glass composition $10Na_2O:(50–x)ZnO:xCaO:40P_2O_5$ *x* = 0 and *x* = 30

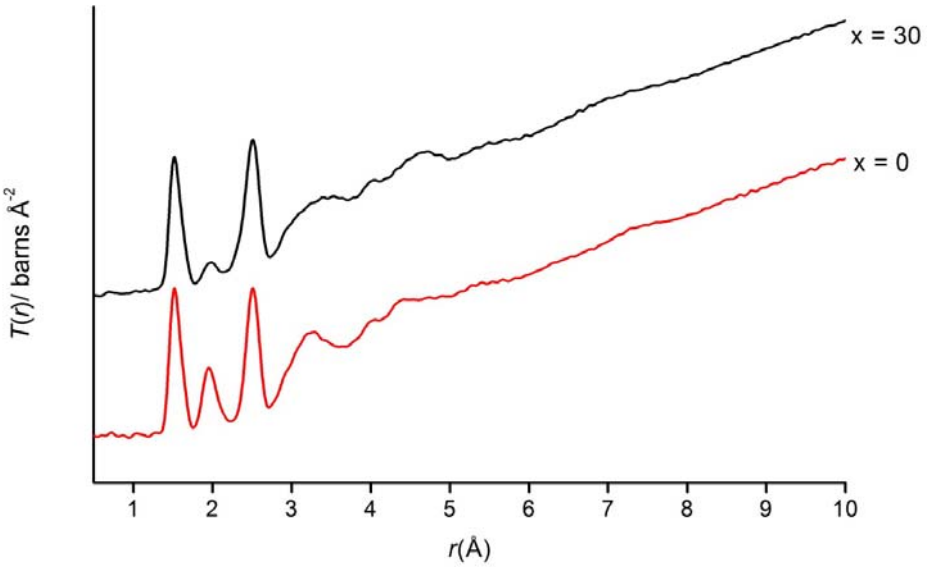

Fig. 5. 21. Real space total correlation function $T(r)$ for glass compositions $10Na_2O:(50–x)ZnO:xCaO:40P_2O_5$ *x* = 0 and *x* = 30.

(a)

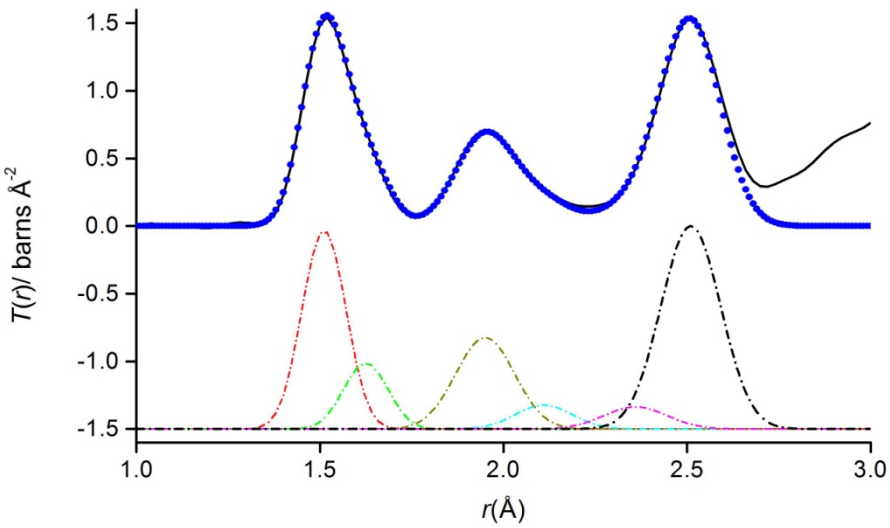

(b)

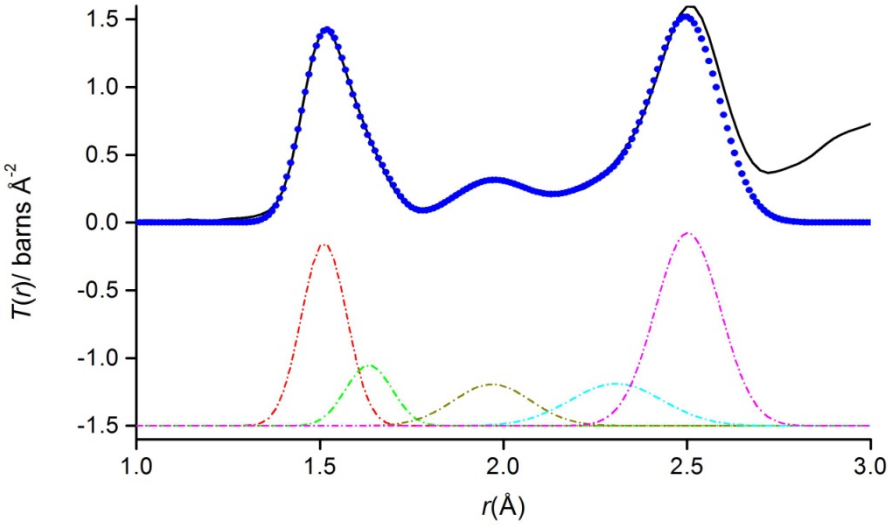

Fig. 5. 22. Real space correlation function *T*(*r*) (solid black line) together with the fit (dotted blue line). Fit to individual pair distribution functions are dotted colored lines, shown offset –1.5 for clarity. (a) *x* = 0 and (b) *x* = 30

(a)

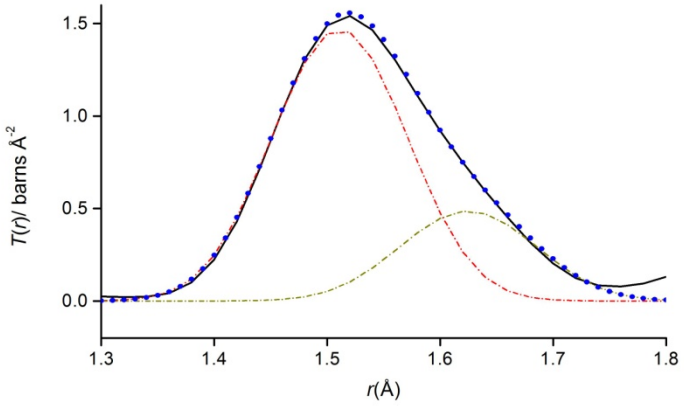

(b)

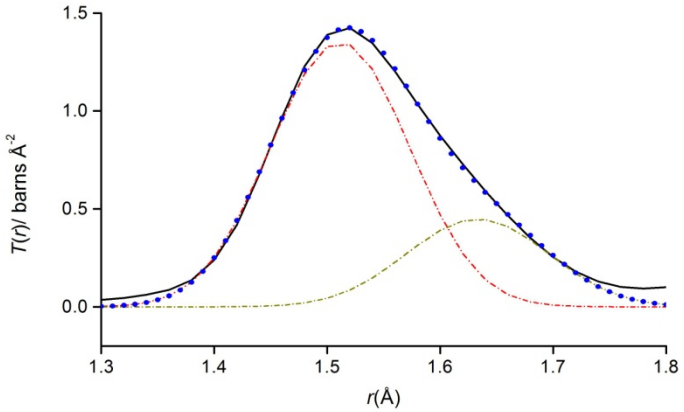

Fig. 5. 23. Fit to *T*(*r*) for P – O corrleation pair (a) x = 0 and (b) x = 30

The fits to *T*(*r*) for glass compositions *x* = 0 and 30 are shown in Fig 5.22, while Fig. 5.23 shows the fits to P–O correlation pair. Co-ordination numbers (N_{i-j}) and correlation distances (r_{i-j}) derived from the fit of *T*(*r*) for glass compositions *x* = 0 and *x* = 30 are presented in Table 5.9. The peak corresponding to the P–O pair is not well resolved into the different bond lengths for P–NBO and P–BO, due to the higher proportion of P–NBO as compared to P –BO. A good agreement is found between fit and experimental data by fitting peak according to Van Wazer's equation (as described in the previous section) for the proportion of P–NBO and P–BO in phosphate glasses, based on proportion of phosphate content. The Zn–O correlation was modelled on two peaks at distances of 1.95 and 2.11 Å for the *x* = 0 glass composition, and gave a total

co-ordination number of 4.16. The peak for the O–O correlation was modelled using a fixed coordination number as described earlier, with the rest of the area under the peak around this value of *r* fitted as the Na–O correlation (or Na–O and Ca–O for the x = 30 composition). This gave an Na–O coordination number of about 4.1 in the x = 0 composition, whereas for the *x* = 30 composition an average M–O co-ordination number of 8.3 was obtained.

Table 5. 9 Coordination numbers (N_{i-j}) and correlation distances (r_{i-j}) derived from the fit of *T*(*r*) four glass compositions $10Na_2O$: (50–*x*) ZnO: *x*CaO: $40P_2O_5$ *x* = 0 and *x* = 30

X	**0**		**30**	
Correlation	r_{i-j} **(Å)**	N_{i-j}	r_{i-j} **(Å)**	N_{i-j}
P –NBO	1.51	2.8	1.51	2.67
P –BO	1.61	1.0	1.63	0.98
P –O (Total)		3.8		3.65
Zn –O(1)	1.95(0)	3.270)	1.97	4.74
Zn –O(2)	2.11	0.89		
M – O (ave)	2.36	4.07	2.31	8.27
O – O	2.51	3.58	2.50	3.69

5.3 Conclusions

An Increase in glass transition temperature with decrease in zinc oxide content in both series of glasses confirms that zinc oxide aids in glass fomation and increases the glass formation window, as observed previously where zinc containing phosphate glasses with phosphate contents as low as 28 mole% have been produced successfully[11]. Spectral parameters derived from ^{31}P MAS–NMR show that Q^2 and Q^1 species have axially asymetirc environments, whereas Q^0 species are axially symetric and do not change with composition. The presence of Q^0– Q^1 correlations in the ^{31}P–^{31}P 2D spectrum of $10Na_2O$:60ZnO:$30P_2O_5$ (x = 0) glass composition is consistent with insertion of ZnO_4 tetrahedra between PO_4 terahedra, which is further supported by the absence of Q^0– Q^0 correlations in this composition, while being observed in the spectrum of the *x* = 30 composition. The greater splitting of Q^2 peaks in ^{31}P DQ MAS–

NMR spectra of glass composition $10Na_2O:50ZnO:40P_2O_5$ (x = 0) compared to the $10Na_2O:25ZnO:25CaO:40P_2O_5$ glass composition (chapter 4) is another indication of insertion of ZnO_4 tetrahedra between PO_4 at higher zinc concentrations.

A relatively high Zn–O co-ordination number, calculated from fitting of neutron diffraction data for glass compositions with lower amounts of zinc oxide in both series, indicates the existence of Zn in higher coordinations (5 or 6) in these glass compositions, whereas zinc co-ordination is more close to tetrahedral in glass compositions with higher zinc content.

5.4 References

1. J. Vogel, P. Wange, S. Knoche and C. Russel, *Glass Science and Technology*, 2004, **77**, 82-87.
2. J. P. Andrew, A. Ifty, H. Papia, F. Ben, I. K. N. Muhammad, S. W. Gavin and D. R. Chris, *Journal of Bionics Engineering*, 2009, **6**, 318-323.
3. D. S. Brauer, R. M. Wilson and T. Kasuga, *Journal of Non-Crystalline Solids*, 2012, **358**, 1720-1723.
4. D. S. Brauer, N. Karpukhina, R. V. Law and R. G. Hill, *Journal of Non-Crystalline Solids*, 2010, **356**, 2626-2633.
5. T. Kasuga, *Acta Biomaterialia*, 2005, **1**, 55-64.
6. H. S. Liu and T. S. Chin, *Physics and Chemistry of Glasses*, 1997, **38**, 123-131.
7. R. K. Brow, D. R. Tallant, S. T. Myers and C. C. Phifer, *Journal of Non-Crystalline Solids*, 1995, **191**, 45-55.
8. U. Hoppe, G. Walter, G. Carl, J. Neuefeind and A. C. Hannon, *Journal of Non-Crystalline Solids*, 2005, **351**, 1020-1031.
9. G. G. Boiko, N. S. Andreev and A. V. Parkachev, *Journal of Non-Crystalline Solids*, 1998, **238**, 175-185.
10. G. Walter, J. Vogel, U. Hoppe and P. Hartmann, *Journal of Non-Crystalline Solids*, 2001, **296**, 212-223.
11. G. Walter, U. Hoppe, J. Vogel, G. Carl and P. Hartmann, *Journal of Non-Crystalline Solids*, 2004, **333**, 252-262.
12. R. J. Kirkpatrick and R. K. Brow, *Solid State Nuclear Magnetic Resonance*, 1995, **5**, 9-21.
13. D. Massiot, F. Fayon, M. Capron, I. King, S. Le Calve, B. Alonso, J. O. Durand, B. Bujoli, Z. H. Gan and G. Hoatson, *Magnetic Resonance in Chemistry*, 2002, **40**, 70-76.
14. I. Abrahams, Queen Mary University of London, 2003.
15. M. Feike, C. Jager and H. W. Spiess, *Journal of Non-Crystalline Solids*, 1998, **223**, 200-206.
16. H. Geen, J. Gottwald, R. Graf, I. Schnell, H. W. Spiess and J. J. Titman, *Journal of Magnetic Resonance*, 1997, **125**, 224-227.
17. R. Witter, P. Hartmann, J. Vogel and C. Jager, *Solid State Nuclear Magnetic Resonance*, 1998, **13**, 189-200.

18. A. S. Lipton, M. D. Smith, R. D. Adams and P. D. Ellis, *Journal of the American Chemical Society*, 2002, **124**, 410-414.

19. S. Bruni, F. Cariati, A. Corrias, P. H. Gaskell, A. Lai, A. Musinu and G. Piccaluga, *Journal of Physical Chemistry*, 1995, **99**, 15229-15235.

20. J. M. Smith, S. P. King, E. R. Barney, J. V. Hanna, R. J. Newport and D. M. Pickup, *Journal of Chemical Physics*, 2013, **138**, 34501-34508.

21. U. Hoppe, G. Walter, R. Kranold, D. Stachel and A. Barz, *Journal of Non-Crystalline Solids*, 1995, **193**, 28-31.

22. R. M. Moss, E. A. Abou Neel, D. M. Pickup, H. L. Twyman, R. A. Martin, M. D. Henson, E. R. Barney, A. C. Hannon, J. C. Knowles and R. J. Newport, *Journal of Non-Crystalline Solids*, 2010, **356**, 1319-1324.

23. U. Hoppe, *Journal of Non-Crystalline Solids*, 1996, **195**, 138-147.

24. R. K. Brow, *Journal of Non-Crystalline Solids*, 2000, **263**, 1-28.

25. R. K. Brow, C. C. Phifer, G. L. Turner and R. J. Kirkpatrick, *Journal of the American Ceramic Society*, 1991, **74**, 1287-1290.

26. I. Abrahams, K. Franks, G. E. Hawkes, G. Philippou, J. Knowles, P. Bodart and T. Nunes, *Journal of Materials Chemistry*, 1997, **7**, 1573-1580.

27. F. Fayon, D. Massiot, K. Suzuya and D. L. Price, *Journal of Non-Crystalline Solids*, 2001, **283**, 88-94.

28. Y. Zhang, S. Mukherjee and E. Oldfield, *Journal of the American Chemical Society*, 2005, **127**, 2370-2371.

29. Y.-I. Kim, S. Cadars, R. Shayib, T. Proffen, C. S. Feigerle, B. F. Chmelka and R. Seshadri, *Physical Review B*, 2008, **78**, 195205-195217.

30. A. S. Lipton, R. W. Heck, G. R. Staeheli, M. Valiev, W. A. De Jong and P. D. Ellis, *Journal of the American Chemical Society*, 2008, **130**, 6224-6230.

Chapter 6 Glass-ionomer Cements

6.0 Introduction

Glass-ionomer cements are restorative materials used in dentistry for filling teeth and as luting cements. Recently, there has been an interest in modifying these materials from dentistry to orthopaedic applications, where they can potentially overcome the limitations of polymethyl methacrylate (PMMA) cements, which undergo shrinkage after setting. In addition, PMMA cements set with an exothermic reaction, which causes irritation in the surrounding tissue. Moreover, PMMA cements do not bond chemically with the bone due to the different chemical nature of bone and polymer, whereas glass-ionomer cements have been shown to develop apatite[1], a mineral component of bone[2, 3].

As described in chapter 1, glass-ionomer cements are based on an acid base reaction between a glass powder and a polyalkenoic acid. The glass is usually a flouroalumino silicate. Aluminium plays very important role in the dissolution and setting of these cements[4, 5]. However, there are concerns over the neuro-toxicity of aluminium. In addition, aluminium negatively affects bone mineralization[6-9]. There is therefore a need for aluminium-free cements to be used for orthopaedic applications. In the present work, we have attempted to develop aluminium-free zinc containing phosphate glass based glass-ionomer cements. Phosphates are more closely related to natural bone and are more likely to develop into apatite more easily. Studies have shown that high phosphate content in bioactive glasses enhances apatite formation[10]. Zinc is added to the glass as an alternative to aluminium because zinc is also believed to work as a network intermediate and it is assumed that it will have the same structural role as aluminium in the setting and mechanical strength of the resultant cement. In addition, zinc promotes bone formation[11] and shows a bactericidal effect[12, 13].

Various aluminium-free silicate glass compositions with additional properties such as bactericidal, therapeutic or promotion of remineralisation, have been prepared for orthopaedic applications. Towler *et al*.[12, 14-19] studied various aspects of aluminium-

free zinc containing silicate glass based polyalkenoate cements. Brauer *et al.*[20] prepared bioactive SiO_2:CaO:CaF_2:MgO based bactericidal polyalkenoate injectable cements, with mechanical strengths up to 35 MPa. To our knowledge, no previous work has been carried out on zinc containing phosphate glass based glass-ionomer cements.

6.1 Experimental

6.1.1 Cement Preparation

All cements were made by mixing glass powder with either poly acrylic acid (PAA) or vinyl phosphonic acid-acrylic acid (VPA-AA) co-polymer and distilled water or tartaric acid solution (TA), on a glass slab. Cements were prepared with different glass: poly acid: water ratios as summarised in Table 6.1.

6.1.2 Setting Time

Samples were prepared by filling mixed cement paste in round plastic moulds of 6 mm diameter. Setting time was studied with the help of Gilmore needles as described in chapter 2.

6.1.3 Compressive Strength

Compressive strength was measured for a minimum four samples for each composition as described in chapter2.

Table 6. 1 Summary of attempted cement preparations (G: A: L is glass: acid: liquid ratio, TA is tartaric acid)

Glass series	*x*	Glass composition	Acid	G:A:L	TA
$Na_{1-x}Zn_{1+x/2}(PO_3)_3$	0.5	$8.33Na_2O:41.67ZnO:50P_2O_5$	PAA	4:1:1	
$Na_{1-x}Zn_{1+x/2}(PO_3)_3$	1.0	$50ZnO:50P_2O_5$	PAA	4:1:1	
$NaZn_{1-x}Ca_x(PO_3)_3$	0.0	$16.7Na_2O:33.3ZnO:50P_2O_5$	PAA	4:1:1	
$NaZn_{1-x}Ca_x(PO_3)_3$	0.5	$16.7Na_2O:16.7ZnO:16.7CaO:50P_2O_5$	PAA	4:1:1	
$NaZn_{1-x}Ca_x(PO_3)_3$	1.0	$16.7Na_2O:33.3CaO:50P_2O_5$	PAA	4:1:1	
$NaZn_{1-x}Sr_x(PO_3)_3$	0.5	$16.7Na_2O:16.7ZnO:16.7SrO:50P_2O_5$	PAA	4:1:1	
$NaZn_{1-x}Sr_x(PO_3)_3$	1.0	$16.7Na_2O:33.3SrO:50P_2O_5$	PAA	4:1:1	
$10Na_2O:(20+x/2)ZnO:(20+x/2)CaO:(50-x)P_2O_5$	0	$10Na_2O:20ZnO:20CaO:50P_2O_5$	PAA	4:1:1	
$10Na_2O:(20+x/2)ZnO:(20+x/2)CaO:(50-x)P_2O_5$	5	$10Na_2O:22.5ZnO:22.5CaO:45P_2O_5$	PAA	4:1:1	
$10Na_2O:(20+x/2)ZnO:(20+x/2)CaO:(50-x)P_2O_5$	10	$10Na_2O:25ZnO:25CaO:40P_2O_5$	PAA	4:1:1	
$10Na_2O:(20+x/2)ZnO:(20+x/2)CaO:(50-x)P_2O_5$	15	$10Na_2O:27.5ZnO:27.5CaO:35P_2O_5$	PAA	4:1:1	
$10Na_2O:(20+x/2)ZnO:(20+x/2)CaO:(50-x)P_2O_5$	20	$10Na_2O:30ZnO:30CaO:30P_2O_5$	PAA	4:1:1	
ART1		$25CaO:25Al_2O_3:50SiO_2$	VPAAA	1:4:1	
ART1		$25CaO:25Al_2O_3:50SiO_2$	VPAAA	3:2:1	
ART1		$25CaO:25Al_2O_3:50SiO_2$	VPAAA	4:2:1	
ART1		$25CaO:25Al_2O_3:50SiO_2$	VPAAA	4:1:1	
$NaZn_{1-x}Ca_x(PO_3)_3$	1.0	$16.7Na_2O:33.3CaO:50P_2O_5$	VPAAA	4:1:1.5	
$NaZn_{1-x}Sr_x(PO_3)_3$	0.5	$16.7Na_2O:16.7ZnO:16.7SrO:50P_2O_5$	VPAAA	4:1:1.5	
$10Na_2O:(20+x/2)ZnO:(20+x/2)CaO:(50-x)P_2O_5$	0	$10Na_2O:20ZnO:20CaO:50P_2O_5$	VPAAA	4:1:1.5	
$10Na_2O:(20+x/2)ZnO:(20+x/2)CaO:(50-x)P_2O_5$	5	$10Na_2O:22.5ZnO:22.5CaO:45P_2O_5$	VPAAA	4:1:1.5	
$10Na_2O:(20+x/2)ZnO:(20+x/2)CaO:(50-x)P_2O_5$	10	$10Na_2O:25ZnO:25CaO:40P_2O_5$	VPAAA	4:1:1.5	
$10Na_2O:(20+x/2)ZnO:(20+x/2)CaO:(50-x)P_2O_5$	15	$10Na_2O:27.5ZnO:27.5CaO:35P_2O_5$	VPAAA	4:1:1.5	
$10Na_2O:(20+x/2)ZnO:(20+x/2)CaO:(50-x)P_2O_5$	20	$10Na_2O:30ZnO:30CaO:30P_2O_5$	VPAAA	4:1:1.5	
$10Na_2O:(20+x/2)ZnO:(20+x/2)CaO:(50-x)P_2O_5$	20	$10Na_2O:30ZnO:30CaO:30P_2O_5$	VPAAA	3:2:1.5	
$10Na_2O:(20+x/2)ZnO:(20+x/2)CaO:(50-x)P_2O_5$	20	$10Na_2O:30ZnO:30CaO:30P_2O_5$	VPAAA	4:2:1.5	

Table 6.1 continued

Glass series	*x*	Glass composition	Acid	G:A:L	TA
$10Na_2O$:(30-*x*/2)ZnO:(30- *x*/2)CaO:xSrO:$30P_2O_5$	20	$10Na_2O$:20ZnO:20CaO:20SrO:$30P_2O_5$	VPAAA	3:2:1.5	
$10Na_2O$:(30-*x*/2)ZnO:(30- *x*/2)CaO:xSrO:$30P_2O_5$	20	$10Na_2O$:20ZnO:20CaO:20SrO:$30P_2O_5$	VPAAA	1:1:1.5	
$10Na_2O$:(60-*x*)ZnO:*x*CaO:$30P_2O_5$	0	$10Na_2O$:60ZnO:$30P_2O_5$	VPAAA	3:1:1	
$10Na_2O$:(60-*x*)ZnO:*x*CaO:$30P_2O_5$	10	$10Na_2O$:50ZnO:10CaO:$30P_2O_5$	VPAAA	3:1:1	
$10Na_2O$:(60-*x*)ZnO:*x*CaO:$30P_2O_5$	20	$10Na_2O$:40ZnO:20CaO:$30P_2O_5$	VPAAA	3:1:1	
$10Na_2O$:(60-*x*)ZnO:*x*CaO:$30P_2O_5$	10	$10Na_2O$:50ZnO:10CaO:$30P_2O_5$	VPAAA	3:1:1	1%
$10Na_2O$:(60-*x*)ZnO:*x*CaO:$30P_2O_5$	10	$10Na_2O$:50ZnO:10CaO:$30P_2O_5$	VPAAA	3:1:1	0.5%
$10Na_2O$:(60-*x*)ZnO:*x*CaO:$30P_2O_5$	10	$10Na_2O$:50ZnO:10CaO:$30P_2O_5$	VPAAA	3:1:1	1%
$10Na_2O$:(60-*x*)ZnO:*x*CaO:$30P_2O_5$	10	$10Na_2O$:50ZnO:10CaO:$30P_2O_5$	VPAAA	3:1:1	1.5%
$10Na_2O$:(60-*x*)ZnO:*x*CaO:$30P_2O_5$	10	$10Na_2O$:50ZnO:10CaO:$30P_2O_5$	VPAAA	3:1:1	3%
$10Na_2O$:(60-*x*)ZnO:*x*CaO:$30P_2O_5$	10	$10Na_2O$:50ZnO:10CaO:$30P_2O_5$	VPAAA	3:1:1	5%
$10Na_2O$:(60-*x*)ZnO:*x*CaO:$30P_2O_5$	10	$10Na_2O$:50ZnO:10CaO:$30P_2O_5$	VPAAA	6:1:1	3%
$10Na_2O$:(60-*x*)ZnO:*x*CaO:$30P_2O_5$	10	$10Na_2O$:50ZnO:10CaO:$30P_2O_5$	VPAAA	3:1:1	3%
$10Na_2O$:(60-*x*)ZnO:*x*CaO:$30P_2O_5$	10	$10Na_2O$:50ZnO:10CaO:$30P_2O_5$	VPAAA	2.4:1:1	3%
$10Na_2O$:(60-*x*)ZnO:*x*CaO:$30P_2O_5$	10	$10Na_2O$:50ZnO:10CaO:$30P_2O_5$	VPAAA	6:1:1	5%
$10Na_2O$:(60-*x*)ZnO:*x*CaO:$30P_2O_5$	10	$10Na_2O$:50ZnO:10CaO:$30P_2O_5$	VPAAA	3:1:1	5%
$10Na_2O$:(60-*x*)ZnO:*x*CaO:$30P_2O_5$	10	$10Na_2O$:50ZnO:10CaO:$30P_2O_5$	VPAAA	2.4:1:1	5%

Table 6.1 continued

Glass series	*x*	Glass composition	Acid	G:A:L	TA
x% w/w Gskmmo5.3:(1-*x*)% w/w ($10Na_2O$:50ZnO:10CaO:$30P_2O_5$)	100	Gskmmo5.3	VPAAA	3:1:1	
x% w/w Gskmmo5.3:(1-*x*)% w/w ($10Na_2O$:50ZnO:10CaO:$30P_2O_5$)	5	5% w/w Gskmmo5.3 : 95% w/w ($10Na_2O$:50ZnO:10CaO:$30P_2O_5$)	VPAAA	3:1:1	
x% w/w Gskmmo5.3:(1-*x*)% w/w ($10Na_2O$:50ZnO:10CaO:$30P_2O_5$)	10	10% w/w Gskmmo5.3 : 90% w/w ($10Na_2O$:50ZnO:10CaO:$30P_2O_5$)	VPAAA	3.3:1:1	
x% w/w Gskmmo5.3:(1-*x*)% w/w ($10Na_2O$:50ZnO:10CaO:$30P_2O_5$)	15	15% w/w Gskmmo5.3 : 85% w/w ($10Na_2O$:50ZnO:10CaO:$30P_2O_5$)	VPAAA	3:1:1	
x% w/w Qmmm07:(1-*x*)% w/w ($10Na_2O$:50ZnO:10CaO:$30P_2O_5$)	100	Qmmm07	VPAAA	3.3:1:1	
x% w/w Qmmm07:(1-*x*)% w/w ($10Na_2O$:50ZnO:10CaO:$30P_2O_5$)	5	5% w/w Qmmm07 : 95% w/w ($10Na_2O$:50ZnO:10CaO:$30P_2O_5$)	VPAAA	3.3:1:1	
x% w/w Qmmm07:(1-*x*)% w/w ($10Na_2O$:50ZnO:10CaO:$30P_2O_5$)	10	10% w/w Qmmm07 : 90% w/w ($10Na_2O$:50ZnO:10CaO:$30P_2O_5$)	VPAAA	3.3: 1: 1	
(1-*x*)% w/w ($10Na_2O$:50ZnO:10CaO:$30P_2O_5$): *x*% w/w (HA)	5	95% w/w ($10Na_2O$:50ZnO:10CaO:$30P_2O_5$): 5% w/w (HA)	VPAAA	3:1:1	
(1-*x*)% w/w ($10Na_2O$:50ZnO:10CaO:$30P_2O_5$): *x*% w/w (HA)	10	90% w/w: ($10Na_2O$:50ZnO:10CaO:$30P_2O_5$): 10% w/w (HA)	VPAAA	3:1:1	
(1-*x*)% w/w ($10Na_2O$:50ZnO:10CaO:$30P_2O_5$): *x*% w/w (HA)	15	85% w/w ($10Na_2O$:50ZnO:10CaO:$30P_2O_5$): 15% w/w (HA)	VPAAA	3:1:1	
(1-*x*)% w/w ($10Na_2O$:50ZnO:10CaO:$30P_2O_5$): *x*% w/w (HA)	20	80% w/w ($10Na_2O$:50ZnO:10CaO:$30P_2O_5$): 20% w/w (HA)	VPAAA	3:1:1	

6.1.4 Compressive Strength Measurement After Immersion in Tris Buffer

Cylindrical specimens 6 mm in height and 4 mm in diameter were prepared in stainless steel moulds and left to set for 24 hours in an incubator at 37°C. Set samples were immersed in tris buffer for various time periods. After each time period, samples were removed from the buffer solution and the compressive strength of the wet samples was measured with an Instron universal test machine (Instron 5567, Instron Europe, High Wycombe, UK) with a static load cell ± 1 kN. Specimens were placed in a vertical position with load at a crosshead speed of 1 mm/min until failure occurred. Compressive strength values were calculated by dividing force in N (Newton) by specimen cross section area to get values in MPa (Mega Pascal).

6.1.5 MAS-NMR

^{31}P and ^{27}Al MAS–NMR spectra were recorded on a Bruker Avance 600 MHz spectrometer at resonance frequencies of 242.9 and 156.3 MHz respectively. orthophosphoric acid (85% solution) and 1 M aqueous aluminium nitrate were used as the respective references. Powdered glass samples were measured in a 4 mm o.d. zirconia rotor at a spinning speed of 12 kHz. Recycle delays of 60 s and 0.5 s were used for ^{31}P, ^{23}Na and ^{27}Al scans respectively with a total of 16 scans in the case of ^{31}P and 1024 for ^{27}Al.

6.2 Results and Discussion

6.2.1 Polyacrylic Acid Cements

Results of preliminary attempts to form cements from different glass compositions and polyacrylic acid (PAA) are summarised in Table 6.2. None of the investigated glass compositions formed cements with PAA.

Table 6.2 Summary of results for cements of metaphosphate glasses with polyacrylic acid (G: A: L is glass: acid: liquid)

Glass composition	Polymeric acid	G: A: L	Inference
$Na_{1-x}Zn_{1+x/2}(PO_3)_3$ x = 0.5, 1.0	Polyacrylic acid	4:1:1	No reaction
$NaZn_{1-x}Ca_x(PO_3)_3$ x = 0, 0.5, 1.0	Polyacrylic acid	4:1:1	No reaction
$NaZn_{1-x}Sr_x(PO_3)_3$ x = 0, 0.5, 1.0	Polyacrylic acid	4:1:1	No Reaction
$10Na_2O$:$(20+x/2)$ZnO:$(20+x/2)$ CaO:$(50-x)P_2O_5$ x = 0, 5,10,15,20	Polyacrylic acid	4:1:1	No reaction.

6.2.2 (VPA-AA) Co-polymer Cements

6.2.2.1 (VPA-AA) Co-polymer Reactivity

Salts of (VPA-AA) co-polymer with ZnO, $Ca(OH)_2$ and NaOH were prepared in order to check the reactivity of (VPA-AA) co-polymer with sodium, calcium and zinc ions and the effect on ^{31}P chemical shift. A 0.1M solution or powder of the metal oxide or hydroxide was mixed with (VPA-AA) co-polymer powder (1:1 ratio), dried in air and then ground into powder for ^{31}P MAS-NMR spectra.

Fig. 6.1 shows the ^{31}P MAS-NMR spectra of (VPA-AA) co-polymer salts of sodium, calcium and zinc. It is observed from the spectra that the isotropic resonance peak shifts towards less positive values with salt formation, due to the higher electronegativity and shielding effect of the metal cations as compared to the acid protons.

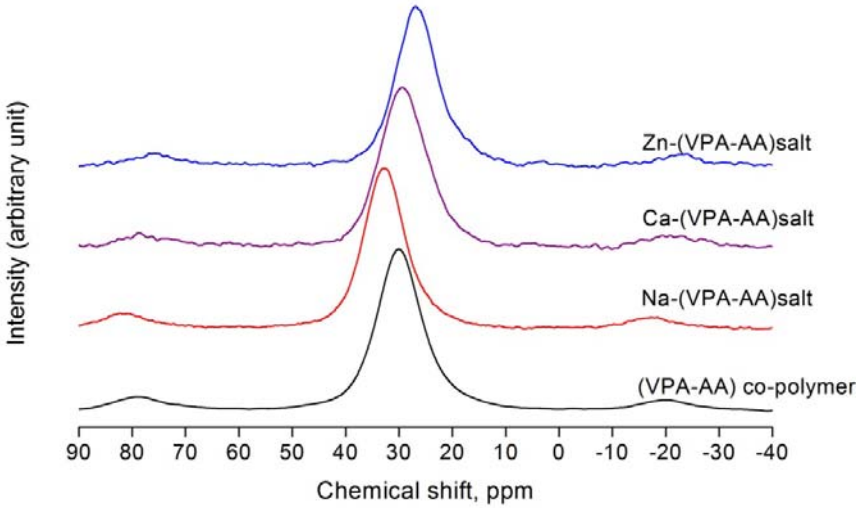

Fig. 6. 1. ^{31}P MAS-NMR spectra of (VPA-AA) and its salts with NaOH, $Zn(OH)_2$, $Ca(OH)_2$.

6.2.2.2 Silicate Glass ART 1 and (VPA-AA) Co-polymer Cements

ART 1 glass ($CaO:Al_2O_3:2SiO_2$), the first glass used to make glass-ionomer cement with poly acrylic acid, was used to produce cement with (VPA-AA) co-polymer to check the reactivity of this polymer to form glass-ionomer cement. The cement was completely set after 24 hrs.

^{31}P MAS-NMR spectra of set cements with different glass to acid ratios are presented in Fig. 6.2 (a). (VPA-AA) co-polymer shows an isotropic chemical shift at about 31 ppm. All cement spectra show much broader peaks, with less positive chemical shift compared to that of the parent (VPA-AA) co-polymer. The chemical shift moves towards less positive values with increasing glass:acid ratio, with the chemical shift for the cement formed at a 4:1 glass:acid ratio being the least positive.

Fig. 6.2(b) shows ^{27}Al MAS-NMR spectra of cements with different glass to acid ratio together with that of the original glass. The glass shows a main peak at about 60 ppm which is assigned to four coordinate Al (IV) and a shoulder at about 30 ppm assigned to five coordinate Al (V)[21]. A very small peak observed at about -10 ppm,

which corresponds to six coordinate Al (VI)[22]. All cement spectra show peaks corresponding to Al (IV), (V) and (VI) at about 55 ppm, 34 ppm and -10 ppm, respectively. The intensity of the peak corresponding to Al (VI) increases with increasing glass:acid ratio. Al (VI) cross links the phosphonic and carboxyl groups of VPA-AA co-polymer and strengthens the cement.

(a)

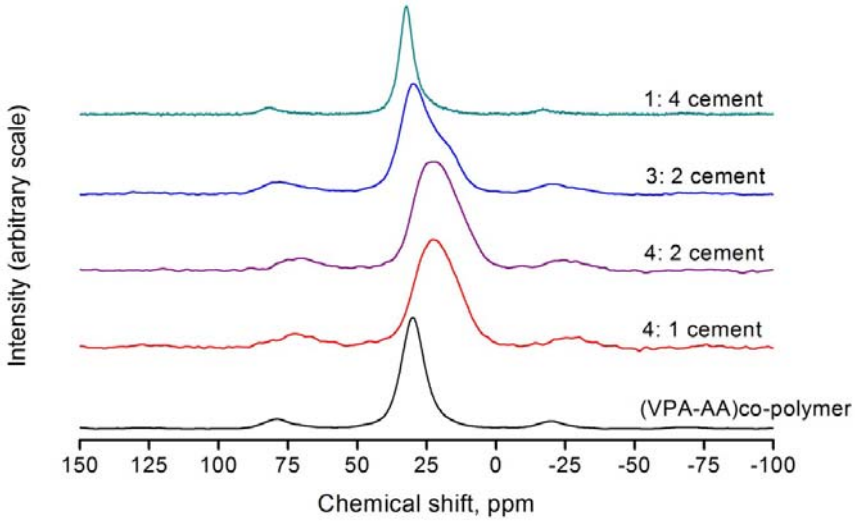

(b)

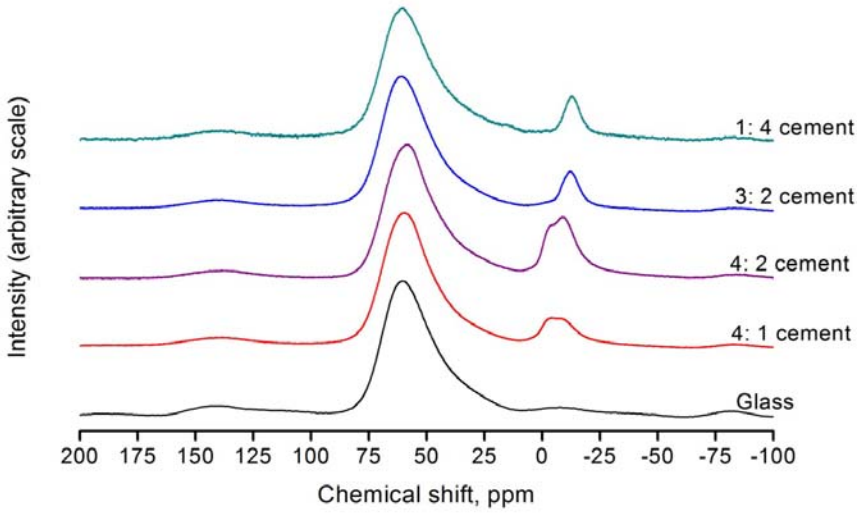

Fig. 6. 2. (a) ^{31}P and (b) ^{27}Al MAS-NMR spectra of (VPA-AA) co-polymer and its cements with ART 1 glass with different glass to acid ratios.

6.2.2.3 Phosphate Glass and (VPA –AA) Co-polymer Cements

Glass compositions $10Na_2O:(20+x/2)ZnO:(20+x/2)CaO:(50-x)P_2O_5$ (x = 5, 10, 15 and 20) and $16.7Na_2O:33.3\text{-}33.3xZnO:33.3xCaO:50P_2O_5$ (i.e. $NaZn_{1-x}Ca_x(PO_3)_3$) (x = 0.5 and 1.0) were used to prepare cements from (VPA-AA) co-polymer powder and water at a ratio of 4:1:1.5 respectively. These glass compositions produced cements, however the setting times were greater than 24 h.

6.2.2.4 Hydrolytic Stability of Set Cements

Visual solubility results after 24 hours are presented in Table 6.3. Cements from metaphosphate glass compositions dissolved completely after 24 hours, whereas those from glasses with lower phosphate content showed only partial or no visible dissolution.

Table 6.3 Dissolution of cements of different glass composition with (VPA-AA) co-polymer

Glass composition	*x*-value	Solubility
$16.7Na_2O:33.3\text{-}33.3xZnO:33.3xCaO:50P_2O_5$	0.5	Dissolved Completely
$16.7Na_2O:33.3\text{-}33.3xZnO:33.3xCaO:50P_2O_5$	1.0	Dissolved Completely
$10Na_2O:(20+1/2x)ZnO:(20+1/2x)CaO:(50-x)P_2O_5$	5	Partially dissolved
$10Na_2O:(20+1/2x)ZnO:(20+1/2x)CaO:(50-x)P_2O_5$	10	Partially dissolved
$10Na_2O:(20+1/2x)ZnO:(20+1/2x)CaO:(50-x)P_2O_5$	15	No significant dissolution
$10Na_2O:(20+1/2x)ZnO:(20+1/2x)CaO:(50-x)P_2O_5$	20	No significant dissolution

Based on the hydrolytic stability results, the glass composition $10Na_2O:30ZnO:30CaO:30P_2O_5$ (x = 20) was further investigated. Fig. 6.3 shows ^{31}P MAS-NMR spectra of cements from this glass composition and (VPA-AA) co-polymer with different glass to acid ratio, together with that from the original glass. The glass shows two main resonances at about -5.5 p.m. and 5.0 ppm corresponding to Q^1 and Q^0 species, respectively, whereas the original co-polymer shows a resonance at about 31 ppm. A decrease in intensity of the peak corresponding to Q^0 is observed in cements, with a decrease in isotropic chemical shift for both species. The resonance

corresponding to the phosphonic group of the co-polymer is observed slightly downfield in the cements compared to the original polymer. A very small sharp peak at about 0 ppm is observed in the 3:2 ratio cement, which indicates the formation of a crystalline phase.

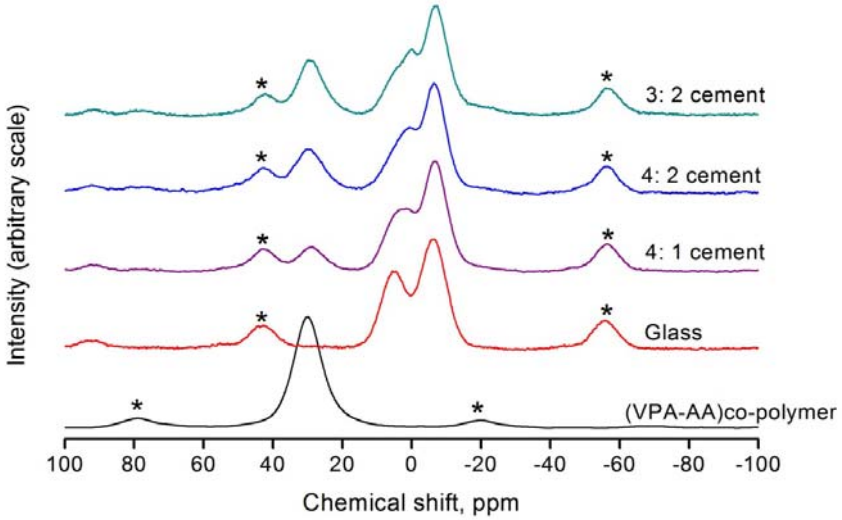

Fig. 6. 3. ^{31}P MAS-NMR spectra of (VPA-AA) co-polymer and glass composition $10Na_2O:30ZnO:30CaO:30P_2O_5$ (*x* = 20) and their cements at different glass:acid ratio. * marks represent spinning side bands.

6.2.3 Optimisation of Invert Phosphate Glass Composition

In order to improve the properties of the cement based on the invert glass composition $10Na_2O:30ZnO:30CaO:30P_2O_5$, various modifications of this glass composition were investigated.

6.2.3.1 Addition of Strontium Oxide

Strontium oxide was added to the above original glass at the expense of CaO and ZnO. The glass composition $10Na_2O:20ZnO:20CaO:20SrO:30P_2O_5$, showed no improvement in setting time. Fig 6.4 shows ^{31}P MAS-NMR spectra of the strontium substituted glass and its cements. The glass shows resonances corresponding to Q^1 and

Q^0. No significant difference is observed in glass and cement spectra apart from a slight decrease in the amount of Q^0 species.

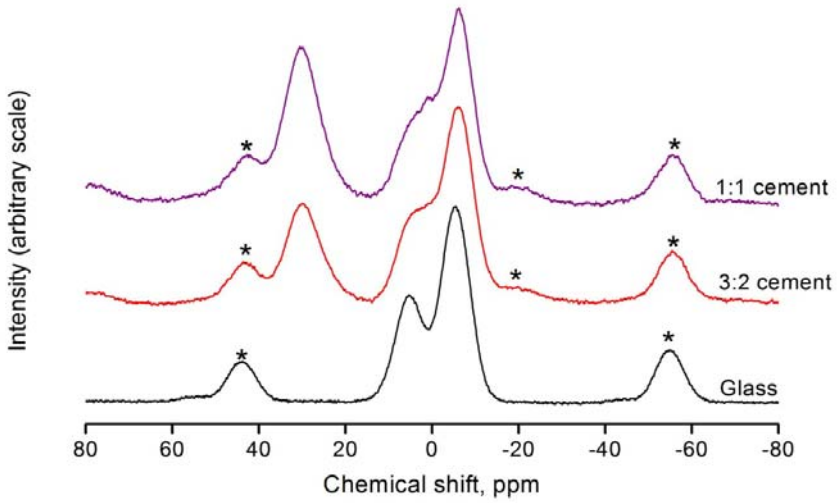

Fig. 6. 4. ^{31}P MAS-NMR spectra of glass composition $10Na_2O:20ZnO:20CaO:20SrO:30P_2O_5$ and its cements with (VPA-AA) co-polymer. * symbols represent spinning side bands. * marks represent spinning side bands.

6.2.3.2 Glass Compositions $10Na_2O:(60-x)ZnO:xCaO:30P_2O_5$ (x = 0,10,20)

Glass compositions of general formula $10Na_2O:(60-x)ZnO:xCaO:30P_2O_5$ with varying amount of ZnO and CaO were used to make cements with (VPA-AA) co-polymer and water. Setting time and glass to acid ratio are tabulated in Table 6.4. Setting time is seen to vary with ZnO content. The glass composition with x = 10 exhibited the minimum initial and final setting times.

Table 6.4 Setting time of cements of glass compositions $10Na_2O:(60-x)ZnO:xCaO:30P_2O_5$ with (VPA-AA) co-polymer

x value	G: A: L	Initial setting time (min)	Final setting time (hrs)
0	3: 1: 1	25-30	> 2
10	3: 1: 1	20-25	1 – 1.3
20	3: 1: 1	> 60	> 24

^{31}P MAS-NMR spectra of above set cements are presented in Fig. 6.5(a) and can be compared with the spectra of the glasses in Fig. 6.5(b) All glass compositions show resonances at about -10 ppm and 5 ppm corresponding to Q^1 and Q^0 species as expected, based on the phosphate content. The ^{31}P MAS-NMR spectra of cements show narrower peaks and an additional shoulder at about -12 ppm, which is an indication of the reaction between the glass and (VPA-AA) co-polymer and formation of some crystalline phase in the set cements.

(a)

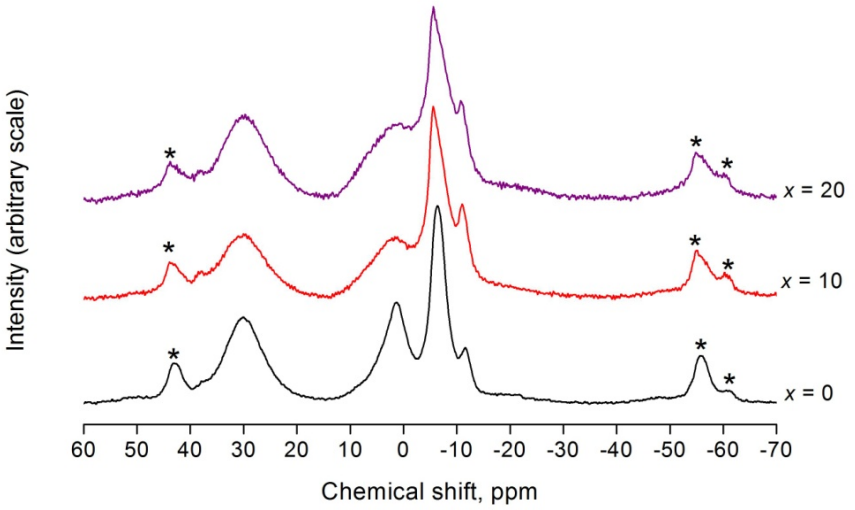

(b)

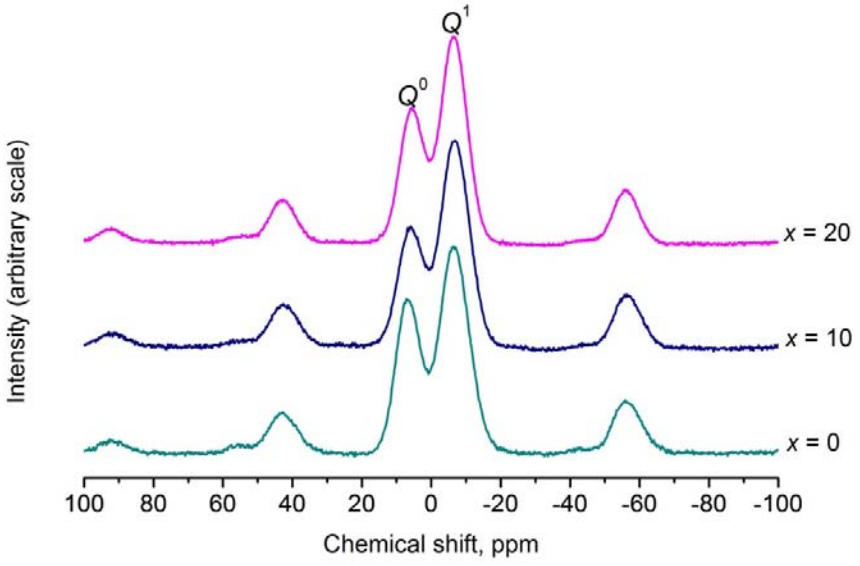

Fig. 6. 5. ^{31}P MAS-NMR spectra of (a) cements from glass compositions $10Na_2O$:(60-*x*)ZnO:*x*CaO:$30P_2O_5$ and (VPA-AA) co-polymer; (b) glass compositions $10Na_2O$:(60-*x*)ZnO:*x*CaO:$30P_2O_5$. * marks represent spinning side bands.

6.2.3.3 Addition of Tartaric Acid (TA)

Glass composition $10Na_2O:(60-x)ZnO:xCaO:30P_2O_5$ (x = 10) was considered the best composition in terms of setting time. However, the setting time for this composition was still not ideal. Tartaric acid decreases the setting time by chelating with metal cations leached from glass. 1% TA solution was used to make cement from this glass compositions and (VPA-AA) co-polymer. ^{31}P MAS-NMR spectra of set cement prepared from 1% TA is compared with the cement prepared from water is compared in Fig. 6.6, whereas initial and final setting time are compared in Table 6.5. Both spectra indicate the formation of some crystalline pyrophosphate phase. No significant difference is observed two spectra apart from shaper peaks observed in the spectrum of cement prepared from water. 1% TA did not decrease the setting time considerably.

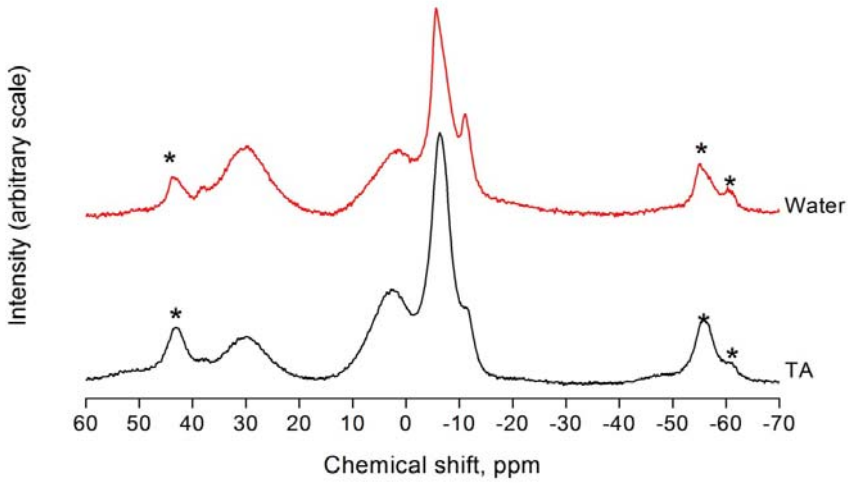

Fig. 6. 6. ^{31}P MAS-NMR spectra of cements prepared from glass composition $10Na_2O:(60-x)ZnO:xCaO:30P_2O_5$ (x = 10) with 1% tartaric acid solution (TA) and water. * marks represent spinning side bands.

Table 6.5 Setting time of cements of glass compositions $10Na_2O:(60-x)ZnO:xCaO:30P_2O_5$ (x = 1) with (VPA-AA) co-polymer

	G: A: L	Initial setting time (min)	Final setting time (hrs)
Water	3: 1: 1	20-25	1-1.3
TA	3: 1: 1	25-28	1-1.4

6.2.3.4 Optimisation of Setting Time

Improvement in the setting reaction was investigated in following ways.

6.2.3.4.1 Tartaric Acid Concentration

Setting time was optimised by varying the concentration of TA with a fixed glass to acid ratio. Setting time with different TA concentrations are presented in Table 6.6. The results indicate optimum setting times at 3 to 5% TA.

Table 6.6 Effect of tartaric acid concentration on cement setting time.

TA conc %	Initial setting time (min)
0.5	> 30
1	24
1.5	20
3	20
5	15

6.2.3.4.2 Glass to Acid Ratio

Setting time was measured as a function of glass:acid ratio at fixed TA concentrations. The results are presented in Table 6.7.

Table 6.7 Effect of changing glass to (VPA-AA) co-polymer (G/A) ratio on cement setting time.

G/A	Initial setting time (min)	TA %
6	24	3
3	10	3
2.4	10	3
6	25	5
3	18	5
2.4	17	5

Minimum setting time was observed with 3% TA and 3 and 2.4 G/A ratio. The compressive strength of cements prepared from 3% TA and 3 G/A ratio was measured after 3 days in order to compare it with cement prepared from the same G/A ratio but with no TA. The results are summarised in Table 6.8.

Table 6. 8 Compressive strength (CS) of cements prepared from glass composition $10Na_2O$: 60-xZno: xCaO: $30P_2O_5$. (x = 10) with different tartaric acid (TA) concentrations compared with the commercial Rock Salt GIC. (esd ±5 MPa)

TA%	G : PA: L	CS MPa
3	3: 1: 1	57.5
0	3: 1 : 1	78
Rock salt		120

It is observed from these results that the addition of tartaric acid reduced initial setting time however it negatively affected the mechanical strength of set cements.

6.2.3.5 Addition of Silicate Glass

Most commercial glass-ionomer cements involve a silicate glass, which gives the cement greater compressive strength. In order to investigate whether inclusion of a silicate glass improves the cement properties two silicate formulations, Gskmm0 ($45SiO:24.92Na_2O:27.54CaO:2.54P_2O_5$) and Qmmm07 ($34.6SiO_2:50.4CaO:5.7P_2O_5:9.3CaF_2$) were added in different proportions to the $10Na_2O:50ZnO:10CaO:30P_2O_5$ glass composition and cements formed using VPA-AA and water. Table 6.9 summarises the measured setting times.

Table 6.9 Setting times of cements formed from silicate glasses and $10Na_2O:50ZnO:10CaO:30P_2O_5$

Silicate glass	Weight % silicate glass	G:A:L	Initial setting time	Final Setting time
Gskmmo5.3	100	3: 1: 1	Did not produce cement	
Gskmmo5.3	5	3: 1: 1	> 1hr	
Gskmmo5.3	10	3.3: 1: 1	20-25 min	> 2 hrs
Gskmmo5.3	15	3: 1: 1	15-20 min	1.5 hrs
Qmmm07	100	3.3: 1: 1	Did not produce cement	
Qmmm07	5	3.3: 1: 1	30-35 min	2hr
Qmmm07	10	3.3: 1: 1		1.5hrs

Addition of 15% Gskmmo5.3 gave a small improvement in setting time compared to the pure phosphate glass (Table 6.4). However, samples were not hydrolytically stable as they cracked after immersion in tris buffer and SBF and therefore CS could not be measured. It was concluded that addition of silicate glass did little to improve the properties of the cement.

6.2.3.6 Addition of Hydroxyapatite (HA)

The effect of inclusion of commercial hydroxyapatite (HA) with the glass component was investigated in order to improve the bone adhesion properties of the cement, without adversely affecting its setting and mechanical properties. Three compositions were studied with 5, 10, and 20 weight % HA (i.e. (1-*x*)% w/w ($10Na_2O:50ZnO:10CaO:30P_2O_5$): *x*% w/w (HA). The properties of the resulting cements are presented in Table 6.10. Addition of HA decreases the setting time and increases compressive strength after immersion in tris buffer.

Table 6. 10 Setting times and compressive strengths of HA incorporated cements (compressive strength measured after immersion in Tris buffer for 7 days).

HA%	Initial setting time (min)	Final setting time (min)	CS MPa
0	20-25	60-70	13
10	15	40-45	18
20	15	35	16

Fig. 6.7 shows the XRD patterns of the cement samples before (Fig. 6.7(a)) and after immersion in tris buffer for 1 week. (Fig. 6.7(b)) The pattern for the cement formed with no HA component shows only very weak Bragg peaks and is predominantly amorphous. The XRD patterns of all HA containing cements, prior to immersion, show sharp peaks between 20° and 35° 2θ, corresponding to HA. This is in good agreement with previous studies on aluminosilicate glass based GICs[23, 24]. After immersion in tris buffer for 1 week, all cement samples develop sharp peaks between 5°-10° 2θ, indicating the formation of crystalline phase(s). There is little further change in the XRD patterns after 4 weeks immersion (Fig. 6.8).

(a)

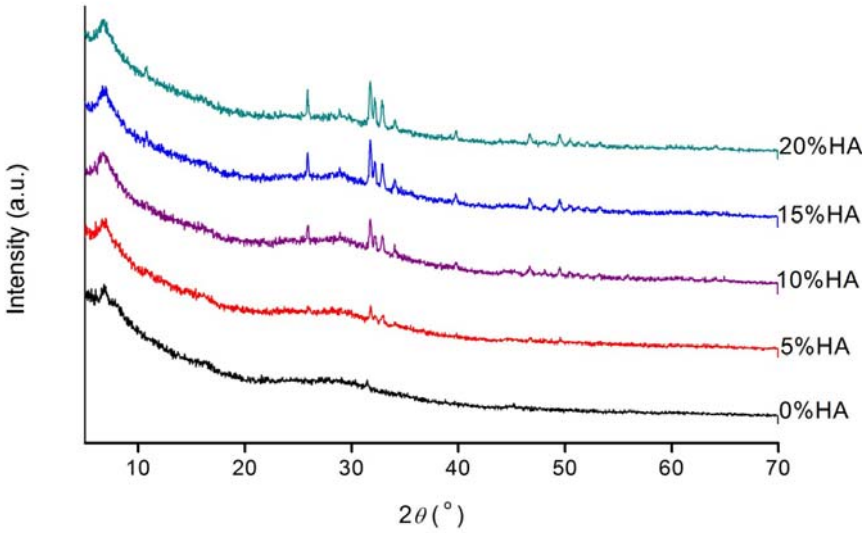

(b)

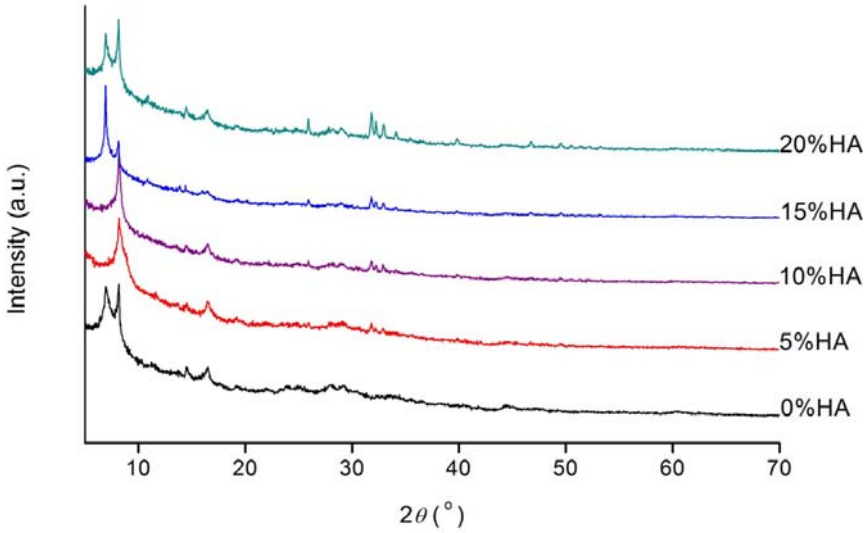

Fig. 6. 7. XRD patterns of HA substituted cement samples (a) prior to immersion (b) after immersion in tris buffer for 1 week.

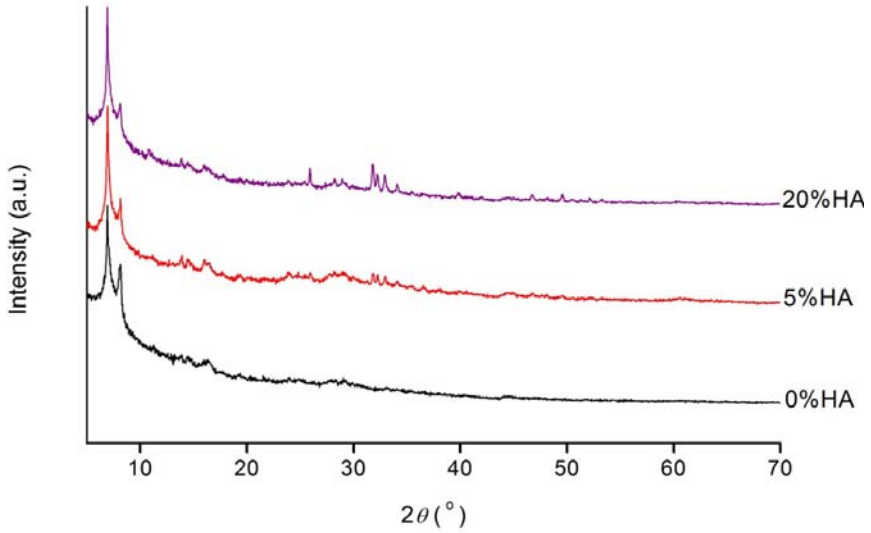

Fig. 6. 8. XRD patterns of HA substituted cement samples after immersion in tris buffer for 4 weeks.

^{31}P MAS-NMR spectra of the cement samples before and after immersion in tris buffer up to 1 year are shown in Fig. 6.9. Cement samples with no HA show relatively narrow peaks at about -7 ppm and -10 ppm corresponding to Q^1 species, in addition to the broad peak at about 6 ppm corresponding to Q^0 species in the precursor glass. HA incorporated samples show a sharp peak at about 2.9 ppm corresponding to HA in addition to those of the glass phase.

In order to quantify the amount of HA remaining in the cement after immersion in tris buffer for various time periods, the spectra were fitted (Fig. 6.10). The derived spectral parameters are given in Table 6.11. The relative intensities of the peaks corresponding to pyrophosphate species decreases as the cement matures, whereas the intensity of the broad peak corresponding to Q^0 species increases with the chemical shift moving towards less positive value and an increase in FWHM. No significant difference is observed in the intensity of the HA peak after immersion in tris buffer for various periods of time.

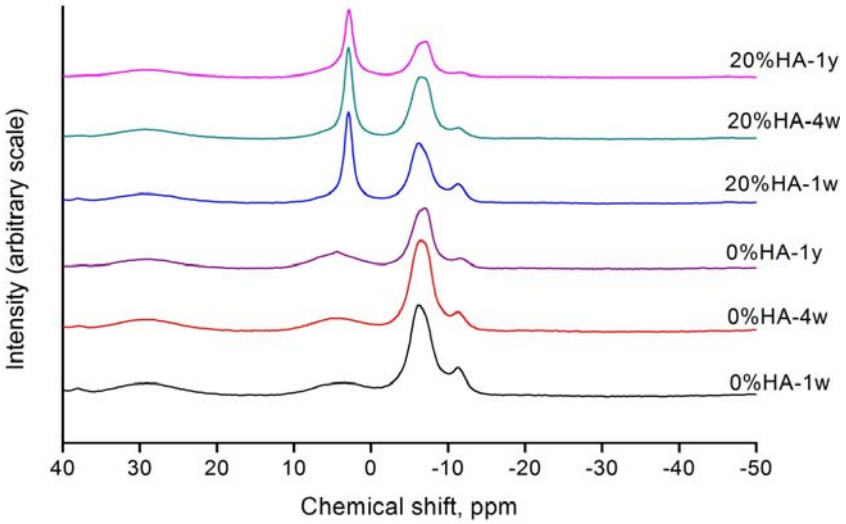

Fig. 6. 9. ^{31}P MAS-NMR spectra of pure glass and HA containing cement samples after immersion in tris buffer (w = week, y = year).

Table 6.11 ^{31}P MAS-NMR spectral parameters for 20%HA incorporated cement samples after immersion in tris buffer for various time periods.

Sample	δ, ppm	FWHM, ppm	Q^n	%Intensity
1 week	2.94	1.29	Q^0	37
	6.22	3.86	Q^0	3
	-6.38	3.07	Q^1	50
	-11.22	2.28	Q^1	10
4 weeks	2.94	1.30	Q^0	39
	6.17	4.00	Q^0	4
	-5.83	2.40	Q^1	33
	-7.16	2.02	Q^1	17
	-10.81	3.50	Q^1	8
1 year	2.94	1.25	Q^0	39
	4.67	5.69	Q^0	15
	-6.25	2.37	Q^1	27
	-7.0	1.50	Q^1	16
	-11.4	2.05	Q^1	3

(a)

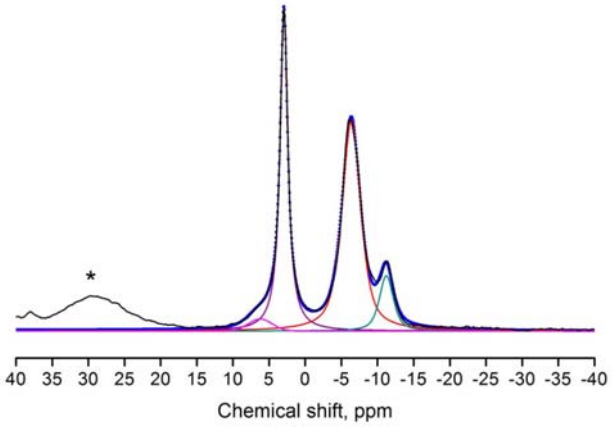

(b)

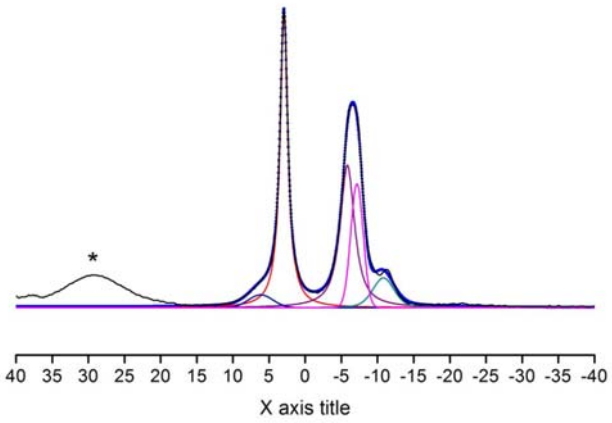

(c)

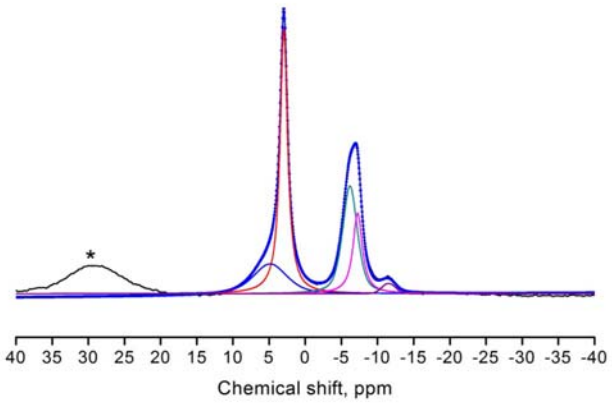

Fig. 6. 10. Fitted ^{31}P MAS-NMR spectra of HA incorporated cement sample after immersion in Tris buffer (a) 1 week, (b) 4 weeks and (c) 1 year.

During the setting process the (VPA-AA) co-polymer attacks the glass and releases ions such as Ca^{2+}, Na^{+} and Zn^{2+}. A decrease in setting time by incorporation of HA indicates that HA releases more calcium ions to chelate the polyalkenoic acid after the initial acid attack. There is no decrease in intensity of the apatite ^{31}P NMR after immersion in tris buffer, which indicates that once the cement is set, HA is not hydrolysed or further involved in the acid base reaction of the cement.

6.3 Conclusions

None of the investigated phosphate glasses formed cements with PAA. VPA-AA copolymer readily formed salts with Ca^{2+}, Zn^{2+} and Na^{+} ions and was successfully used to prepare cements from a number of phosphate formulations, as well as a representative silicate glass formulation ART1. The glass formulation $10Na_2O{:}30ZnO{:}30CaO{:}30P_2O_5$ showed good hydrolytic stability, but had a relatively long setting time in excess of 24 h. Inclusion of the contrast agent SrO in the formulation had little effect on the setting time.

The formulation $10Na_2O{:}50ZnO{:}10CaO{:}30P_2O_5$ was found to give reasonable setting times, which were further improved by inclusion of 3-5% tartaric acid in the liquid component. However this had the effect of decreasing the compressive strength. Glass to acid ratios close to 3:1 were found to be optimal. Incorporation of silicate glasses in the formulation did little to improve setting times and made the cements less hydrolytically stable. Incorporation of HA was found to decrease setting time and increase compressive strength of cements after immersion in tris buffer.

6.4 References

1. S. Sauro, R. Osorio, R. Fulgencio, T. F. Watson, G. Cama, I. Thompson and M. Toledano, *Journal of Materials Chemistry B*, 2013, **1**, 2624-2638.
2. L. Gineste, M. Gineste, X. Ranz, A. Ellefterion, A. Guilhem, N. Rouquet and P. Frayssinet, *Journal of Biomedical Materials Research*, 1999, **48**, 224-234.
3. M. C. Chang, C. C. Ko and W. H. Douglas, *Biomaterials*, 2003, **24**, 2853-2862.
4. J. W. Nicholson and B. Czarnecka, *Journal of Biomaterials Applications*, 2009, **24**, 293-308.
5. T. Munhoz, N. Karpukhina, R. G. Hill, R. V. Law and L. H. De Almeida, *Journal of Dentistry*, 2010, **38**, 325-330.
6. S. V. Verstraeten, L. Aimo and P. I. Oteiza, *Archives of Toxicology*, 2008, **82**, 789-802.
7. H. M. Bolt and J. G. Hengstler, *Archives of Toxicology*, 2008, **82**, 787-788.
8. N. Zainuddin, N. Karpukhina, R. G. Hill and R. V. Law, *Dental Materials*, 2009, **25**, 290-295.
9. M. C. Blades, D. P. Moore, P. A. Revell and R. Hill, *Journal of Materials Science-Materials in Medicine*, 1998, **9**, 701-706.
10. M. Mneimne, R. G. Hill, A. J. Bushby and D. S. Brauer, *Acta Biomaterialia*, 2011, **7**, 1827-1834.
11. A. Ito, M. Otsuka, H. Kawamura, M. Ikeuchi, H. Ohgushi, Y. Sogo and N. Ichinose, *Current Applied Physics*, 2005, **5**, 402-406.
12. O. Clarkin, A. Wren, R. Thornton, J. Cooney and M. Towler, *Journal of Biomaterials Applications*, 2011, **26**, 277-292.
13. P. W. R. Osinaga, R. H. M. Grande, R. Y. Ballester, M. R. L. Simionato, C. Rodrigues and A. Muench, *Dental Materials*, 2003, **19**, 212-217.
14. D. Boyd and M. R. Towler, *Journal of Materials Science-Materials in Medicine*, 2005, **16**, 843-850.
15. D. Boyd, M. R. Towler, R. V. Law and R. G. Hill, *Journal of Materials Science-Materials in Medicine*, 2006, **17**, 397-402.
16. D. Boyd, O. M. Clarkin, A. W. Wren and M. R. Towler, *Acta Biomaterialia*, 2008, **4**, 425-431.

17. A. Wren, D. Boyd and M. R. Towler, *Journal of Materials Science-Materials in Medicine*, 2008, **19**, 1737-1743.

18. A. W. Wren, A. Coughlan, M. M. Hall, M. J. German and M. R. Towler, *Journal of Materials Science-Materials in Medicine*, 2013, **24**, 2255-2264.

19. A. W. Wren, D. Boyd, R. Thornton, J. C. Cooney and M. R. Towler, *Journal of Biomedical Materials Research Part B-Applied Biomaterials*, 2009, **90B**, 700-709.

20. D. S. Brauer, N. Karpukhina, G. Kedia, A. Bhat, R. V. Law, I. Radecka and R. G. Hill, *Journal of the Royal Society Interface*, 2013, **10**, 20120647.

21. K. MacKenzie and M. E. Smith, *Multinuclear Solid-State NMR of Inorganic Materials*, Pergamon, 2002.

22. G. Gongyi, *Solid state nuclear magnetic resonance*, 1998, **13**, 119-122.

23. A. Moshaverinia, S. Ansari, M. Moshaverinia, N. Roohpour, J. A. Darr and I. Rehman, *Acta Biomaterialia*, 2008, **4**, 432-440.

24. Y. W. Gu, A. U. J. Yap, P. Cheang and K. A. Khor, *Biomaterials*, 2005, **26**, 713-720.

Chapter 7 Concluding Remarks

The structures of phosphate glasses of different compositions and their potential to form glass-ionomer cements with acrylic acid and vinyl phosphonic acid co-polymer has been described in this thesis. The applications of solid state NMR techniques, involving the use of several methods aimed at the observation of through space coupling between ½ spin ^{31}P nuclei and low gamma quadrupolar 5/2 spin ^{67}Zn nuclei as well as investigation of their corresponding NMR parameters and fitting of neutron diffraction data has enabled an extensive characterisation of phosphate glasses, an important class of biomaterial. In addition to the different conclusions about different types of phosphate glasses and resultant cements described at the ends of corresponding chapters some general conclusions about the work in thesis are highlighted here.

Structural studies began with the binary zinc metaphosphate system, $Zn(PO_3)_2$, including the glass and corresponding crystalline polymorphs, and continued with the ternary glass system $Na_{1-x}Zn_{1+x/2}(PO_3)_3$ and the quaternary glass system $NaZn_{1-x}M_x(PO_3)_3$. ^{67}Zn NMR spectroscopy of crystalline zinc metaphosphates gave line shapes for tetrahedral and octahedral coordinations of zinc, however glass compositions show a featureless shape, indicative of a disordered environment for Zn. It is well known that distortion of bonds around certain nuclei cause the distribution of NMR parameters such that it gives rise to a Gaussian like line shape[1-3]. Simulations of ^{67}Zn NMR spectra of glass compositions confirmed tetrahedral zinc as the predominant species in the studied glasses, which was further supported by neutron diffraction data.

The structure-solubility relationship was studied in quaternary phosphate glasses with general formula $10Na_2O:(20+x/2)ZnO:(20+x/2)CaO:(50-x)\ P_2O_5$ ($0 \leq x \leq 20$), which includes glass compositions from metaphosphate to invert phosphate. The presence of zinc allowed glass formation with phosphate contents as low as 30 mol%. Metaphosphate glass compositions are highly soluble due to the abundance of easily hydrolysable P–O–P linkages, as already known and confirmed in this work. This results in a decrease in pH of the surrounding medium. Solubility decreases with decreasing

phosphate content and increasing CaO and ZnO content. Ca^{2+} and Zn^{2+} ion cross linking increases in the invert phosphate glasses, making them less soluble in aqueous media. $^{31}P–^{31}P$ double quantum correlation experiments show the presence of P–O–Zn bonds and the higher solubility suggests that this linkage is equally prone to hydrolysis. No significant difference in coordination environment of zinc is observed through the range of glasses from metaphosphate to invert phosphate. Glass compositions with phosphate contents from 45 mol% to 40 mol% were found to be suitable compositions for potential biomedical applications in terms of their degradation rate and effect on pH of the surrounding medium. However further biological studied are required depending on the type of application.

The structural investigation of two series of invert phosphate glasses with general formula $10Na_2O:(60–x)ZnO:xCaO:30P_2O_5$ and $10Na_2O:(50–x)ZnO:xCaO:40P_2O_5$ revealed the insertion of ZnO_4 tetrahedra between PO_4 tetrahedra, thus forming —O—Zn—O—P—O—P— type chains.

It has been shown that invert phosphate glasses with high zinc content have the potential to form glass-ionomer cements for at least non-load bearing applications. These materials can also be used for 3D printed biodegradable bone scaffolds due to hydrolysable nature of (vinylphosphonic acid – acrylic acid) co-polymer. Incorporation of HA improves the properties of cements in terms of setting time and mechanical strength. As seen in the ^{31}P MAS-NMR spectra of cements immersed in tris buffer for about 1 year, the presence of HA has a positive effect. Additionally, its presence could initiate deposition of HA and the formation of natural bone in a physiological environment.

Solid state NMR methodologies to study highly sensitive nuclei in crystalline and amorphous systems have been successfully used in this work. Investigation of the structure of glasses for use in biomedical applications is crucial in designing new compositions, since the structure determines the properties. So far, the techniques employed by biomedical scientists to explore the structure of glasses has been mainly restricted to single pulse MAS-NMR of nuclei such as ^{31}P, ^{29}Si , ^{19}F and ^{11}B and to some extent neutron diffraction. It is hoped that this work will stimulate the use of advanced

techniques in NMR to study other low gamma quadrupolar biologically important nuclei such as magnesium, strontium etc. and cover the gap between the availability of solid state NMR methodologies and super conducting ultra-high field magnets. It is therefore pertinent to use these techniques to explore the structure of biologically important materials and, with a view to developing new materials as well as the development of the techniques themselves.

7.1 Further Research Work

Phosphate glass compositions developed for glass-ionomer cements can be improved to yield cements with improved mechanical properties e.g by addition of gallium oxide. This should decrease the setting time and increase compressive strength. In addition mechanical properties of cements could also be improved by addition of nano hydroxyapatite and flouroapatite.

Solid state NMR techniques can be further utilized to understand the structure of phosphate based glasses and hence develop glass compositions for various applications, e.g the Refocused INADEQUATE pulse sequence could be used to measure through bond coupling and hence confirm the structural role of zinc or other intermediate cations.

Calcium ions are important cations in glasses for biomaterial applications. Results in this study have revealed interesting information about the calcium environment in different glass compositions. ^{43}Ca NMR spectroscopy could be used to investigate the coordination environment of Ca^{2+} in glasses and predict their properties.

Further work is required to develop the RMC modelling of the neutron diffraction data to yield longer range structural models of the studied glass compositions. These calculations will be greatly aided by density functional theory (DFT) calculations to yield energetically sensible starting models for the RMC calculations.

7.2 References

1. S. E. Ashbrook and M. E. Smith, *Chemical Society Reviews*, 2006, **35**, 718-735.
2. A. SuTrisno, V. V. Terskikh and Y. Huang, *Chemical Communications*, 2009, 186-188.
3. A. S. Lipton, R. W. Heck, G. R. Staeheli, M. Valiev, W. A. De Jong and P. D. Ellis, *Journal of the American Chemical Society*, 2008, **130**, 6224-6230.

Appendices

Appendix A1 Supplementary Information for Chapter 2

A1.1 Neutron Diffraction Data Analysis

A1.1.1 Software Installation

To be able to process and analyse GEM data following software were downloaded and installed.

OpenGenie

Available from http://www.opengenie.org/Main_Page

OpenGenie was set up following the simple setup instructions

Gudrun

GUDRUN2 was used in combination with OPENGENIE and xsect to analyse data and fit total correlation function T(r) to get pair distances and coordination number, whereas data were analysed using GUDRUN4 to use for RMC calculations.

Gudrun4 was downloaded from http://www.disordmat.moonfruit.com/

Gemsqraw

Available from http://wwwisis2.isis.rl.ac.uk/disordered/ACH/Software/index.htm

Following environment variables were created in the computer.

Variable Name	***Variable value***	
gem_data	c:/gem/gem_data/	
gcl	c:/gem/gemsqraw/gcl/	
gsq_source	c:/gem/gemsqraw/source/	
gem_tables	c:/gem/gemsqraw/tables/	
vansm	c:/gem/gemsqraw/vansm/	
gp	c:/gem/gemsqraw/progs/	
g_f	c:\gem\g_f	(needed for Xsect)

Xscet

Available from http://wwwisis2.isis.rl.ac.uk/disordered/ACH/Software/index.htm

1) The file was unzipped and placed in Gem directory c:\gem

A1.1.2. Information about sample

Before beginning data analysis following information about your sample were collected.

Sample composition

Sample height

Sample weight

Sample diameter

Packing density if a powder

Accurate density (e.g. by pychnometry)

the .raw files for the samples and the normalisation, i.e. empty diffractometer, empty can, vanadium rod etc were copied to the folder c:\gem\gem_data

A1.1.3. Running Gudrun

Gudrun was started by clicking on the gudrunn.bat or GudrunGui.bat (for gudrun2) shortcut created on installation. an existing startup file was loaded and and modified. (To do this use File > Open and browse for an existing file. Failing that, some startup files for various instruments are in c:\gudrun\StartupFiles)

Location of data files and of input files was changed accordingly. file was saved using Save As in working directory (the same as the input file directory) using a .txt suffix and an appropriate file name (eg the run number).

There was little to change on the instrument page. (Fig. 2.)

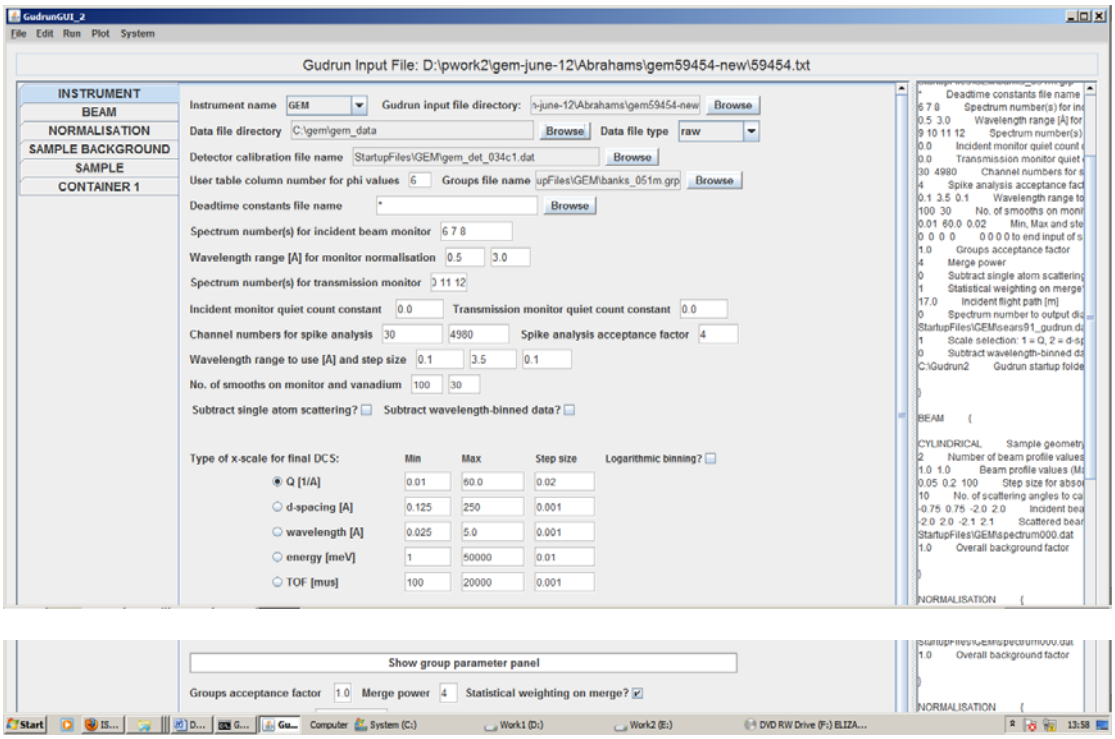

Fig. A1. 1. Instrument page of program GUDRUN.

Then on the beam page there was nothing to change (Fig. 2.)

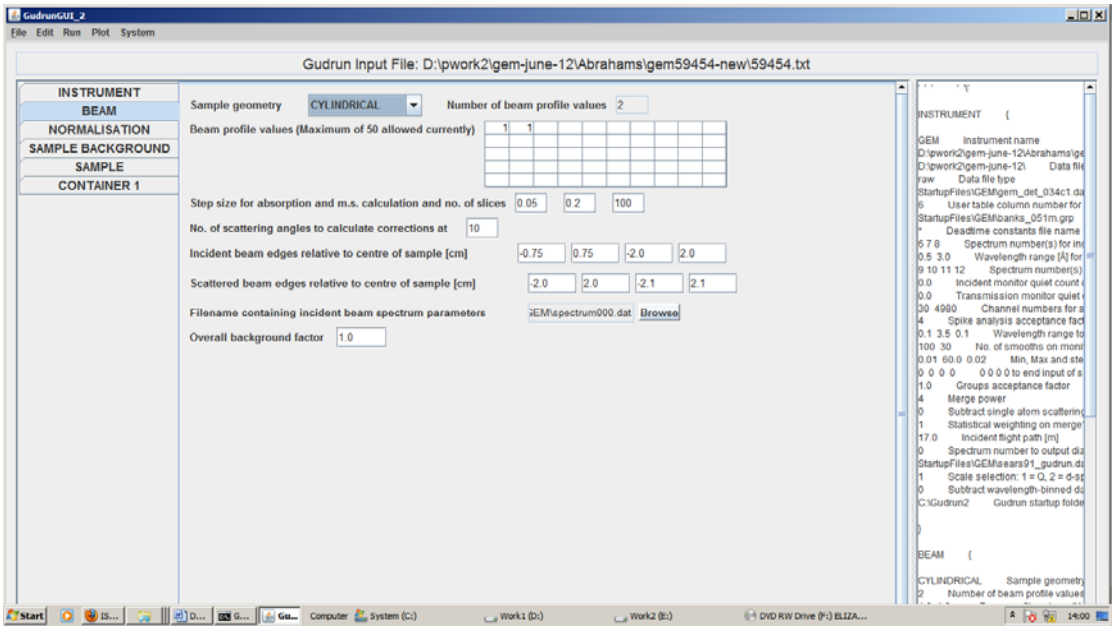

Fig. A1. 2. Beam page of data input for program GUDRUN.

On the Normalisation page the vanadium rod file(s) was entered in Normalisation data files

and the empty diffractometer data in Normalisation background data files (Fig. 2.)

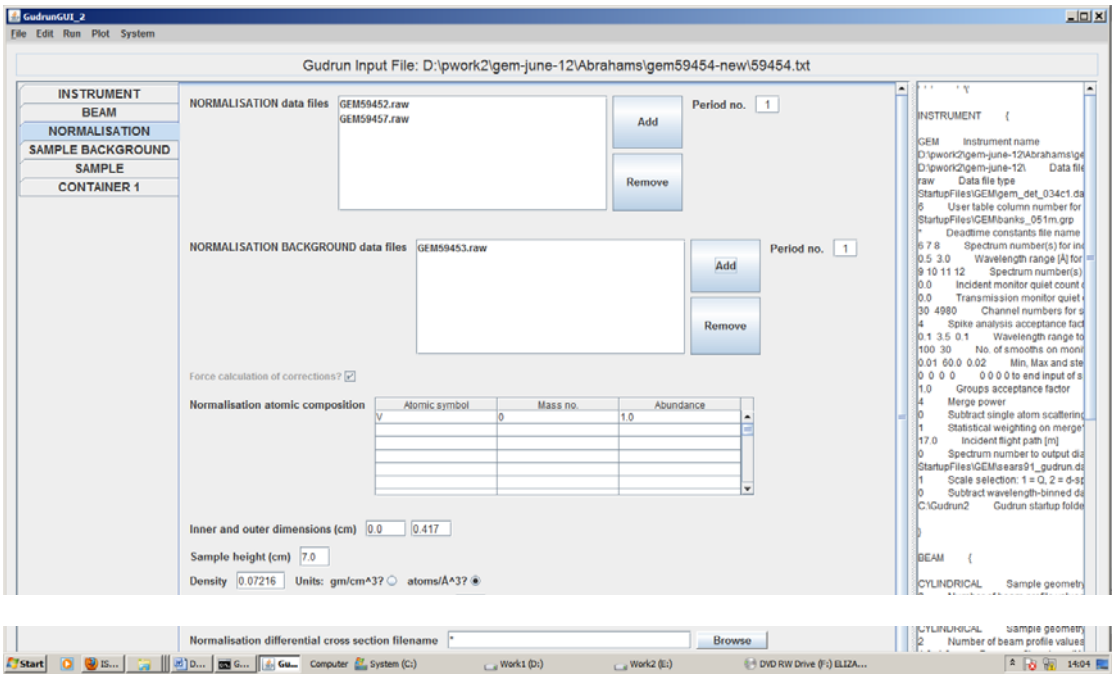

Fig. A1. 3. Normalisation page of data input for GUDRUN

On the sample Background page the empty diffractometer data file name was entered. Fig. 2.)

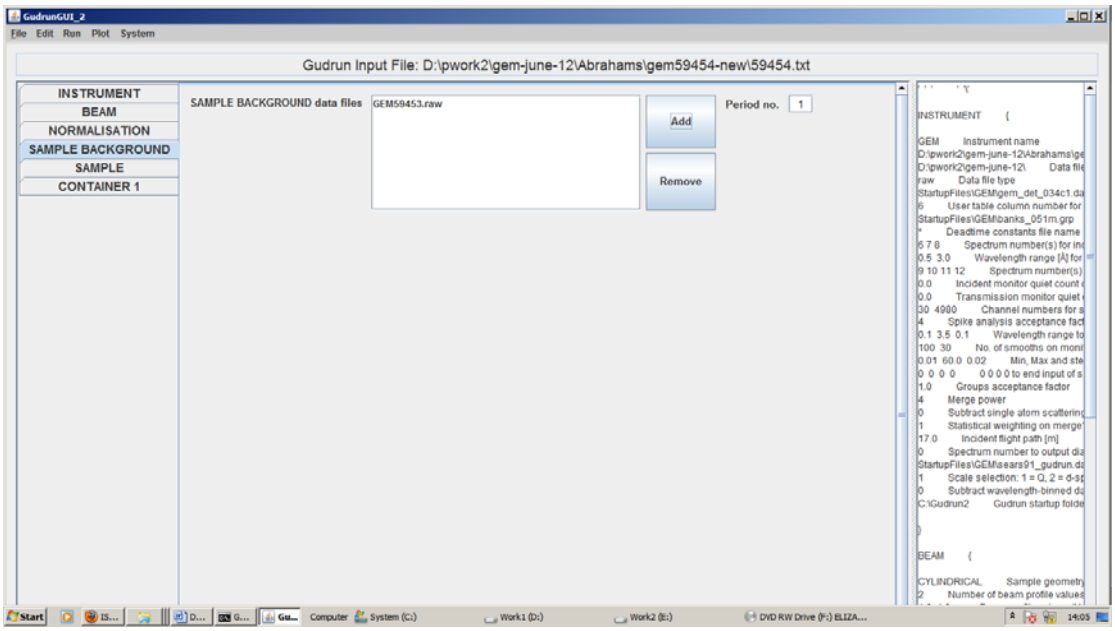

Fig. A1. 4. Sample background page of data input for GUDRUN.

the sample page was renamed appropriately Edit > Rename

Then the sample data file name was entered.

the atomic composition (note Mass no of 0 is for naturally abundant elements) was entered. the sample inner and outer radii and height and density were entered (inner zero for solid rod) in cm

the temperature was set to 0

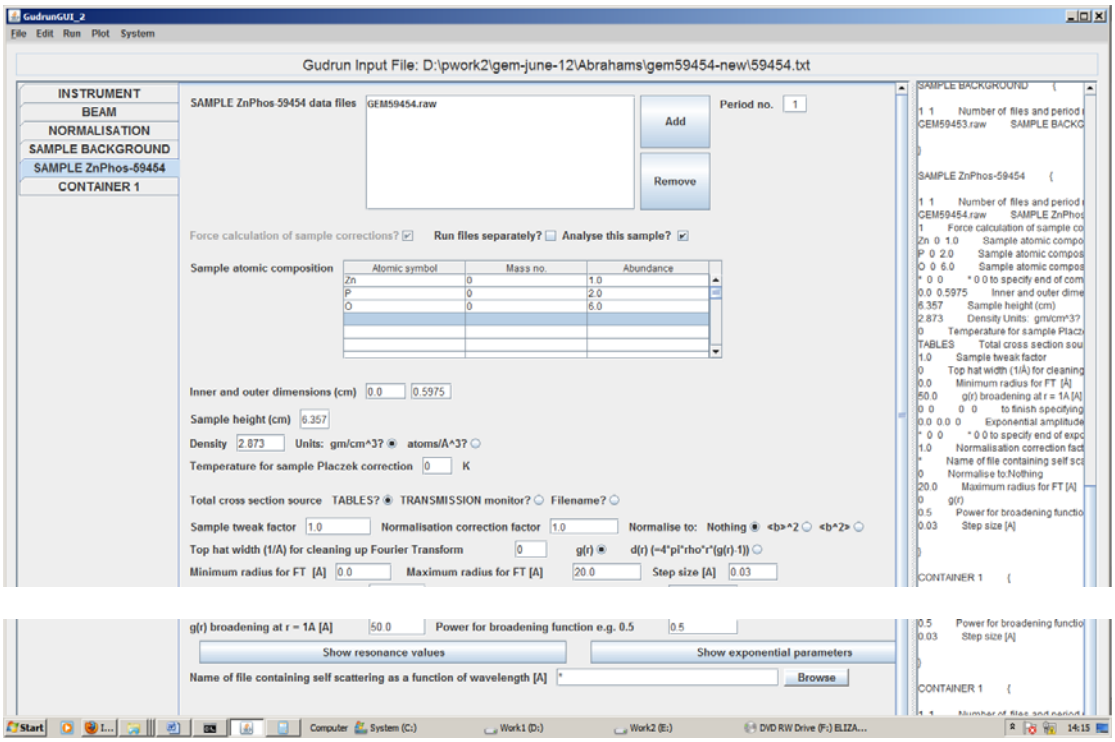

Fig. A1. 5. Sample page of data input for GUDRUN. Sample is renamed ZnPhos 59454.

The container page was deleted since no container was used for glass rods.

(Edit > Delete)

When ready Run > Check files Exist

Run > Write purge file

Run > Run purge

Run > Run GudrunN

In the accompanying command prompt window check that the DCS level differs by no more than 10%. If it is then check the density, composition and dimensions again.

A1.1.4. Checking the dcs data.

Gudrun produces a dcs file. To check this use OpenGenie

1) In Opengenie change directory to the folder where the dcs file is stored (same directory where you created it).

e.g. cd “d:\gem\gem54955”

2) type guddcs <runnumber>

eg. guddcs 59455

Hit return to accept the default instrument name (GEM). The data are stored in variable dcs where:

Bank 5 = dcs[6], Bank 4 = dcs[5], bank 3 = dcs[4], bank 2 = dcs[3] etc

3) display bank 5

d/l dcs[6]

then plot the other banks to check for consistency p/l dcs[4] etc.

The background levels should not be wildly different.

A1.1.5. Xsect

1) Open a command prompt window and navigate to the current working directory.

2) type xsect

Enter 1 for naturally abundant elements

Accept the suggested sears91.dat file

Enter the number of different elements in the composition

Enter in turn each element and the number of these per formula unit

Enter the density in g cm-3

Enter a filename prefix for the .xsect file

A1.1.6. Inelasticity calculations

1) In OpenGenie enter platom

2) Use default for most options. For the xsect file name prefix enter the name of the file you created above.

3) Plot the dcs bank and overlay the slf (self scattering)

d/l dcs[6]

p/l slf[6]

4) type pc and use default options to create dcs***.PC and slf****.PC files

A1.1.7. Creating the merged file

1) In Windows open up the spreadsheet template IntMer.xls.

2) On the QLim worksheet enter the run number and save to your working directory.

3) Read into new workbooks the files DCS***.PC and SLF***.PC (*** = run number). Copy and paste these over the data in the DCS and SLF worksheets in the IntMer spreadsheet.

4) On the QLim worksheet enter zero for Qmax for all data banks apart from Bank 5.

5) Go to the Bank 5 worksheet set alpha to 1 gradient to 0 and intercept to 0

6) Adjust alpha so that the self scattering (red) passes through pattern.

7) Adjust the gradient so the merged pattern is parallel to the total scattering then adjust the intercept until they overlap. Then decide what the max Q value should be based on how noisy the data are.

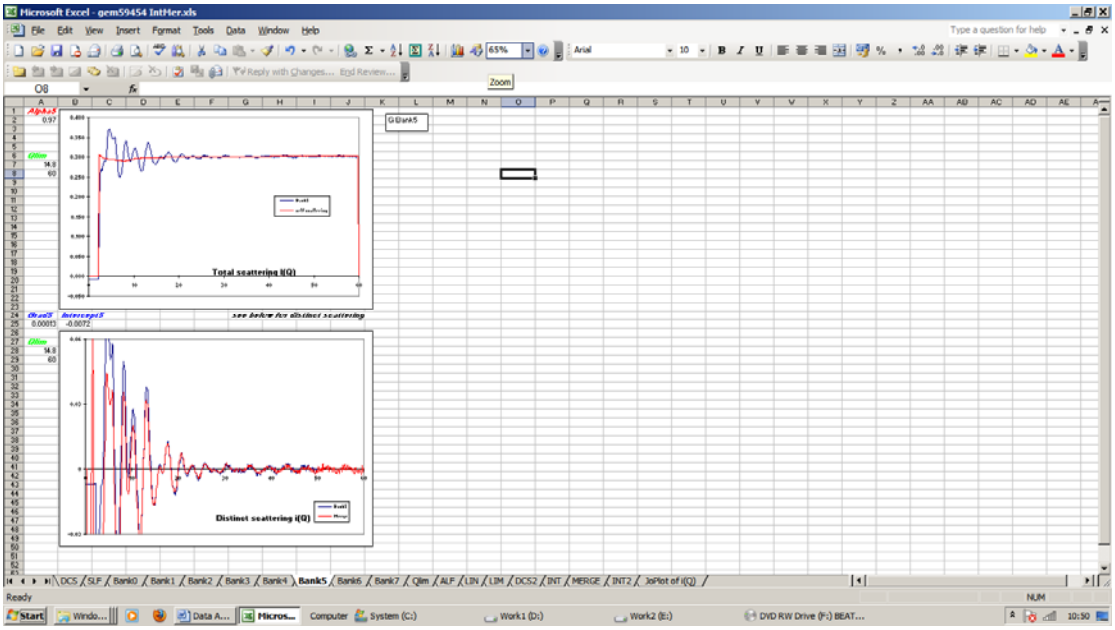

Fig. A1. 6. QLim worksheet of IntMer spreadsheet for creating the merged file.

You may need to adjust the scale on the distinct scattering. The QMin value should correspond to a trough or peak. Enter the values for Qmax and Qmin on the Qlim page

Repeat the process for Banks 4 3 and 2.

When complete press the save parameters button on the QLim page (You may need to enable macros in Excel if automatically disabled).

A1.1.8. Calculation of interference pattern (subtraction of self scattering)

1) In OpenGenie type interfere

Use defaults or enter the run number as appropriate use option 3 (default) for output.

2) type merge

Use default options or enter run number (e.g. Qstep = 0.02, Max Q = 60)

3) d/l soq to display the S(Q) data

4) i2t soq for Fourier transform

Neutron diffraction with no sharpening (0)

Max Q = 60.0

Lorch function (1)

Rmax (10.0)

Dr(0.01)

Tor constant (none)

5) d/l dor to view

A1.1.9. Initial fitting of background slope in D(r)

1) in OpenGenie type lowq

Use this to help decide on linear region. Set the max Q for plot ca. 1. You may need to adjust this e.g. 1.5

Set the minimum Q for the fit ca 0.5

Set the maximum Q for the fit ca 0.9

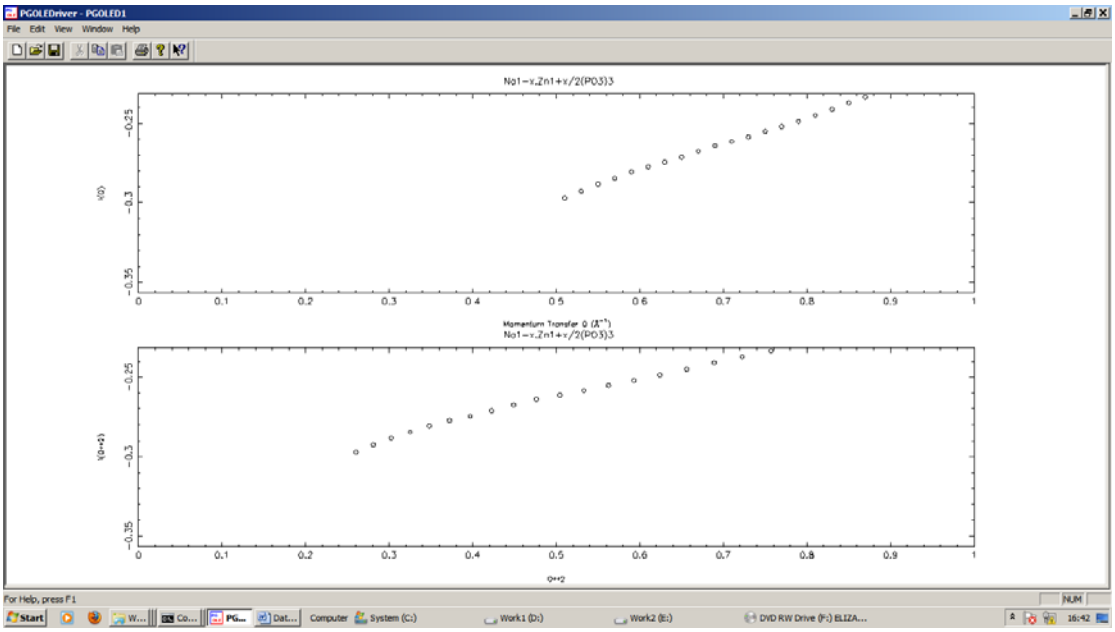

Fig. A1. 7. Initial fitting of background slope in D(r)

Ignoring the first few points try and obtain the best fit to the data. Repeat the process and when happy save the output using option 1

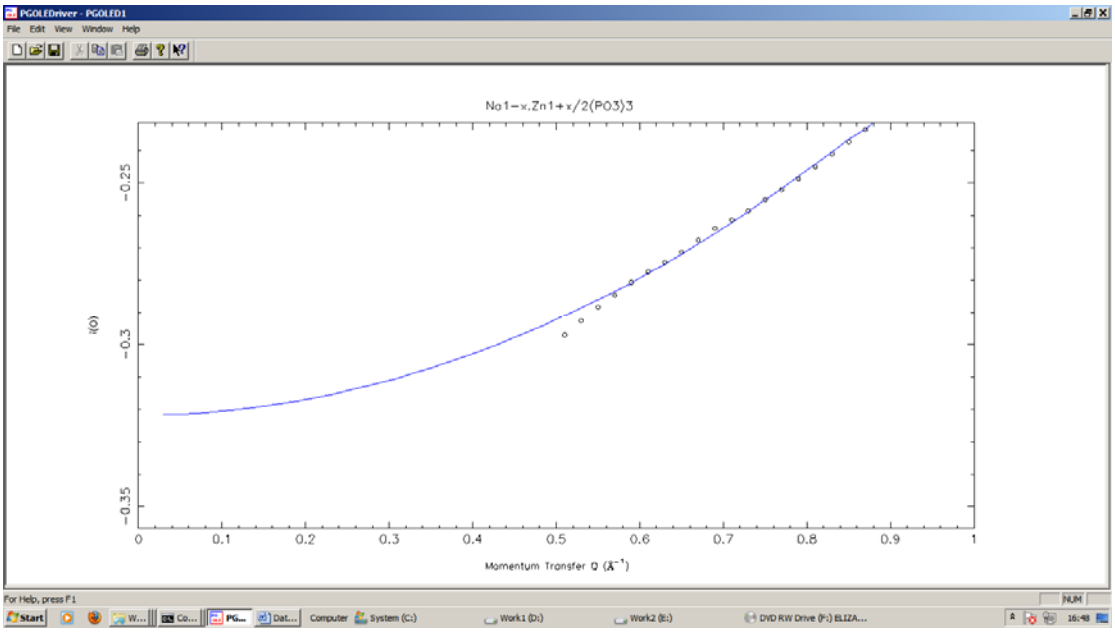

Fig. A1. 8. Best fit for initial fitting of background slope in D(r).

2) i2t soq_lowq (Fourier transform)

d/l dor

you may need to alter the range e.g d/l dor 0 10 -1 1.2

Use the plot to work out the approximate fitting ranges for the peaks. Use the cursor if necessary.

c (for cursor)

in the graphics window x gives position y height and e to exit cursor mode.

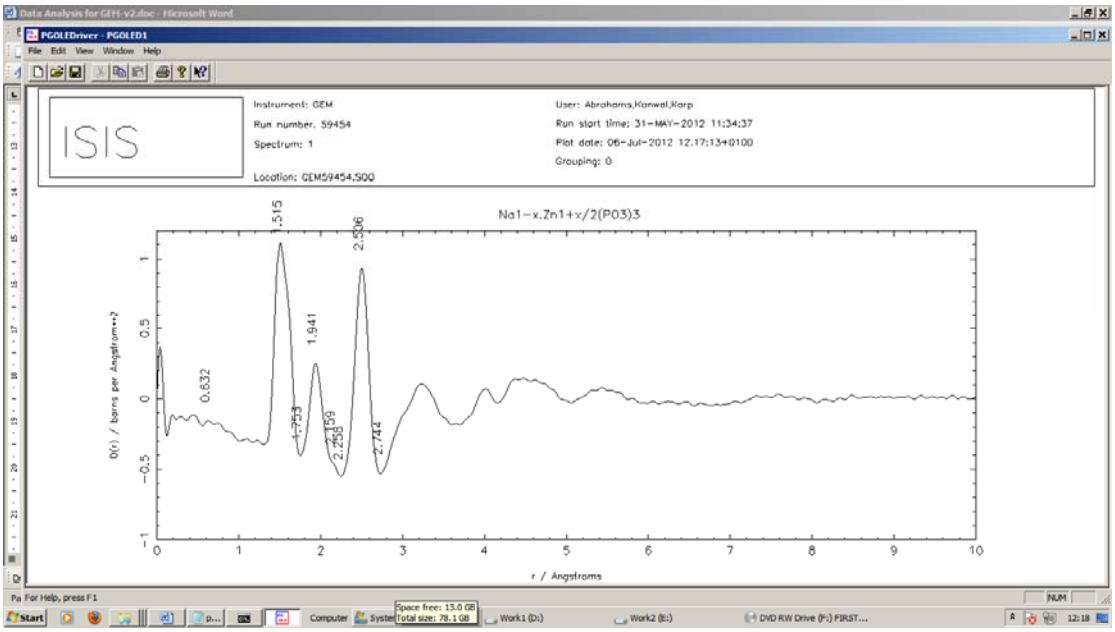

Fig. A1. 9. Final fit to *T*(*r*)

3) In OpenGenie type pnfit dor (this is to fit the D(r) data to get the slope at the start of the data)

Enter the fitting range for the peak e.g. 0.5 1.75

Enter parameters from a previous file (3) or type them in directly (1)

For direct entry:

Enter number of peaks in model e.g. 2

s p (set parameters)

Background constant = 0

Slope = -0.2

Position 1 = 1.5

Sigma 1 = 0.05

Area 1 = 1

Position 2 = 1.6

Sigma = 0.05

Area 2 = 0.5

(Adjust values accordingly)

f 1 (fixes the first background parameter)

help is available if required (help)

d p displays parameters

g for go

repeat for a few cycles, until convergence.

Make a note of the value of slope

e to exit

save the parameters with errors to the default file pnfit.param

d/l dor 0.5 1.8 (for example)

a/pc $blue (changes plot colour)

p/l pnfit[3] the fit to each peak is an array element the total fit is the last array element (so for a 2 peak fit pnfit[3] is the total fit)

Using notepad edit the xsect file to get To(r) per atom

Need to rescale data by To(r)/|background slope| from the fit (also in pnfit.param)

soq2 = soq_lowq* To(r)/|background slope|

wr soq2 “gem59454_soq_scale” This is the I(Q) i.e. distinct scattering (i.e. minus self)

i2t soq2 to get the Fourier transform of corrected S(Q)

this time put the correct T(r) constant per atom

A1.1.10. Final fit to T(r)

The corrected T(r) data are in tor[1]

Pnfit tor[1]

Name of file= pnfit.tor

Fitting range 0.5 2.75

Qmax = 60

Lorch function 1

Then either read a previous file or enter new parameters

For new parameters enter the number of peaks. This time try to fit all the peaks in the range. You may need to fix some of the parameters and introduce them later. Use s p to enter the parameters. Use clear to clear a fixed parameter.

Set the first to background pars to 0

f 1,2 fixes first two background pars

g for go

do you wish to restore parameters N

This keeps the new parameters

E

Save the parameters with user specified name eg. final-fit.pnparm

Ascii file option 1 ascii data in pnfit.dat

To view the plot in OpenGenie

a/pc $black

d/l tor[1] 0.5 2.75

a/pc $red

p/l pnfit[6] (overlays the total fit for a 5 peak model)

a/pc $blue

p/l pnfit[1]

p/l pnfit[2]

p/l pnfit[3]

p/l pnfit[4]

p/l pnfit[5] (overlays the individual peaks)

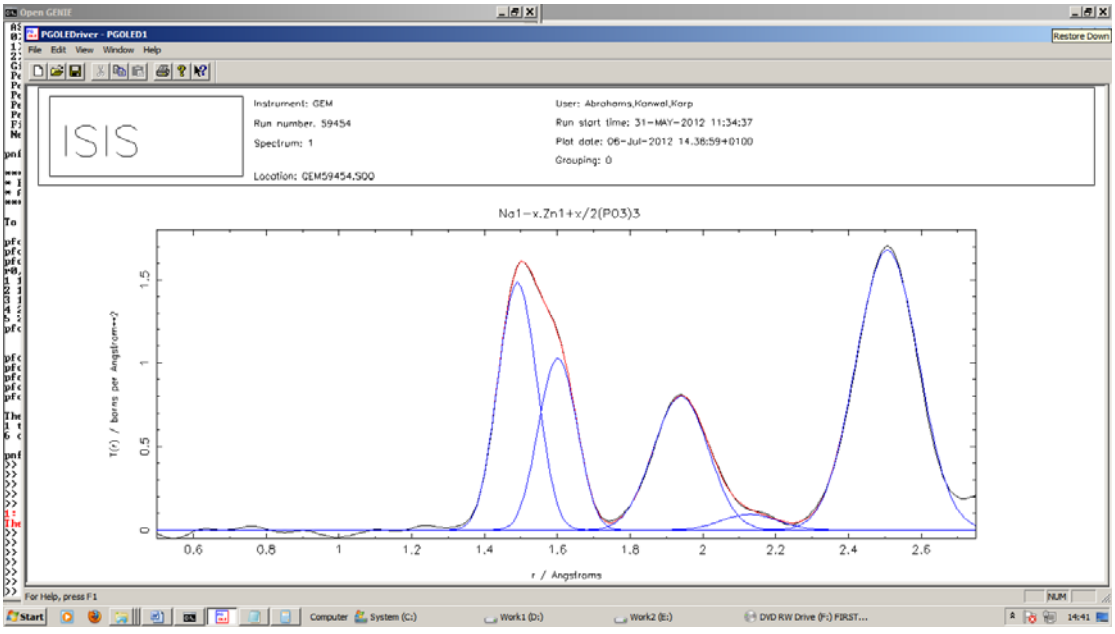

Fig. A1. 10. Final fit to T(r).

To save a hard copy of the current plot type hardcopy. This saves the file into genie.ps which can be opened using gsview etc. and saved as a jpg or other format as required.

In command prompt (you can spawn a subprocess directly from genie using j/p (exit to return back)

%gp%pn2px This gives the coordination numbers with esds.

Enter the file name from the best fit default pnfit.pnparm Then enter the options as below.

Fig. A1. 11. Coordination numbers displayed in command prompt window.

The results are stored in the .pxparm file.

Appendix A2 Supplementary Information for Chapter 6

A2.1 Cement formation with Ti and Al containing invert phosphate glass formulations

Table A2. 1 Summary of cements prepared from Al and Ti containing glasses

Glass composition	Acid	G:A:L
$5.41Na_2O:8.1TiO_2:27ZnO:27CaO:32.4P_2O_5$	VPAAA	4:1:1.5
$5.1Na_2O:5.1Al_2O_3:29.5ZnO:29.5:CaO.32.5P_2O_5$	VPAAA	4:1:1.5

A2.1.1 $5.41Na_2O:8.1TiO_2:27ZnO:27CaO:32.4P_2O_5$

Titanium containing glass of composition $5.41Na_2O:8.1TiO_2:27ZnO:27CaO:32.4P_2O_5$ was prepared and used for making cement with (VPA-AA) co-polymer. Fig.A2.1 shows ^{31}P MAS-NMR spectra of the glass and set cement. The glass spectrum shows a main resonance at about 8 ppm corresponding to Q^1 species with a shoulder at about 3 ppm attributed to Q^0 species.

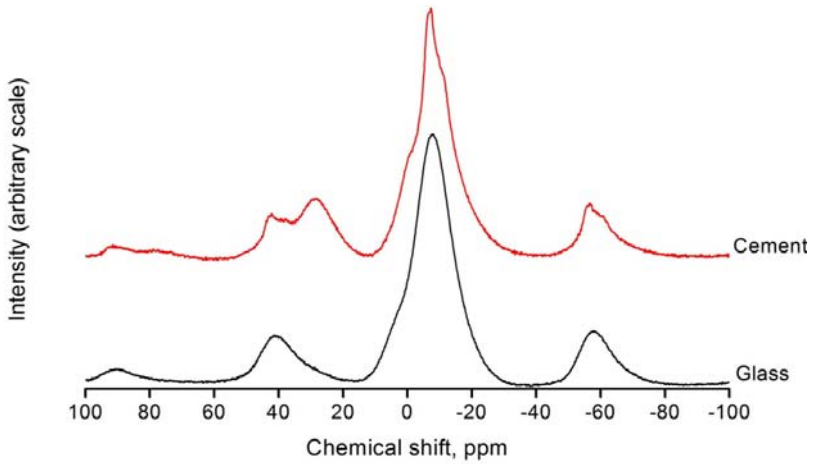

Fig. A2. 1. ^{31}P MAS-NMR spectra of titanium substituted glass and its cement with (VPA-AA) co-polymer.

The cement spectrum shows the same basic resonances as the glass, with addition of a sharp Q1 resonance, indicating some crystallisation. Resonance for (VPA-AA)co-polymer is observed for 28.4 ppm.

A.2.2 $5.1Na_2O:5.1Al_2O_3:29.5ZnO:29.5:CaO.32.5P_2O_5$

Cement formation with the glass composition $5.1Na_2O:5.1Al_2O_3:29.5ZnO:29.5:CaO.32.5P_2O_5$ was investigated. Cements set completely in 24 h. ^{31}P and ^{27}Al MAS-NMR spectra of the glass and set cement are presented in Fig. A2.2.

(a)

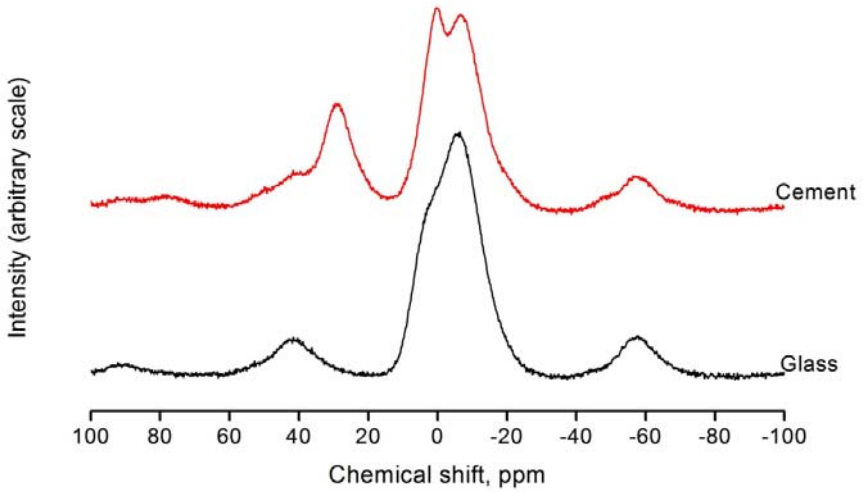

(b)

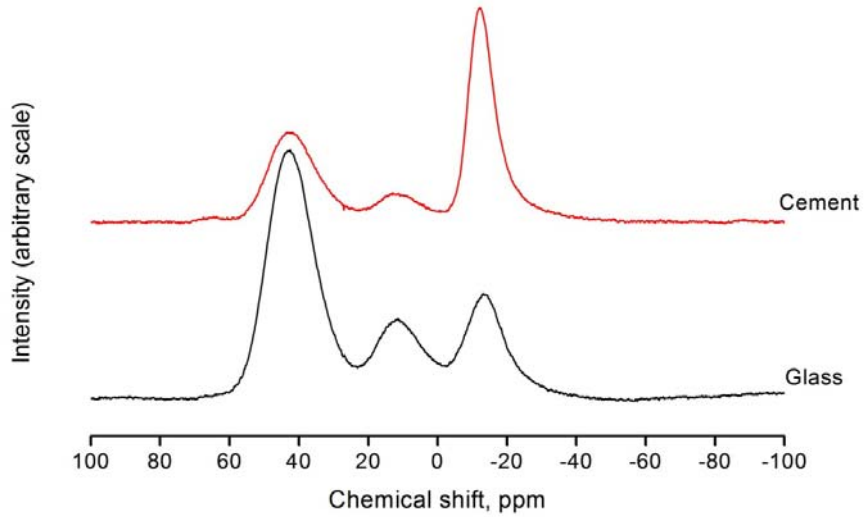

Fig. A2. 2. (a) ^{31}P and (b) ^{27}Al MAS-NMR spectra of glass composition $5.1Al_2O_3$:29.5ZnO: 29.5CaO: $32.5P_2O_5$ and its cement with (VPA-AA) co-polymer.

The ^{31}P MAS-NMR spectrum of the glass shows resonances at -6 ppm and 3.8 ppm which correspond to Q^1 and Q^0 species, respectively. The cement of this glass composition shows a decrease in chemical shift and an increase in proportion of Q^0 species.

The ^{27}Al spectrum for the glass shows peaks at about 44 ppm, 11 ppm and -13 ppm corresponding to Al (IV), Al(V) and Al(VI) respectively. The ^{27}Al spectrum of the cement shows the same resonances however a significant decrease in intensity of Al(IV)and Al(V) and an increase in Al (VI) is observed, which indicates the chelating role of aluminium in these cements